Collective plasmonic excitations in two- dimensional metamaterials based on near-field coupled metallic nanoparticles

François Fernique

UNIVERSITÉ DE STRASBOURG

ÉCOLE DOCTORALE PHYSIQUE ET CHIMIE PHYSIQUE

Institut de Physique et Chimie des Matériaux de Strasbourg (IPCMS)

THÈSE

présentée par :

François FERNIQUE

soutenue le : **18 juillet 2019**

pour obtenir le grade de : **Docteur de l'université de Strasbourg**

Discipline/ Spécialité : Physique de la matière condensée

Collective plasmonic excitations in two-dimensional metamaterials based on near-field coupled metallic nanoparticles

THÈSE dirigée par :

M. WEICK Guillaume	Maître de Conférences, Université de Strasbourg

RAPPORTEURS :

M. FELBACQ Didier	Professeur, Université de Montpellier
M. MARIANI Eros	Senior lecturer, University of Exeter

AUTRES MEMBRES DU JURY :

Mme HALTE-FILIPPI Valérie	Professeure, Université de Strasbourg
M. JALABERT Rodolfo	Professeur, Université de Strasbourg
M. WEINMANN Dietmar	Directeur de Recherche, IPCMS

A Morgane,

Contents

Remerciements

Je souhaite tout d'abord remercier les membres du jury, Didier Felbacq, Eros Mariani, Valérie Halte-Filippi, Rodolfo Jalabert et Dietmar Weinmann qui ont accepté de lire et d'évaluer ce travail.

Comme il se doit, je tiens également à remercier chaleureusement mon directeur de thèse, Guillaume Weick pour ces quatre années durant lesquelles il m'a guidé tout au long de mes recherches (en réalité il m'a supporté pendant six ans). Merci à lui d'avoir initié ce projet qui devait (au départ) compléter une théorie déjà bien établie et qui s'est transformé petit à petit en une entité tentaculaire. Jamais plus un preprint de 30 pages à deux auteurs, pour la prochaine fois on le coupera en deux c'est décidé ! Un grand merci également à lui d'avoir insisté pour que je fasse trois années de monitorat qui m'ont permises de garder un pied dans l'enseignement. Ses conseils dans ce domaine ont toujours été très avisés et précieux.

Merci aussi aux autres membres permanents de l'Equipe de Physique Quantique Mésoscopique quantique, Rodolfo et Dietmar sur qui j'ai toujours pu compter en cas de questions sur mes recherches. Merci Dietmar pour ces tutoriels Python indispensables. Merci également aux autres post-doctorants et doctorants de l'équipe qui se sont succédés durant ma thèse, Charles, Christina, Keith, Adam, Ousmane et Mauricio avec qui j'ai pu discuter de sciences et de bien plus encore au quotidien.

Bien évidemment, je remercie tous mes amis et collègues avec qui j'ai partagé mes journées pendant mes années à l'IPCMS. Mention particulière à Etienne, Léo, Mauricio, Luis, Matias, Guillaume, BenBen et BigBen, Anna (j'en oublie très certainement) qui ont dû me supporter pendant la rédaction de cette thèse. Merci aussi à mes amis en dehors des murs du laboratoire pour ces sessions du « club lecture » chez Arthur et Oussama.

Un grand merci à ma famille et à mes proches qui ont su me soutenir pendant ces années de thèse. Ils m'ont offert des échappatoires temporaires mais salutaires durant les périodes compliquées de mon doctorat (en particulier la période de rédaction simultanée de la thèse et de l'article). Merci particulièrement à mon père pour ses conseils afin d'aborder cette thèse dans un contexte plus large et de pouvoir voir plus loin d'un point de vue personnel.

Enfin merci à mon épouse, Morgane pour son soutien indispensable au quotidien durant ces quatre années. Merci de m'avoir soutenu lorsque la rédaction me semblait insurmontable.

Résumé

Depuis plusieurs décennies l'étude des métamatériaux[1] a permis de repousser les limites fondamentales de la physique dans un certain nombre de domaines. Un exemple important est la démonstration à la fois théorique [7, 11] et expérimentale [15] de la possibilité de réaliser des lentilles avec une résolution en-deçà de la limite de diffraction (gouvernée par le critère de Rayleigh [6]). Ces lentilles particulières s'appuient sur le concept de réfraction négative [7, 10] qui permet la focalisation de la lumière à des échelles sub-longueur d'onde. De même, la possibilité de contrôler la lumière à de telles échelles de tailles a conduit à la démonstration en 2006 du concept de « cape d'invisibilité » [39] qui, pour une longueur d'onde donnée, permet de dissimuler une certaine région des perturbations électromagnétiques et ainsi d'empêcher une détection optique de cette région. Bien qu'ayant concerné dans un premier temps la recherche de nouvelles propriétés optiques, les métamatériaux permettent à présent également l'étude de nouvelles propriétés mécaniques [22, 24, 36, 37].

Dans ce manuscrit de thèse nous nous concentrons sur les métamatériaux plasmoniques et en particulier sur les métamatériaux bi-dimensionnels constitués de nanoparticules métalliques. En effet, de telles nanostructures supportent des excitations collectives appelées *plasmons de surface localisés* (dénotés LSPs pour Localized Surface Plasmons ou plasmons dans le manuscrit) présentant des propriétés électromagnétiques intéressantes. Ces plasmons correspondent à une oscillation collective des électrons de surface appartenant à la nanoparticule. La fréquence de résonance de telles excitations est reliée à la fréquence de Mie [58] correspondant, pour les métaux nobles, aux longueurs d'onde associées au spectre du visible ou du proche infrarouge. En pratique, la fréquence de Mie ne correspond pas exactement à la fréquence de résonance réelle. En effet, plusieurs mécanismes induisent un décalage de la fréquence de résonance mesurée expérimentalement par rapport à celle évaluée avec la théorie de Mie. Ces mécanismes, (i) l'effet de spill-out, (ii) un décalage radiatif et (iii) un autre dû aux interactions entre le plasmon et les paires électrons-trous à l'intérieur de la nanoparticule apportent chacun une contribution bien distincte au décalage en fréquence observé. L'effet de spill-out [56–58] induit une réduction de la fréquence de résonance qui peut être expliquée en traitant le plasmon comme un objet quantique et non classique. Pour des nanoparticules de petites tailles, la fonction d'onde permettant de calculer la densité électronique s'étend en réalité au-delà des limites géométriques de l'objet. Ainsi, une partie des électrons ne contribuent pas à la résonance plasmonique ce qui diminue la fréquence de résonance (correspondant à un décalage vers le rouge). Les deux derniers mécanismes sont reliés au couplage du plasmons avec les différents environnements (photonique et électronique) de la nanoparticule. Le décalage radiatif

[1] Du grec $\mu\varepsilon\tau\alpha$ « méta » qui signifie « au-delà ».

correspondant à une augmentation de la fréquence de résonance (donc à un décalage vers le bleu) et étant proportionnel au rayon a à la puissance 4 de la nanoparticule est analogue au *décalage de Lamb* [65, 66] observé en physique atomique. La dernière contribution est induite par le couplage avec l'environnement électronique et correspond à un second décalage vers le rouge. Cet effet, purement quantique, est proportionnel à l'inverse du rayon de la nanoparticule (à un facteur logarithmique près) [67, 68]. Expérimentalement, la fréquence de résonance des plasmons peut être extraite à l'aide de techniques de mesures spectroscopiques (absorption ou diffusion par exemple). Ce type de mesures permet également de déterminer le temps de vie de ces excitations par l'étude de la largeur à mi-hauteur γ_0 du pic observé qui est inversement proportionnel à ce temps de vie ($t_0 \propto 1/\gamma_0$). Pour le cas des plasmons, cette largeur provient de plusieurs mécanismes. D'une part, de processus non radiatifs, à savoir des pertes ohmiques ainsi que *l'amortissement Landau* (qui est un effet purement quantique) et d'autre part, de pertes radiatives.

Dans des réseaux ordonnés de nanoparticules métalliques la situation présentée ci-dessus est cependant modifiée de manière importante en raison des interactions électromagnétiques entre chacun des constituants du métamatériau. Ces interactions donnent lieu à l'apparition de nouveaux modes plasmoniques appelés *plasmons collectifs* qui s'étendent sur l'intégralité de la structure les supportant. Ces modes présentent un grand intérêt de par la possibilité de les utiliser afin de propager de la lumière confinée (à une échelle sub-longueur d'onde) sur des distance de l'ordre du μm. Ainsi, la chaîne régulière composée de nanoparticules métalliques constitue une plateforme idéale pour l'étude des propriétés des plasmons collectifs et en particulier concernant la propagation. De nombreux travaux aussi bien expérimentaux [78, 126, 129–131] que théoriques [76, 80, 112, 127, 132–135] ont été conduits afin de décrire la propagation des plasmons collectifs. Expérimentalement, Maier *et al.* [78] ont par exemple observé une longueur de propagation de $900\,\mathrm{nm}$ pour une chaîne régulière constituée de nanocylindres en argent de dimension $90\,\mathrm{nm} \times 30\,\mathrm{nm} \times 30\,\mathrm{nm}$. Dans de telles structures, la fréquence des modes collectifs peut être mesurée grâce à l'étude des spectres d'extinction comme le montre la figure 1 de la même manière que pour les nanoparticules uniques. Un autre aspect important apparaît lorsque l'on considère des structures suffisamment larges comparées à la longueur d'onde du plasmon : les effets retards liés à l'interaction de Coulomb. Ces effets retards affectent de manière cruciale la relation de dispersion (et donc la propagation) des plasmons collectifs de la chaîne. De tels effets ont par exemple été pris en compte dans les travaux de Weber et Ford [133] en se basant sur la résolution numérique des équations de Maxwell qui contiennent de manière exacte les interactions retardées. Ainsi, dans le cas de chaînes de nanoparticules métalliques, il n'est pas possible de considérer uniquement les résultats de la nanoparticule unique. En effet, la présence des interactions de Coulomb modifie de façon drastique la situation dans le cas de plasmons collectifs en comparaison à des LSPs isolés (i.e., effets retards et amortissement).

Dans cette thèse nous nous concentrons plus particulièrement sur l'étude de réseaux plasmoniques à deux dimensions constitués de méta-atomes formant des *métasurfaces*. Actuellement, un nombre important de métasurfaces constituées par des méta-atomes de différents types sont étudiées permettant une manipulation de la lumière de manière très variée (voir e.g., Refs. [81–88]). De telles métasurfaces sont montrées à la figure 2. Les études menées sur ces structures couvrent un large spectre d'aspects fondamentaux. Par exemple, les métasurfaces montrées à la Fig. 2(a) et Fig. 2(c) ont été fabriquées afin d'étudier un type particulier de résonance plasmonique appelée

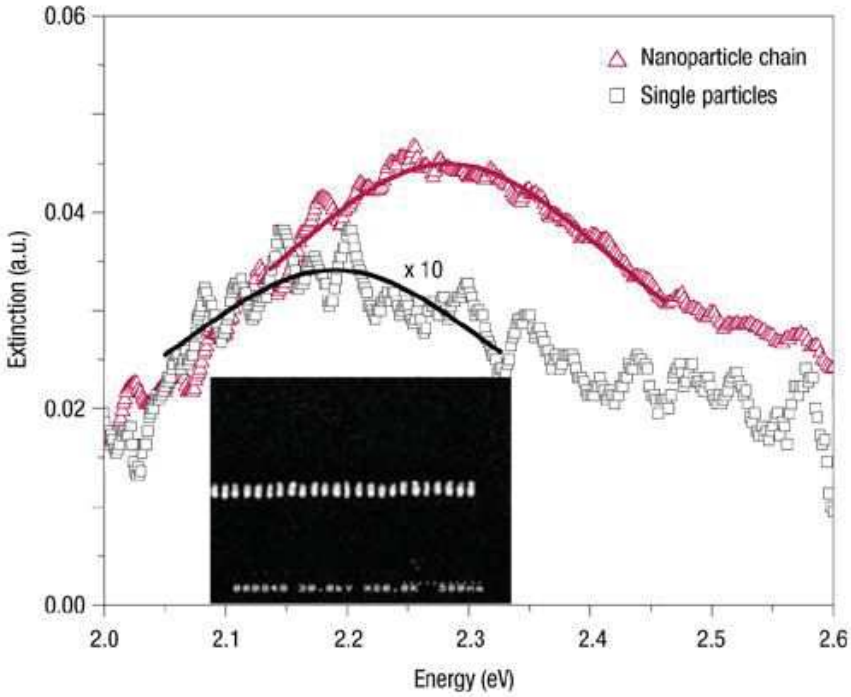

Figure 1: Spectre d'extinction associé à une chaîne de nanocylindres d'argent de dimensions $90\,\mathrm{nm} \times 30\,\mathrm{nm} \times 30\,\mathrm{nm}$ (un micrographe électronique de la chaîne est montré dans l'encart). A l'intérieur de la chaîne, les cylindres sont espacés de $50\,\mathrm{nm}$. Les carrés noirs montrent les résultats obtenus pour un seul cylindre tandis que les triangles rouges correspondent à l'extinction de la chaîne complète en fonction de l'énergie des photons entrants. Les lignes correspondent un un fit lorentzien des données expérimentales. L'axe le plus long des cylindres est orienté perpendiculairement à l'axe de la chaîne. Figure reproduite de la Ref. [78].

résonance de réseau (SLR: Surface Lattice Resonance) dans des réseaux avec des géométries particulières. D'autres métasurfaces ont été développée afin d'améliorer les techniques de fabrication déjà existantes [Figs. 2(f),(g)] ou encore d'étudier l'interaction entre la lumière et la matière [Figs. 2(e)], la fluorescence [Figs. 2(b)] ou bien la manipulation de la polarisation de la lumière [Figs. 2(d)] par exemple.

En principe, les métasurfaces plasmoniques peuvent être étudiées dans trois régimes distincts qui dépendent de la séparation d entre les constituants et de la longueur d'onde λ associée à la résonance plasmonique. Actuellement, le régime le plus exploré expérimentalement est le *régime d'interférences* dans lequel $a \ll d \simeq \lambda$ où a correspond au rayon des nanoparticules qui constituent la métasurface. Dans ce régime, les excitations plasmoniques interfèrent dans le champ lointain pour former des SLRs. De tels modes collectifs apparaissent sous forme de pics très fins dans des expériences spectroscopiques [91–93] ce qui correspond à des modes de grande durée de vie (comparé au plasmons isolés). De par leur longévité, les SLRs constituent donc un support idéal pour l'étude de phénomènes de physique fondamentale. Ainsi, parmi les applications des métasurfaces

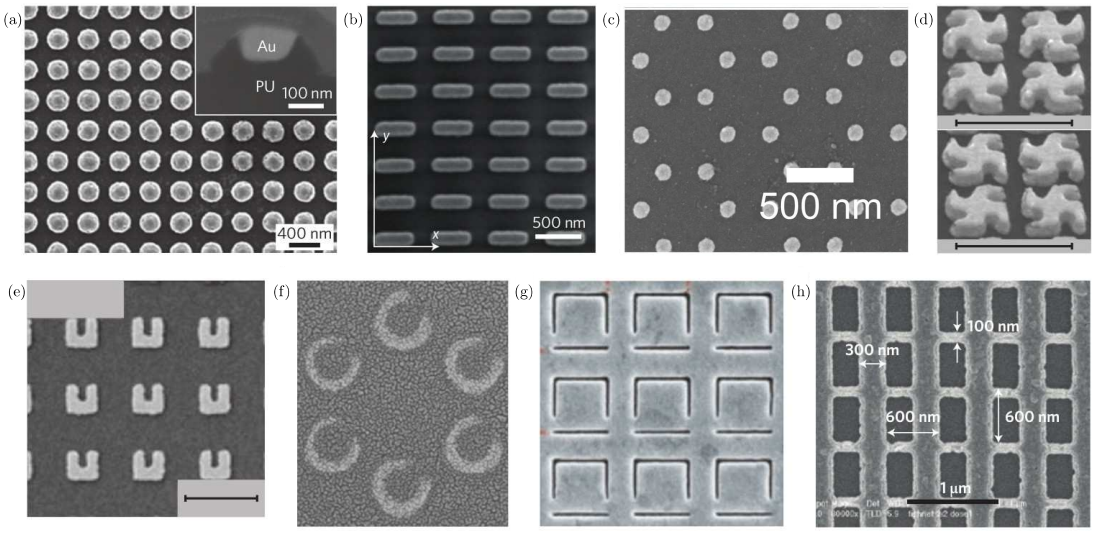

Figure 2: Exemples de métasurfaces plasmoniques réalisées expérimentalement. (a) Réseau de nano-disques (image reproduite de la Ref. [86]). (b) réseau d'antennes plasmoniques nano-imprimées (image reproduite de la Ref. [84]). (c) Réseau en nid d'abeilles composé de nanoparticules sphériques fabriquées par lithographie électronique (image reproduite de la Ref. [88]). (d) gammadions droits (haut) et gauches (bas) formant une métasurface chirale fabriquée par lithographie électronique (image reproduite de la Ref. [81]). (e) réseau de résonateurs magnétiques fabriqués par lithographie électronique (image reproduite de la Ref. [87]). (f) Résonateurs magnétiques fabriqués par lithographie (image reproduite de la Ref. [83]). (g) Résonateurs magnétiques asymétriques fabriqués par flux d'ions (image reproduite de la Ref. [85]). (h) Structure en double filet fabriquée par nano-impression (image reproduite de la Ref. [82]). Les images ont été adaptées des Refs. [33] et [88].

supportant des résonances plasmoniques de réseau on trouve la possibilité de réaliser des diodes émettrices [84, 94] (à des échelles sub-longueur d'onde), la réalisation de lasers [45, 96–100] ou encore de condensats de Bose-Einstein [101, 102]. Le second régime dans lequel les métasurfaces plasmoniques peuvent être étudiées est celui où $a \ll d \ll \lambda$ où les interactions en champ proche peuvent aussi être négligées. Les métasurfaces à gradient de phase sont typiquement étudiées dans un tel régime. Ce type de métasurface permet par exemple de concevoir des outils optiques (comme des lames quart d'onde) [103–105] à des échelles sub-longueur d'ondes ou encore la production d'hologrammes [106].

Le dernier régime pour lequel $a \lesssim d \ll \lambda$ est celui où les interactions de champ proche sont responsables de la création des plasmons collectifs et ne peuvent donc plus être négligées. Dans ce manuscrit, nous nous concentrons de plus sur le régime où $3a \lesssim d$ où il a été montré [76, 77] que la contribution majoritaire provient de l'interaction dipôle-dipôle quasistatique. Ainsi, il est possible de définir une structure de bandes pour les plasmons collectifs de manière analogue à celle utilisée pour le modèle des liaisons fortes décrivant les électrons dans les cristaux. De plus, avec cette description, il a été prédit que certains modes plasmoniques présentent des propriétés

similaires à celles des électrons dans les cristaux comme des plasmons de type Dirac possédant des propriétés relativistes dans des réseaux en nid d'abeilles par exemple [108, 109]. Cependant, les investigations expérimentales sur ce type de modes plasmoniques restent extrêmement limitées de par la complexité à fabriquer des échantillons constitués de petites nanoparticules ($a \sim 10-20\,\mathrm{nm}$) sur de grandes surfaces. Ainsi la plupart des travaux, aussi bien expérimentaux [78, 126, 129–131] que théoriques [76, 80, 112, 127, 132–135], se concentrent sur les systèmes unidimensionnels tel que les chaînes régulières de nanoparticules métalliques.

D'un point de vue théorique, les relations de dispersion des plasmons collectifs peuvent être calculées de plusieurs manières. La première consiste à extraire numériquement les solutions retardées des équations de Maxwell de manière purement classique [76, 112, 127, 132–134]. Cette technique à l'avantage de fournir directement les relations de dispersion plasmoniques avec les effets retards des interactions électromagnétiques ainsi que les amortissements radiatifs associés à ces modes. Cependant une telle méthode nécessite de lourds calculs numériques et doit être réitérée pour chaque géométrie différente. De plus, elle ne permet pas la prise en compte des effets de nature quantique (type amortissement de Landau) qui sont pourtant cruciaux dans le cas de petites nanoparticules. Afin de calculer ces effets de nature quantique, il existe une seconde méthode basée sur l'approche de systèmes quantiques ouverts déjà employée pour l'étude de chaînes plasmoniques [80, 135–137]. Contrairement aux méthodes numériques, cette technique permet de calculer de manière analytique les relations de dispersion plasmoniques en prenant les effets à longue portée des interactions dipolaires. De plus, elle permet d'inclure de manière immédiate les effets quantiques sur la structure de bandes et d'en extraire les propriétés qui en résultent. En contrepartie, les effets retards des interactions électromagnétiques doivent être pris en compte perturbativement et non de manière exacte.

Concernant les métasurfaces plasmoniques dans le régime en champ proche, les avancées théoriques restent relativement restreintes et se limitent aux géométries simples (carré, hexagonale, etc...) ainsi qu'à quelques géométries particulières comme la structure en nid d'abeilles par exemple. Pour une telle structure, chacune des deux méthodes introduites plus haut ont été utilisées [108, 109, 138, 139]. Dans leur étude, Han *et al.* [138] ont extrait la structure de bandes des plasmons collectifs polarisés hors et dans le plan d'une métasurface en nid d'abeilles de manière numérique. De plus, les auteurs de la référence [138] ont également comparé les résultats quasistatiques à ceux tenant compte des effets retards sur la relation de dispersion des plasmons. Quelques années plus tard, la référence [108] a également étudié un système semblable de manière analytique. Les résultats présentés se concentrent sur des interactions entre proches voisins uniquement et les effets retards ne sont pas considérés. Même si une autre étude [139] inclue de tels effets pour le cas du réseau en nid d'abeilles, aucun travaux ne présente pour l'instant de résultats concernant l'amortissement des plasmons dans les réseau bi-dimensionnel et en particulier pour les modes topologiques comme les plasmons de type Dirac dans les réseau en nid d'abeilles [108, 109]. De plus, il serait intéressant de pouvoir étudier d'autre géométries présentant des modes topologiques aux propriétés particulières tel que les réseaux Lieb et kagome.

Cette thèse a donc pour but de présenter le modèle que nous avons développé afin de décrire les plasmons collectifs (et leurs propriétés) dans des métasurfaces de géométries arbitraires. À l'aide d'un formalisme de système quantique ouvert nous développons ici un modèle quantique qui permet le calcul des relations de dispersions de manière analytique en y incluant les interactions à

longue portée. De plus, grâce à l'utilisation de la théorie des perturbation, nous calculons également les effets retards ainsi que les taux d'amortissement associés aux modes plasmoniques.

Ce manuscrit introduit donc dans une première partie (chapitres 2 et 3) les principaux ingrédients théoriques utilisés pour décrire les métasurfaces plasmoniques dans le cadre de l'étude de systèmes simples (nanoparticules uniques) et uni-dimensionnels (dimères et chaînes). Le chapitre 2 introduit l'approche dite de *jellium* pour le cas d'une nanoparticule isolée considérée comme un système quantique ouvert [67, 74]. Partant du hamiltonien microscopique dans la jauge de Coulomb, nous séparons donc les coordonnées du système en cordonnées du centre de masse (correspondant aux plasmons) et coordonnées relatives (correspondant aux électrons), qui donne alors lieu à la forme générale du hamiltonien du système

$$H = H_{\mathrm{pl}} + H_{\mathrm{ph}} + H_{\mathrm{eh}} + H_{\mathrm{pl-ph}} + H_{\mathrm{pl-eh}}, \tag{1}$$

qui est également utilisée dans les chapitres 3 et 4. Dans l'Eq. (1), H_{pl} correspond uniquement au degrés de liberté plasmoniques tandis que H_{ph} et H_{eh} décrivent respectivement les degrés des photons et des électrons de la nanoparticule. Enfin, les hamiltoniens $H_{\mathrm{pl-ph}}$ et $H_{\mathrm{pl-eh}}$ correspondent aux interactions entre le système plasmonique et les photons et avec les électrons respectivement. Le hamiltonien (1) est caractéristique d'un système quantique ouvert, où un petit système quantique (le plasmon) est couplé aux environnements (électronique et photonique) extérieurs. L'utilisation de l'approximation de champ moyen ainsi que de la théorie des perturbations permet alors de dériver les expressions analytiques des différentes contributions à la largeur de bande plasmonique (en évaluant les amortissements radiatif et Landau) ainsi que les décalages en fréquence observés dans les expériences. Ces résultats, déjà décrits par le passé dans la littérature [64, 67, 68], sont résumés aux Secs. 2.3 et 2.4.

Ainsi, à l'aide d'une règle d'or de Fermi pour le hamiltonien $H_{\mathrm{pl-ph}}$, l'expression du taux d'amortissement radiatif pour la nanoparticule unique est donné par

$$\gamma_0 = \frac{2\omega_0^4}{3c^3} a^3, \tag{2}$$

où ω_0 est la fréquence de Mie associée au plasmon. Dans l'expression précédente, c est la vitesse de la lumière et a le rayon de la nanoparticule. On peut noter que l'amortissement radiatif (2) dépend du volume de la particule qui est relié au nombre d'électrons constituant le plasmon. De même l'expression de l'amortissement Landau est donné par (en utilisant une règle d'or sur le hamiltonien $H_{\mathrm{pl-eh}}$)

$$\Gamma_0 = \frac{3v_{\mathrm{F}}}{3a} g\left(\frac{\hbar\omega_0}{E_{\mathrm{F}}}\right), \tag{3}$$

où v_{F} et E_{F} correspondent respectivement à la vitesse et à l'énergie de Fermi et où $g(\nu)$ est donnée par

$$g(\nu) = \frac{2}{\nu} \int_{\max\{1,\nu\}}^{1+\nu} \mathrm{d}x \int_{0}^{x-\nu} \mathrm{d}y \sqrt{(x-y)(x-y-\nu)}. \tag{4}$$

Il est ici intéressant de remarquer que la dépendance avec le rayon de la nanoparticule a des deux taux de décroissance (2) et (3) présente une tendance opposée qui implique une taille de nanoparticule pour laquelle l'amortissement des plasmons est minimal.

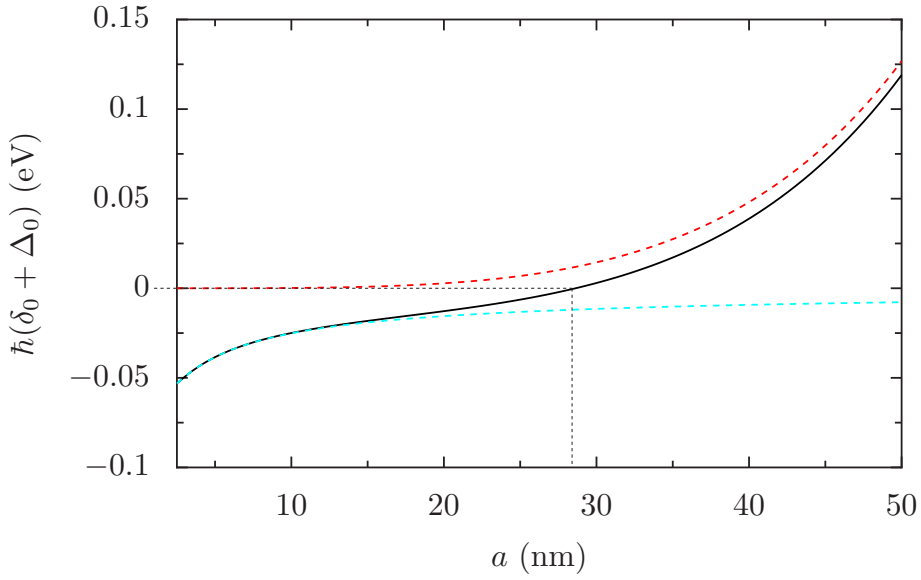

Figure 3: Décalage énergétique total $\hbar(\delta_0 + \Delta_0)$ induit sur la fréquence de Mie d'un particule d'argent unique en fonction de son rayon a. Dans la figure les paramètres pour l'argent sont donnés par $\hbar\omega_0 = 2.6\,\mathrm{eV}$ et $E_\mathrm{F} = 5.5\,\mathrm{eV}$. La ligne noire montre la somme de la contribution radiative (montrée en ligne pointillée rouge) et électronique (montrée en ligne pointillée cyan). Les lignes pointillées noires indiquent la valeur de a pour laquelle $\hbar(\delta_0 + \Delta_0)$ vaut 0 (correspondant à $a \simeq 28\,\mathrm{nm}$).

À l'aide de la théorie des perturbations au second ordre il est également possible d'évaluer les décalages en fréquences radiatif et électronique. Le calcul de la différence d'énergie entre deux niveaux plasmoniques successifs donne alors la fréquence de résonance renormalisée $\omega_0 + \delta_0 + \Delta_0$ où δ_0 (Δ_0) correspond au décalage radiatif (électronique) calculé à partir du hamiltonien de couplage $H_{\mathrm{pl-ph}}$ ($H_{\mathrm{pl-eh}}$). Le décalage total est une fonction qui varie en fonction de la taille de la nanoparticule et qui correspond à un décalage négatif (positif) pour les petites (grandes) tailles comme le montre la figure 3.

Dans le chapitre 3, nous présentons les principaux résultats obtenus dans la littérature sur les dimères et chaînes de nanoparticules métalliques [64, 79, 80, 135]. En effet dans le régime où $3a \lesssim d \ll \lambda$, les interactions dipolaires quasistatiques induisent des modifications importantes sur les modes plasmoniques du système. Ainsi, dans le cas des chaînes infinies, les modes propres du système peuvent être obtenus analytiquement dans l'espace de Fourier et ont pour relation de dispersion [135]

$$\omega_q^\sigma = \omega_0 \sqrt{1 + 2\frac{\Omega}{\omega_0} f_q^\sigma}, \tag{5}$$

où la fonction f_q^σ est donnée par

$$f_q^\sigma = 2\eta^\sigma \sum_{n=1}^{\infty} \frac{\cos(nqd)}{n^3} \tag{6}$$

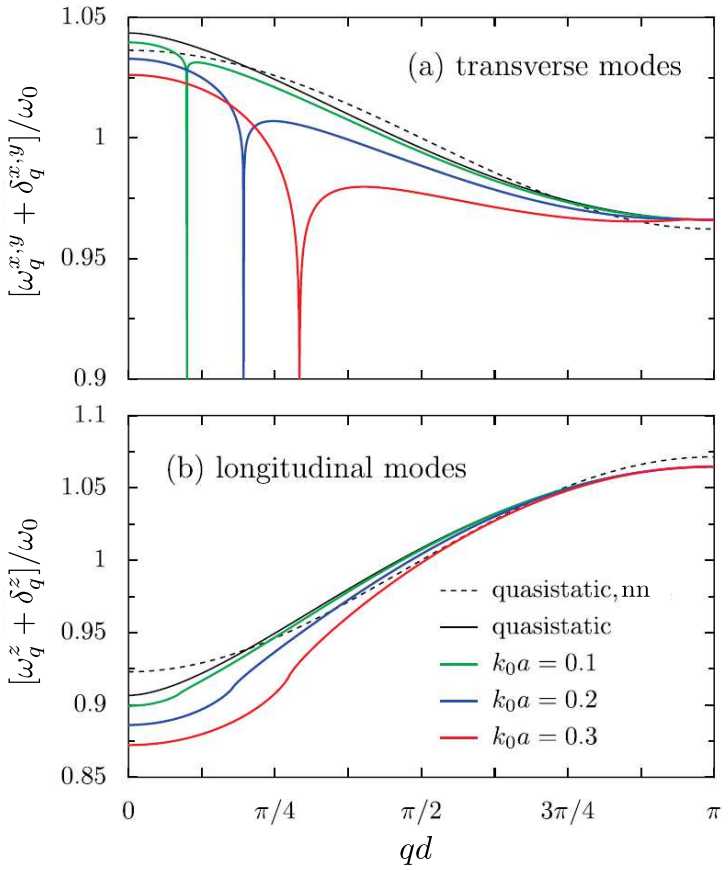

Figure 4: Relations de dispersion plasmoniques en fonction du nombre d'onde q pour les polarisations (a) transverses ($\sigma = x, y$) et (b) longitudinale ($\sigma = z$). Les lignes noires montrent les relations de dispersion quasistatiques (5) tandis que les lignes pointillées se limitent à l'approximation en proches voisins. Lignes colorées : structures de bandes plasmoniques avec prise en compte des effets retards pour $k_0a = 0.1$ (en vert), $k_0a = 0.2$ (en bleu) et $k_0a = 0.3$ (en rouge). Dans la figure, $d = 3a$. Figure adaptée de la Ref. [135].

avec $\eta^\sigma = (1, 1, -2)$ pour $\sigma = (x, y, z)$. Par des techniques similaires à celles utilisées pour la nanoparticule unique, il est possible d'évaluer également les taux d'amortissements ainsi que les décalages en fréquence induits par les environnements photonique et électronique. En particulier, l'évaluation du décalage radiatif est particulièrement cruciale car elle permet de tenir compte des effets retards des interactions de Coulomb qui sont négligés dans l'approche quasistatique donnant la relation de dispersion (5). La figure 4 montre les relations de dispersion retardées (en couleurs) pour les modes plasmoniques polarisés (a) transversalement et (b) longitudinalement par rapport à la direction de la chaîne. Dans la figure, les lignes noires pleines représentent les relations de dispersion quasistatiques [cf. Eq. (5)] tandis que celles en pointillées reposent sur les interactions entre plus proches voisins. Ainsi, on remarque que dans le cas des modes transverses [voir Fig. 3(a)] une singularité apparait dans la structure de bande retardée pour les nombre d'onde où le

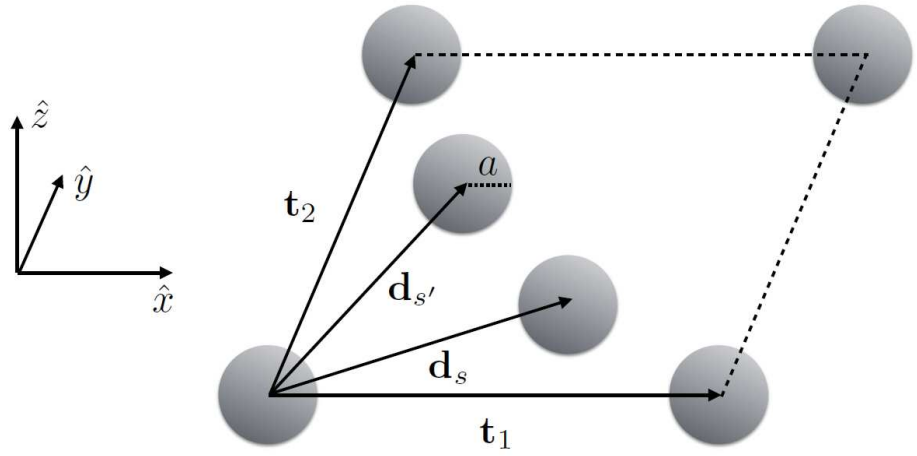

Figure 5: Sketch de la cellule élémentaire d'un réseau générique bi-dimensionnel de nanoparticules métalliques sphériques de rayon a formant un réseau de Bravais muni d'une base. Dans la figure, $\mathbf{t}_1$ et $\mathbf{t}_2$ sont les vecteurs du réseau de Bravais et $\mathbf{d}_s$ ($s = 1, \ldots, \mathcal{S}$) ceux formant le motif. Par convention, $\mathbf{d}_1 = 0$.

cône de lumière $\omega_0 = ck_0$ intersecte la dispersion quasistatique (en noir). Une telle singularité est absente dans le cas de la polarisation longitudinale [voir Fig. 3(b)] où seulement une renormalisation peut être observée. Les résultats montrés à la figure 4 sont en excellent accord avec les études numériques réalisées sur de telles chaînes (e.g. Ref. [133]). Ainsi, nous utilisons une méthode analogue afin d'évaluer les effets retards calcul de tels effets retards pour des systèmes bi-dimensionnels.

Le chapitre 3 présente également les résultats présents dans la littérature concernant les taux d'amortissement radiatifs [80, 135] et Landau [80] et dérive par des méthodes semiclassiques (identiques à celles utilisées dans le cadre de la nanoparticule unique [67, 68]) l'expression du décalage électronique associée aux plasmons collectifs. Tout comme les effets retards, l'amortissement radiatif est fortement modifié dans le cas des chaînes comparativement à la nanoparticule unique. Ces changements sont néanmoins beaucoup plus réduits dans le cas des effets induits par l'environnement électronique.

Au chapitre 4 nous présentons le modèle théorique que nous utilisons pour étudier les plasmons collectifs dans des métasurfaces formées par des nanoparticules métalliques sphériques arrangées dans des géométries génériques. Ainsi, les nanoparticules sont arrangées en un réseau de Bravais muni d'un motif et sont localisées par leurs positions $\mathbf{R}_s = \mathbf{R} + \mathbf{d}_s$. Ici, $\mathbf{R} = n\mathbf{t}_1 + m\mathbf{t}_2$ correspond au réseau de Bravais où $\mathbf{t}_1$ et $\mathbf{t}_2$ sont les deux vecteurs de la maille élémentaire, n et m sont deux entiers positifs et le motif est défini par les vecteurs $\mathbf{d}_s$ où $s = 1, \ldots, \mathcal{S}$. Le réseau générique est donc formé de $\mathcal{S}$ sous-réseaux comme montré à la figure 5. Chaque nanoparticule supporte trois plasmons dégénérés en énergie (un pour chaque direction de l'espace) qui interagissent via les interactions dipôle-dipôle à longue portée. Le hamiltonien de ce système plasmonique est donc

donné dans le formalisme de seconde quantification dans l'espace de Fourier par

$$H_{\rm pl} = \hbar\omega_0 \sum_{\mathbf{q}} \sum_{s} \sum_{\sigma} b_s^{\sigma\dagger}(\mathbf{q}) b_s^{\sigma}(\mathbf{q}) + \frac{\hbar\Omega}{2} \sum_{\mathbf{q}} \sum_{ss'} \sum_{\sigma\sigma'} \left\{ f_{ss'}^{\sigma\sigma'}(\mathbf{q}) b_s^{\sigma\dagger}(\mathbf{q}) \left[b_{s'}^{\sigma'}(\mathbf{q}) + b_{s'}^{\sigma'\dagger}(-\mathbf{q}) \right] + \text{c.h.} \right\}. \tag{7}$$

Dans l'équation ci-dessus, l'opérateur $b_s^{\sigma}(\mathbf{q})$ [$b_s^{\sigma\dagger}(\mathbf{q})$] annihile [créé] un plasmon collectif avec un vecteur d'onde $\mathbf{q}$ sur le sous-réseau s et avec la polarisation σ. La constante $\Omega = \omega_0/2(a/d)^3/2$ provient des interactions dipôle-dipôle et le fonction

$$f_{ss'}^{\sigma\sigma'}(\mathbf{q}) = \sum_{\substack{\boldsymbol{\rho}_{ss'} \\ (\rho_{ss'} \neq 0)}} \left(\frac{d}{\rho_{ss'}}\right)^3 \mathrm{e}^{\mathrm{i}\mathbf{q}\cdot\boldsymbol{\rho}_{ss'}} [\delta_{\sigma\sigma'} - 3(\hat{\sigma}\cdot\hat{\rho}_{ss'})(\hat{\sigma}'\cdot\hat{\rho}_{ss'})] \tag{8}$$

encode toutes les spécificités de l'interaction dipôle-dipôle, où $\boldsymbol{\rho}_{ss'} = \mathbf{R}'_{s'} - \mathbf{R}_s$. Dans l'Eq. (7), le terme $c.h.$ signifie *conjugué hermitique.* Afin d'extraire les quantités importantes du système plasmonique (i.e., valeurs et vecteurs propres), nous diagonalisons le hamiltonien (7) à l'aide d'une transformation de Bogoliubov

$$\beta_{\tau}^{\varepsilon}(\mathbf{q}) = \sum_{s=1}^{\mathcal{S}} \sum_{\sigma=x,y,z} \left[u_{\tau s}^{\varepsilon\sigma}(\mathbf{q}) b_s^{\sigma}(\mathbf{q}) + v_{\tau s}^{\varepsilon\sigma}(\mathbf{q}) b_s^{\sigma\dagger}(-\mathbf{q}) \right] \tag{9}$$

où $u_{\tau s}^{\varepsilon\sigma}(\mathbf{q})$ et $v_{\tau s}^{\varepsilon\sigma}(\mathbf{q})$ sont des coefficients complexes, τ l'indice de bande et ε la polarisation des modes collectifs. Les fréquences propres $\omega_{\tau}^{\varepsilon}(\mathbf{q})$ ainsi que les coefficients de Bogoliubov $u_{\tau s}^{\varepsilon\sigma}(\mathbf{q})$ et $v_{\tau s}^{\varepsilon\sigma}(\mathbf{q})$ peuvent être ensuite calculés de manière analytique (ou numérique) en utilisant les équations du mouvement de Heisenberg pour l'opérateur $\beta_{\tau}^{\varepsilon}(\mathbf{q})$ et en résolvant le système d'équations qui en résulte. Les coefficients $u_{\tau s}^{\varepsilon\sigma}(\mathbf{q})$ et $v_{\tau s}^{\varepsilon\sigma}(\mathbf{q})$ permettent également de calculer la polarisation (par rapport à la direction de propagation des modes collectifs) $\phi_{\tau}^{\varepsilon}(\mathbf{q})$ qui donne des informations intéressantes quant au comportement que l'on peut attendre vis-à-vis de certaines quantités associées aux modes collectifs (e.g., amortissements).

Le chapitre 5 est dédié à l'étude des structures de bandes plasmoniques quasistatiques dans divers réseaux simples, bipartites et tripartites. Nous étudions dans ce chapitre les effets des interactions à longue portée comparativement à celles se limitant aux plus proches voisins. En particulier, nous portons notre attention sur les modifications qui surviennent dans le cas des modes dits *topologiques* tel que les plasmons de type Dirac dans les réseaux en nid d'abeilles [108,109]. Ainsi, dans ce type de réseaux, la relation de dispersion pour les modes polarisés perpendiculairement (au plan de la métasurface) est donnée par

$$\omega_{\tau}^{z}(\mathbf{q}) = \omega_0 \sqrt{1 + 2\frac{\Omega}{\omega_0}\left[f_{11}^{zz}(\mathbf{q}) + \tau |f_{12}^{zz}(\mathbf{q})| \right]}, \tag{10}$$

où $\tau = \pm 1$ et où $f_{11}^{zz}(\mathbf{q})$ tient compte du couplage intra-réseau tandis que $f_{12}^{zz}(\mathbf{q})$ de celui inter-réseau. Avec notre modèle, la structure de bande plasmonique correspondant aux modes polarisés dans le plan est également accessible via une résolution numérique d'un système d'équations 8×8.

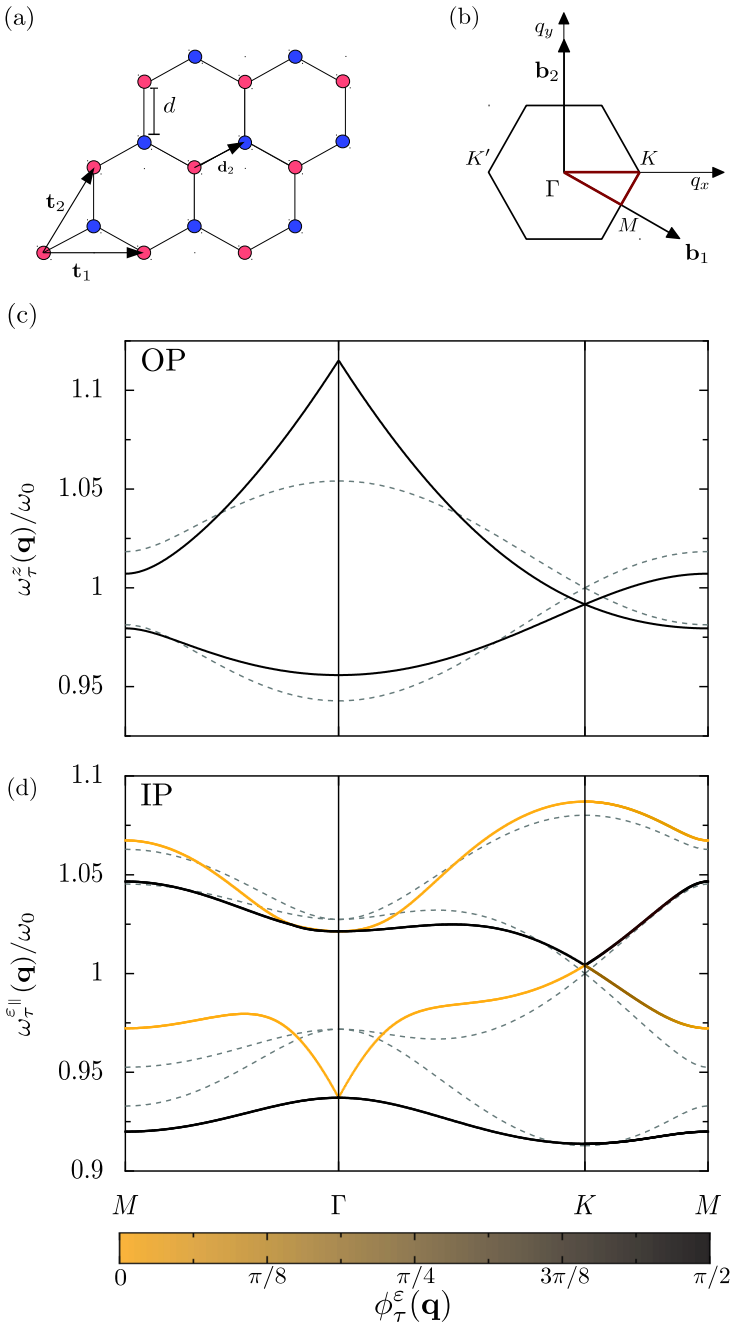

Figure 6: (a) Sketch d'un réseau en nid d'abeilles avec les vecteurs de la maille primitive $\mathbf{t}_1 = d(\sqrt{3}, 0)$ et $\mathbf{t}_2 = d(\frac{\sqrt{3}}{2}, \frac{3}{2})$ et vecteur de base $\mathbf{d}_2 = d(\frac{\sqrt{3}}{2}, \frac{1}{2})$. (b) Première zone de Brillouin avec vecteurs réciproques $\mathbf{b}_1 = \frac{2\pi}{3d}(\sqrt{3}, -1)$ and $\mathbf{b}_2 = \frac{4\pi}{3d}(0, 1)$. (c),(d) Structures de bandes plasmoniques quasistatiques pour les polarisés (c) hors du (OP) et (d) dans le plan (IP) de la métasurface. Les lignes pleines correspondent aux dispersions avec interactions à longue portée et le code couleur encode la polarisation des modes. Les lignes pointillées correspondent à l'approximation aux proches voisins. Dans la figure, la distance entre les particules est $d = 3a$ (correspondant à $\Omega = \omega_0/54$).

En comparant les résultats à longue portée avec ceux obtenus avec l'approximation aux plus proches voisins (déjà reportés dans la littérature [108, 109]) nous avons montré que les interactions à longue portée ne modifient pas qualitativement les modes plasmoniques de type Dirac qui existent aux coins de la zone de Brillouin des réseaux en nid d'abeilles. Ainsi, nous trouvons qu'au voisinage du point $\mathbf{K} = \frac{4\pi}{3\sqrt{3}d}(1,0)$, la relation de dispersion montre une forme conique qui s'écrit

$$\omega_\tau^z(\mathbf{k}) \simeq \omega_0 - \Omega|f_{11}^{zz}(\mathbf{K})| + \tau v^z|\mathbf{k}|. \tag{11}$$

avec $\mathbf{q} = \mathbf{K} + \mathbf{k}$ (avec $|\mathbf{k}| \ll |\mathbf{K}|$) et où $v^z = 1.16\Omega d$ correspond à la vitesse de groupe. Cette vitesse est légèrement inférieur à celle trouvée en ne prenant en compte que les interactions entre plus proches voisins $v_{\rm nn}^z = 3\Omega d/2$. De plus, la dispersion conique est également décalée en énergie compartivement à celle en proche voisin [voir Fig. 6(c)]. Ainsi, le hamiltonien effectif de type Dirac prend la forme

$$\mathcal{H}_{\mathbf{k}}^{\rm eff} = [\hbar\omega_0 - \hbar\Omega|f_{11}^{zz}(\mathbf{K})|]\,\mathbb{1}_2 - \hbar v^z \boldsymbol{\sigma}\cdot\mathbf{k}, \tag{12}$$

où $\mathbb{1}_2$ est la matrice unité de dimension 2 et $\boldsymbol{\sigma} = (\sigma_x, \sigma_y, \sigma_z)$ est le vecteur formé par les matrices de Pauli. Le hamiltonien (12) encode la même physique que celle en proches voisins et les modes au point $\mathbf{K}$ de la première zone de Brillouin possèdent des propriétés similaires aux électrons dans le graphène à savoir une phase de Berry de π, l'absence de rétro-diffusion et un effet tunnel de Klein par exemple [108]. Cependant, notre étude des réseaux Lieb et kagome (deux réseaux tripartites) montre que les modes topologiques (tel que les bandes non-dispersives ou plates) peuvent être fortement affectés par les effets des interactions à longue portée qui détruisent par exemple la bande plate dans le cas de chaque réseau.

Le chapitre 6 se concentre sur les quantités associées aux modes plasmoniques collectifs induits par l'environnement photonique à savoir l'amortissement et le décalage fréquentiel radiatifs. Ce dernier donnant accès aux effets retard, nous l'évaluons de manière identique au cas de la chaîne. Ainsi, la structure de bande retardée est donnée par la différence d'énergie entre deux niveaux plasmoniques successifs où les énergies sont modifiées par le couplage avec les photons. L'expression générale du décalage radiatif est alors donnée par

$$\delta_\tau^\varepsilon(\mathbf{q}) = \pi\omega_0^3\frac{a^3}{\mathcal{V}}\sum_{\mathbf{k},\hat{\lambda}_\mathbf{k}}\frac{\left|\sum_{s\sigma}(\hat{\sigma}\cdot\hat{\lambda}_\mathbf{k})P_{\tau s}^{\varepsilon\sigma}(\mathbf{q})\right|^2}{\omega_\mathbf{k}}\left[\frac{|F_{\mathbf{k},\mathbf{q}}^-|^2}{\omega_\tau^\varepsilon(\mathbf{q})-\omega_\mathbf{k}} - \frac{|F_{\mathbf{k},\mathbf{q}}^+|^2}{\omega_\tau^\varepsilon(\mathbf{q})+\omega_\mathbf{k}}\right]. \tag{13}$$

où $\mathcal{V}$, $\hat{\lambda}_\mathbf{k}$ et $\omega_\mathbf{k} = c|\mathbf{k}|$ sont respectivement le volume de quantification, la polarisation transverse et la fréquence des photons. Dans l'équation ci-dessus $P_{\tau s}^{\varepsilon\sigma}(\mathbf{q}) = u_{\tau s}^{\varepsilon\sigma}(\mathbf{q}) + v_{\tau s}^{\varepsilon\sigma}(\mathbf{q})$ et $F_{\mathbf{k},\mathbf{q}}^\pm$ est le facteur de réseau défini comme

$$F_{\mathbf{k},\mathbf{q}}^\pm = \frac{1}{\sqrt{\mathcal{N}}}\sum_\mathbf{R} \mathrm{e}^{\mathrm{i}(\mathbf{q}\pm\mathbf{k})\cdot\mathbf{R}} \tag{14}$$

et qui est caractéristique de la géométrie étudiée. En supposant un réseau suffisamment grand, nous pouvons évaluer analytiquement le décalage (13) pour n'importe quelle polarisation ε. La figure 7 montre les résultats obtenus pour les structures de bandes retardées en ajoutant ce décalage au relations de dispersion quasistatiques $\omega_\tau^\varepsilon(\mathbf{q})$ pour (a),(d) le réseau carré, (b),(e) le réseau en nid d'abeilles et (c),(f) le réseau Lieb pour les polarisation hors [panneaux (a)–(c)] et dans [panneaux (d)–(f)] le plan.

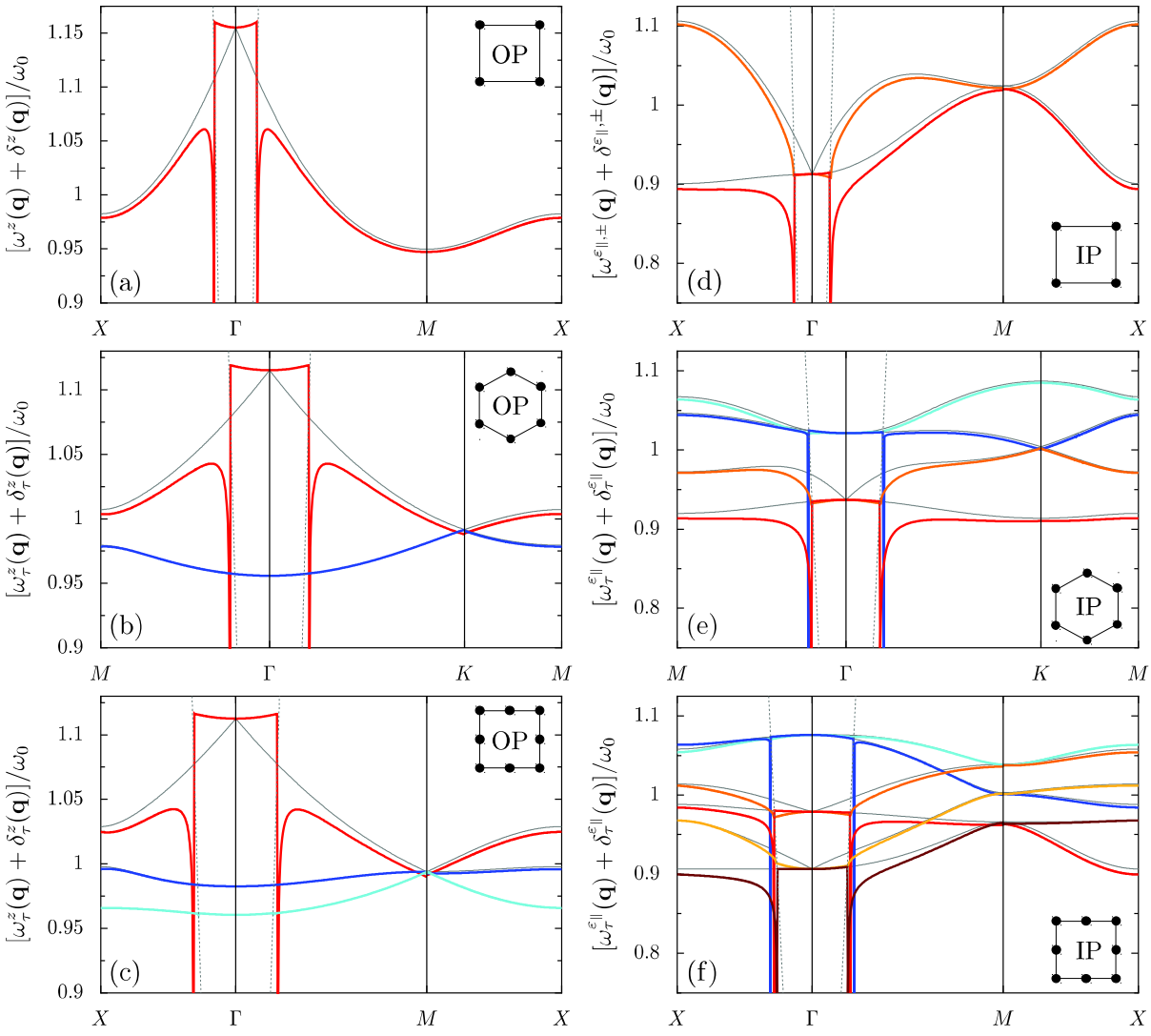

Figure 7: Les lignes de couleurs représentent la structure de bande retardée $\omega_\tau^\varepsilon(\mathbf{q}) + \delta_\tau^\varepsilon(\mathbf{q})$ pour les réseaux (a),(d) carré, (b),(e) en nid d'abeilles et (c),(f) Lieb. Les panneaux (a)–(c) [(d)–(f)] montrent les résultats pour les modes polarisés hors du [dans le] plan. Les traits gris fins reproduisent les structures de bandes quasistatiques pour chaque réseau, tandis que les pointillés correspondent aux cônes de lumière à l'intérieur de chacune des premières zones de Brillouin. Dans la figure, $d = 3a$ et $k_0 a = 0.15$.

La figure 7 montre que les relations de dispersion plasmoniques retardées présentent des profils assez diverses. En effet, certaines bandes présentent des singularités pour les vecteurs d'ondes pour lesquels le cône de lumière croise les dispersions quasistatiques. À l'opposé, certains modes ne souffrent que d'une renormalisation de leur fréquence. Ces deux effets sont liés à la polarisation de ces modes qui peuvent être transverses ou longitudinaux par rapport à leur direction de propagation (donnée par le vecteur $\mathbf{q}$). Cette situation est similaire à celle décrite dans le cas des chaînes plasmoniques [133, 135]. Cependant, les effets retards sur la structure de bande dans les métasurfaces sont nettement plus importants qu'à une dimension car ils permettent de corriger des anomalies physiques apportées par le formalisme quasistatique. À partir de la figure, on peut également conclure que les effets retards n'ont que peu d'influence sur les états topologiques qui existent en bord de zone de Brillouin (par exemple dans les réseaux Lieb et en nid d'abeilles). Une autre caractéristique visible dans la figure est la présence de modes plasmoniques peu affectés par le décalage radiatif (lignes en teinte bleue dans la Fig. 7). Ces modes correspondent à des modes dits *sombres* qui ne se couplent que faiblement à la lumière.

La seconde partie du chapitre porte sur l'évaluation de l'amortissement radiatif des modes collectifs. Pour y parvenir, nous employons une règle d'or de Fermi appliquée au hamiltonien de couplage entre le système plasmonique et les photons pour décrire un mécanisme d'émission spontanée. Cette démarche donne un résultat à nouveau valide pour toutes polarisations ε qui s'écrit

$$\gamma_\tau^\varepsilon(\mathbf{q}) = 2\pi^2\omega_0^3\frac{a^3}{\mathcal{V}}\sum_{\mathbf{k},\hat{\lambda}_\mathbf{k}}\frac{|F^-_{\mathbf{k},\mathbf{q}}|^2}{\omega_\mathbf{k}}\left|\sum_{s\sigma}(\hat{\sigma}\cdot\hat{\lambda}_\mathbf{k})P_{\tau s}^{\varepsilon\sigma}(\mathbf{q})\right|^2\delta\left(\omega_\tau^\varepsilon(\mathbf{q})-\omega_\mathbf{k}\right). \tag{15}$$

Le taux de décroissance (15) peut également être simplifié dans la limite de réseaux larges pour donner un résultat analytique. Ce taux est tracé pour plusieurs types de réseaux dans la figure 8. Le taux d'amortissement radiatif présente deux régimes bien distincts comme le montre la figure 8. Le premier est un régime super-radiant pour lequel $\gamma_\tau^\varepsilon(\mathbf{q}) \gg \gamma_0$ montré par les lignes aux teintes rouges dans la figure. De tels modes ne montrent cependant tous pas la même évolution lorsque le vecteur d'onde s'éloigne du centre de la première zone de Brillouin. Ces évolutions sont similaires à celles observées pour l'amortissement radiatif dans les chaînes [80, 135] sont liées à la polarisation des modes plasmoniques. Le second régime observé est celui pour lequel les modes sont sub-radiants ($\gamma_\tau^\varepsilon(\mathbf{q}) \ll \gamma_0$) et sont représentés par les lignes dans les teintes bleues. Ces modes correspondent aux modes sombres qui ne présentent pas (ou peu) d'amortissement radiatif.

Le chapitre 7 porte sur l'évaluation des effets induits par l'environnement électronique sur les plasmons collectifs à l'aide de techniques semi-classiques. Le cheminement que nous y effectuons suit de très près les méthodes utilisées dans les références [67, 68] pour la nanoparticule unique et à pour but de les généraliser pour des métasurfaces plasmoniques. Contrairement aux effets photoniques présentés au chapitre 6, l'amortissement Landau et le décalage fréquentiel électronique présentent des expressions très proches de celle obtenues pour la nanoparticule isolée. Dans le chapitre, nous présentons en détails les calculs qui mènent aux expressions analytiques de ces deux quantités. Par ailleurs, ces expressions sont valables pour n'importe quelle polarisation ε et restent très simples (elles n'impliquent pas les coefficients de Bogoliubov $u_{\tau s}^{\varepsilon\sigma}(\mathbf{q})$ et $v_{\tau s}^{\varepsilon\sigma}(\mathbf{q})$ contrairement à l'amortissement et au décalage radiatif). Ainsi, l'amortissement de Landau est donné par

$$\Gamma_\tau^\varepsilon(\mathbf{q}) = \frac{3v_\mathrm{F}}{4a}\left(\frac{\omega_0}{\omega_\tau^\varepsilon(\mathbf{q})}\right)^4 g\left(\frac{\hbar\omega_\tau^\varepsilon(\mathbf{q})}{E_\mathrm{F}}\right), \tag{16}$$

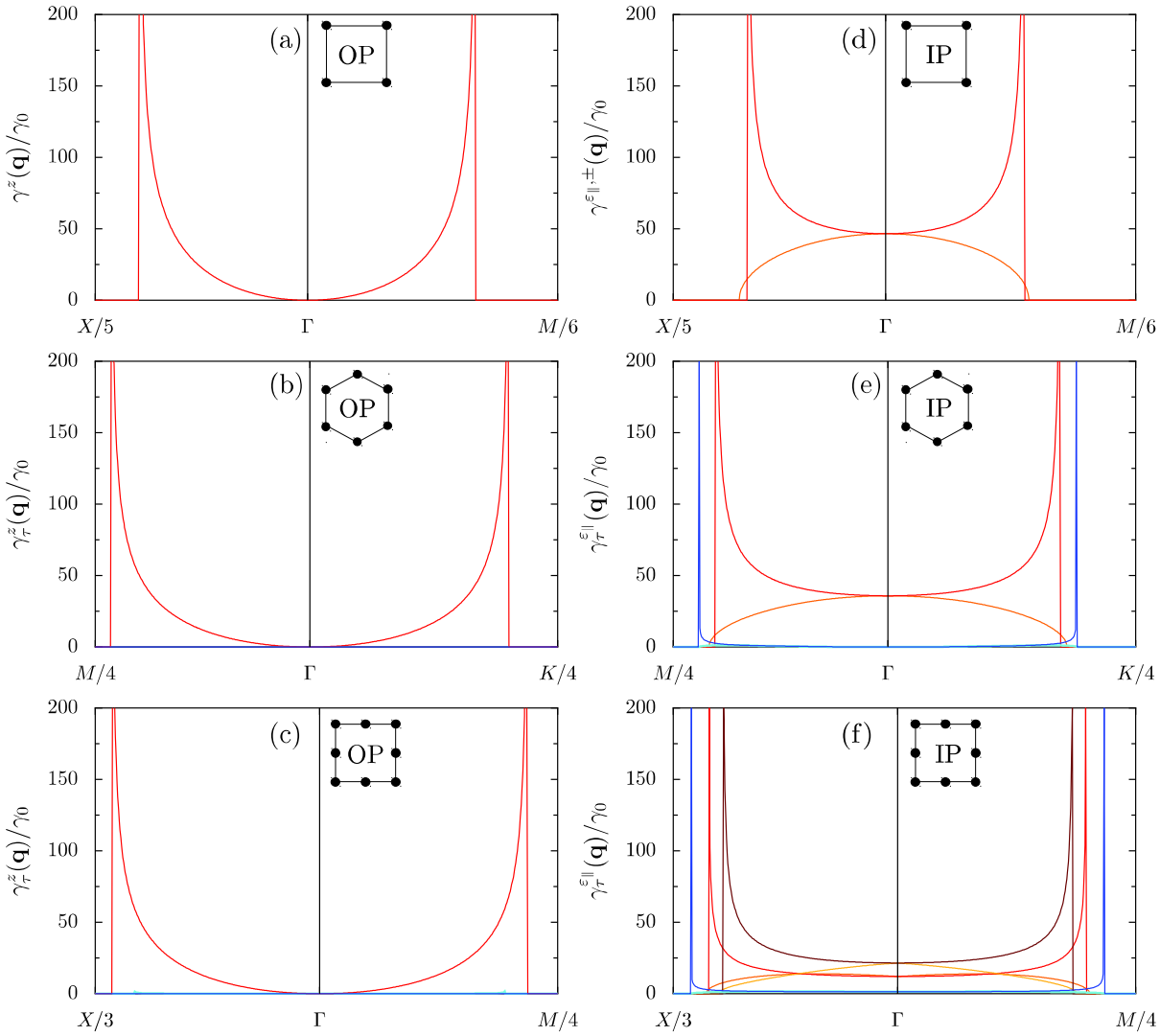

Figure 8: Les lignes de couleurs montrent le taux de décroissance radiatif $\gamma^{\varepsilon}_{\tau}(\mathbf{q})$ écrit à l'Eq. (15) (divisé par γ_0, cf. Eq. (2)] pour les réseaux (a),(d) carré, (b),(e) en nid d'abeilles et (c),(f) Lieb. Les panneaux (a)–(c) [(d)–(f)] montrent les modes polarisés hors du [dans le] plan. Mêmes paramètres que pour la Fig. 7.

qui est proportionnel à l'inverse du rayon a de la nanoparticule [de manière identique aux taux d'amortissement d'une nanoparticule unique Γ_0, cf. Eq. (3)]. De par la dépendance avec la fréquence propre $\omega_\tau^\varepsilon(\mathbf{q})$ dans l'Eq. (16), plus l'énergie du mode plasmonique est importante moins son amortissement Landau l'est. Nos développements concernant le décalage électronique ont également montré que ce décalage est toujours vers le rouge et qu'il induit des effets purement quantitatifs contrairement à que son équivalent photonique (qui est lié aux effets retard). Cependant, plus les nanoparticules considérées sont petites plus ces effets deviennent prédominants et peuvent rendre difficile l'observation expérimentale des plasmons collectifs.

Le but du chapitre 8 est de prédire les réponses expérimentales attendues pour les métasurfaces plasmoniques à l'aide de à notre théorie. En effet, notre modèle donne accès à toutes les quantités nécessaires pour pouvoir discuter de l'observabilité des modes plasmoniques, c'est-à-dire le rapport entre l'espacement entre chaque bande et leur largeur respective. Pour cela, nous avons supposé que le système répond de manière spectrale sous une forme de Breit-Wigner. La réponse spectrale est donc donnée par une somme de lorentzienne

$$\mathcal{A}(\omega, \mathbf{q}) \propto \sum_\tau \frac{1}{\left[\omega - \tilde{\omega}_\tau^\varepsilon(\mathbf{q})\right]^2 + \left[\gamma_\tau^\varepsilon(\mathbf{q})\right]^2} \tag{17}$$

où $\tilde{\omega}_\tau^\varepsilon(\mathbf{q}) = \omega_\tau^\varepsilon(\mathbf{q}) + \delta_\tau^\varepsilon(\mathbf{q}) + \Delta_\tau^\varepsilon(\mathbf{q})$ est la fréquence de résonance renormalisée incluant la dispersion quasistatique ainsi que les décalages en fréquence photonique et électronique. La seconde quantité $\gamma_\tau^\varepsilon(\mathbf{q}) = \gamma_\tau^\varepsilon(\mathbf{q}) + \Gamma_\tau^\varepsilon(\mathbf{q}) + \gamma_\mathrm{O}$ correspond à la largeur à mi-hauteur de la lorentzienne et provient de plusieurs contributions : (i) les pertes radiatives, (ii) l'amortissement Landau et (iii) les pertes ohmiques. Les résultats obtenus à partir de la fonction spectrale (17) sont montrés à la figure 9 pour les réseaux carré, en nid d'abeilles et Lieb pour les polarisations perpendiculaire et parallèle au plan des métasurfaces. Comme on peut le voir dans la figure, la majorité des différentes relations de dispersion peut être résolue avec le régime de paramètres choisis. En particulier, toutes les régions en dehors du cône de lumière sont accessibles du fait de l'absence de pertes radiatives. Ainsi, les modes présentant des propriétés topologiques intéressantes (situés au coin des zones de Brillouin) devrait pouvoir être étudiés expérimentalement. De même, les modes sombres à l'intérieur du cône de lumière sont également bien résolus. Au contraire, les mode dits *brillants* ne sont pas accessibles du fait de leur amortissements radiatif trop important. Il est important de noter ici que les pertes ohmiques ont été négligées et que leur prise en compte (voir Sec. 8.3) rend la résolution globale nettement moins bonne. Ce problème peut néanmoins être atténué en utilisant des milieux à effets de gains [49, 167–170].

En conclusion, notre travail porte sur l'étude des métasurfaces plasmoniques de géométries arbitraires. En particulier, nous avons développé un modèle analytique capable de décrire les propriétés fondamentales des modes plasmoniques collectifs supportés par de tels systèmes. Nous nous sommes concentrés sur le régime en champ proche où les interactions dipôle-dipôle jouent un rôle prédominant. Ainsi, nous avons étudié l'influence des interactions à longue portée par rapport à celles aux plus proches voisins souvent utilisées pour décrire ce type de système dans la littérature. Nous avons pu démontrer que ces interactions peuvent affecter de manière importante la dispersions de certaines bandes plasmoniques et en particulier les modes présentant des propriétés topologiques. Par ailleurs, en utilisant un formalisme de type système quantique ouvert, nous avons pu déterminer les relations de dispersion retardées en calculant les décalages en fréquence de nature

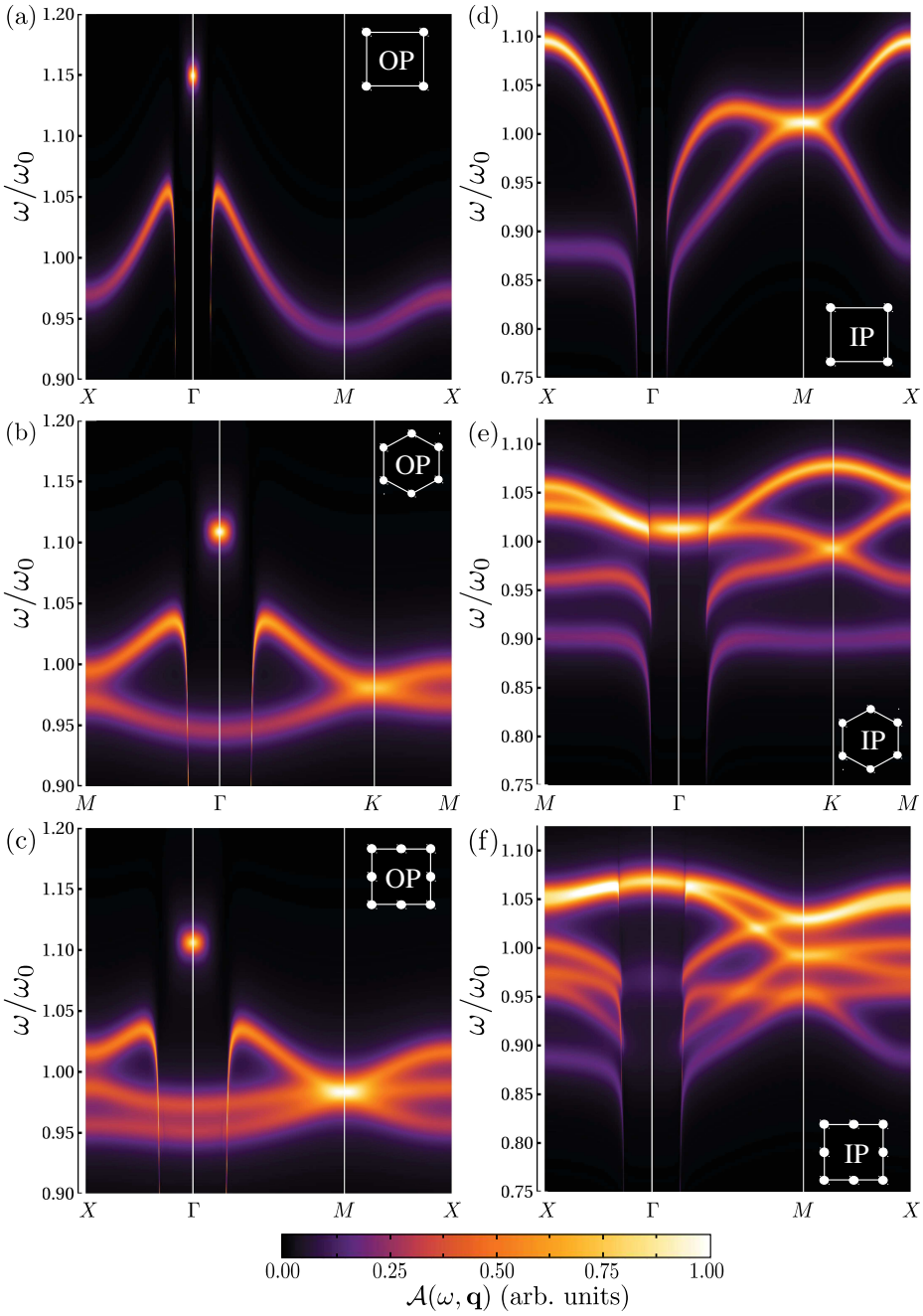

Figure 9: fonction spectrale pour les réseaux (a),(d) carré, (b),(e) en nid d'abeilles et (c),(f) Lieb. Les résultats pour les modes polarisés hors du [dans le] plan sont montrés dans les panneaux (a)–(c) [(d)–(f)]. Dans la figure nous avons choisi les paramètres $\hbar\omega_0/E_\mathrm{F} = 0.47$ et $k_0/k_\mathrm{F} = 1.1 \times 10^{-3}$,correspondant à des nanoparticules d'argent pour une taille de $k_0 a = 0.15$. Ici, k_F correspond au vecteur d'onde de Fermi. Par ailleurs, nous avons pris $d = 3a$ donnant $\Omega = \omega_0/54$ et nous avons négligé les pertes Ohmiques γ_O dans la largeur de bande. Les pertes Ohmiques sont ici négligées.

radiative. Grâce à ce formalisme, nous avons donc pu montrer que les effets retards sont cruciaux à prendre en compte puisqu'ils modifient considérablement les structures de bande quasistatiques. De même, nous avons été en mesure de fournir des expressions analytiques pour l'amortissement de ces modes qui constitue une quantité cruciale dans les expériences. L'avantage principal de ce formalisme est également la possibilité d'inclure les effets quantiques (cruciaux pour des petites nanoparticules) de manière aisée, ne nous reposant que sur quelques approximations. Ainsi, notre théorie nous a permis d'évaluer de manière analytique la réponse spectrale (expérimentale) de réseaux de géométries arbitraires ouvrant la voie pour de futures investigations sur des réseaux supportant des modes plasmoniques avec des propriétés attractives tels que des modes de type Dirac ou non dispersifs.

Related publication

The results presented in Chapters 4 to 8 of the present manuscript are based on the following preprint:

- F. Fernique, G. Weick, "*Plasmons in two-dimensional lattices of near-field coupled nanoparticles*", arXiv:1905.06727, for publication (2019).

List of symbols

Symbol	Quantity
$\|\nu\rangle$	Dirac ket notation for the quantum state ν
$\langle\nu\|$	Dirac bra notation for the quantum state ν
$\|\mathrm{vac}\rangle$	photonic vacuum state
$\|\mu_i\rangle$	electronic ground state in the nanoparticle located at the position i
a	nanoparticle radius
$a_{\mathbf{k}}^{\hat{\lambda}_{\mathbf{k}}}$	photonic annihilation operator
${a_{\mathbf{k}}^{\hat{\lambda}_{\mathbf{k}}}}^{\dagger}$	photonic creation operator
$\mathbf{A}(\mathbf{r})$	vector potential
$\mathcal{A}_q(\omega), \mathcal{A}(\omega, \mathbf{q})$	spectral response
$\mathcal{A}_{l_i,l_j,\aleph}^{m_i,m_j}$	angular part dipolar matrix element
$\mathbf{b}_1, \mathbf{b}_2$	reciprocal lattice vectors
$b^\sigma, b_n^\sigma, b_s^\sigma(\mathbf{R}_s)$	plasmonic annihilation operators in direct space
$b^{\sigma\dagger}, b_n^{\sigma\dagger}, b_s^{\sigma\dagger}(\mathbf{R}_s)$	plasmonic creation operators in direct space
$b_q^\sigma, b_s^\sigma(\mathbf{q})$	plasmonic annihilation operators in reciprocal space
$b_q^{\sigma\dagger}, b_s^{\sigma\dagger}(\mathbf{q})$	plasmonic creation operators in reciprocal space
$\beta_\tau^\sigma, \beta_q^\sigma, \beta_\tau^\varepsilon(\mathbf{q})$	collective plasmon annihilation operators
$\beta_\tau^{\sigma\dagger}, \beta_q^{\sigma\dagger}, \beta_\tau^{\varepsilon\dagger}(\mathbf{q})$	collective plasmon creation operators
$\beth(\omega)$	function involved in the electronic shift calculation
c	velocity of light
c_i	annihilation operator of a single electronic state $\|i\rangle$
$c_i^\dagger$	creation operator of a single electronic state $\|i\rangle$
d	interparticle distance between nearest-neighboring nanoparticles
$\mathbf{d}_{ij}$	matrix elements of the electronic wavefunction
$\mathbf{d}_s$	basis vectors
$\boldsymbol{\mathcal{D}}_{\mathcal{S}}^{\varepsilon}(\mathbf{q})$	matrix originating from the Heisenberg equation of motion
$\delta_0, \delta_\tau^\sigma, \delta_q^\sigma, \delta_\tau^\varepsilon(\mathbf{q})$	radiative frequency shift
$\Delta_0, \Delta_\tau^\sigma, \Delta_q^\sigma, \Delta_\tau^\varepsilon(\mathbf{q})$	electronic frequency shift
$\gimel_0, \gimel_\tau^\sigma, \gimel_q^\sigma, \gimel_\tau^\varepsilon(\mathbf{q})$	total plasmonic linewidth

Symbol	Quantity
e	elementary electronic charge
E_{F}	Fermi energy
$E^{(i)}_{n^\sigma}, E^{(i)}_{n^\sigma_\tau}, E^{(i)}_{n^\sigma_q}, E^{(i)}_{n^\varepsilon_\tau(\mathbf{q})}$	photonic corrections to the energy of a plasmonic mode
ϵ_i	energy of a single electronic state $\|i\rangle$
$\varepsilon_\tau(\mathbf{q})$	collective plasmon polarization in metasurfaces
$\mathcal{E}^{(i)}_{n^\sigma}, \mathcal{E}^{(i)}_{n^\sigma_\tau}, \mathcal{E}^{(i)}_{n^\sigma_q}, \mathcal{E}^{(i)}_{n^\varepsilon_\tau(\mathbf{q})}$	photonic corrections to the energy of a plasmonic mode
η^σ	polarization-dependent factor
$f_q, f^{\sigma\sigma'}_{ss'}(\mathbf{q})$	lattice sum
$\mathcal{F}^{\pm}_{\mathbf{k},q}, F^{\pm}_{\mathbf{k},\mathbf{q}}$	array factor
$g(\nu)$	function involved in the Landau damping calculation
$\mathbf{G}$	crystal vector in reciprocal space
$\gamma_0, \gamma^\sigma_\tau, \gamma^\sigma_q, \gamma^\varepsilon_\tau(\mathbf{q})$	radiative damping rate
$\Gamma_0, \Gamma^\sigma_\tau, \Gamma^\sigma_q, \Gamma^\varepsilon_\tau(\mathbf{q})$	Landau damping rate
$\hbar$	reduced Planck constant
$\mathbf{h}_n(\mathbf{R}_n)$	displacement field associated with the NP located at $\mathbf{R}_n$
H	Total Hamiltonian of the system
H_{pl}	Hamiltonian of the plasmonic subsystem
$H_{\mathrm{ph}}/H_{\mathrm{eh}}$	Hamiltonian of the photonic/electronic environment
$H_{\mathrm{pl-ph}}/H_{\mathrm{pl-eh}}$	coupling Hamiltonian to the photonic/electronic environment
$\mathcal{I}_1(\alpha), \mathcal{I}_2(\alpha)$	integrals involved in the radiative frequency shift
$\mathcal{J}(\beta)$	integral involved in the radiative frequency shift
k_{F}	Fermi wavevector
$\mathbf{k}$	photonic wavevector
k_0	wavenumber associated with the light cone
$\mathcal{K}_1(\alpha), \mathcal{K}_2(\alpha)$	integrals involved in the radiative linewidth
l	angular momentum quantum number
λ	wavelength
$\hat{\lambda}_{\mathbf{k}}$	transverse light polarization
Λ	constant entering the plasmon-electron coupling Hamiltonian
m	magnetic angular momentum quantum number
m_{e}	mass of an electron
M	total mass of the electrons
$M^{\varepsilon\sigma}_{\tau s}(\mathbf{q})$	quantity defined for the electronic-induced quantities

Symbol	Quantity
n_{e}	electronic density
$n^{\sigma}, n_{\tau}^{\sigma}, n_{q}^{\sigma}, n_{\tau}^{\varepsilon}(\mathbf{q})$	plasmonic quantum number
$\mathcal{N}_{\mathrm{e}}$	number of valence electrons
$\mathcal{N}; \mathcal{N}_1, \mathcal{N}_2$	number of unit cells
ω_{p}	plasma frequency
ω_0	Mie frequency
ω_{sp}	Mie frequency including the spill-out
$\omega_{\tau}^{\sigma}, \omega_{q}^{\sigma}, \omega_{\tau}^{\varepsilon}(\mathbf{q})$	frequency of the collective plasmonic modes
Ω	coupling frequency
$P_{\tau s}^{\varepsilon\sigma}(\mathbf{q})$	quantity defined for the photonic-induced quantities
$\mathbf{\Pi}_n(\mathbf{R}_n)$	conjugate momentum of the displacement field $\mathbf{h}_n(\mathbf{R}_n)$
$\Pi^{zz}(\mathbf{q})$	quantity introduced for the eigenfrequencies in tripartite lattices
$q, \mathbf{q}$	plasmonic wavenumber and wavevector
$\mathbf{r}$	position of an electron
$\mathbf{R}, \mathbf{R}_n, \mathbf{R}_s$	position of the center of the nanoparticle
$\mathcal{R}(\epsilon, \epsilon')$	radial part of dipolar matrix element
$\boldsymbol{\rho}_{ss'}$	vector connecting two nanoparticles in the metasurface
$\varrho(\epsilon)$	electronic density of states
$\varrho_l(\epsilon)$	angular-dependent electronic density of states
$s, \mathcal{S}$	sublattice index, total number of sublattices
S_x, S_y, S_z	matrices related to the Gell-Mann matrices in the Lieb lattice
σ	polarization index
$\sigma_x, \sigma_y, \sigma_z$	Pauli matrices
$\Sigma^{\sigma}(\omega)$	function involved in the electronic-induced quantities
$\Sigma^{zz}(\mathbf{q})$	quantity introduced for the eigenfrequencies in tripartite lattices
$\varsigma^{\sigma\sigma}(\mathbf{q})$	quantity introduced for the plasmonic quasistatic dispersions
$\mathbf{t}_1, \mathbf{t}_2$	primitive vectors of the Bravais lattice
τ	plasmonic band index
$u_{\tau s}^{\varepsilon\sigma}(\mathbf{q})$	first Bogoliubov coefficients
$v_{\tau s}^{\varepsilon\sigma}(\mathbf{q})$	second Bogoliubov coefficients
v_{F}	Fermi velocity
θ, φ	azimuthal and polar angle
$\phi_{\tau}^{\varepsilon}(\mathbf{q})$	plasmonic polarization angle
$\mathbf{\Psi}_{\mathbf{k}}$	spinor operator
$\zeta_{\pm}^{\sigma}(\mathbf{q})$	quantity introduced for the plasmonic quasistatic dispersions

Chapter 1

Introduction

The use and the creation of tools in order to realize specific tasks (difficult or impossible for the human body alone) are what distinguishes the human species from a large majority of other wildlife species [1]. Across the centuries, mankind continued to found new ways to utilize the materials (bounded to the physical laws) existing on Earth. Until the development of Mathematics during antiquity, the understanding of the physical properties of these tools was very limited leading to a purely practical utilization. During the same period of time, one started also to use specific materials for their physical properties only (despite being unable to fully apprehend them). For instance, the rudimentary use of polished glasses as lenses is dated back to the 5th century BC and was referred to as *burning-glasses* [2] (see Fig. 1.1). As progress in Mathematics (and other sciences) had been realized, so did the complexity of the objects which had been manufactured. The more these disciplines evolved, the more we (as a species) understood that the universal laws of nature impose theoretical limitations to our use of the properties of the materials. From the 16th century the advances of modern physics initiated by the works of Isaac Newton on the Universal laws of gravitation (see e.g., Ref. [3]) and followed by the development of the electrodynamic theory by James C. Maxwell in 1862 (see e.g., Refs. [4, 5]) contributed to push these theoretical limitations further and further. One can mention, for instance, the Rayleigh criterion [6]

$$\mathcal{R} = \frac{0.61\lambda}{\mathrm{NA}} \tag{1.1}$$

which dictates the maximum resolution that an optical apparatus can achieve and thus limiting the size of objects one can image with optical microscopes. In the latter equation, $\mathcal{R}$ corresponds to the optical resolution of the microscope, λ to the wavelength of the light, while NA denotes the numerical aperture of the objective (here, we have assumed the numerical aperture of both the condenser and the objective to be identical). In Eq. (1.1), the constant 0.61 is the first zero of the reduced Bessel function of the first kind $J_1(x)$ divided by 2π. In practice the best objectives possess a numerical aperture of typically $\mathrm{NA} = 1.45$ limiting the resolution to $\mathcal{R} \approx \lambda/2$. Such a value thus corresponds to a maximum resolution of $200\,\mathrm{nm}$ with visible light (since $\lambda \approx 400 - 800\,\mathrm{nm}$ within the visible range).

The optical resolution limit was not questioned until the work of Veselago [7][1] in 1967 which,

[1] Note that the reference corresponds to the English translation of the original work of Veselago written in Russian.

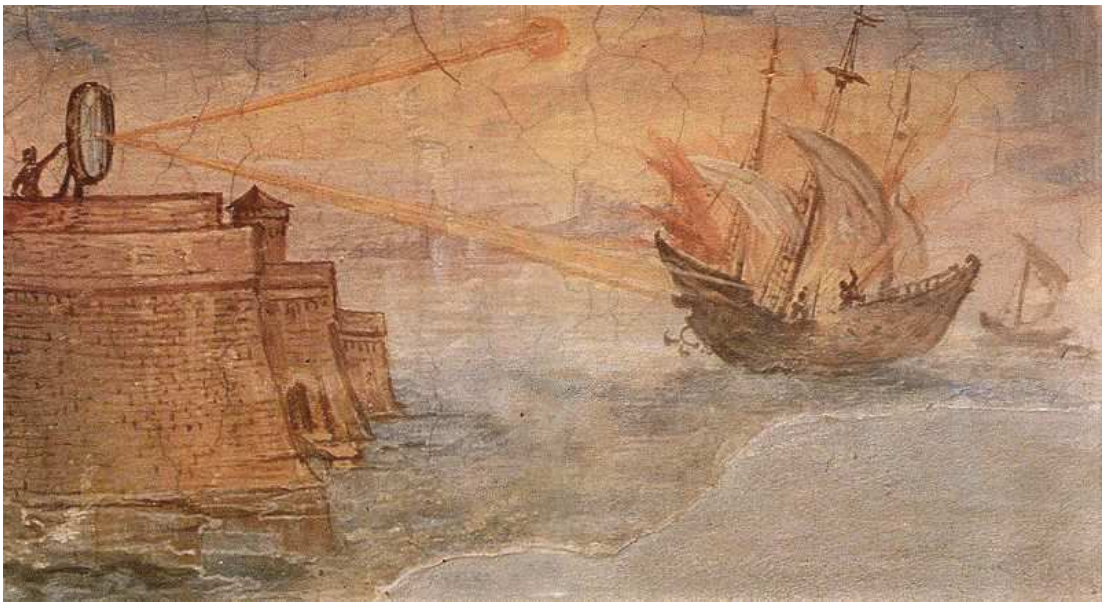

Figure 1.1: A wall painting from the Uffizi Gallery, Stanzino delle Matematiche, in Florence (Italy) painted in 1600 by Giulio Parigi. The painting shows the Greek mathematician Archimedes burning Roman military ships with the help of a large mirror (note that despite the fact of historical evidence that the Greek possessed mirror-like objects [2], the historic events described by Parigi had unlikely occurred as shown in the painting). Image taken from the website of the Uffizi Gallery, Stanzino delle Matematiche: https://www.uffizi.it/.

assuming the existence of a medium with both negative electric permittivity $\varepsilon_{\rm r}$ and magnetic permeability $\mu_{\rm r}$ for the material[2], demonstrated the possibility to perform *anomalous reflection* of light rays [see Fig. 1.2(b)]. In principle, materials exhibiting simultaneously negative $\varepsilon_{\rm r}$ and $\mu_{\rm r}$ have a *negative refractive index* (referred to as *left-handed materials* in the work of Veselago). This negative index is related with the opposite direction of propagation between the wavevector of the light and its energy flux (given by the Poynting vector $\mathbf{S}$). Indeed, for regular materials, the wavevector $\mathbf{k}$, and the electric and magnetic fields $(\mathbf{E}, \mathbf{H})$ associated with the light form a right-hand set of vectors ($\mathbf{k} \propto \mathbf{E} \times \mathbf{H}$) similarly to the triplet $(\mathbf{S}, \mathbf{E}, \mathbf{H})$ so that the energy flux propagates in the same direction as the light. In contrast, it can be shown from Maxwell's equations [7] that for left-handed materials the triplet $(\mathbf{k}, \mathbf{E}, \mathbf{H})$ forms a left-handed set of vectors so the light propagates in the opposite direction of its energy flux. This particular property is then encoded within the negative refractive index. For left-handed materials, an incident beam with wavevector $\mathbf{k}_{\rm i} = (k_{x,{\rm i}}, k_{y,{\rm i}})$ (with $k_{x,{\rm i}}$,$k_{y,{\rm i}}$ the x–, y–components of the wavevector associated with the incident light beam) impinging on a material and coming from the left of the normal plane of the air/material interface (see Fig. 1.2) is refracted in the material with a wavevector $\mathbf{k} = (k_{x,{\rm r}}, k_{y,{\rm r}})$ to the left hand side of the normal plane ($k_{x,{\rm r}} < 0$) as shown in Fig. 1.2(b). This contrasts with the usual case for which

[2]We recall that the usual reflection and refraction laws of geometrical optics are dictated by the refraction index $n = \sqrt{\varepsilon_{\rm r}\mu_{\rm r}}$ of the considered medium (see e.g., Ref. [6]).

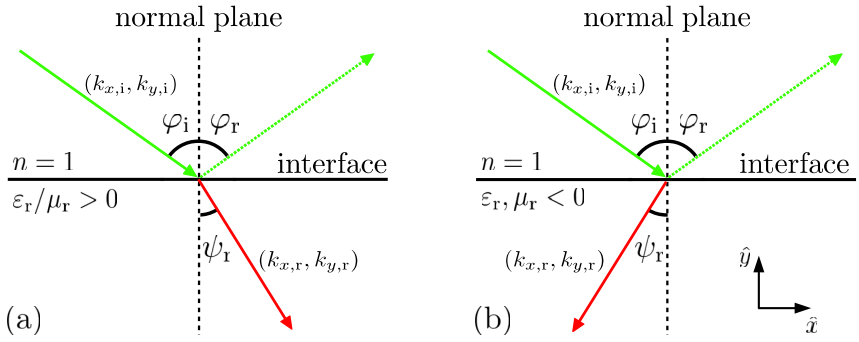

Figure 1.2: Sketch of the reflection and refraction of an incident light beam [with wavevector $\mathbf{k}_\mathrm{i} = (k_{x,\mathrm{i}}, k_{y,\mathrm{i}})$] impinging on a material with an incident angle φ_i. In both sketches, the interface is shown as a thick line while the dashed line corresponds to the normal plane to the interface. For normal materials [panel (a)], the incident beam coming from the left ($k_{x,\mathrm{i}} > 0$) of the normal plane is refracted in the material to the right ($k_{x,\mathrm{r}} > 0$) of the normal plane with an angle ψ_r. In contrast, for left-handed materials, the incident beam coming from the left on the normal plane ($k_{x,\mathrm{i}} > 0$) is refracted in the material back to the left ($k_{x,\mathrm{r}} < 0$) of the normal plane (with an angle ψ_r). For both cases, the beam is reflected with an angle $\varphi_\mathrm{r} = \varphi_\mathrm{i}$.

the beam is refracted to the right of the normal plane within the material ($k_{x,\mathrm{r}} > 0$) as shown in Fig. 1.2(a). Such an unusual property is normally impossible to achieve experimentally with common materials found in nature since all known materials do not exhibit simultaneously negative ε_r and μ_r.

Parallel to the investigations of Veselago, the development of quantum mechanics at the turn of the 20th century, changed fundamentally the understanding of the physical laws at the microscopic scale opening new ways to investigate the properties of smaller structures. Improving jointly with the theoretical progresses of the quantum theories, the fabrication techniques allowed for the constant miniaturization of the newly developed devices during the middle of the 20th century. With the possibility to design microscale and nanoscale structures, the conception of microscopic devices with an inner composite architecture (see devices in Fig. 1.3) witnessed a growing interest at the end of the 1990's. Indeed, as it is well known from classical electrodynamics, composite structured objects may induce effective electromagnetic parameters (ε_eff and μ_eff) for the whole material formed in such a manner. Thus, making use of novel fabrication techniques, researchers have developed new devices in order to tailor new properties with existing materials [8, 9].

Such progresses on composite microstructures ultimately led to the creation of a new category of materials referred to as *metamaterials*[3] in the beginning of the 21th century. Such a class of materials hence regroups all the devices which exhibit unusual properties which cannot be found in nature. One of the first achievements in the field of metamaterials was the experimental realization of a material presenting a negative refractive index by Shelby and coworkers [10] demonstrating the concept formulated thirty years earlier by Veselago [7] and rediscovered in 2000 by Pendry [11]. Such a major step was the conclusion of a large number of studies on the subject

[3]From the Greek word $\mu\varepsilon\tau\alpha$ "meta" signifying "beyond".

within the 2000's [10–14]. In Ref. [11], Pendry also predicted that composite materials with negative refractive index would allow for perfect focusing of light beams below the wavelength limit [cf. Eq. (1.1)]. These *superlenses* were designed few years later [15] consolidating the growing interest of the research community towards metamaterials.

Following these preliminary studies, the field of metamaterials then experienced an important diversification at the turn of the 21th century. Focusing first on novel optical properties, some metamaterials provide now a playground to investigate new *mechanical* features. Indeed, since the mechanical (acoustic and elastic) wave equations share several characteristic with its electromagnetic counterparts, looking for effective mechanical properties may be of great interest. For example, considering an homogeneous medium, the acoustic wave equation reads as [16]

$$\nabla^2 P(\mathbf{r},t) - \frac{1}{v_\mathrm{s}^2}\frac{\partial^2 P(\mathbf{r},t)}{\partial t^2} = 0 \tag{1.2}$$

where $P(\mathbf{r},t)$ is the local pressure of the medium (at time t and position $\mathbf{r}$) and with $v_\mathrm{s} = \sqrt{\kappa_\mathrm{a}/\rho_\mathrm{a}}$ the speed of the sound. In the latter, ρ_a is the mass density and κ_a the bulk modulus. Interestingly, Eq. (1.2) shows striking mathematical resemblances with the electromagnetic wave equation despite the longitudinal scalar nature of the acoustic waves (in contrast with the electromagnetic waves which are transverse vector waves). In analogy with electrodynamics, one may map the parameters in Eq. (1.2) as $\rho_\mathrm{a} \to \varepsilon_\mathrm{eff}$ and $\kappa_\mathrm{a} \to \mu_\mathrm{eff}^{-1}$. Consequently one can, in principle, conceive acoustic metamaterials hosting similar unusual characteristics as their optical counterparts using an identical composite architecture. Consequently, researchers recently developed devices with double-negative parameters ($\rho_\mathrm{a}, \kappa_\mathrm{a} < 0$) for acoustic [17–22] and elastic [23–25] metamaterials. In a similar fashion as in optics, researchers thus managed to focus on the pressure distribution below the characteristic sound wavelength (in the medium) [26–29] leading to the realization of *acoustic superlenses* [30–32].

During the past two decades, metamaterials have been used extensively to tailor (electromagnetic and mechanical) wave properties in unprecedented ways within various devices. We here give a few examples of what has been achieved so far with metamaterials.[4] We show in Fig. 1.3 some of the metamaterials which have been designed in various experiments.

Among the greatest accomplishments to be put to the credit of metamaterials is the realization of the *optical cloak*. Such a device, first built by Schurig and coworkers in 2006 [39], was based on a composite cylindrical structure composed of split-ring resonators [see Fig. 1.3(c)]. The "cloak" is based on the deviation of the electromagnetic waves (at a given wavelength λ_cloak) away from the center of the cylindrical structure thus hiding this particular area from optical probing. This concept of cloaking was further developed for mechanical waves as well, leading to acoustic [41], elastic [42] and even seismic [43] cloaks.

Another abundant topic dealing with metamaterials is the improvement of current devices. Such a kind of research is active for both optical and mechanical metamaterials. The purpose of these investigations is to take advantage of the unusual properties offered by metamaterials in order to realize a new generation of devices which are used daily by the industrial or medical sectors. So

[4] The interested reader may nevertheless check few excellent reviews about optical [33–35], acoustic [22, 36] and elastic [24, 37] metamaterials.

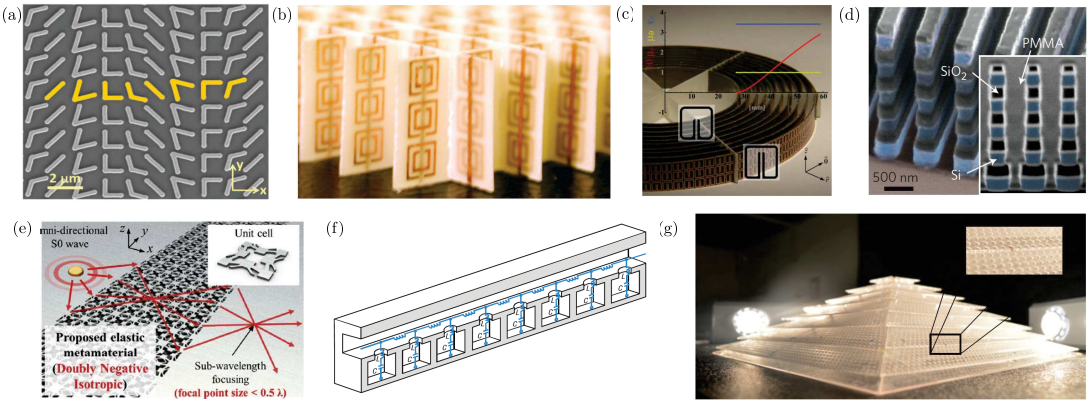

Figure 1.3: Various examples of experimentally realized metamaterials. The structures on the top row [(a)–(d)] correspond to photonic metastructures while the second row [(e)–(g)] shows structures with exotic mechanical (elastic and acoustic) properties. (a) Scanning electron microscope image of a two-dimensional array of golden nanorods on silicone (reproduced from Ref. [38]). (b) Photograph of an electromagnetic perfect lens consisting of a two-dimensional array of copper split-ring resonators arranged on a fiber glass board material (reproduced from Ref. [10]). (c) Photograph of a cylindrical two-dimensional electromagnetic cloak constituted by split-ring resonators (reproduced from Ref. [39]). (d) Ion beam focused images of three-dimensional all-dielectric nanorods (reproduced from Ref. [40]). (e) Sketch of a two-dimensional array of coupled aluminum unit cells forming a metamaterial (reproduced from Ref. [25]). (f) Sketch of a one-dimensional array of coupled aluminum Helmoltz resonators (reproduced from Ref. [18]). (g) Photograph of a three-dimensional acoustic cloak made from air-filled cubes (reproduced from Ref. [41]).

far, metamaterials (mostly optical ones) have been employed to overcome the traditional theoretical resolution limits of current detectors or sensing devices. Recently, metamaterials allowed to performed lasing at a subwavelength scale [44–48] opening the way for further miniaturized lasers.

Within the scope of optics, metamaterials hosting strong local resonances in the visible range of the electromagnetic spectrum are nowadays of particular interest. Such structures, based on regular arrays of metallic (see e.g., Ref. [38]) or dielectric components (see e.g., Ref. [40]), harvest the local features of their composite constituent in order to shape the properties of the metamaterials. As such, metallic nano-objects [such as nanoparticles or nano-antennas, cf. Fig. 1.3(a)] are of prime relevance since they exhibit so-called *localized surface plasmon resonances* (referred to as "LSPs" or "plasmons" for short in the remainder of the thesis). In metallic nanostructures, LSPs which arise from the collective oscillations of the electrons inside the nano-object leads to an enhancement of the electric field inside the structure as well as in the near-field region right outside its geometrical boundaries [49]. Such a property then allows to achieve sub-wavelength optics as well as improving sensing devices. In this particular domain, one can mention for instance the amplification of Raman responses of specific molecules [50–52] allowing for a better sensing resolution. Recently, all-dielectric metamaterials [53–55] have also drawn a lot of attention since dielectric spheres exhibit both electric and magnetic resonances (which can be rigorously derived within the

Mie theory). Such peculiar properties can then be used to perform similar applications as to the metallic nanoparticles.

1.1 Plasmonic metamaterials

Due to the recent advances in fabrication techniques, ideas for developing the next generation of electronic devices using the new properties offered by metamaterials have emerged. For achieving such a goal, a promising direction is the use of plasmonic excitations in order to perform sub-wavelength optics with nanoscale devices. The latter field of research is therefore referred to as *plasmonics*. The field of plasmonics can be classified into three distinct categories corresponding to the different kinds of plasmonic excitations involved.[5] For the purpose of this manuscript, we concentrate on metamaterials constituted by metallic nano-objects. In such a case, the plasmonic structures host localized surface plasmons (within each constituent).

1.1.1 The localized surface plasmon: an overview

One of the most peculiar optical properties of metallic nanoparticles is the presence of a localized surface plasmon resonance when the nanoparticle is excited by an external electric field [56–58]. We sketch in Figure 1.4 the process leading to the formation of the LSP. Let us consider an external electric field $\mathbf{E}(\mathbf{r}, t)$ with wavelength λ impinging on an isolated spherical metallic nanoparticle of radius a (represented as a grey sphere in the figure). If $\lambda \gg 2a$, the force exerted by the electric field on the electric charges (ions and valence electrons) would be identical for all the electric charges at the scale of the nanoparticle. Since the mass of the ions are three orders of magnitude larger than the one of the electrons, only the electrons are displaced from their equilibrium positions. Such a displacement then leaves uncompensated positive and negative charges at both extremities of the nanoparticle (within the direction of the electric field). These surface charges thus produce a restoring electric force (as shown in Fig. 1.4) which induces an oscillatory motion of the electronic cloud around its equilibrium position.

Practically, the plasmonic resonance occurring within the nanoparticle may be probed with photoabsorption experiments. In these measurements, the LSP appears as a peak centered around a given frequency as shown in Fig. 1.5 for silver and gold clusters. Such a resonance frequency can be calculated with the Mie theory [6,58,59]. In his theory dated from 1908, Mie applied Maxwell's equations to a sphere with proper boundary conditions. Such procedure allowed to extract the expressions for the scattering σ_{scat} and extinction σ_{ext} cross-sections of the sphere as an infinite summation of multipolar modes. Under the condition that the radius of the sphere is much smaller than the wavelength of the incoming light, the photoabsorption cross-section $\sigma_{\mathrm{abs}} = \sigma_{\mathrm{ext}} - \sigma_{\mathrm{scat}}$

[5] Plasmonic excitations can be of different nature, referred to as *bulk plasmons* or *surface plasmons* [49]. In the former, the plasmon arises from the collective oscillations of the conduction electron within bulk materials while in the latter, the excitation stems from surface effects. Concerning surface plasmons, one distinguishes as well the so-called *surface plasmon-polariton* (SPP) from the localized surface plasmon. On the one hand, the SPP corresponds to an evanescent wave propagating longitudinally to a metal-dielectric interface. On the other hand, the LSP appearing in finite-size structures originates as described in the main text.

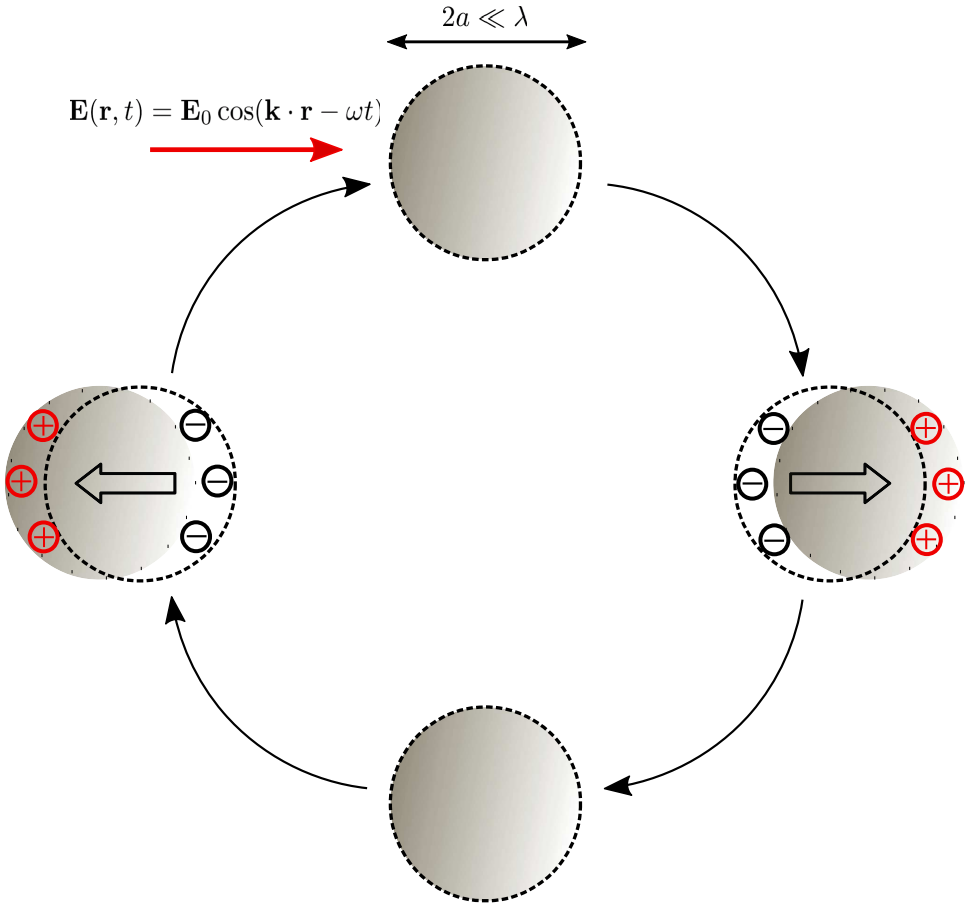

Figure 1.4: Schematic representation of a localized surface plasmon in a spherical metallic nanoparticle. In the figure, the grey disks represent the positive ionic background of the cluster, while the dashed circles its electronic cloud. When excited by an external electric field $\mathbf{E}(\mathbf{r},t)$ with an associated wavelength $\lambda \gg 2a$, the electronic cloud is displaced from its equilibrium position while the ions remain at rest (since an ion is a thousand times heavier than an electron). Such a process thus leaves unbalanced electric charges at the surface of the nanoparticle yielding a restoring force opposing the applied electric field. As a result, the electronic cloud starts to oscillate around its equilibrium position.

reads[6] within the Mie theory as [58]

$$\sigma_{\text{abs}}(\omega) = \frac{9\omega\varepsilon_{\text{m}}^{3/2}\mathcal{V}_0}{c}\frac{\varepsilon_2(\omega)}{[\varepsilon_1(\omega)+2\varepsilon_{\text{m}}]^2+\varepsilon_2^2(\omega)} \tag{1.3}$$

for metallic nanoparticles. In the equation above, ω is the frequency of the exciting field, c the

[6]Within the small nanoparticle limit, the scattering cross section is in fact negligible as compared to the extinction, so that $\sigma_{\text{abs}} \simeq \sigma_{\text{ext}}$ [58].

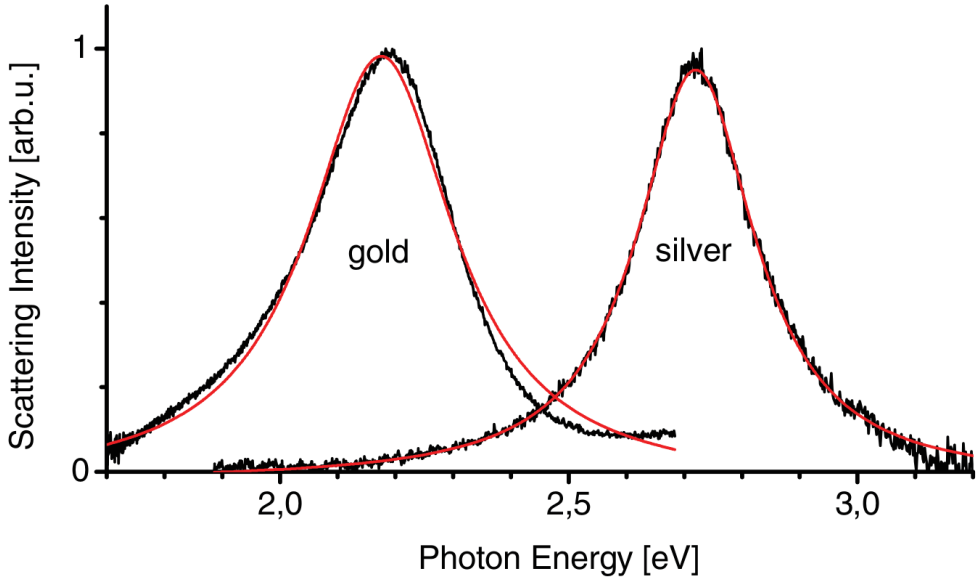

Figure 1.5: Black curves: light-scattering spectra from a single gold and a single silver cluster with $60\,\mathrm{nm}$ diameter as a function of the photon energy. The red lines correspond to Lorentzian fits to the data. Reproduced from Ref. [61].

speed of light, $\mathcal{V}_0 = 4\pi a^3/3$ the volume of the nanoparticle, and ε_m the dielectric function of the embedding medium. In Eq. (1.3), the complex dielectric function associated to the metal reads $\varepsilon_\mathrm{M}(\omega) = \varepsilon_1(\omega) + \mathrm{i}\varepsilon_2(\omega)$. Within a simple Drude model [60], the condition for metallic nanoparticles to display a resonance in the absorption cross-section simplifies to $\varepsilon_1(\omega) \simeq -2\varepsilon_\mathrm{m}$ since the imaginary part of ε_M is very small as compared to its real part.[7] Within this regime, the resonance condition leads to the Mie frequency

$$\omega_\mathrm{M} = \frac{\omega_\mathrm{p}}{\sqrt{\varepsilon_\mathrm{d} + 2\varepsilon_\mathrm{m}}} \tag{1.4}$$

at which the resonance is observed. In Eq. (1.4), $\omega_\mathrm{p} = \sqrt{4\pi n_\mathrm{e} e^2/m_\mathrm{e}}$ corresponds to the plasma frequency[8] with $-e\,(<0)$ the charge of an electron, m_e its mass and n_e the electronic density, while ε_d is a constant adding up to the dielectric constant ε_M to take into account the screening coming from the electrons belonging to the d-bands. In the particular case where $\varepsilon_\mathrm{d} = \varepsilon_\mathrm{m} = 1$, the Mie frequency reduces to

$$\omega_0 = \frac{\omega_\mathrm{p}}{\sqrt{3}}. \tag{1.5}$$

In the remainder of this manuscript, we will consider the plasmonic resonance frequency as a parameter and thus use the frequency (1.5) in the calculations.

[7] In the Drude picture, the imaginary part of the dielectric function is related to the relaxation time γ_O^{-1} of the electrons (i.e., the Ohmic losses). The rate γ_O is typically small as compared to the optical frequency in metals [60].

[8] We use cgs units in the whole manuscript.

To study the dynamics (resolved in time) of the LSPs, one often employs pump-probe experiments [62, 63] to excite the plasmon within the nanoparticle. In these kind of experiments a high-energy laser pulse is sent to the nanoparticle exciting the plasmon resonance. An other pulse, the probe (with weaker energy than the pump) then tests the absorption spectrum of the nanoparticle after a certain time delay. By tuning the time between the pump and the probe, one is then able to study the relaxation of the system at various timescales.

Frequency shifts of the plasmon resonance

The Mie frequency (1.5) discussed above does not correspond to the measured frequency to which the Lorentzian is centered to in Fig. 1.5. As a matter of fact, several contributions induce a frequency shift of the center of the peak of the Lorentzian with respect to the bare Mie frequency. Such a deviation arises from three distinct effects: (i) the so-called *spill-out effect*, (ii) a radiatively-induced shift and (iii) a shift due to the interactions with the electron-hole pairs inside the nanoparticle.

The spill-out effect [56–58] corresponds to a global reduction of the experimental resonance frequency with respect to the Mie frequency calculated above. Such an observed redshift can be understood by treating the plasmon as a quantum object instead of classically. For small enough nanoparticles, the electronic density is evaluated with a many-body wave function which extends outside the physical boundaries of the cluster. Consequently, a part $\mathcal{N}_{\mathrm{e,\,out}}$ of the electrons lies on average outside the nanoparticle and needs to be disregarded for the evaluation of the resonance frequency. As a results, the Mie frequency should be replaced by [57]

$$\omega_{\mathrm{sp}} = \omega_0 \sqrt{1 - \frac{\mathcal{N}_{\mathrm{e,\,out}}}{\mathcal{N}_{\mathrm{e}}}}, \tag{1.6}$$

with $\mathcal{N}_{\mathrm{e}}$ the total number of electrons belonging to the nanoparticle.

The two remaining sources which induce the shift with respect to the bare Mie frequency originate from the coupling between the plasmon and its different environments. As we will see in Chapter 2, the radiative frequency shift arises from the coupling of the plasmon to the photonic vacuum modes. Such a coupling induces a blueshift of the frequency ω_{sp} which scales with the forth power of the radius a of the nanoparticle [64]. This shift is reminiscent of the so-called *Lamb shift* observed in atomic physics [65, 66]. The last contribution to the frequency shift originates from the coupling between the plasmon (i.e., the electronic center-of-mass) and the electron-hole pairs within the nanoparticle. As a result, the resonance frequency is redshifted with respect to the Mie frequency [67, 68]. Such an effect scales with the inverse radius of the nanoparticle, up to a logarithmic factor. The detailed calculations giving access to the environment-induced shifts in isolated nanoparticles will be discussed extensively in Chapter 2.

Linewidth of the plasmon

As can be clearly seen in Fig. 1.5, the photoabsorption cross-section displays a Lorentzian profile. Such a function corresponds to the typical spectral response one may obtain in experiments and gives crucial information about the system one aims to study. In addition to the resonance frequency

around which the Lorentzian is centered, the full width at half maximum (FWHM) of the absorption cross-section is related to the damping of the measured excitation. Importantly, one may relate this damping rate to the lifetime of the excitation exhibiting the spectral response. Indeed, the lifetime is given by the inverse of the FWHM as $t_{\mathrm{E}} = \gamma_{\mathrm{E}}^{-1}$ where t_{E} and γ_{E} are the lifetime and the damping rate of the excitation, respectively. For the localized surface plasmon excitations, the total linewidth of the spectrum arises from distinct contributions. First, since the LSP originates from the oscillations of electric charges, the collective mode dissipates its energy radiatively. We will derive exactly, in Chapter 2 such a rate which amounts to

$$\gamma_0 = \frac{2\omega_0^4 a^3}{3c^3}. \tag{1.7}$$

Note that the latter equation scales with the volume of the cluster since the total radiated power is proportional to the number of electrons (and thus the electronic density) contained within the nanoparticle. Consequently, the radiative damping becomes predominant for large nanoparticles. In addition, the plasmon experiences two non-radiative decay mechanisms, the Ohmic losses which is in first approximation size-independent and the so-called *Landau damping*. While the former result essentially from electron-phonon scattering at room temperature, the latter arises from the decay of the plasmon into electron-hole pairs within the nanoparticle. Such a purely quantum[9] damping mechanism was first evaluated by Kawabata and Kubo in 1966 [69] in small metallic clusters. In their study, the authors found for the Landau damping

$$\Gamma_{0,\mathrm{KK}} = \frac{3v_{\mathrm{F}}}{4a} g_{\mathrm{KK}}\left(\frac{\hbar\omega_0}{E_{\mathrm{F}}}\right), \tag{1.8}$$

with v_{F} and E_{F} the Fermi velocity and energy, respectively. In the latter equation, the function $g_{\mathrm{KK}}(\nu)$ corresponds to

$$g_{\mathrm{KK}}(\nu) = \frac{1}{\nu^3}\int_{\nu_0}^{1} \mathrm{d}x \sqrt{x^3(x+\nu)}, \tag{1.9}$$

where $\nu_0 = 1 - \nu$, for $\nu < 1$ and $\nu_0 = 0$ for $\nu > 1$. The early result (1.8) for the Landau damping was later corrected by Ruppin and Yatom [70] for calculation errors and further by Yannouleas and Broglia [71] to incorporate corrections due to the used asymptotes of Bessel function in Ref. [69]. The result (1.8) was also extended to include the influence of important effects such as the temperature, as well as the oscillations of the linewidth as a function of the radius of the nanoparticle with and without the presence of an embedding matrix [67, 72–75]. The calculations leading to the corrected Landau damping are presented in Chapter 2. Note that the Landau decay rate (1.8) scales with the inverse size of the nanoparticle so that such a non-radiative damping mechanism becomes important for small size nanoparticles (i.e., for $a \lesssim 10\,\mathrm{nm}$). Importantly, the opposite scaling between the radiative and the Landau dampings, implies the existence of an optimal radius of the nanoparticle for which the total linewidth of the LSP is minimized (see Sec. 2.3.3).

[9] Both the radiative and Ohmic losses can be evaluated within a classical electrodynamic formalism.

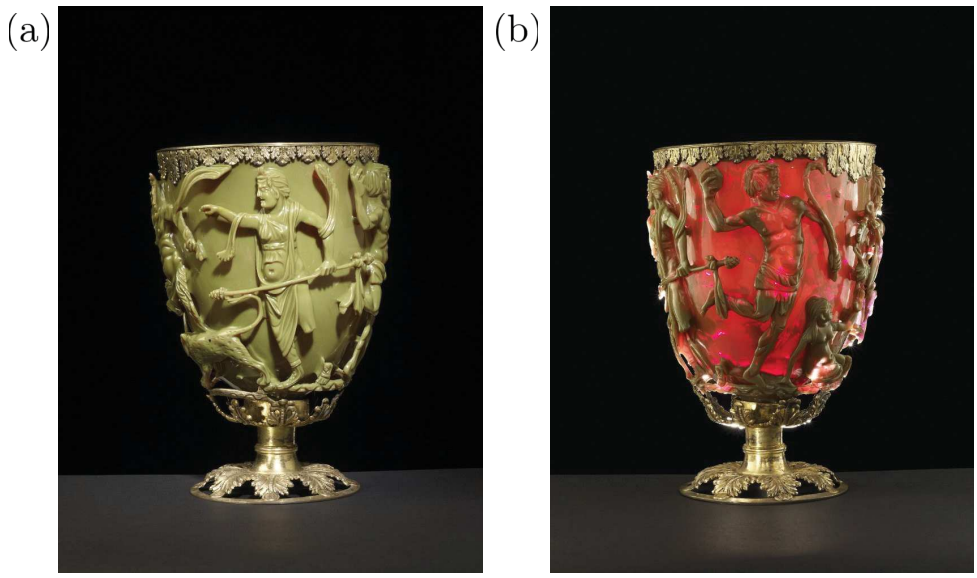

Figure 1.6: The Lycurgus cup dated from the Roman empire in the 4^{th} century AC (picture taken from The British Museum website: https://www.britishmuseum.org/). The cup, when illuminated from outside, appears as green [panel (a)] while showing red colors [panel (b)] when brightened from the inside.

1.1.2 Metamaterials based on nano-objects

In the context of metamaterials, nanoparticle-based (or nano-object-based) structures are at present the subject of important investigations in order to control the electromagnetic properties at a sub-wavelength scale. Although the controlled conception of structures composed by nanoparticles is only about two decades old, the use of nanoparticles for their peculiar optical properties is much older. Indeed, already in the Roman Empire, ornamental cups with intriguing optical properties were fabricated (such as the Lycurgus cup, see Fig. 1.6). These unusual properties originate from silver and gold nanoparticles embedded within the glass. Similar effects can be also observed in stained-glass windows decorating the Gothic churches constructed during the Middle Age.

Nowadays, the advances on the fabrication techniques and especially in terms of miniaturization, allows for a proper control of the optical properties of the nanoparticles. Consequently, composite metastructures formed by nanoparticles started to be developed in the purpose of harvesting new optical properties. As a matter of fact, it appears that placing two (or more) nanoparticles (or objects hosting plasmonic resonances) sufficiently close to one another induces the appearance of new plasmonic modes, the so-called *collective plasmons*. Such collective modes which extend over the whole structure arise from Coulomb interactions between each individual LSPs. In the particular regime $3a \lesssim d \ll \lambda$, with d the interparticle distance, the dominant interactions leading to the collective plasmons are the long-ranged dipole-dipole interactions between the plasmons [76, 77]. In such a regime which will be used in the whole manuscript (cf. Chapter 3), the nanoparticles are situated not too close which allows to neglect the multipolar interactions beyond the dipolar one

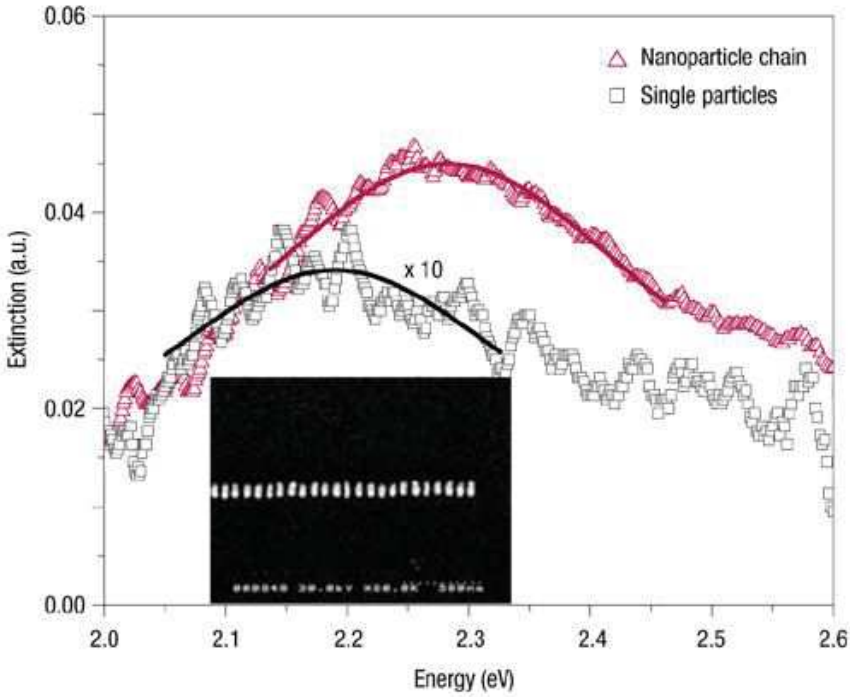

Figure 1.7: Extinction spectrum for a chain of $90\,\mathrm{nm} \times 30\,\mathrm{nm} \times 30\,\mathrm{nm}$ silver nanorods (scanning electron micrograph showed in the inset). In the chain, the rods are separated by a distance of $50\,\mathrm{nm}$. The black squares show the results for isolated nanorods while the red triangles, correspond to the extinction for the whole chain as a function of the energy of the incoming photons. The lines correspond to a Lorentzian fit of the data. The long axis of the rods is perpendicular to the axis of the chain. Reproduced from Ref. [78].

as well as the tunneling of electrons between two nanoparticles. In addition, the nanoparticles are situated not too far away either in order to disregard the retardation effects of the electromagnetic interactions between neighboring nanoparticles. These retardation effects are nevertheless crucial to take into account in the context of extended structures.

Experimentally, the collective plasmonic modes can be probed within similar extinction measurements as those used for isolated nanoparticles. We show in Figure 1.7, the results of such experiments done by Maier and coworkers [78] on chains of silver elongated-shape nanoparticles with dimensions $90\,\mathrm{nm} \times 30\,\mathrm{nm} \times 30\,\mathrm{nm}$ and separated by a distance of $50\,\mathrm{nm}$. As can be clearly seen in the figure, the absorption spectrum of the chain (red curve and triangles) shows a peak centered around a different frequency than the spectrum associated to a single nanoparticle (black curve and squares). In addition, one can verify that the two Lorentzians display two distinct linewidths [78]. This indicates that one needs to evaluate properly the linewidth of the collective modes and cannot rely on the single nanoparticle results only. We will dedicate an important part of Chapter 3 to the details concerning the evaluation of those damping rates responsible for the linewidth of the collective plasmons in one-dimensional structures [79, 80].

Plasmonic arrays

For the past twenty years, the study of plasmonic arrays of meta-atoms (i.e., nano-objects) has been an increasing area of study due to the high versatility of properties offered by metamaterials. For the purpose of this thesis, we will concentrate on two-dimensional (2D) arrays of regularly separated interacting meta-atoms, later reffered to as *metasurfaces*. Due to their potential appealing properties, a large number of plasmonic metasurfaces based on various meta-atoms were designed to manipulate efficiently the properties of the light in various regimes (see e.g., [81–88]). In Fig. 1.8, we show a few examples of metasurfaces which have been realized with different plasmonic building blocks. As can be seen in the figure, these building blocks can be simple spherical nanoparticles [panels (a) and (c)], nanorods [panels (b) and (h)], split-ring resonators [panels (e)–(g)] or even twisted nano-objects [panel (d)]. The studies performed on these various structures cover a broad field of fundamental aspects. For instance, some structures as shown in Fig. 1.8(a) and 1.8(c) have been designed for the general study of the so-called *surface lattice resonances* (SLR) (we will detail briefly such a concept in the next section of this introduction) within particular array geometries. Other regular metasurfaces [see Figs. 1.8(f),(g)] have been used as a platform to testify of the improvement concerning existing experimental techniques concerning split-ring resonators. More generally, plasmonic metasurfaces have been used to study various effects such as the fluorescence of molecules [Fig. 1.8(b)], the retardation effects contained within the light-matter interactions [Fig. 1.8(e)] or the realization of negative refractive index metasurfaces [Fig. 1.8(g)]. Interestingly, since the plasmonic excitations strongly interact with light, chiral structures [Fig. 1.8(d)] have also been developed to manipulate the polarization of light.[10]

In the reminder of this manuscript, we will concentrate on structures constituted by a regular array of identical spherical metallic nanoparticles. Consequently, each nanoparticle hosts three degenerate LSP (one for each direction of space) with Mie frequency ω_0 [cf. Eq. (1.5)] interacting with each other within the structure. Such interactions thus give rise to the collective modes. As stated in the literature [33, 34], one can distinguish three distinct regimes for the collective plasmonic modes in plasmonic metasurfaces. Such regimes depend on the interparticle distance d with respect to the wavelength λ associated with the plasmon resonance. The following section is dedicated to detailing these three regimes.

1.2 Collective plasmons in metasurfaces

Concerning plasmonic metasurfaces, most of the structures are studied within the regime where the nanoparticle separation is of the order of the wavelength of plasmonic resonance ($d \simeq \lambda$). Within this regime of parameters, the metasurfaces exhibit surface lattice resonances. The aforementioned resonances are associated with the collective plasmonic modes hosted by the metasurfaces and arise due to in-phase coherent interactions between the nanoparticles. As a matter of fact, each element composing the array scatters the incoming electric field away from the metasurface resulting into an interference pattern far away from the structure. The spectral responses of such SLRs are generally narrower than the ones of the isolated nanoparticles [91–93] making these collective resonances

[10] Such studies are also realized with SPP (see e.g., Refs. [89, 90]).

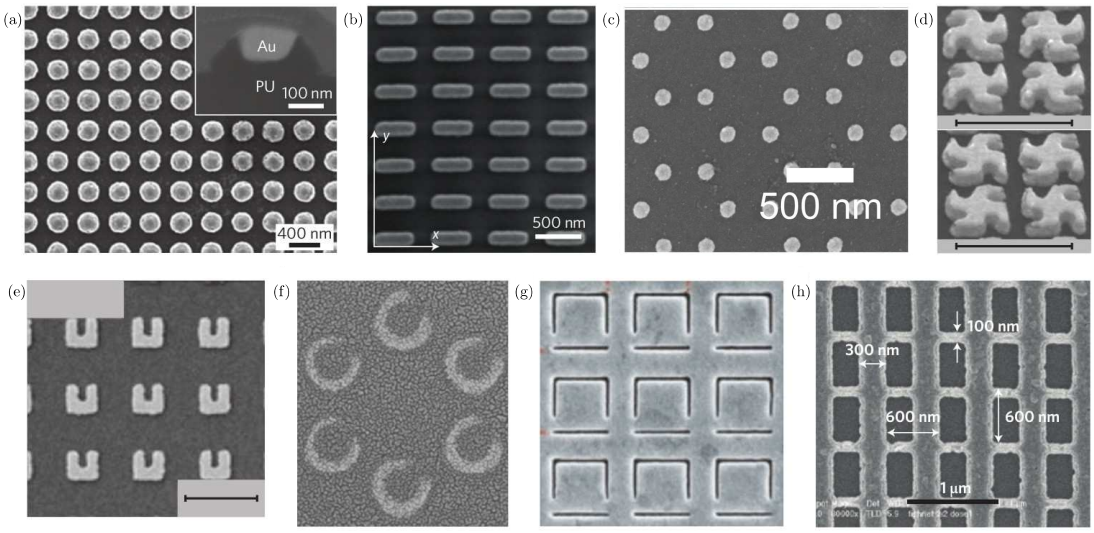

Figure 1.8: Various examples of experimentally realized plasmonic metasurfaces. (a) Nanodisks fabricated by template stripping (image taken from Ref. [86]). (b) Nanoimprinted rod antennas (image taken from Ref. [84]). (c) A honeycomb metasurface composed of spherical nanoparticles fabricated by electron-beam lithography (image taken from Ref. [88]). (d) Double-layer right-handed (top) and left-handed (bottom) gammadions forming a chiral metasurface fabricated by electron-beam lithography (image taken from Ref. [81]). (e) Split-ring resonators fabricated by electron-beam lithography (image taken from Ref. [87]). (f) Split-ring resonators fabricated by nanosphere lithography (image taken from Ref. [83]). (g) Inverse asymmetric split-ring resonators fabricated by ion-beam milling 25-nm-wide slits into a gold film resulting in meta-atoms, which are arranged on a square lattice. (image taken from Ref. [85]). (h) Double fishnet structure fabricated by nanoimprint (image taken from Ref. [82]). Images adapted from Refs. [33] and [88].

very appealing for fundamental applications. In Fig. 1.9, we show experimental data from the work of Auguié and Barnes [93] where such sharp resonances were measured within golden nanorods arrays. In the figure, one can clearly see the pronounced peak centered around $\lambda \sim 800\,\mathrm{nm}$. Such a peak is the signature of the presence of a SLR which is long-lived (as compared to the isolated plasmons) in the array. In terms of applications, the surface lattice resonances have opened the path for interesting experimental developments. In particular, the way that such resonances allow for coupling the light to emitters have been explored for the realization of light-emitting diodes [84, 94]. Another extensively debated topic is the bright and dark plasmonic modes [95]. Those modes show a net dipole moment (in terms of far-field radiation) for the bright modes while display a vanishing dipole moment for the dark ones. Note that such kinds of modes also exist for collective plasmons arising from near-field coupling interactions as presented in Chapter 3 for nanoparticle dimers. Array structures hosting surface lattice resonances may also be harnessed to achieve lasing [45, 96–100] or to realize Bose-Einstein condensation [101, 102].

The second regime which is extensively studied is the one where the interparticle distance is much smaller than the resonance wavelength but still large with respect to the dimension of the

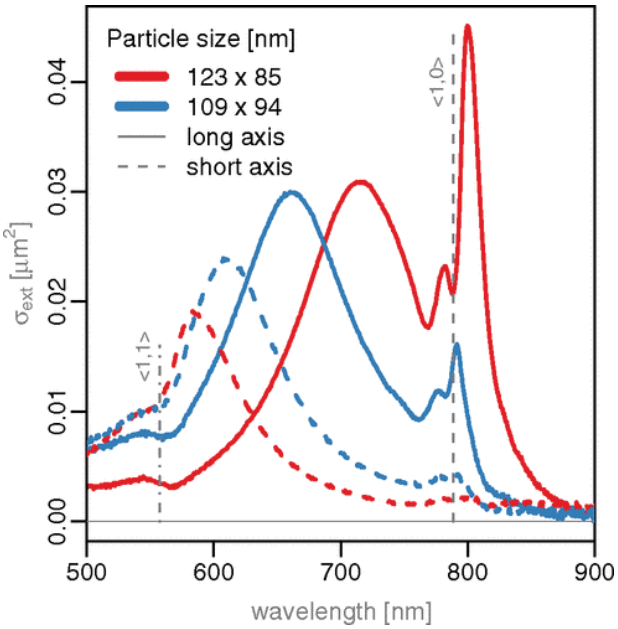

Figure 1.9: Measured extinction spectra as a function of the photon wavelength for two gold nanorod arrays. The colors correspond to two distinct dimensions (see legend). The solid (dashed) lines display the spectrum along the long (short) nanorod axis. Figure reproduced from Ref. [93].

meta-atoms, i.e., $a \ll d \ll \lambda$. Therefore, the present regime and the latter we have discussed (for which $d \simeq \lambda$) have in common that one may neglect the near-field interactions between the metasurface components and only consider the interference effects. A particular kind of metasurface falls into the latter category, that is the phase-gradient metasurfaces. In those structures, one can efficiently tailor the scattered wavefront (both the amplitude and the phase) by modifying the shape of the meta-atoms composing the metasurface. The first metasurface which demonstrated such a control over the wavefront was realized by Yu and co-workers [38] with an array of V-shaped nanorods [see Fig. 1.3(a)]. This pioneering work then allowed for the development of regular optical tools using metasurfaces such as quarter-wave plates [103] and planar lenses [104, 105]. Another kind of application that phase-graded metasurfaces have achieved is the production of holograms. About six years ago, Huang *et al.* demonstrated the possibility to create a holographic reconstruction in three dimensions (3D) using such a kind of phase-graded metasurfaces [106].

The last regime one may consider when dealing with collective plasmonic modes is the so-called *near-field regime* where the interparticle distance is still smaller than the resonance wavelength but of the same order of magnitude as the size of the elements constituting the metasurfaces, i.e., $a < d \ll \lambda$. In this regime, the near-field interactions, i.e., the multipolar electromagnetic interactions are responsible for the creation of the collective modes. Within the limit $3a \lesssim d$, the dominant contribution of such interactions arises from the quasistatic dipole-dipole interactions [76, 77] as we mentioned in Sec. 1.1. Consequently, one may obtain the collective plasmon dispersion relations with an analogue procedure as in tight-binding models, generally used for cal-

culating the electronic bandstructure in solid state materials [60, 107]. Importantly, within such a description, some interesting effects reminiscent of those observed in tight-binding systems have been predicted in plasmonic metasurfaces. An important example is the presence of Dirac-like bosons in honeycomb arrays of metallic nanoparticles [108, 109]. Such modes possess similar properties of the pseudo-relativistic electrons in graphene such as a Berry phase of π or the absence of back-scattering from smooth impurities [110]. In Chapter 5, we will give extensive details concerning the bandstructure associated to the plasmonic collective modes in honeycomb arrays of metallic nanoparticles. Despite the promising properties that could be harvested in nanoparticle-based metasurfaces within the near-field regime, realizing such structures remains experimentally challenging. These difficulties stem from the fact that the current experimental techniques struggle to produce regular arrays of small ($a \sim 10 - 20\,\mathrm{nm}$) nanoparticles separated by a distance $d = 3a$ on large areas. Indeed, the latter value for the interparticle distance corresponds to the one giving the best results for the plasmon propagation.

1.3 One-dimensional plasmonic structures based on near-field coupled metallic nanoparticles

Concerning plasmonic metastructures composed of near-field interacting nanoparticles, a vast majority of experimental and theoretical developments have been dedicated to one-dimensional arrays. This conclusion stems from the fact that one-dimensional arrays are simpler to realize with the current experimental techniques. In the following, we will review the advances found in the literature concerning nanoparticle dimers and chains.

1.3.1 Nanoparticle dimers

The extension of the Mie theory [59] by Ruppin in 1982 [111] in order to resolve the problem of the scattering of an electromagnetic field by two interacting metallic spheres constituted the initial step towards the complete description of the plasmonic collective modes hosted by nanoparticle dimers. Since then, various methods have been employed to study theoretically the properties of nanoparticle dimers [64, 79, 112–117]. The most direct approach consists in resolving Maxwell's equations for the dimer case starting from the Mie theory as done in Refs. [111, 112]. The advantage of such a method lies in the fact that the calculations can be carried out in a complete exact way numerically and contains multipolar effects. Other computational methods [113] rely on neglecting the multipolar effects and only consider the dipolar interactions between the two clusters. This allowed the authors of Ref. [113] to discriminate the *bonding state* from the *anti-bonding state* associated to the collective plasmons. We will discuss such collective modes in Chapter 3. Later on, studies have included the analysis of the linewidths of the plasmonic modes considering only the radiative contribution [114] or taking into account the purely quantum effects [116, 117]. Recently, an other method based on an open-quantum system approach has allowed to derive analytical solutions for the collective plasmons eigenfrequencies and their respective linewidths [79]. Such a work describes the individual plasmon degrees of freedom by treating separately the electronic center-of-mass (i.e., the LSP) and the relative coordinates [67, 118]. The analytical results presented

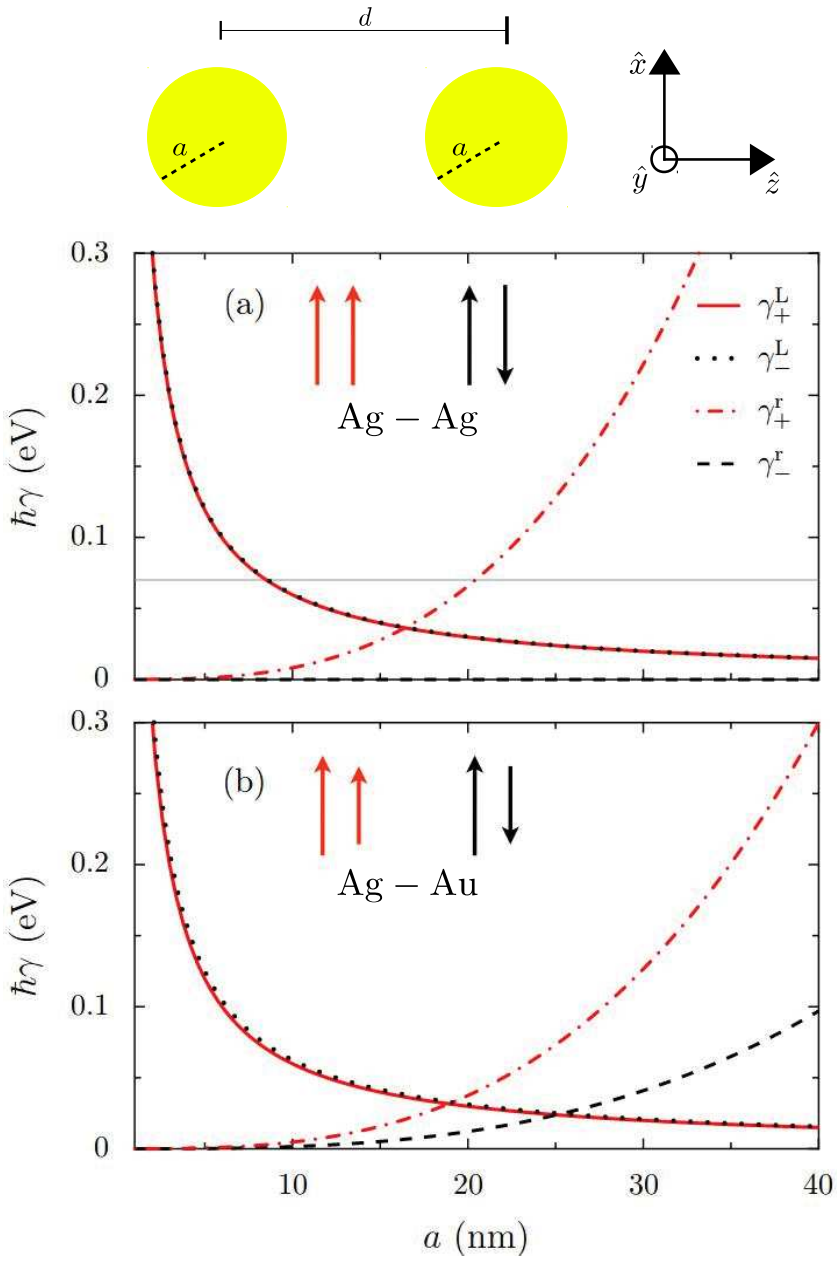

Figure 1.10: Top: Sketch of a nanoparticle dimer along the z–direction of space. Panels (a),(b): Different contributions of the total damping rates of the hybridized plasmonic modes with transverse polarization ($\sigma = x, y$) for (a) a homogeneous Ag–Ag dimer and (b) a heterogeneous Ag-Au dimer as a function of the nanoparticule radius a. In both panels, the red solid (dot-dashed) lines depict the Landau (radiative) damping rate for the bright modes ($\tau = +1$). The black dotted and dashed lines show the same quantities for the dark plasmonic modes ($\tau = -1$). In panel (a) the thin gray line shows the absorption losses. The Landau (radiative) decay rate is referred to as $\gamma_\tau^{\rm L}$ ($\gamma_\tau^{\rm r}$) while the total damping is denoted γ. In the figure, the interparticle distance is $d = 3a$. Figure adapted from Ref. [79].

in Ref. [79] show very good agreement with those obtained by solving exactly (numerically) the Maxwell's equations [113, 115–117] despite the dipolar approximation required in the model. In addition to providing a general analytical framework for describing the relevant quantities associated with plasmonic dimers (i.e., eigenfrequencies and linewidths), the model of Ref. [79] also extended the results to heterogeneous dimers (either for nanoparticle with different radii or made of different materials). Within this model, the eigenfrequencies for heterogeneous dimers (sketched in Fig. 1.10) aligned along the z–axis (within a 3D space $Oxyz$) reads as

$$\omega_{\tau}^{\sigma} = \sqrt{\frac{(\omega_1+\omega_2)^2}{4} + \tau\sqrt{\frac{\left(\omega_1^2-\omega_2^2\right)^2}{4} + 4\left[\eta^{\sigma}\right]^2\Omega^2\omega_1\omega_2}}. \tag{1.10}$$

In the equation above, ω_1 (ω_2) corresponds to the Mie frequency associated with the first (second) nanoparticle, $\tau = \pm 1$, $\eta^{\sigma} = (1, 1, -2)$ for polarization $\sigma = (x, y, z)$ and Ω is the coupling frequency arising from the dipole-dipole interactions (cf. Sec. 3.1.2). The key results of this study concerning the hybridized plasmons are presented in Fig. 1.10 for homogeneous [Fig. 1.10(a)] and heterogeneous [Fig. 1.10(b)] Ag dimers. In the case of homogeneous dimers [Fig. 1.10(a)], one can immediately note that the dark modes are indeed immune to the radiation losses (dashed black lines) while the bright modes show a corresponding rate scaling with the volume of the nanoparticle (as the isolated nanoparticle). Importantly, the Landau decay rate is present for both the bright and dark modes. Such an observation indicates that the dark modes have a finite lifetime and can be excited experimentally (with non-optical techniques). The results shown in Fig. 1.10 emphasize the fact that it is crucial to evaluate the various decay rates of the collective modes since they may be completely different with respect to those of the isolated nanoparticle.

Similarly to the isolated nanoparticle, the collective modes resonance frequencies are shifted with respect to the calculated eigenfrequencies (1.10) due to the interactions between the plasmonic subsystem with its environments. Recently, Downing *et al.* [64] have studied the influence of the photonic environment on the collective plasmon eigenfrequencies. From their work, the authors demonstrated that for a given collective mode polarization, the radiative shift is positive for the first mode and negative for the second one. Such a conclusion is in contrast with the single nanoparticle case where the radiative shift corresponds to a blueshift [64]. In Chapter 3, we will survey those effects and complete the model presented in Ref. [64] by adding the calculation of the electronic shift.

Experimentally, the realization of near-field coupled dimers only started in the beginning of the 21$^{\text{th}}$ century with the progresses of the experimental techniques [119–126]. Most of the samples studied were fabricated using standard lithographic techniques (see e.g., Ref. [125]) which allow to efficiently control the samples parameters (such as the dimensions and the separation). The authors of Ref. [121] have performed absorption experiment on pairs of silver nanodisks and demonstrated a deacrease of the collective modes resonance frequencies and associated linewidths as they increased the separation distance. Such a conclusion agreed with the previous theoretical works.

One major drawback of using optical techniques to probe the hybridized modes in dimers arises from the fact that the dark modes are intrinsically immune to radiation and cannot be observed optically since they do not show a net dipole moment. Such a limitation was overcame with the

use of *electron energy loss spectroscopy* (EELS) techniques [123, 124]. Within such experiments, a high energetic electron beam is sent on the dimer so that the electric field associated with the beam excites the hybridized modes. In the special case were the beam is sent right between the two nanoparticles, the repulsive nature of the Coulomb interaction between electrons allows to excite only the anti-bonding modes (i.e., the dark modes) [124] within a direction perpendicular to the incoming beam. Using EELS techniques thus allows, in addition to excite the dark modes, for the detection of the non-radiative mechanism contributions to the total linewidth.

1.3.2 Chains of nanoparticles

The early experimental developments on regular chains of nanoparticles has been motivated by a theoretical proposal in 1998 by Quinten *et al.* [127] to use such structures to transport light over macroscopic distances, but laterally confined to sub-wavelength scales. The first experimental detection of the near-field associated with the collective plasmons in chains was performed by Krenn *et al.* [128] one year after the theoretical proposal of Ref. [128] using a photon scanning tunneling microscope. Further observations of the signatures of the collective plasmons hosted by chains of nanoparticles were conducted by Maier *et al.* [78, 129] using standard far-field absorption experiments on chains of silver and gold nanoparticles. In these experiments (cf. Fig. 1.7), the collective mode responses are similar to the one of a single plasmon, that is a Lorentzian profile centered around the respective frequencies of the modes. The linewidths of these Lorentzians are thus associated with the decay mechanisms undergone by the collective plasmons within the chains. Except from the work of Krenn *et al.* [128] which consists of a proof of concept for the collective plasmons, the vast majority of experimental studies [78, 126, 129–131] aim to study the propagation of the plasmonic modes along the chains.

Similarly to the plasmonic dimers, one may use different theoretical models to describe collective plasmons in chains of nanoparticles [76, 80, 112, 127, 132–135]. The first model consists to solve exactly Maxwell's equations applied to the chains and to extract the relevant quantities associated with the collective plasmons [76, 112, 127, 132–134]. In such a method, one considers the plasmonic eigenfrequencies as complex numbers $\omega_{\mathrm{P}} = \omega_k + \mathrm{i}\gamma_k$ whose real part gives the eigenfrequency ω_k while the imaginary part corresponds to the total linewidth γ_k of a given mode k, respectively. Here k represent the plasmonic wavevector in the Fourier space. Several models [76, 133, 134] have neglected the multipolar interactions between the electrons and have treated the plasmons as point-like dipoles interacting through fully-retarded dipole-dipole interactions. In particular, Weber and Ford [133] conducted, within such a limit, a well documented study on chains of nanoparticles focusing on the influence of the retardation effects on the plasmonic mode dispersion relations. Indeed, even if, within the near-field regime the interactions between the neighboring nanoparticles are quasistatic, one need to consider the retardation effects between the far away nanoparticles when dealing with large structures (as the chains). Their theoretical predictions are summarized in Fig. 1.11 for the transverse [panel (a)] and longitudinal [panel (b)] polarized (with respect to the axis of the chain) plasmonic modes. In their work, the authors of Ref. [133] calculated the dispersion relations of 20 nanoparticle chains as a function of the wavevector k. They performed three distinct calculations: (i) for lossless metals within the quasistatic limit (black dots), (ii) including the retardation effects of the dipolar interactions (red triangles) and (iii) the fully-retarded solutions

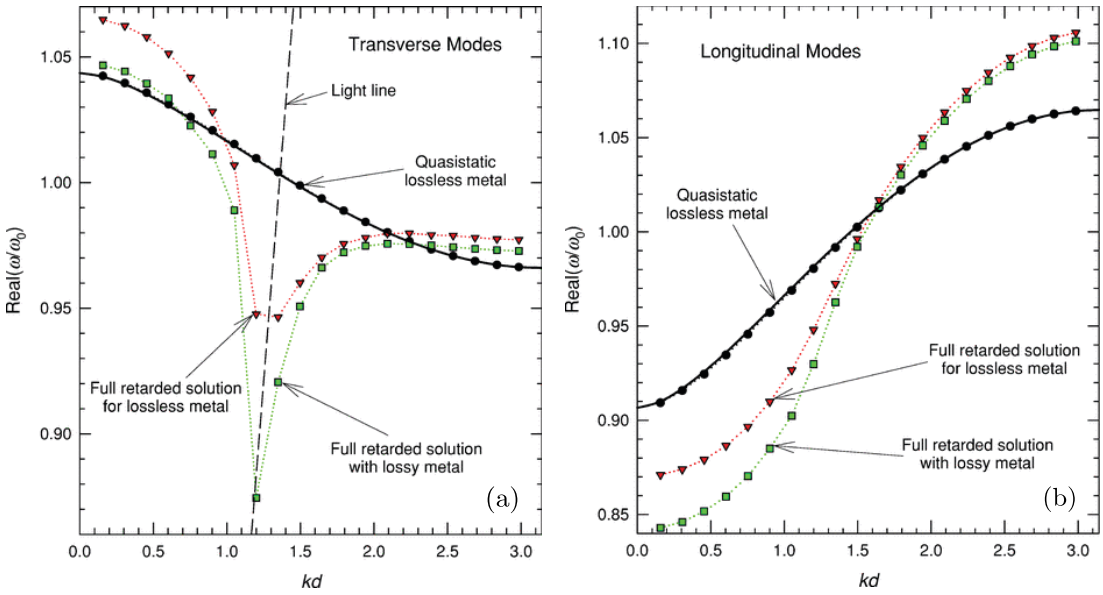

Figure 1.11: Dispersion relation curves for (a) transverse and (b) longitudinal collective modes. The solid lines display the corresponding quasistatic plasmonic dispersion relations for an infinite chain of Ag nanoparticles of radius $25\,\mathrm{nm}$ and separated by a distance of $75\,\mathrm{nm}$. The points correspond to numerical calculations for a finite 20-sphere chain: Black circles for the quasistatic approximation, green squares for the fully-retarded solutions with a lossy metal, while red triangles are for the full solutions and an ideal metal. The dashed line in panel (a) shows the light line, $\omega = ck$. Figure adapted from Ref. [133].

for typical metals (green squares). In Fig. 1.11(a), corresponding to transverse polarized modes, one immediately notice the strong renormalization of the quasistatic bandstructure when the retardation effects are included. Importantly, a strong cusp occurs at the intersection of the quasistatic dispersion with the light cone (dashed line). The latter effect is increased for lossy metals (see green squares). In Fig. 1.11(b) we display the results obtained in Ref. [133] for longitudinal plasmonic modes. Contrary to the transverse collective modes, the effects of the retarded interactions are less important showing no singularities. Nevertheless, the quasistatic dispersion relation experiences a renormalization when considering retardation effects. This renormalization becomes more important for lossy metals similarly to the transverse case. The results shown in Ref. [133] and comfirmed in Ref. [134] show that, accounting for the fully-retarded interactions for the plasmonic modes is crucial since they affect qualitatively the plasmonic dispersion relations [cf. Fig. 1.11(a)].

Alongside methods obtaining the collective plasmons by solving numerically Maxwell's equations, other approximated analytical methods have been conducted for regular [80, 135] and bipartite [136, 137] chains of nanoparticles. In a similar way as done for the nanoparticle dimers, the isolated LSPs are treated as a collection of interacting point dipoles. The quasistatic long-ranged dipole-dipole interactions thus give rise to the collective modes. The evaluation of the total linewidths as well as the retardation effects (in the dipolar interactions) are included within a per-

turbative approach of the environments to which the plasmonic subsystem are coupled (i.e., the photonic and electronic environments). In Chapter 3, we will overview the results developed in Refs. [80, 135]. Although the open quantum system approach is an approximate method, it offers advantages as compared to the fully computational calculations. First, such a method gives analytic results which are easier to obtain as compared to lengthy computational methods. Second, it allows to study the quantum effects occurring in the plasmonic subsystem (i.e., the Landau decay mechanism and the electronic shift) as well as to study the effects of each environments separately.

1.4 Theoretical advances on plasmonic metasurfaces

As mentioned in Sec. 1.2, at the time we write this manuscript and to the best of our knowledge, there are almost no experimental studies performed on plasmonic metasurfaces within the near-field regime. Consequently, most of the advances on this matter are theoretical works.

1.4.1 Advances on plasmonic metasurfaces

Within plasmonic metasurfaces, one particular regular array has concentrated a lot of attention, that is the honeycomb lattice. To study the collective plasmonic modes within honeycomb lattices of metallic nanoparticles, one may find in the literature various studies employing the two distinct theoretical methods exposed in the previous section (see Sec. 1.3) [108, 109, 138, 139].

In particular, Han *et al.* [138] calculated the fully-retarded plasmonic dispersion relation solving numerically Maxwell's equations for a honeycomb lattice sketched in Fig. 1.12(a). The corresponding first Brillouin zone is given in Fig. 1.12(b). We show the results they obtained in Fig. 1.12(c),(d). Interestingly, they considered the dipolar modes [Fig. 1.12(c)] as well as the quadrupolar ones [Fig. 1.12(d)] within the quasistatic approximation and including the retardation effects. Since the authors of Ref. [138] considered spherical nanoparticles, the out-of-plane polarized dipolar modes are fully decoupled from their in-plane counterpart. In the figure, the former are depicted as solid red lines in panel (c) while the latter correspond to black lines. From their work, Han *et al.* predicted the presence of a Dirac-like spectrum at the corner K of the Brillouin zone. The authors have also reported similar features for the quadrupolar modes [see panel (d)]. Interestingly, the authors took into account the long-range nature of the multipolar interactions giving rise to the cusps observed in panel (c) (we will provide an insight of such an effect in Chapter 5). As can be seen in the figure, taking into account the retardation effects (green dots in the figure) modifies the plasmonic dispersions especially close to the light line [see for instance in Fig. 1.12(c)] where the dispersions diverge. Such an effect is reminiscent of the one observed in plasmonic chains by Weber and Ford [133]. Importantly, Han *et al.* did not present the fully-retarded plasmonic bandstructure within the light cone. Indeed, the authors argued that within this particular region, the plasmonic modes are not well defined as they are coupled to free photons limiting their accessibility. In Chapter 6, we will calculate the fully-retarded solutions using a perturbative theory for the whole first Brillouin zone.

More recently, Ref. [108] studied the collective plasmonic modes supported by a honeycomb

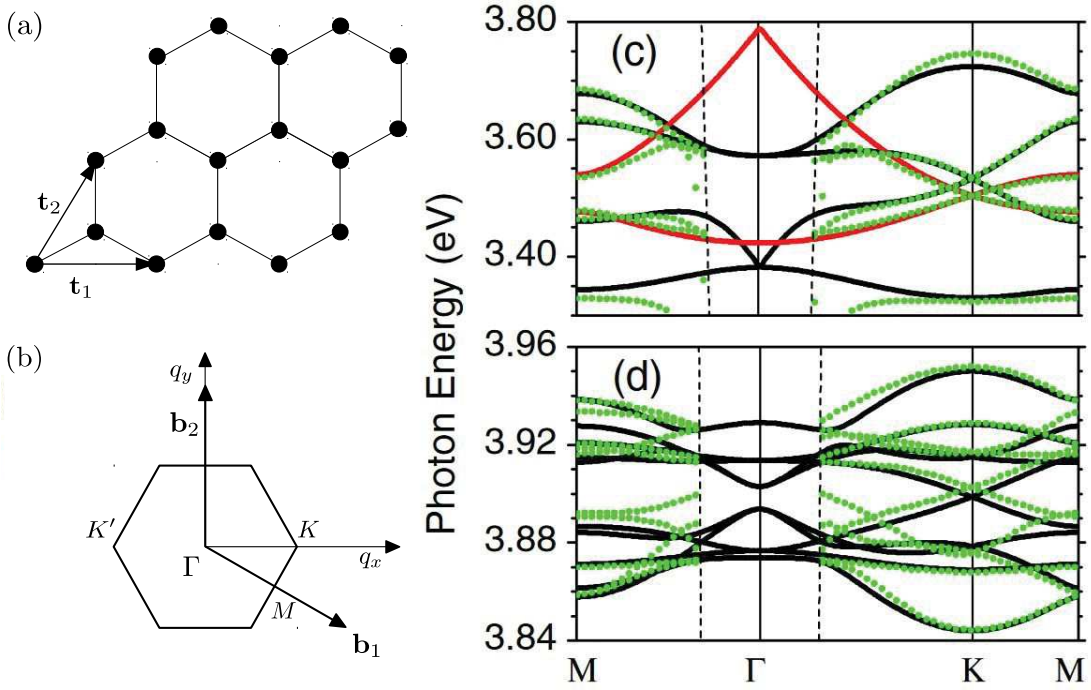

Figure 1.12: (a) Sketch of the honeycomb plasmonic lattice with $\mathbf{t}_1$ and $\mathbf{t}_2$ the primitive vectors. (b) Corresponding first Brillouin zone with $\mathbf{b}_1$ and $\mathbf{b}_2$ the vectors of the reciprocal lattice. (c),(d) Dispersion relations for (c) the dipolar and (d) the quadrupolar plasmonic modes in a honeycomb array of metallic spherical nanoparticles along the high symmetry lines within the first Brillouin zone. The solid lines correspond to quasistatic calculations while the green dots are the fully-retarded numerical results. In panel (c), the red (black) lines show the out-of-plane (in-plane) modes. In both panels, the dashed lines depict the light line. In the figure, the nanoparticles with a radius of $10\,\mathrm{nm}$ are separated by a center-to-center distance of $60\,\mathrm{nm}$. Figure adapted from Ref. [138].

lattice of metallic nanoparticles.[11] Contrary to Ref. [138], the authors treated the plasmonic system within the quasistatic approximation assuming a nearest-neighbors coupling only. Consequently, the plasmonic dispersion relation obtained by the authors is reminiscent of the electronic band-structure of graphene (for purely out-of-plane LSPs). From their results the authors of Ref. [108] extracted analytic results for the plasmonic eigenfrequencies and eigenstates. In addition, they demonstrated that, within such assumptions, the honeycomb lattice hosts Dirac-like bosons with similar properties as the pseudo-relativistic electrons in graphene. Moreover they demonstrated that, with orientated dipolar moments, one may open gaps in the dispersion relations and control actively the shape of the bandstructure. After this initial study, the authors also included the influence of asymmetries within the lattice [109]. Importantly, neither of these works on honeycomb

[11] Note that in their work, the authors of Ref. [108] mentioned "spherical" nanoparticles but considered arbitrary oriented dipole moments which can be found in ellipsoids.

lattices have taken into account the retardation effects nor calculated the linewidths of the collective modes. Consequently, it is crucial to evaluate the decay rates of the collective modes to determine if the Dirac-like plasmons which have been predicted could be probed experimentally. Finally, Ref. [139] studied the Dirac points existing in plasmonic honeycomb arrays placed between two perfect mirrors acting as a cavity. In particular, the authors evaluated the influence of the cavity height on the Dirac-like bosons. In this work, the plasmons cannot be considered solely and need to be treated as plasmon-polaritons (i.e., photon-plasmon hybridized quasiparticles) due to the strong coupling with the photons of the cavity. Although this study intrinsically includes the retardation effects for the plasmon-polaritons, no complete survey of the damping rates has been conducted in Ref. [139].

One of the advantages offered by two-dimensional structures is the important versatility in terms of possible geometries (with respect to one-dimensional chains) that could be used to study appealing plasmonic properties. In particular, numerous structures have shown interesting topological modes (e.g., non-dispersive bands) within thigh-binding electronic systems (such as the Lieb or kagome lattices, see e.g., Refs. [140–144]). Consequently, it would be of prime interest to be able to describe all the possible geometries of the arbitrary plasmonic metasurfaces within a single analytical model. In addition, such a model would allow to investigate the topological plasmonic modes existing in peculiar arrays (as in the honeycomb lattice).

1.4.2 Approach of this thesis

In this thesis, we will consider arbitrary periodic lattices composed of metallic spherical nanoparticles within a near-field regime. Separating the electronic center-of-mass from its relative coordinates, we will describe the interacting isolated plasmons within a quantum formalism. Along the lines of Refs. [80, 135] we will consider the regime of parameters $3a \lesssim d \ll \lambda$. We will thus consider the long-ranged dipole-dipole interactions as the dominant contribution to the creation of the collective modes. As we deal with spherical nanoparticles, we will discriminate the out-of-plane (with respect to the metasurface) polarized modes from the in-plane ones. The latter may have non-trivial polarizations depending on the symmetries of the arrays.

Moreover, we will evaluate the various effects of the environments using a perturbative approach characteristic to open quantum systems. In particular, we will calculate the radiative decay rates. Building on the work of Downing *et al.* [135], we will also evaluate the retardation effects of the dipolar interactions by calculating the radiative shift induced by the photonic environment. The electronic-induced effects (i.e., Landau decay rate and electronic shift) will be calculated using semi-classical expansion of the electronic density of states along the lines of Refs. [67, 68, 73, 74].

1.5 Content of this thesis

This thesis aims at providing a global analytical theory describing the collective plasmonic modes within arbitrary metasurfaces based on regular array of near-field coupled spherical metallic nanoparticles. In order to describe the isolated LSPs, we will separate the plasmonic degrees of freedom from the relative coordinates which allows to treat the plasmons as oscillating dipoles. Considering only dipole-dipole interactions we are able to calculate the resulting dispersion relations for the

collective plasmons for arbitrary lattices. Then, treating the metasurfaces as open-quantum systems, we evaluate the environment-induced properties of the collective modes. Finally, equipped with these crucial properties we compute the theoretical spectral response of arbitrary plasmonic metasurfaces. The present manuscript is organized as follows:

In Chapter 2, we review the properties one may calculate for the isolated plasmon using the scheme mentioned above. In particular, we provide in Sec. 2.1 the methods used to separate the electronic coordinates within the jellium approximation and how one may quantize the plasmonic system in Sec. 2.2. Then, in Sec. 2.3, we systematically give the procedure one can use to analytically derive the expressions of the total linewidth of the LSP. The evaluation of the frequency shifts induced by the different environments is finally discussed in Sec. 2.4.

Chapter 3 is dedicated to collective modes hosted by regular one dimensional arrays of nanoparticles. In Sec. 3.1, we present the theoretical description Brandstetter *et al.* [79] have conducted for the hybridized modes in nanoplasmonic dimers. The evaluation of the various environment-related properties is then discussed in Sec. 3.2. To conclude this chapter on one dimensional arrays, we expose in Sec. 3.3 the advances performed for simple chains of nanoparticles in the near-field regime. Importantly, throughout this chapter we systematically complete the existent studies including the electronic shifts for both plasmonic dimers and chains which has not been reported in the previous works of Refs. [64, 79, 80, 135]. Finally, we evaluate the spectral response for a chain of nanoparticles in Sec. 3.3.4 considering various nanoparticle sizes.

In Chapter 4, we present our model for arbitrary metasurfaces. Treating the plasmonic system as a open-quantum system, we derive quantum-mechanically in Sec. 4.1 the various Hamiltonians corresponding to the plasmonic subsystem, the environments and their respective couplings. The Section 4.2 is dedicated to the general diagonalization of the plasmonic sub-system. We then discuss in Sec. 4.3, the collective modes polarizations. As we will see, such a quantity gives insight on several behaviors of the modes concerning the photonic-induced properties.

In Chapter 5, we apply our model to generic simple Bravais (Sec. 5.1), bipartite (Sec. 5.2) and tripartite (Sec. 5.3) lattices to investigate the plasmonic quasistatic dispersion relations. Whenever possible, we provide analytic expressions for the eigenfrequencies and eigenstates. Then, we study in detail some examples of lattices such as the square, the honeycomb, the Lieb and the kagome lattices. Importantly, in the last three examples, we concentrate on the topological states existing in those lattices. In particular, we provide a mean-field theory to attempt to explain some of the features appearing in the quasistatic bandstructures presented in Sec. 5.1.

Chapter 6 is dedicated to the study of the photon-induced quantities of the plasmonic dispersion relations. In Sec. 6.1, we present our perturbation theory we developed to account for the retardation effects onto the quasistatic bandstructures, which give rise to a frequency shift. In Sec. 6.2, we calculate analytically the plasmonic radiative linewidth associated with the photonic environment using Fermi golden rule. In particular, we distinguish the case of the out-of-plane (Sec. 6.2.2) from the in-plane polarized modes (Sec. 6.2.3).

In Chapter 7, we discuss the Landau decay rate and the electronic redshift arising from the coupling between the collective plasmons and the electronic bath. Using semi-classical tools developed in previous works [67, 68, 73, 74], we analyze in Sec. 7.1 the Landau damping of the collective modes for which we provide an analytic formula. In Sec. 7.2, we finally evaluate the electronic shift.

The results presented in Chapters 6 and 7 then allow us to study in Chapter 8 the spectral function associated with the collective plasmonic modes to determine the viability of our findings against experimental conditions. Consequently, after computing the spectral function for the different bandstructure, we analyze the splitting between the bands with respect to their linewidths neglecting first (Sec. 8.2) the effects of the Ohmic losses, while taking them into account later on in Sec. 8.3.

We finally conclude our work and give future perspectives in Chapter 9.

Chapter 2

Lifetime and frequency shifts of plasmon resonances in isolated spherical metallic nanoparticles

The localized surface plasmon supported by isolated metallic nanoparticles suffers from different kinds of energy losses, together with a renormalization of the resonance frequency due to the coupling between the plasmon and the photonic and electronic environments. The distinct damping mechanisms are of radiative and non-radiative natures (the Ohmic losses and Landau damping). Contrary to the bulk Ohmic losses, the radiative and the Landau damping as well as the renormalization of the frequency shifts (related to the photonic and electronic environments) are depending on the size of the nanoparticles. Although single nanoparticles do not support collective plasmonic modes (arising from interactions between LSPs), which are the main interest of this manuscript, they constitute the elementary building blocks of any larger structures. In this chapter, we thus provide a general overview of the theoretical procedure one can apply to investigate the size-dependent damping rates and frequency shifts of the localized surface plasmons in single spherical metallic nanoparticles.

2.1 Hamiltonian description within the jellium approximation

We consider a spherical metallic nanoparticle of radius a centered at a position $\mathbf{R}$ and containing $\mathcal{N}_{\mathrm{e}}$ valence electrons. Nanoparticles of interest for plasmonic applications are typically composed of noble metals (such as silver or gold). In what follows, we assume for simplicity that the nanoparticle is placed in vacuum and neglect the screening due to the core electrons of the nanoparticle. Using the Born-Oppenheimer approximation [60], which amounts to neglect the ion dynamics, the electrons of such a system can be studied with a classical Hamiltonian description. In addition, we study the system within the so-called *jellium approximation* [57]. In the latter approximation, the ions are considered as a uniform positively charged spherical background of radius a. In such a

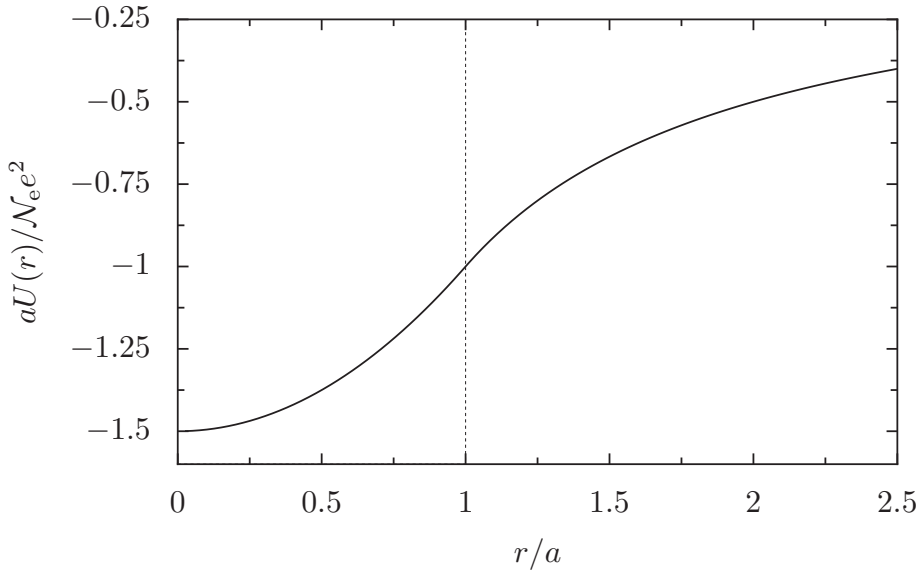

Figure 2.1: Single electron confinement potential which originates from the positive ionic background. This potential is referred to as "Harlomb" [68] since it is harmonic inside the nanoparticle ($r < a$) and Coulomb-like outside ($r > a$).

case, the electronic Hamiltonian then reads in the Coulomb gauge [4] as

$$H = \sum_{i=1}^{\mathcal{N}_e} \left\{ \frac{\left[\mathbf{p}_i + (e/c)\mathbf{A}(\mathbf{r}_i)\right]^2}{2m_e} + U(r_i) \right\} + \frac{1}{2} \sum_{\substack{i,j=1 \\ (i \neq j)}}^{\mathcal{N}_e} \frac{e^2}{|\mathbf{r}_i - \mathbf{r}_j|} + H_{\rm ph}, \tag{2.1}$$

with $-e$ (< 0) the charge of an electron and m_e its mass. In Eq. (2.1), $\mathbf{r}_i$ corresponds to the position of the $i^{\rm th}$ electron where $r_i = |\mathbf{r}_i|$ and $\mathbf{p}_i$ is its associated momentum. The fourth term of the right hand side (r.h.s.) of (2.1) arises from the electron-electron interaction while $U(r_i)$ is the potential due to the ionic background felt by the $i^{\rm th}$ electron. Imposing that $U(r)$ vanishes for $r \to \infty$ and the continuity of the electrostatic potential at $r = a$, one obtains

$$U(r) = \frac{\mathcal{N}_e e^2}{2a^3} \left(r^2 - 3a^2\right) \Theta(a - r) - \frac{\mathcal{N}_e e^2}{r} \Theta(r - a), \tag{2.2}$$

with $\Theta(x)$ the Heaviside step-function. This potential is harmonic with the Mie frequency [6] $\omega_0 = \sqrt{\mathcal{N}_e e^2/m_e a^3}$ inside the nanoparticle and Coulomb-like outside (see Fig. 2.1). Finally in Eq. (2.1), $\mathbf{A}(\mathbf{r}_i)$ is the vector potential at the position $\mathbf{r}_i$ while $H_{\rm ph}$ stems for the free photon field energy and reads

$$H_{\rm ph} = \frac{1}{8\pi} \int {\rm d}^3\mathbf{r} \left[E_\perp^2(\mathbf{r}) + c^2 B^2(\mathbf{r})\right]. \tag{2.3}$$

In Eq. (2.3), $\mathbf{E}_\perp(\mathbf{r})$ and $\mathbf{B}(\mathbf{r})$ are, respectively, the transverse components of the electric and magnetic fields associated with the vector potential. In Eq. (2.1), the Coulomb gauge ($\nabla \cdot \mathbf{A}(\mathbf{r}) = 0$)

is the usual one used in quantum optics. Such a choice allows to make transparent the transverse nature of the free electromagnetic field [it is also the usual one used to perform the procedure of canonical quantization of the radiation field by accessing the dynamical variables of the field, $\mathbf{E}_\perp(\mathbf{r})$ and $\mathbf{A}(\mathbf{r})$].

Although the jellium approximation gives accurate results for a large number of electrons [57], the Hamiltonian (2.1) is still not analytically tractable for experimentally achievable structures. Indeed, even if we consider small nanoparticles, there are already too many electrons to be able to solve the problem exactly and retrieve the eigenstates of the system. However, since we only concentrate on the description of the collective motion of the electrons (i.e., the plasmon), it exists an elegant solution to obtain an analytically-tractable model, that is the introduction of center-of-mass (describing the degrees of freedom of the plasmon) and relative coordinates [67,118]. Writing the electronic center-of-mass coordinate as $\mathbf{h}(\mathbf{R}) = \sum_{i=1}^{\mathcal{N}_\mathrm{e}} \mathbf{r}_i/\mathcal{N}_\mathrm{e}$ and its associated momentum $\mathbf{\Pi}(\mathbf{R}) = \sum_{i=1}^{\mathcal{N}_\mathrm{e}} \mathbf{p}_i$, one can then express the Hamiltonian (2.1) as

$$H = \frac{[\mathbf{\Pi}(\mathbf{R})]^2}{2\mathcal{N}_\mathrm{e} m_\mathrm{e}} + H_\mathrm{eh} + \sum_{i=1}^{\mathcal{N}_\mathrm{e}} [U(|\mathbf{h}(\mathbf{R}) - \mathbf{r}_i'|) - U(r_i')] + H_\mathrm{ph} + H_\mathrm{pl-ph}. \tag{2.4}$$

In the equation above,

$$H_\mathrm{eh} = \sum_{i=1}^{\mathcal{N}_\mathrm{e}} \left[\frac{\mathbf{p}_i'^2}{2m_\mathrm{e}} + U(r_i') \right] + \frac{1}{2} \sum_{\substack{i,j=1 \\ (i \neq j)}}^{\mathcal{N}_\mathrm{e}} \frac{e^2}{|\mathbf{r}_i' - \mathbf{r}_j'|} \tag{2.5}$$

is the Hamiltonian of the relative coordinates with $\mathbf{r}_i' = \mathbf{r}_i - \mathbf{h}(\mathbf{R})$ and $\mathbf{p}_i' = \mathbf{p}_i - \mathbf{\Pi}(\mathbf{R})/\mathcal{N}_\mathrm{e}$. In Eq. (2.4), H_ph is given by (2.3) and $H_\mathrm{pl-ph}$ represents the coupling between the electronic center-of-mass and the photonic degrees of freedom and it reads

$$H_\mathrm{pl-ph} = \frac{e}{m_\mathrm{e} c} \mathbf{\Pi}(\mathbf{R}) \cdot \mathbf{A}(0) + \frac{\mathcal{N}_\mathrm{e} e^2}{2m_\mathrm{e} c^2} \mathbf{A}^2(0). \tag{2.6}$$

In the equation above, the vector potential $\mathbf{A}(\mathbf{r}_i)$ is assumed to be the same in the entire nanoparticle and is therefore evaluated at its center. This assumption stems from the fact that one evaluate the effects induced by the photonic environment in the dipolar approximation ($2a \ll \lambda$). Indeed, the frequency associated with the photon responsible for the radiative damping lies within the same range of the Mie frequency ω_0, that is the optical range.

Considering now that the displacement of the electronic center-of-mass $\mathbf{h}(\mathbf{R})$ is sufficiently small compared to a, one may expand the third term of Eq. (2.4) up to second order in the displacement to give

$$U(|\mathbf{h}(\mathbf{R}) - \mathbf{r}_i'|) - U(r_i') \simeq \mathbf{h}(\mathbf{R}) \cdot \nabla U(r') + \frac{1}{2} [\mathbf{h}(\mathbf{R}) \cdot \nabla]^2 U(r'), \tag{2.7}$$

where the derivatives are taken at $\mathbf{r} = \mathbf{r}'$. Using expression (2.2), the two terms in the r.h.s. of the

above equation read as

$$\mathbf{h}(\mathbf{R})\cdot\nabla U(r') = \frac{\mathcal{N}_\mathrm{e}e^2}{a^3}\mathbf{h}(\mathbf{R})\cdot\left[\mathbf{r}'\Theta(a-r') + \frac{\mathbf{r}'a^3}{r'^3}\Theta(r'-a)\right], \tag{2.8}$$

and

$$\begin{aligned}\left(\mathbf{h}(\mathbf{R})\cdot\nabla\right)^2 U(r') &= \left[\mathbf{h}(\mathbf{R})\right]^2\mathcal{N}_\mathrm{e}e^2\left[\frac{1}{a^3}\Theta(a-r') + \frac{1-3\cos^2\theta'}{r'^3}\Theta(r'-a)\right]\\ &\simeq \left[\mathbf{h}(\mathbf{R})\right]^2\frac{\mathcal{N}_\mathrm{e}e^2}{a^3}\Theta(a-r').\end{aligned} \tag{2.9}$$

In Eq. (2.9), one can only keep the first term of the confinement of the center of mass since it is the dominant contribution. The second term in (2.9) is indeed negligible with respect to the first-order coupling of (2.8). Inserting the expressions (2.8) and (2.9) into Eq. (2.4) then gives for the total Hamiltonian

$$H = H_\mathrm{pl} + H_\mathrm{ph} + H_\mathrm{eh} + H_\mathrm{pl-ph} + H_\mathrm{pl-eh}. \tag{2.10}$$

In expression (2.10), the first term describes the LSP degrees of freedom and reads

$$H_\mathrm{pl} = \frac{\left[\mathbf{\Pi}(\mathbf{R})\right]^2}{2M} + \frac{1}{2}M\omega_\mathrm{sp}^2\left[\mathbf{h}(\mathbf{R})\right]^2, \tag{2.11}$$

with $M = \mathcal{N}_\mathrm{e}m_\mathrm{e}$ the total mass of the valence electrons. In Eq. (2.11), the resonance frequency ω_sp takes into account the spill-out effect [56–58] and is given by Eq. (1.6). This frequency is thus redshifted with respect to the Mie frequency (1.5). The second and third terms of Eq. (2.10) correspond to the free photon field energy [Eq. (2.3)] and to the Hamiltonian of the relative coordinates [Eq. (2.5)], respectively. Finally, the last two terms of Eq. (2.10) correspond respectively to the coupling between the plasmon and the vacuum electromagnetic modes defined in Eq. (2.6) and to the coupling between the center-of-mass coordinates and the relative ones

$$H_\mathrm{pl-eh} = \sum_{i=1}^{\mathcal{N}_\mathrm{e}}\mathbf{h}(\mathbf{R})\cdot\left[\nabla U(r_i')\right]\Big|_{\mathbf{h}(\mathbf{R})=0}. \tag{2.12}$$

This last coupling term arises due to the Coulomb-like tail of the confinement potential (see Fig. 2.1) and originates from the breakdown of Kohn's theorem [145]. Such a theorem states that for a fully harmonic potential (that is for all r), the center-of-mass and relative coordinates would be fully decoupled and Eq. (2.12) would vanish.

The full Hamiltonian written in the form of Eq. (2.10) is characteristic of an open quantum system. In such a case, we describe a small subsystem [described by Eq. (2.11) in the present case] coupled to different environments [described by Eqs. (2.3) and (2.5), respectively] considered to contain a much larger number of degrees of freedom than the subsystem. These photonic and electronic couplings are responsible for the energy relaxation of the system into the different environments (i.e., *baths*). In the case of the isolated metallic nanoparticles, the plasmon-photon coupling (2.6) leads to the dissipation of the LSPs into photons (through spontaneous emission pro-

cesses) while the coupling to the electronic environment (2.12) to the Landau damping. The latter mechanism corresponds to the decay of the plasmonic excitation into electron-hole pairs inside the nanoparticle. In addition to these damping mechanisms, the baths also renormalize the LSP resonance frequency with respect to $\omega_{\rm sp}$. For the purpose of this work, we will from now on neglect the effect of the spill-out in the plasmonic resonance frequency. Therefore, we perform the substitution $\omega_{\rm sp} \to \omega_0$ in the remainder of this manuscript.

2.2 Second quantization procedure and mean-field approximation

Even if the decomposition procedure presented in the previous section emphasizes efficiently the coupling between the collective motion of the electrons (e.g., the plasmon) and the relative ones [see Eq. (2.12)], it still remains a difficult task to treat the relative coordinates exactly. One may however use a mean-field approximation [67, 72–74] in order to be able to treat analytically the electronic degrees of freedom. In addition to this mean-field approximation, one can also rewrite the Hamiltonian (2.10) in the second quantization formalism [146]. Such a quantization procedure is required for evaluating the electronic-induced quantities such as the electronic frequency shift and the Landau damping which are purely quantum effects. In addition, evaluating the frequency shift associated to the plasmon-photon coupling quantum-mechanically provides more accurate results than the classical calculations (using the Abraham-Lorentz equation of motion [4]). Note, finally, that the radiative damping of the plasmonic system arising from the coupling to the photonic environment can be nevertheless obtained classically with ease since the radiation damping (which correspond to a spontaneous emission process of photons) can be evaluated with classical electrodynamics [4].

To write the Hamiltonian (2.10) in second quantized form one first introduces operators [147]

$$b^\sigma = \sqrt{\frac{M\omega_0}{2\hbar}}\mathbf{h}(\mathbf{R})\cdot\hat{\sigma} + \mathrm{i}\frac{\mathbf{\Pi}(\mathbf{R})\cdot\hat{\sigma}}{\sqrt{2\hbar M\omega_0}} \tag{2.13a}$$

and

$$b^{\sigma\dagger} = \sqrt{\frac{M\omega_0}{2\hbar}}\mathbf{h}(\mathbf{R})\cdot\hat{\sigma} - \mathrm{i}\frac{\mathbf{\Pi}(\mathbf{R})\cdot\hat{\sigma}}{\sqrt{2\hbar M\omega_0}}, \tag{2.13b}$$

where b^σ ($b^{\sigma\dagger}$) annihilates (creates) a plasmon with frequency ω_0 on the nanoparticle with the polarization $\hat{\sigma} = \hat{x}, \hat{y}, \hat{z}$.[1] Such operators satisfy the usual bosonic commutation relations $[b^\sigma, b^{\sigma'\dagger}] = \delta_{\sigma\sigma'}$ and $[b^\sigma, b^{\sigma'}] = [b^{\sigma\dagger}, b^{\sigma'\dagger}] = 0$.[2] With such a notation, Eq. (2.11) reads as

$$H_{\rm pl} = \sum_{\sigma=x,y,z} \hbar\omega_0 b^{\sigma\dagger} b^\sigma. \tag{2.14}$$

The eigenstates $|n^\sigma\rangle$ of the latter Hamiltonian (with n^σ a positive integer) correspond to plasmonic

[1] Throughout the manuscript, unit vectors are designated by hats.

[2] Here and in the remainder of this thesis the symbol δ_{ij} denotes the Kronecker-Delta symbol.

states with polarization σ and energy $\hbar\omega_0 n^\sigma$, and follow the algebra $b^{\sigma\dagger}|n^\sigma\rangle = \sqrt{n^\sigma+1}|n^\sigma+1\rangle$ and $b^\sigma|n^\sigma\rangle = \sqrt{n^\sigma}|n^\sigma-1\rangle$.

Using the second quantized form of the vector potential [148]

$$\mathbf{A}(\mathbf{r}) = \sum_{\mathbf{k},\hat{\lambda}_\mathbf{k}} \sqrt{\frac{2\pi\hbar c^2}{\mathcal{V}\omega_\mathbf{k}}}\hat{\lambda}_\mathbf{k}\left(a_\mathbf{k}^{\hat{\lambda}_\mathbf{k}} e^{i\mathbf{k}\cdot\mathbf{r}} + a_\mathbf{k}^{\hat{\lambda}_\mathbf{k}\dagger} e^{-i\mathbf{k}\cdot\mathbf{r}}\right), \tag{2.15}$$

where $a_\mathbf{k}^{\hat{\lambda}_\mathbf{k}\dagger}$ ($a_\mathbf{k}^{\hat{\lambda}_\mathbf{k}}$) creates (annihilates) a photon with wavevector $\mathbf{k}$, transverse polarization $\hat{\lambda}_\mathbf{k}$ ($\mathbf{k}\cdot\hat{\lambda}_\mathbf{k}=0$) and frequency $\omega_\mathbf{k} = c|\mathbf{k}|$, the Hamiltonian $H_{\rm ph}$ of the free-photon modes becomes in its second quantized form [148]

$$H_{\rm ph} = \sum_{\mathbf{k},\hat{\lambda}_\mathbf{k}} \hbar\omega_\mathbf{k} a_\mathbf{k}^{\hat{\lambda}_\mathbf{k}\dagger} a_\mathbf{k}^{\hat{\lambda}_\mathbf{k}}. \tag{2.16}$$

Then, using the expression (2.15) for the vector potential, one can express the plasmon-photon coupling Hamiltonian (2.6) as

$$\begin{aligned} H_{\rm pl-ph} = i\hbar \sum_{\sigma=x,y,z}\sum_{\mathbf{k},\hat{\lambda}_\mathbf{k}} \sqrt{\frac{\pi\omega_0^3 a^3}{\mathcal{V}\omega_\mathbf{k}}}\left(b^{\sigma\dagger} - b^\sigma\right)\hat{\sigma}\cdot\hat{\lambda}_\mathbf{k}\left(a_\mathbf{k}^{\hat{\lambda}_\mathbf{k}} + a_\mathbf{k}^{\hat{\lambda}_\mathbf{k}\dagger}\right) \\ + \pi\hbar\omega_0^2\frac{a^3}{\mathcal{V}}\sum_{\substack{\mathbf{k},\hat{\lambda}_\mathbf{k}\\ \mathbf{k}',\hat{\lambda}_{\mathbf{k}'}}} \frac{\hat{\lambda}_\mathbf{k}\cdot\hat{\lambda}_{\mathbf{k}'}}{\sqrt{\omega_\mathbf{k}\omega_{\mathbf{k}'}}}\left(a_\mathbf{k}^{\hat{\lambda}_\mathbf{k}} + a_\mathbf{k}^{\hat{\lambda}_\mathbf{k}\dagger}\right)\left(a_{\mathbf{k}'}^{\hat{\lambda}_{\mathbf{k}'}} + a_{\mathbf{k}'}^{\hat{\lambda}_{\mathbf{k}'}\dagger}\right). \end{aligned} \tag{2.17}$$

In order to overcome the difficulty of treating exactly the electron-electron interactions appearing in the Hamiltonian of the relative coordinates $H_{\rm eh}$, one can replace Eq. (2.5) by its counterpart within the mean-field approximation [67, 72–75]. Hence, the Hamiltonian of the relative coordinates reads in second quantization form as

$$H_{\rm eh} = \sum_i \epsilon_i c_i^\dagger c_i. \tag{2.18}$$

Here, c_i ($c_i^\dagger$) annihilates (creates) an electron in the state $|i\rangle$ with energy ϵ_i in the self-consistent potential V (which then contains the exchange between the electrons) calculated in a mean-field approximation.[3] The potential V, represented in Fig. 2.2, can be obtained numerically from Kohn-Sham local density approximation (LDA) calculations [67]. We see from the figure that the mean-field potential $V(r)$ remains almost flat inside the nanoparticle and experiences a steep increase at $r = a$. Therefore, we further approximate such a potential by a spherical square well with height V_0, $V(r) = V_0\Theta(a-r)$. One finally assumes that the work function $W = V_0 - E_{\rm F}$, with $E_{\rm F}$ the Fermi energy, is large enough compared to the plasmon energy $\hbar\omega_0$ to avoid any ionization of the electrons.

Since the height of the potential V_0 is large enough with respect to the Fermi energy, one can

[3] Importantly, in the second quantization formalism used for the electronic environment throughout the thesis, the index i [see e.g. (2.18)] is a dumb index denoting a single-particle state and is not related to the $i^{\rm th}$ electron of the nanoparticles.

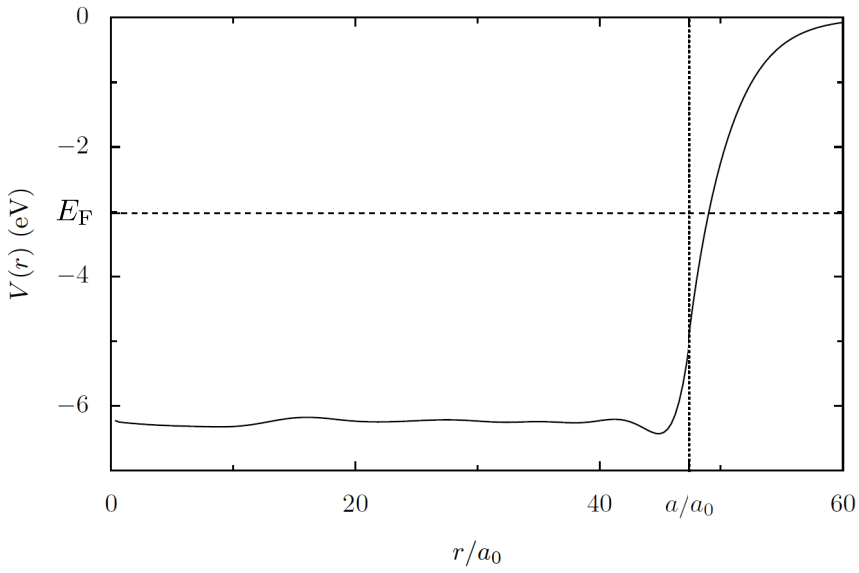

Figure 2.2: Self-consistent potential V for a sodium nanoparticle obtained from LDA numerical calculations as a function of the radial coordinate r. In the figure, E_{F} denotes the Fermi energy while a_0 is the Bohr radius and a the nanoparticle radius. Figure adapted from Ref. [67].

consider as well an infinite height for the self-consistent potential V. The electron-plasmon coupling Hamiltonian $H_{\mathrm{pl-eh}}$ thus reads in second quantized form as

$$H_{\mathrm{pl-eh}} = \sum_{\sigma=x,y,z} \sum_{ij} \Lambda \left(b^{\sigma} + b^{\sigma\dagger} \right) \hat{\sigma} \cdot \mathbf{d}_{ij} c_i^{\dagger} c_j, \tag{2.19}$$

with the constant

$$\Lambda = \sqrt{\frac{\hbar m_{\mathrm{e}} \omega_0^3}{2\mathcal{N}_{\mathrm{e}}}} \tag{2.20}$$

and where

$$\mathbf{d}_{ij} = \langle i|\mathbf{r}|j\rangle. \tag{2.21}$$

In the equation above, the matrix elements $\mathbf{d}_{ij}$ can be written as [149]

$$\mathbf{d}_{ij} = \mathcal{R}(\epsilon_i, \epsilon_j) \left(\sum_{\aleph=\pm 1} \mathcal{A}_{l_i,l_j,\aleph}^{m_i,m_j} \frac{\hat{x} - \mathrm{i}\aleph\hat{y}}{\sqrt{2}} + \mathcal{A}_{l_i,l_j,0}^{m_i,m_j} \hat{z} \right), \tag{2.22}$$

where l_i (l_j) and m_i (m_j) are the angular momentum quantum numbers of the wave function describing the single-particle state $|i\rangle$ ($|j\rangle$). In Eq. (2.22), the radial part can be obtained by following

the procedure described in Ref. [71] and reads

$$\mathcal{R}(\epsilon_i,\epsilon_j)=\frac{2\hbar^2}{m_{\mathrm{e}}a}\frac{\sqrt{\epsilon_i\epsilon_j}}{(\epsilon_i-\epsilon_j)^2}. \tag{2.23}$$

The angular part is expressed in terms of Wigner-3j symbols as

$$\mathcal{A}_{l_i,l_j,\aleph}^{m_i,m_j}=(-1)^{m_i+\aleph}\sqrt{(2l_i+1)(2l_j+1)}\begin{pmatrix} l_i & l_j & 1\\ 0 & 0 & 0\end{pmatrix}\begin{pmatrix} l_i & l_j & 1\\ -m_i & m_j & \aleph\end{pmatrix}. \tag{2.24}$$

The latter expression encapsulates the angular momentum selection rules $l_i=l_j\pm1$, $m_i=m_j$ (for $\aleph=0$) and $m_i=m_j\pm1$ (for $\aleph=\pm1$).

The two coupling Hamiltonians $H_{\mathrm{pl-ph}}$ and $H_{\mathrm{pl-eh}}$ written in Eqs. (2.17) and (2.19) in their second quantized form can then be used to evaluate the quantities related to the coupling between the plasmonic system and the environments. These quantities are, namely, the radiation and Landau damping decay rates and the associated frequency shifts arising from the coupling to the photonic and electronic baths, respectively.

2.3 Linewidth of the plasmon resonance

We start the analysis of the quantities arising from the coupling to the environment by considering the damping rates of the plasmon resonance. Such rates are responsible for the finite linewidth of the absorption cross-section of a single nanoparticle. Usually, the total linewidth results from the two damping mechanisms mentioned above in addition to the Ohmic losses. However, we do not treat here this last contribution since these losses (dominated by electron-phonon scattering at room temperature) can be considered constant as a function of the radius a for the typical nanoparticle sizes we investigate in the present manuscript. Therefore, such constant losses depend only on the metal one aims to study.

2.3.1 Radiative damping

We consider first the radiation damping of the plasmon which is size-dependent. Indeed, as we consider the plasmon as an oscillating electric dipole [cf. Eq. (2.14)], it dissipates energy by emitting photons in the free space. Such an emission rate can be obtained through a Fermi golden rule for the plasmon-photon coupling Hamiltonian (2.17). The radiative damping rate then reads as

$$\gamma_0=\frac{2\pi}{\hbar^2}\sum_{\mathbf{k},\hat{\lambda}_{\mathbf{k}}}\left|\langle 0^\sigma,1_{\mathbf{k}}^{\hat{\lambda}_{\mathbf{k}}}|H_{\mathrm{pl-ph}}|1^\sigma,\mathrm{vac}\rangle\right|^2\delta(\omega_0-\omega_{\mathbf{k}}), \tag{2.25}$$

where $\delta(x)$ stands for the Dirac-delta distribution. Note that the decay rate (2.25) is calculated at $T=0\,\mathrm{K}$.[4] In the equation above, $|1^\sigma\rangle$ is a single plasmonic state with frequency ω_0 and polarization σ and $|0^\sigma\rangle$ its corresponding ground state. The states $|1_{\mathbf{k}}^{\hat{\lambda}_{\mathbf{k}}}\rangle$ and $|\mathrm{vac}\rangle$ represent a one photon state

[4] We will use such a limit in the remainder of this manuscript.

(with momentum $\mathbf{k}$ and transverse polarization $\hat{\lambda}_{\mathbf{k}}$) and the photonic vacuum state, respectively.[5] Note that even though the plasmonic states are polarized in the direction σ, the damping rates stay identical for all directions due to the spherical symmetry of the cluster.

Inserting the expression of the Hamiltonian (2.17) into (2.25) then leads to

$$\gamma_0 = \frac{2\pi^2\omega_0^3 a^3}{\mathcal{V}} \sum_{\mathbf{k},\hat{\lambda}_{\mathbf{k}}} \frac{|\hat{\sigma}\cdot\hat{\lambda}_{\mathbf{k}}|^2}{\omega_{\mathbf{k}}} \delta(\omega_0 - \omega_{\mathbf{k}}). \tag{2.26}$$

In order to evaluate the latter expression, one can first carry out the summation over the photon polarization using [148]

$$\sum_{\hat{\lambda}_{\mathbf{k}}} (\hat{\sigma}\cdot\hat{\lambda}_{\mathbf{k}})(\hat{\sigma}'\cdot\hat{\lambda}_{\mathbf{k}}) = \delta_{\sigma\sigma'} - (\hat{\sigma}\cdot\hat{k})(\hat{\sigma}'\cdot\hat{k}), \tag{2.27}$$

and then by taking the continuous limit

$$\sum_{\mathbf{k}} \to \frac{\mathcal{V}}{(2\pi)^3} \int \mathrm{d}^3\mathbf{k} \tag{2.28}$$

corresponding to the limit $\mathcal{V} \to \infty$ in Eq. (2.26), yielding for the radiative decay rate

$$\gamma_0 = \frac{\omega_0^3 a^3}{4\pi} \int \frac{\mathrm{d}^3\mathbf{k}}{\omega_{\mathbf{k}}} [1 - (\hat{\sigma}\cdot\hat{k})^2] \delta(\omega_0 - \omega_{\mathbf{k}}). \tag{2.29}$$

Choosing spherical coordinates together with $\omega_{\mathbf{k}} = c|\mathbf{k}|$, the above integral can be replaced by

$$\gamma_0 = \frac{\omega_0^3 a^3}{4\pi c^2} \int_0^{\pi} \mathrm{d}\theta \sin\theta \int_0^{2\pi} \mathrm{d}\varphi [1 - (\hat{\sigma}\cdot\hat{k})^2] \int_0^{+\infty} \mathrm{d}k\, k\delta\left(\frac{\omega_0}{c} - k\right). \tag{2.30}$$

Defining the quantity

$$\eta^{\sigma} = (1, 1, -2) \tag{2.31}$$

for $\sigma = (x, y, z)$, one can evaluate the integral over the polar angle φ which then reads

$$\int_0^{2\pi} \mathrm{d}\varphi [1 - (\hat{\sigma}\cdot\hat{\mathbf{k}})^2] = |\eta_{\sigma}|\pi \left(1 + \mathrm{sgn}\{\eta^{\sigma}\}\cos^2\theta\right). \tag{2.32}$$

Thus inserting the result Eq. (2.32) into Eq. (2.30), the integrals over the solid angle give $8\pi/3$ for each direction of space $\sigma = x, y, z$. Evaluating the last integral on k, the radiative damping rate is finally given by Eq. (1.7) introduced in Sec. 1.1.1.

As can be seen from Eq. (1.7), the radiative damping rate scales with the volume of the considered nanoparticle. Such scaling is due to the fact that the radiative emission rate is directly proportional to the number of valence electrons in the nanoparticle. Note that the rate presented in

[5] Here, $|\mathrm{vac}\rangle$ represents the short notation of the many-body photonic ground state $|0^{\hat{\lambda}_{\mathbf{k}}}_{\mathbf{k}_1}, 0^{\hat{\lambda}_{\mathbf{k}}}_{\mathbf{k}_2}, \ldots, 0^{\hat{\lambda}_{\mathbf{k}}}_{\mathbf{k}_\infty}\rangle$ and the one-photon state is then given by $|0^{\hat{\lambda}_{\mathbf{k}}}_{\mathbf{k}_1}, 0^{\hat{\lambda}_{\mathbf{k}}}_{\mathbf{k}_2}, \ldots, 1^{\hat{\lambda}_{\mathbf{k}}}_{\mathbf{k}}, \ldots, 0^{\hat{\lambda}_{\mathbf{k}}}_{\mathbf{k}_\infty}\rangle$. Here, the quantity $\mathbf{k}_i$ are the different accessible values for the photonic wavevector.

(1.7) can also be obtained classically by explicitly evaluating the total emitted power of an oscillating electric dipole through the calculation of the Poynting vector [4].

2.3.2 Landau damping

The second size-dependent mechanism involved in the dissipation of the plasmon energy is the Landau damping which will be discussed in the following. Such a damping rate stems from the decay of a plasmonic state into electron-hole pairs inside the nanoparticle. Similarly to the radiative losses rate (see Sec. 2.3.1), one can evaluate (assuming weak coupling to the electronic bath) the Landau damping with the help of a Fermi golden rule for the coupling Hamiltonian $H_{\mathrm{pl-eh}}$ [cf. Eq. (2.19)]. Such a procedure thus gives

$$\Gamma_0^\sigma = \frac{2\pi}{\hbar} \sum_{eh} |\langle 0^\sigma, eh | H_{\mathrm{pl-eh}} | 1^\sigma, \mu \rangle|^2 \, \delta(\hbar\omega_0 - \epsilon_{eh}), \tag{2.33}$$

with $\epsilon_{eh} = \epsilon_e - \epsilon_h$ the energy of a single electron-hole pair and where the summation goes over all the electron $|e\rangle$ and hole $|h\rangle$ states with energy ϵ_e and ϵ_h, respectively. In the expression above, $|1^\sigma\rangle$ and $|0^\sigma\rangle$ are respectively the plasmonic first excited state (with frequency ω_0 and the ground state with polarization σ while $|\mu\rangle$ and $|eh\rangle$ correspond to the electronic ground state (with no electron-hole pair) and an electron-hole pair state, respectively.

Inserting Eq. (2.19) into the Fermi golden rule (2.33) then gives

$$\Gamma_0^\sigma = \Sigma^\sigma(\omega_0), \tag{2.34}$$

where the function $\Sigma^\sigma(\omega)$ is given by [67]

$$\Sigma^\sigma(\omega) = \frac{2\pi}{\hbar} \sum_{eh} |\Lambda \hat{\sigma} \cdot \mathbf{d}_{eh}|^2 \, \delta(\hbar\omega - \epsilon_{eh}). \tag{2.35}$$

Note that the latter equation is only valid at zero temperature. Since the electronic wavefunctions are spherically symmetric, the expression $\Sigma^\sigma(\omega)$ evaluated in Appendix A for $\sigma = z$ [cf. Eq. (A.8)] can be replaced by the isotropic expression so that

$$\Sigma^\sigma(\omega) = \Sigma^z(\omega) = \Sigma(\omega). \tag{2.36}$$

Thus, inserting Eq. (2.36) into the expression (2.34) to yield [67, 71, 72]

$$\Gamma_0 = \frac{3v_\mathrm{F}}{4a} g\left(\frac{\hbar\omega_0}{E_\mathrm{F}}\right), \tag{2.37}$$

where the function $g(\nu)$ is given in Eq. (A.10) and where v_F is the Fermi velocity. As can be seen from Eq. (2.37), the Laudau damping scales with the inverse radius of the nanoparticle meaning that it becomes significant for small-sized nanoparticles.

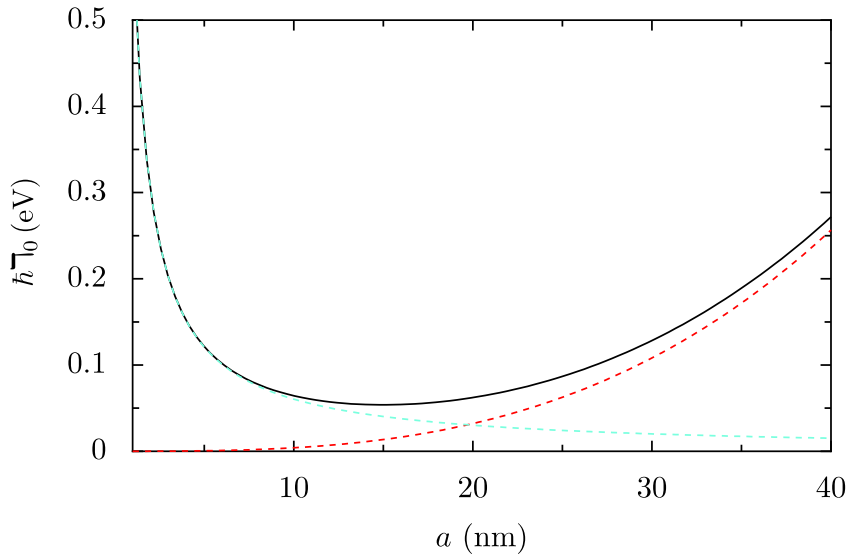

Figure 2.3: Total linewidth $\hbar\gamma_0$ (Ohmic losses are neglected in the figure) of a plasmon for a single Ag nanoparticle as a function of its radius a. We observe a clear minimum of the rate for $a \simeq 15\,\mathrm{nm}$. The solid black line represents the total linewidth while the red and cyan dashed lines show the radiative ($\hbar\gamma_0$) and Landau ($\hbar\Gamma_0$) contributions, respectively. In the figure, we choose $\hbar\omega_0 = 2.6\,\mathrm{eV}$ and $E_\mathrm{F} = 5.5\,\mathrm{eV}$ corresponding to a silver nanoparticle.

2.3.3 Comparison of the radiative and Landau damping rates

The radiative and Landau dampings display opposite scaling with respect to the nanoparticle radius a. The radiative damping γ_0 scales with the volume of the nanoparticle ($\propto a^3$) while the Landau damping Γ_0 shows a $1/a$ dependence. Therefore, one can expect to observe a clear minimum in the total size-dependent losses $\gamma_0 = \gamma_0 + \Gamma_0$ as the nanoparticle radius increases. We show in Figure 2.3 the total linewidth $\hbar\gamma_0$ of a silver cluster as a function of its radius (we use the same parameters as those used in Sec. 2.4.3). Ohmic losses are not included in γ_0 shown in Fig. 2.3 since they only constitute a global increase of the total damping rate in the nanoparticule range which are studied here. As clearly seen from the figure, the damping rate γ_0 displays a minimum around $a \simeq 15\,\mathrm{nm}$. Below this critical value, the energy losses of the plasmon are dominated by the Landau mechanism. In contrast, the spontaneous photon emission processes become significant for larger clusters.

We will show in the next chapter that such simple scaling of the dampings can be strongly modified in the presence of more than one nanoparticle.

2.4 Environment-induced frequency shifts

In addition to induce a finite linewith to the plasmonic resonance, the environments to which the plasmonic system is coupled lead to a renormalization of the plasmon frequency ω_0. Since the

plasmonic system is coupled to two different environments, the global shift arises from two distinct contributions coming from the photonic and electronic baths, respectively.

2.4.1 Radiative frequency shift

In the following, we first discuss the frequency shift induced by the coupling to the photonic vacuum modes (i.e., the photonic bath). Such a shift is analogous to the Lamb shift in atomic physics which was introduced to interpret the experimental observations of the energy spectrum of atoms [65, 150].

In the present case of plasmonic resonances, the *plasmonic radiative shift* can be calculated from the plasmon-photon coupling Hamiltonian (2.17) using non-degenerate second-order perturbation theory. Within such a description, the energy of a single plasmonic level $|n^\sigma\rangle$ with polarization σ is given by $E_{n^\sigma} = \hbar\omega_0 n^\sigma + E^{(1)}_{n^\sigma} + E^{(2)}_{n^\sigma}$, where $\hbar\omega_0 n^\sigma$ is the unperturbed energy of a single plasmonic level. The first and second order corrections (induced only by the photonic bath) of the energy are given by [147]

$$E^{(1)}_{n^\sigma} = \langle n^\sigma, \mathrm{vac}|H_{\mathrm{pl-ph}}|n^\sigma, \mathrm{vac}\rangle \tag{2.38a}$$

and

$$E^{(2)}_{n^\sigma} = \frac{1}{\hbar}\sum_{\substack{m^\sigma \\ (m^\sigma \neq n^\sigma)}} \frac{\left|\langle m^\sigma, 1^{\hat{\lambda}_\mathbf{k}}_\mathbf{k}|H_{\mathrm{pl-ph}}|n^\sigma, \mathrm{vac}\rangle\right|^2}{(n^\sigma - m^\sigma)\,\omega_0 - \omega_\mathbf{k}}, \tag{2.38b}$$

respectively. It can be shown [64] that the first-order correction (2.38a), arising from the second term in the r.h.s. of (2.6), does not contribute to the radiative shift δ^σ_0 since it does not depend on the quantum number n^σ. The second-order correction which stems from the first term in Eq. (2.17), does in contrast depend on the plasmonic quantum number. Substituting (2.17) into (2.38b) yields

$$E^{(2)}_{n^\sigma} = \pi\hbar\omega_0^3\frac{a^3}{\mathcal{V}}\sum_{\mathbf{k},\hat{\lambda}_\mathbf{k}}\frac{|\hat{\sigma}\cdot\hat{\lambda}_\mathbf{k}|^2}{\omega_\mathbf{k}}\frac{(2n^\sigma+1)\,\omega_\mathbf{k} - \omega_0}{\omega_0^2 - \omega_\mathbf{k}^2} \tag{2.39}$$

which is linearly divergent. One can however regularize such a divergence using a procedure analogous to the one used by Bethe while analyzing the Lamb shift in atomic physics [65, 66]. Such a procedure (discussed more extensively in Ref. [64]), consists into two steps. First, one introduces an ultraviolet cutoff $k_\mathrm{c} = 1/a$ to the summation over the wavevectors $\mathbf{k}$ in Eq. (2.39). This particular value corresponds to a critical frequency $\omega_\mathrm{c} = ck_\mathrm{c}$ below which the dipolar approximation used in Eq. (2.6) does not hold any longer. Secondly, one subtracts the energy corresponding to the free electrons (with frequency ω_0) into Eq. (2.39). Such a quantity is obtained by taking the limit $\omega_0 \to 0$ into the summation over $\mathbf{k}$ only [66]. Thus, one obtains for the regularized second order correction to the energy

$$\bar{E}^{(2)}_{n^\sigma} = \pi\hbar\omega_0^4\frac{a^3}{\mathcal{V}}\sum_{\mathbf{k},\hat{\lambda}_\mathbf{k}}\frac{|\hat{\sigma}\cdot\hat{\lambda}_\mathbf{k}|^2}{\omega_\mathbf{k}^2}\frac{(2n^\sigma+1)\,\omega_0 - \omega_\mathbf{k}}{\omega_0^2 - \omega_\mathbf{k}^2}, \tag{2.40}$$

which diverges only logarithmically. The renormalized frequency difference between two succes-

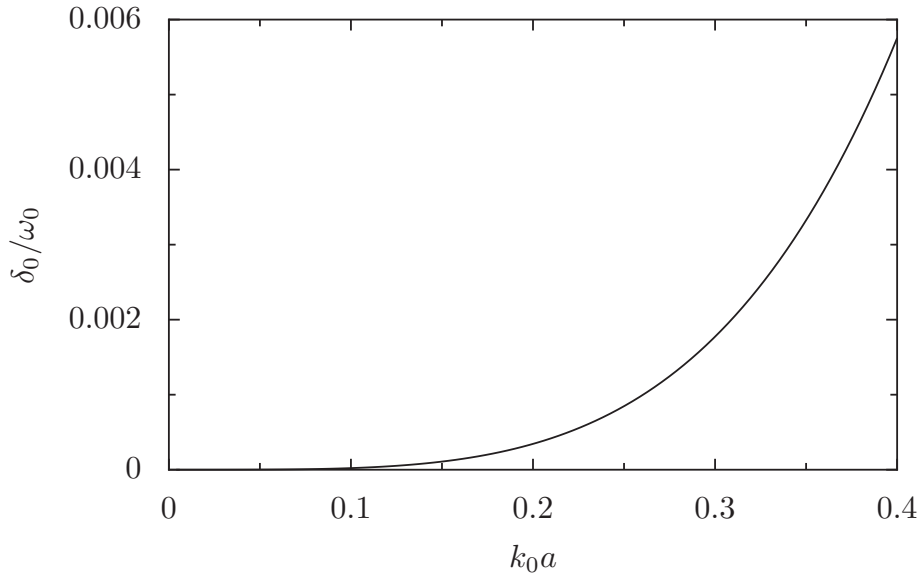

Figure 2.4: Radiative frequency shift (2.43) of an isolated nanoparticle scaled by the LSP frequency ω_0 as a function of the (reduced) nanoparticle radius $k_0 a$. In the figure, $\omega_c = c/a$.

sive plasmonic levels $\bar{\omega}_0 = (\bar{E}_{n^\sigma+1} - \bar{E}_{n^\sigma})/\hbar$ does not depend of the quantum number n^σ and reads $\bar{\omega}_0 = \omega_0 + \delta_0$ where the radiative shift is given by

$$\delta_0^\sigma = 2\pi\hbar\omega_0^5 \frac{a^3}{\mathcal{V}} \sum_{\mathbf{k},\hat{\lambda}_\mathbf{k}} \frac{|\hat{\sigma}\cdot\hat{\lambda}_\mathbf{k}|^2}{\omega_\mathbf{k}^2} \frac{1}{\omega_0^2 - \omega_\mathbf{k}^2}. \tag{2.41}$$

The latter expression can be evaluated by taking the continuum limit (2.28) and carrying out the summation over the photon polarization using Eq. (2.27). Performing these different steps yields for the radiative shift the expression

$$\delta_0 = \frac{\omega_0^5 a^3}{(2\pi c)^2} \mathcal{P} \int_0^{k_c} \frac{\mathrm{d}k}{\omega_0^2 - (ck)^2} \int_0^\pi \mathrm{d}\theta \sin\theta \int_0^{2\pi} \mathrm{d}\varphi [1 - (\hat{\sigma}\cdot\hat{k})^2], \tag{2.42}$$

with $\omega_c > \omega_0$ and where $\mathcal{P}$ denotes the Cauchy principal value. Inserting the result for the integral over the polar angle φ given by Eq. (2.32) into Eq. (2.42) one can finally perform the remaining integrals to yield the radiative frequency shift [64]

$$\delta_0 = \frac{\omega_0}{3\pi} (k_0 a)^3 \ln\left(\frac{\omega_c/\omega_0 + 1}{\omega_c/\omega_0 - 1}\right), \tag{2.43}$$

with $k_0 = \omega_0/c$. Note that, in the equation above, the radiative shift δ_0 is equivalent for all polarization σ due to the isotropy of the system. The latter equation being always positive with the choice of ω_c, the shift induced by the photonic environment corresponds to a blueshift with respect to the

bare Mie frequency ω_0. We plot Eq. (2.43) as a function of $k_0 a$ in Fig. 2.4. In the limit $k_0 a \ll 1$, the expression (2.43) reduces to $\delta_0 \simeq 2\omega_0 (k_0 a)^4/3\pi$ and thus scales with the fourth power of the radius a of the nanoparticle. Such a behavior can be clearly seen from Fig. 2.4.

2.4.2 Shift induced by the electronic bath

As mentioned previously, the electronic environment of the plasmon also contributes to a shift of the Mie frequency which adds up to the radiative shift [cf. Eq. (2.43)] discussed above. To evaluate this shift, one can use a second-order perturbation theory in the plasmon-electron coupling Hamiltonian $H_{\rm pl-eh}$ in a similar fashion as done for the radiative shift (see Sec. 2.4.1). Thus, following closely the procedure presented in Ref. [67], one can first notice that due to the form of $H_{\rm pl-eh}$ there is no first-order correction to the energy since the dipole matrix elements $\mathbf{d}_{ij}$ entering Eq. (2.19) are purely off-diagonal. Therefore one can directly write the second-order term as

$$\mathcal{E}^{(2)}_{n^\sigma} = \frac{1}{\hbar} \sum_{\substack{m^\sigma \\ (m^\sigma \neq n^\sigma)}} \sum_{eh} \frac{|\langle m^\sigma, eh | H_{\rm pl-eh} | n^\sigma, \mu \rangle|^2}{(n^\sigma - m^\sigma)\,\omega_0 - \omega_{eh}}, \tag{2.44}$$

where $\omega_{eh} = \epsilon_{eh}/\hbar$. Summing over all possible final plasmonic states in (2.44) and evaluating the quantity $(\mathcal{E}^{(2)}_{n^\sigma+1} - \mathcal{E}^{(2)}_{n^\sigma})/\hbar$ one obtains the *electronic shift*

$$\Delta^\sigma_0 = -\frac{2}{\hbar^2} \mathcal{P} \sum_{eh} |\Lambda \hat{\sigma} \cdot \mathbf{d}_{eh}|^2 \frac{\omega_{eh}}{\omega^2_{eh} - \omega^2_0}, \tag{2.45}$$

where $\mathbf{d}_{eh}$ was introduced in Eq. (2.21) in Section 2.2. In order to evaluate the summation over the electron-hole pairs in (2.45), one may use the function $\Sigma^\sigma(\omega)$ defined in Eq. (2.35). One can then relate the expression Eq. (2.35) to the electronic shift (2.45) through the Kramers-Krönig relation

$$\Delta^\sigma_0 = -\frac{1}{\pi} \mathcal{P} \int_{-\infty}^{+\infty} \mathrm{d}\omega \frac{\omega \Sigma^\sigma(\omega)}{\omega^2 - \omega^2_0}. \tag{2.46}$$

To perform the integral in Eq. (2.46), one now follows Ref. [67] and replaces the expression (A.8) for the function $\Sigma^\sigma(\omega)$ entering (2.46). Since the system is spherically symmetric, the result (A.8) is valid for all polarization σ. In Eq. (2.46), one can first notice that the integral can be approximated introducing a frequency cutoff by

$$\Delta_0 \simeq -\frac{1}{\pi} \mathcal{P} \int_{\omega_0 - \eta\Gamma_0}^{+\infty} \mathrm{d}\omega \frac{\omega \Sigma^z(\omega)}{\omega^2 - \omega^2_0}, \tag{2.47}$$

where η is a constant of the order of unity. Here, the quantity Γ_0 appearing in the low boundary corresponds to the linewidth of the absorption cross-section of the nanoparticle. Note that, the polarization index σ in Eq. (2.46) have been dropped in Eq. (2.47) since the electronic shift is the same for all directions x, y, z. Indeed, the polarization dependence of the frequency shift is only related to the function $\Sigma^\sigma(\omega)$ which is isotropic. In the latter equation, this choice of cutoff for the lower boundary is motivated by the fact that not all electron-hole pairs of the environment

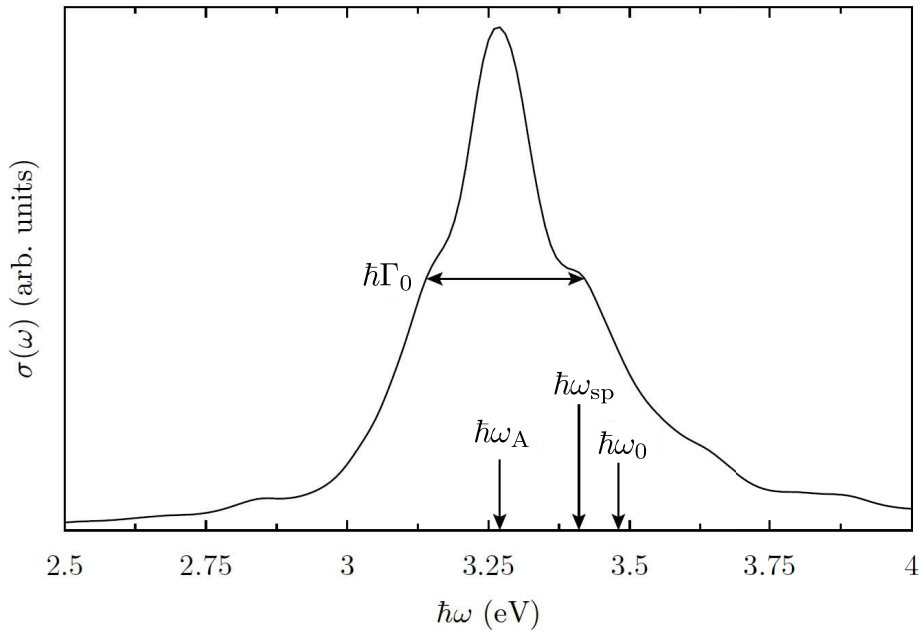

Figure 2.5: Absorption cross-section extracted from TDLDA calculations for a sodium cluster [67] as a function of the photon energy. In the figure ω_0 denotes the classical Mie frequency, $\omega_{\rm sp}$ the plasmon frequency including the spill-out effect and $\omega_{\rm A}$ corresponds to the frequency at the position of the maximum of the absorption curve. Γ_0 is the linewidth of the absorption curve which can be related to the damping rate of the plasmonic excitations (in the present case, the radiative and Ohmic linewidths are neglected). Figure adapted from Ref. [67].

participate to the shift Δ_0. On the one hand, Yannouleas and coworkers stated that the Hilbert space of the electron-hole pairs contained in the nanoparticle can be separated in two distinct parts within the random phase approximation [71]. The first part, corresponding to a restricted subspace with low energy, contains the electron-hole pairs constituting the plasmon. Indeed, in such a description, the plasmon can be seen as a coherent superposition of basis states of the restricted subspace. The second part, the additional subspace with higher energy, corresponds to the subspace of the pairs participating to the damping of the plasmon via the Landau damping. Therefore, only the electron-hole pairs belonging to the high-energy sector participates to the shift. On the other hand, numerical calculations based on time-dependent local density approximation (TDLDA) [67], show that the absorption cross-section displays a large excitation peak centered around the resonance frequency $\omega_{\rm A}$ as shown in figure 2.5. Although this peak supports almost the entire dipole strength, some of the electron-hole excitations surrounding this peak become noticeable for frequency larger than $\omega_0 - \eta\Gamma_0$ and one needs to take these pairs into account in the evaluation of Eq. (2.46).

Since only the frequencies larger than $\omega_0 - \eta\Gamma_0$ are considered, the function $g(\nu)$ appearing in the expression of the function $\Sigma^z(\omega)$ [see Eq. (A.8)] can be replaced by its asymptotic expansion

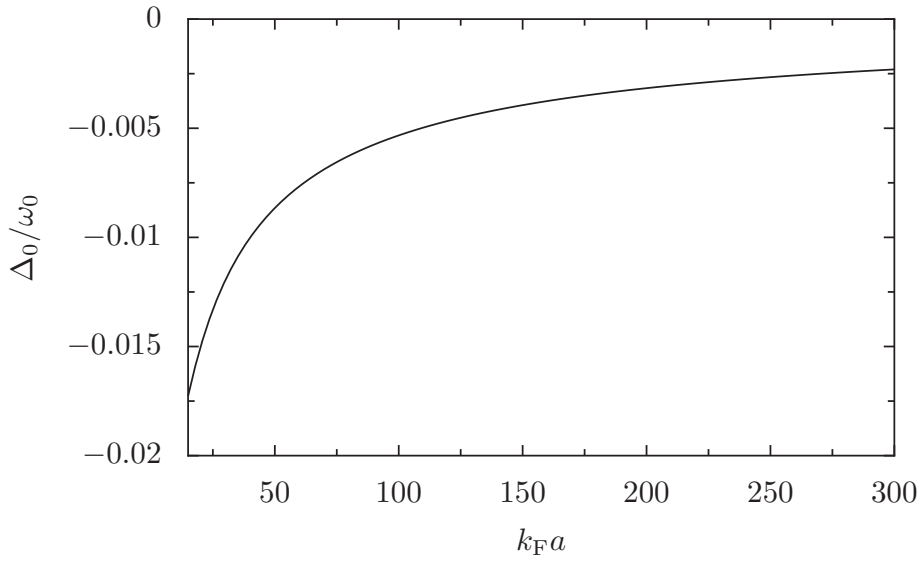

Figure 2.6: Electronic (or Landau) frequency shift (2.52) of an LSP supported by an Ag nanoparticle as a function of the (reduced) radius $k_{\mathrm{F}}a$ of the nanoparticle. In the figure, the parameters are $\hbar\omega_0 = 2.6\,\mathrm{eV}$, $E_{\mathrm{F}} = 5.5\,\mathrm{eV}$ and $\eta = 1/2$.

for $E_{\mathrm{F}} \ll \hbar\omega_0$ at zero temperature

$$g\left(\frac{\hbar\omega}{E_{\mathrm{F}}}\right) \simeq \frac{8}{15}\sqrt{\frac{E_{\mathrm{F}}}{\hbar\omega}}. \tag{2.48}$$

Inserting (A.8) together with Eq. (2.48) for the g function into (2.47) then gives

$$\Delta_0 = -\frac{2v_{\mathrm{F}}}{5\pi a} I\left(\frac{\hbar\omega_0}{E_{\mathrm{F}}}, \eta\frac{\hbar\gamma}{E_{\mathrm{F}}}\right), \tag{2.49}$$

where the function $I(\xi,\alpha)$ is given by

$$I(\xi,\alpha) = \xi^3 \mathcal{P}\int_{\xi-\alpha}^{+\infty} \frac{\mathrm{d}x}{x^{5/2}\left(x^2-\xi^2\right)}. \tag{2.50}$$

According to Ref. [68], the latter function $I(\xi,\alpha)$ reduces to

$$I(\xi,\alpha) \simeq \frac{1}{\sqrt{\xi}}\left[\frac{1}{2}\ln\left(\frac{4\xi}{\alpha}\right) - \frac{\pi}{2} - \frac{4}{3}\right] \tag{2.51}$$

in the limit $\xi \gg \alpha$. Thus, substituting Eq. (2.51) into Eq. (2.49) finally yields

$$\Delta_0 = -\frac{3v_{\mathrm{F}}}{4a}\beth(\omega_0), \tag{2.52}$$

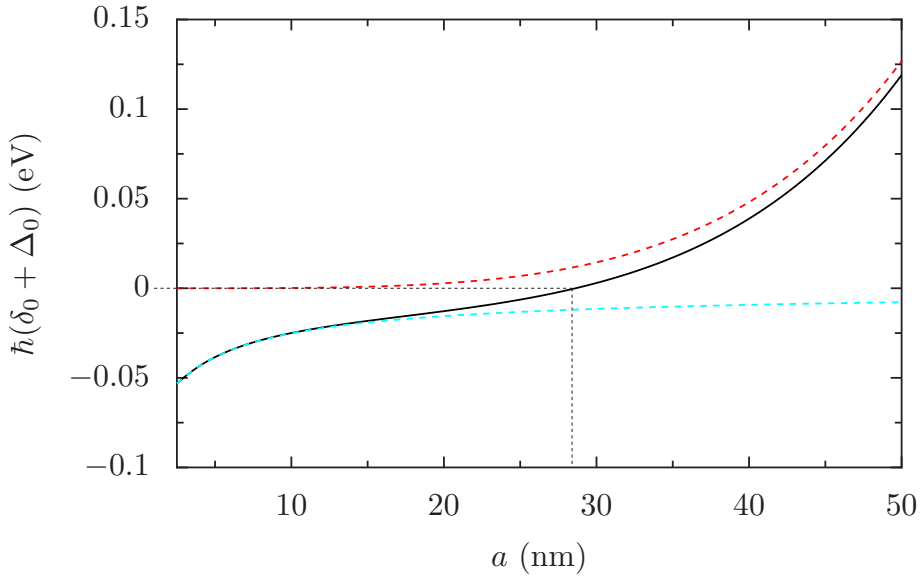

Figure 2.7: Total energy shift $\hbar(\delta_0+\Delta_0)$ induced on the Mie frequency of a single Ag nanoparticle as a function of its radius a. In the figure, the relevant parameters for the silver are $\hbar\omega_0 = 2.6\,\mathrm{eV}$ and $E_\mathrm{F} = 5.5\,\mathrm{eV}$. The solid black line represents the total shift while the red and cyan dashed lines show the radiative ($\hbar\delta_0$) and Landau ($\hbar\Delta_0$) contributions, respectively. The black dashed line indicates the value of a for which $\hbar(\delta_0+\Delta_0)$ vanishes. We find for such a value $a \simeq 28\,\mathrm{nm}$.

where the function $\beth(\omega)$ is given by

$$\beth(\omega) = \frac{4}{15\pi}\sqrt{\frac{E_\mathrm{F}}{\hbar\omega}}\left(\frac{\omega_0}{\omega}\right)^4\left[\ln\left(\frac{8\hbar\omega k_\mathrm{F} a}{3\eta E_\mathrm{F} g(\hbar\omega/E_\mathrm{F})}\left[\frac{\omega}{\omega_0}\right]^4\right) - \frac{\pi}{2} - \frac{4}{3}\right]. \tag{2.53}$$

In the equation above k_F denotes the Fermi wavevector. The figure 2.6 shows the Landau shift (2.52) scaled by the Mie frequency as a function of the (reduced) radius a of a silver cluster. For such Ag nanoparticles, one has $\hbar\omega_0 = 2.6\,\mathrm{eV}$ and $E_\mathrm{F} = 5.5\,\mathrm{eV}$.

Since the function $\beth(\omega)$ is a monotonic positive function of the radius a of the nanoparticle (see Appendix B for details), the expression (2.52) remains always negative as can be seen in Fig. 2.6. Therefore, the electronic environment induces a redshift of the plasmon frequency. Such a behavior is coherent with respect to the shift observed between the Mie frequency and the frequency ω_A (which correspond to the position of the maximum of the curve) on the absorption curve in Fig. 2.5. Here, we point out that, while the Landau damping [cf. Eq. (2.37) in Sec. 2.3] scales as $1/a$, the associated shift scales as $1/a$ up to a logarithmic factor.

2.4.3 Comparison of the radiative and Landau shifts

We now briefly discuss the scaling of the total shift, $\delta_0+\Delta_0$, induced on the Mie frequency ω_0 as a function of the size of the nanoparticle. We have seen that while the radiative shift δ_0 corresponds to

a blueshift (when choosing an ultraviolet cutoff), the Landau shift Δ_0 is associated with a redshift of the Mie frequency. Such opposite behaviors suggests that we can find a critical radius a for the nanoparticle for which the two shifts compensate each other, thus suppressing completely the frequency shift (i.e., $\delta_0 = -\Delta_0$). We show in Figure 2.7 the total energy shift $\hbar(\delta_0 + \Delta_0)$ as a function of the nanoparticle radius a for a silver cluster.

For Ag nanoparticles, we have the Mie frequency $\hbar\omega_0 = 2.6\,\mathrm{eV}$ and the Fermi energy $E_\mathrm{F} = 5.5\,\mathrm{eV}$. From Fig. 2.7, we see that the shift $\hbar(\delta_0 + \Delta_0)$ goes to zero for the value of the nanoparticle radius $a \simeq 28\,\mathrm{nm}$. Since the radiative and electronic shifts depend both on the Mie frequency (which is different for each metals[6]), the critical radius for which the frequency shift is canceled can vary depending on the metal composing the cluster.

2.5 Conclusion for Chapter 2

In this chapter, we have introduced the fundamental quantities characterizing the resonance frequency of the localized surface plasmons in isolated spherical metallic nanoparticles based on the work of Refs. [64, 67, 68]. In particular, we focused on the coupling between the plasmonic system and its photonic and electronic environments. Such couplings give rise to the radiative and Landau dampings, respectively, as well as a frequency shift of the plasmon resonance frequency. Starting from a Hamiltonian description of the microscopic system in the Coulomb gauge, one can decompose the system into relative and center-of-mass coordinates corresponding to the electronic bath and to the plasmon, respectively. Then, we described the second order perturbation theory procedure required to obtain the shifts induced on the plasmon frequency by the coupling to the baths. We have briefly presented the expressions for the photonic and electronic frequency shifts. We have seen that the radiative shift shows a scaling with the fourth power of the nanoparticle radius a. Such a shift corresponds to a blueshift of the plasmon frequency. By contrast the electronic shift, later referred to as Landau shift, corresponds to a redshift of the frequency of the plasmon. This second contribution to the frequency renormalization scales (up to a logarithmic factor), like the associated Landau damping, with the inverse of the radius of the nanoparticle. Then, using two Fermi golden rules for the coupling between the plasmonic system and each environments, we showed how one can evaluate the linewidth of the plasmon resonances. The two kinds of damping one obtains behave differently as a function of the nanoparticle radius a. Indeed, while the radiative damping scales with the volume of the nanoparticle ($\propto a^3$), the non-radiative damping rate (i.e., the Laudau damping) scales with the inverse radius ($\propto 1/a$). Finally, we have briefly shown the scaling with the radius a of both the total frequency shift and damping rates in the context of sodium clusters. We have found, in such a situation, critical values for the radius a for which the shift $\delta_0 + \Delta_0$ vanishes and the linewidth γ_0 is minimal, respectively.

In the next chapter, we will focus on how this relatively simple picture for the damping rates and frequency shifts is altered in the case of simple structures composed of interacting spherical metallic nanoparticle. Indeed, while nanoparticle dimers and chains are only one-dimensional structures, one can obtain from their study relevant results, interesting for the investigations on extended two-dimensional arrays of nanoparticles.

[6] Note that, the Fermi energy entering the Landau shift depends also of the considered metal.

Chapter 3

Collective plasmons in one-dimensional assemblies of metallic nanoparticles

As emphasized in the previous chapter, new plasmonic modes arise when considering assemblies of nanoparticles due to the coupling between individual plasmonic resonances supported by each nanoparticles. Such collective plasmons are subject to the photonic and electronic environments and thus suffer from similar effects as the surface plasmons. Although this manuscript aims to study such excitations in two-dimensional arrays of nanoparticles, starting with simpler structures helps to understand the fundamental differences between the properties of the localized surface plasmons and those of the collective plasmons. In this chapter, we thus begin to study the properties of these collective modes supported by nanoparticle dimers which constitute the building blocks of larger arrays. Following previous studies [64, 79], we describe systematically the procedure to obtain the collective plasmonic modes of the dimers as well as the quantities induced by the coupling between the plasmonic system and the environments, namely, the energy shifts and the damping rates, respectively. Importantly, we complete the theory developed by Downing and coworkers [64] by adding the electronic shift in addition to the radiative one used in Ref. [64]. The second part of this chapter focuses on the study of Refs. [80, 135] of larger scale structures: the nanoparticle chain which also exhibit such collective plasmons. In this section, we introduce a new feature appearing in large structures, that is the retardation effects encapsulated in the light-matter interactions which modify the frequency of the collective plasmons. Such a description is accompanied by a general study of the other environment-related quantities of the plasmonic excitations.

3.1 Hybridized plasmons in nanoparticle dimers

The simplest nanostructure one can build when considering assemblies of nanoparticles is the dimer, that is, two nanoparticles brought close together at a distance $3a \lesssim d \ll \lambda$ so that the nanoparticles are near-field coupled. In such a situation, the total Hamiltonian (2.10) introduced in the previous chapter needs to be modified in order to take into account the interactions between the two clusters.

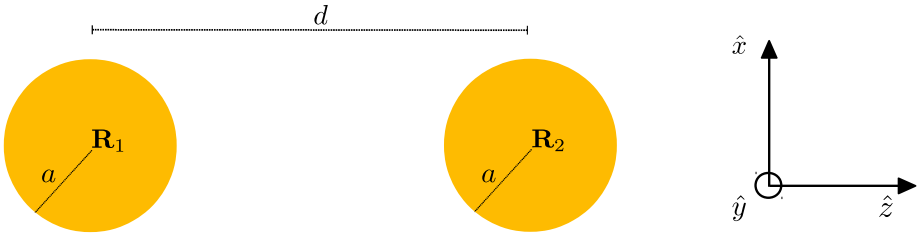

Figure 3.1: Sketch of a plasmonic dimer composed of two spherical metallic nanoparticles with radii a and aligned along the z-direction. Their centers, separated by a distance d, are designated by $\mathbf{R}_1$ and $\mathbf{R}_2$, respectively.

3.1.1 Total Hamiltonian of the plasmonic dimer

We consider in the following a dimer formed by two identical spherical metallic nanoparticles of radii a containing $\mathcal{N}_\mathrm{e}$ valence electrons and separated by a center-to-center distance d (see sketch in Fig. 3.1). The two centers of the clusters are located at $\mathbf{R}_1$ and $\mathbf{R}_2$, respectively. With this nomenclature we define the separation between the nanoparticles by $d = |\mathbf{R}_2 - \mathbf{R}_1|$. Each of the nanoparticles supports three degenerate plasmonic modes (one for each direction of space $\hat{\sigma} = \hat{x}, \hat{y}, \hat{z}$) with resonance frequency ω_0. Since these plasmons can interact with each other, new plasmonic modes known as *hybridized plasmonic modes* arise from the interactions between the two nanoparticles.

To derive the total Hamiltonian of the dimer, we closely follow the procedure introduced in Refs. [79, 80]. Assuming the regime $3a \lesssim d \ll k_0^{-1}$ which amounts to neglect the tunneling of electrons between the nanoparticles as well as multipolar effects [77], one can obtain a simple form for the Hamiltonian of the plasmonic dimer. Similarly to the previous chapter, starting from an electronic Hamiltonian within the jellium approximation in the Coulomb gauge and introducing the center-of-mass coordinates, one gets for the total Hamiltonian [79]

$$H = H_\mathrm{pl} + H_\mathrm{ph} + H_\mathrm{eh} + H_\mathrm{pl-ph} + H_\mathrm{pl-eh}, \tag{3.1}$$

which is characteristic of an open-quantum system in a similar way as the single nanoparticle [cf. Eq. (2.10)]. In Eq. (3.1), H_pl corresponds to the motion of the center-of-mass coordinates, and reads as

$$\begin{aligned} H_\mathrm{pl} = \sum_{n=1}^{2} \left(\frac{[\mathbf{\Pi}_n(\mathbf{R}_n)]^2}{2M} + \frac{M}{2}\omega_0^2 [\mathbf{h}_n(\mathbf{R}_n)]^2 \right) \\ + \frac{(e\mathcal{N}_\mathrm{e})^2}{d^3} \left[\mathbf{h}_1(\mathbf{R}_1) \cdot \mathbf{h}_2(\mathbf{R}_2) - 3(\mathbf{h}_1(\mathbf{R}_1) \cdot \hat{n})(\mathbf{h}_2(\mathbf{R}_2) \cdot \hat{n}) \right], \end{aligned} \tag{3.2}$$

where $\hat{n} = (\mathbf{R}_2 - \mathbf{R}_1)/|\mathbf{R}_2 - \mathbf{R}_1|$ is the unit vector linking the centers of the clusters, $\mathbf{h}_n(\mathbf{R}_n)$ the displacement field associated to the LSP hosted by the nanoparticle located at $\mathbf{R}_n$ and $\mathbf{\Pi}_n(\mathbf{R}_n)$ its corresponding conjugate momentum. In the situation depicted in Fig. 3.1, one has simply $\hat{n} = \hat{z}$. Compared to the plasmonic Hamiltonian (2.11), Eq. (3.2) corresponds to the summation of two

individual terms equivalent to the Hamiltonian (2.11) (where the spill-out effect is neglected) and of an interaction term. Such a contribution arises from the quasistatic dipole-dipole interactions between the individual plasmons supported by the two nanoparticles. Such interactions are the dominant contributions in the chosen near-field regime of study ($k_0 d \ll 1$).

The term $H_{\rm ph}$ in the Hamiltonian (3.1), corresponding to the photonic environment, is given by Eq. (2.3). The term $H_{\rm eh}$ which arises from the electronic environment, takes into account the relative coordinates of both nanoparticles and reads as [79]

$$H_{\rm eh} = \sum_{n=1}^{2}\sum_{i=1}^{\mathcal{N}_{\rm e}}\left[\frac{{\mathbf{p}'_{n,i}}^2}{2m_{\rm e}} + U(r'_{n,i})\right] + \frac{1}{2}\sum_{n=1}^{2}\sum_{\substack{i,j=1\\(i\neq j)}}^{\mathcal{N}_{\rm e}}\frac{e^2}{|\mathbf{r}'_{n,i}-\mathbf{r}'_{n,j}|}. \tag{3.3}$$

In the latter equation, $\mathbf{r}'_{n,i}$ denotes the relative coordinates of the i^{th} electron belonging to the nanoparticle n and $\mathbf{p}'_{n,i}$ its conjugate momentum. The potential $U(r)$ is defined in Eq. (2.2) and one has $r'_{n,i} = |\mathbf{r}'_{n,i}|$. The remaining terms $H_{\rm pl-ph}$ and $H_{\rm pl-eh}$ of the Hamiltonian (3.1) are the coupling terms between the plasmonic system and the photonic and electronic environments, respectively. Following Ref. [151], the plasmon-photon coupling term reads as

$$H_{\rm pl-ph} = \frac{e}{m_{\rm e}c}\sum_{n=1}^{2}\mathbf{\Pi}_n(\mathbf{R}_n)\cdot\mathbf{A}(\mathbf{R}_n) + \frac{\mathcal{N}_{\rm e}e^2}{2m_{\rm e}c^2}\sum_{n=1}^{2}\mathbf{A}^2(\mathbf{R}_n), \tag{3.4}$$

where the quantized vector potential is given by (2.15). Finally, one has for the plasmon-electron coupling

$$H_{\rm pl-eh} = \sum_{n=1}^{2}\sum_{i=1}^{\mathcal{N}_{\rm e}}\mathbf{h}_n(\mathbf{R}_n)\cdot\left[\nabla U(r'_{n,i})\right]\Big|_{\mathbf{h}_n(\mathbf{R}_n)=0}. \tag{3.5}$$

Note that Eqs. (3.4) and (3.5) constitute a generalization to two nanoparticles of the coupling Hamiltonians (2.6) and (2.12) presented in Chapter 2 for an isolated nanoparticle. These two coupling Hamiltonians are responsible for the decay as well as the frequency shifts of the hybridized modes discussed hereafter (cf. Sec. 3.1.2).

3.1.2 Plasmonic eigenmodes

Similarly to the isolated nanoparticle case, quantizing the Hamiltonian (3.1) is necessary for the purpose of evaluating the quantities which arise from the coupling of the plasmonic Hamiltonian to the photonic and electronic environment (in particular, the Landau damping). Introducing the ladder operators

$$b_n^{\sigma} = \sqrt{\frac{M\omega_0}{2\hbar}}\mathbf{h}_n(\mathbf{R}_n)\cdot\hat{\sigma} + \mathrm{i}\frac{\mathbf{\Pi}_n(\mathbf{R}_n)\cdot\hat{\sigma}}{\sqrt{2\hbar M\omega_0}} \tag{3.6a}$$

and

$$b_n^{\sigma\dagger} = \sqrt{\frac{M\omega_0}{2\hbar}}\mathbf{h}_n(\mathbf{R}_n)\cdot\hat{\sigma} - \mathrm{i}\frac{\mathbf{\Pi}_n(\mathbf{R}_n)\cdot\hat{\sigma}}{\sqrt{2\hbar M\omega_0}}, \tag{3.6b}$$

which respectively annihilates and creates a plasmon with frequency ω_0 [cf. Eq. (1.5)] and polarization σ on the n^{th} nanoparticle, one can rewrite the Hamiltonian (3.2) in second quantized form as [79]

$$H_{\text{pl}} = \hbar\omega_0 \sum_{n=1}^{2} \sum_{\sigma=x,y,z} b_n^{\sigma\dagger} b_n^{\sigma} + \hbar\Omega \sum_{\sigma=x,y,z} \eta^{\sigma} \left(b_1^{\sigma} + b_1^{\sigma\dagger}\right)\left(b_2^{\sigma} + b_2^{\sigma\dagger}\right), \tag{3.7}$$

with η^{σ} the quantity introduced in Eq. (2.32) and where

$$\Omega = \frac{\omega_0}{2}\left(\frac{a}{d}\right)^3 \tag{3.8}$$

arises from the dipole-dipole interactions. Such a frequency amounts to the coupling strength between the plasmons belonging to the nanoparticles. Therefore, in the regime where $3a \lesssim d$ one has $\Omega \ll \omega_0$. Note that the operators given in Eq. (3.6) need to satisfy the usual bosonic commutation relations $[b_n^{\sigma}, b_{n'}^{\sigma'\dagger}] = \delta_{nn'}\delta_{\sigma\sigma'}$ and $[b_n^{\sigma}, b_{n'}^{\sigma'}] = [b_n^{\sigma\dagger}, b_{n'}^{\sigma'\dagger}] = 0$. In Eq. (3.7), the interaction part accounts for two distinct kinds of terms. On the one hand, the resonant terms ($\propto b_1^{\sigma\dagger} b_2^{\sigma}$) create an LSP with polarization σ on the first nanoparticle while annihilating an LSP on the second nanoparticle. On the other hand, the non-resonant terms ($\propto b_1^{\sigma\dagger} b_2^{\sigma\dagger}$) create an LSP with polarization σ on both nanoparticles simultaneously. The reverse processes are encoded into the respective Hermitian conjugates in the Hamiltonian (3.7).

In order to obtain the energy losses as well as the shift of the hybridized plasmonic modes, one needs first to diagonalize H_{pl} to access the eigenfrequencies and eigenstates of the nanoparticle dimer. One can perform such a diagonalization using the following Bogoliubov transformation [79]

$$\beta_{\tau}^{\sigma} = \sum_{n=1}^{2} \left(u_{\tau,n}^{\sigma} b_n^{\sigma} + v_{\tau,n}^{\sigma} b_n^{\sigma\dagger}\right), \tag{3.9}$$

where $u_{\tau,n}^{\sigma}$ and $v_{\tau,n}^{\sigma}$ are complex coefficients with $\tau = \pm$. In the equation above, the new bosonic operators β_{τ}^{σ} fulfill the commutation relations $[\beta_{\tau}^{\sigma}, \beta_{\tau'}^{\sigma'\dagger}] = \delta_{\tau\tau'}\delta_{\sigma\sigma'}$ and $[\beta_{\tau}^{\sigma}, \beta_{\tau'}^{\sigma'}] = [\beta_{\tau}^{\sigma\dagger}, \beta_{\tau'}^{\sigma'\dagger}] = 0$. Such commutation rules together with Eq. (3.9) and the bosonic commutation relations of the b_n^{σ} operators thus imply the normalization condition

$$\sum_{n=1}^{2} \left(|u_{\tau,n}^{\sigma}|^2 - |v_{\tau,n}^{\sigma}|^2\right) = 1. \tag{3.10}$$

In the new basis, the Hamiltonian (3.7) is diagonal and reads as

$$H_{\text{pl}} = \hbar \sum_{\tau=\pm} \sum_{\sigma=x,y,z} \omega_{\tau}^{\sigma} \beta_{\tau}^{\sigma\dagger} \beta_{\tau}^{\sigma}. \tag{3.11}$$

In Eq. (3.11), ω_{τ}^{σ} are the eigenfrequencies of the hybridized plasmonic modes. One can evaluate these frequencies by solving the eigenvalue problem resulting from the Heisenberg equation of motion $[\beta_{\tau}^{\sigma}, H_{\text{pl}}] = \hbar\omega_{\tau}^{\sigma}\beta_{\tau}^{\sigma}$ where H_{pl} and β_{τ}^{σ} are given by Eqs. (3.7) and (3.9), respectively.

Performing these steps, one gets for the frequencies

$$\omega_{\pm}^{\sigma} = \omega_0 \sqrt{1 \pm 2\frac{\Omega}{\omega_0}|\eta^{\sigma}|}. \tag{3.12}$$

Inserting then the frequencies (3.12) into the eigenvalue problem and using the normalization condition (3.10) one has for the Bogoliubov coefficients [80]

$$u_{\pm,n}^{\sigma} = \mathrm{sgn}\{\pm\eta^{\sigma}\}^{n-1} \frac{\omega_{\pm}^{\sigma} + \omega_0}{2\sqrt{2\omega_{\pm}^{\sigma}\omega_0}} \tag{3.13a}$$

and

$$v_{\pm,n}^{\sigma} = \mathrm{sgn}\{\pm\eta^{\sigma}\}^{n-1} \frac{\omega_{\pm}^{\sigma} - \omega_0}{2\sqrt{2\omega_{\pm}^{\sigma}\omega_0}}. \tag{3.13b}$$

In Eq. (3.13), $\mathrm{sgn}\{x\}$ denotes the sign function. The operators β_{τ}^{σ} ($\beta_{\tau}^{\sigma\dagger}$) defined in Eq. (3.9) act on the eigenstates $|n_{\tau}^{\sigma}\rangle$ of the plasmonic Hamiltonian (3.11) as $\beta_{\tau}^{\sigma}|n_{\tau}^{\sigma}\rangle = \sqrt{n_{\tau}^{\sigma}}|n_{\tau}^{\sigma} - 1\rangle$ ($\beta_{\tau}^{\sigma\dagger}|n_{\tau}^{\sigma}\rangle = \sqrt{n_{\tau}^{\sigma} + 1}|n_{\tau}^{\sigma} + 1\rangle$) with n_{τ}^{σ} a positive integer. The states $|n_{\tau}^{\sigma}\rangle$ represent hybridized plasmonic modes with polarization σ and energy $n_{\tau}^{\sigma}\hbar\omega_{\tau}^{\sigma}$.

Physical interpretation of the plasmonic eigenmodes

The eigenstates of the plasmonic dimer with frequencies $\omega_{\pm}^{\sigma}$, acquired through the diagonalization procedure presented above, have a simple physical interpretation. Importantly, the eigenfrequencies $\omega_{\pm}^{\sigma}$, are well separated in energy. Indeed, by examining Eq. (3.12), one notice that the hybridized modes have either low ($\tau = -1$) or high ($\tau = +1$) energy with respect to the Mie frequency ω_0. Such modes exist for both polarizations. Importantly, as the coupling constant (3.8) entering the eigenfrequencies scales as d^{-3}, the splitting between the high and low energy in Eq. (3.12) decreases as the interparticle distance is increased.

Interestingly, the two kinds of hybridized modes existing within the nanoparticle dimer are reminiscent of the normal modes of a system of two masses coupled by springs in classical mechanics (see e.g., Ref. [3]). For both dipole moment orientations (transverse and longitudinal to the direction of the dimer), the system shows modes where the dipole moments of the two individuals LSPs are aligned in the same direction in addition to modes with anti-aligned dipole moments. Due to the anisotropy of the dipole-dipole interaction, the lowest energy modes correspond to the out-of-phase configuration for the transverse modes while the opposite case (in-phase modes) occurs for longitudinal modes. Such different configurations are summarized in Fig. 3.2. In addition to displaying a schematic view of the energy diagram for the hybridized modes of the nanoparticle dimer, Fig. 3.2 also shows which modes radiates energy in the far field, the so-called *bright* modes and those which do not, therefore called *dark* modes. Basically, the former correspond to aligned LSPs and the latter to anti-aligned LSPs. Such a picture can be understood simply by the fact that sufficiently far away from the system, bright modes display a net dipole moment while the dark modes show no net dipole moment. Therefore, the bright modes are coupled to light and radiate energy in the far field whereas the dark modes in first approximation, do not loose energy radiatively since they do not couple to light. This physical picture will be formally justified in the section below.

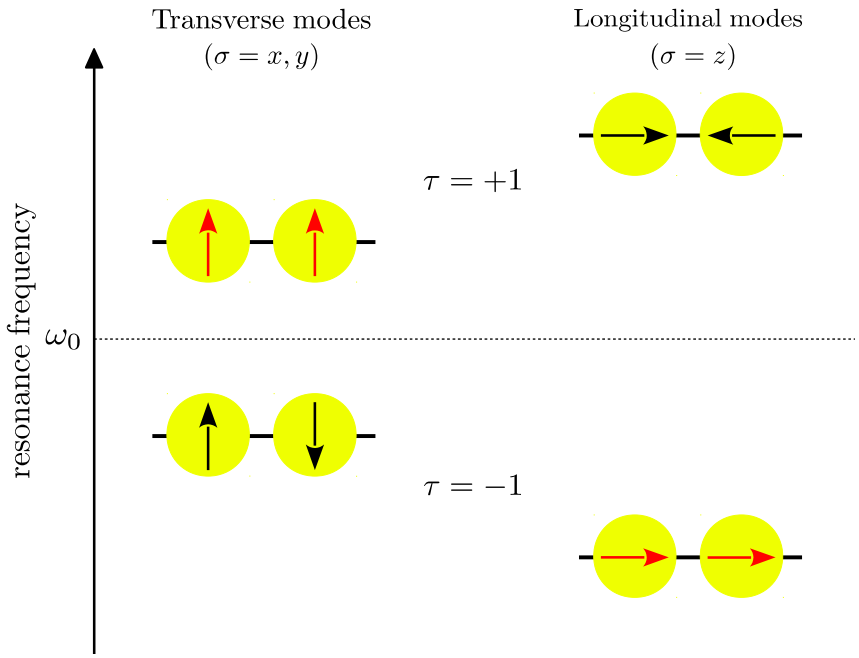

Figure 3.2: Schematic description of the hybridized plasmonic modes frequency diagram. In the sketch, the transverse and longitudinal modes correspond to $\sigma = x, y$ and $\sigma = z$, respectively. The resonance frequencies of the hybridized modes (3.12) are lower (higher) than the Mie frequency ω_0 for $\tau = -1$ ($\tau = +1$). In the figure, the red (black) arrows show the states where the isolated LSPs are in-phase (out-of-phase) resulting into bright (dark) modes.

3.2 Environment-induced effects on the hybridized modes

Similarly to the localized surface plasmons (see Chapter 2), the hybridized plasmonic modes are affected by the photonic and electronic environments to which they are coupled. Formally, these couplings are made transparent through the Hamiltonians $H_{\mathrm{pl-ph}}$ and $H_{\mathrm{pl-eh}}$ described by Eqs. (3.4) and (3.5), respectively. Thus, we here briefly detail how one can evaluate the induced frequency shifts as well as the damping rates of the collective plasmons (i.e., the hybridized modes) following the procedures detailed in Refs. [64, 79].

3.2.1 Effect of the photonic environment

Similarly to the isolated nanoparticle, the hybridized modes are coupled to the photonic vacuum modes. Such a coupling thus implies a frequency renormalization δ_τ^σ which adds to the resonance frequencies ω_τ^σ as well as a radiative contribution γ_τ^σ to the linewidth of the collective modes. In the following, we will briefly present the procedure one may employ to calculate these two quantities.

Radiative shift

For isolated nanoparticles, the radiative shift is reminiscent of the Lamb shift in atomic physics. Such an analogy can be made as well for the plasmonic dimer since the radiative shift can be compared to the Lamb shift in group of atoms and molecules [152, 153]. One can evaluate this shift using second-order perturbation theory in a similar fashion as done for the single nanoparticle (cf. Sec. 2.4.1). One can access the radiative shift δ_τ^σ by first evaluating the second order radiative correction $E_{n_\tau^\sigma}^{(2)}$ of the hybridized-modes energy $E_{n_\tau^\sigma} = n_\tau^\sigma \hbar\omega_\tau^\sigma + E_{n_\tau^\sigma}^{(1)} + E_{n_\tau^\sigma}^{(2)}$, with $n_\tau^\sigma \hbar\omega_\tau^\sigma$ the energy of the unperturbed collective plasmonic levels. It can be shown [64] that only the second-order correction contributes to the frequency shifts between two successive hybridized plasmonic levels. Therefore, one has for the second order correction

$$E_{n_\tau^\sigma}^{(2)} = \frac{1}{\hbar} \sum_{\substack{m_\tau^\sigma \\ (m_\tau^\sigma \neq n_\tau^\sigma)}} \sum_{\mathbf{k},\hat{\lambda}_\mathbf{k}} \frac{\left| \langle m_\tau^\sigma, 1_\mathbf{k}^{\hat{\lambda}_\mathbf{k}} | H_{\mathrm{pl-ph}} | n_\tau^\sigma, \mathrm{vac} \rangle \right|^2}{(n_\tau^\sigma - m_\tau^\sigma)\,\omega_\tau^\sigma - \omega_\mathbf{k}}, \tag{3.14}$$

where $|n_\tau^\sigma\rangle$ and $|m_\tau^\sigma\rangle$ are two hybridized plasmonic states and where $|1_\mathbf{k}^{\hat{\lambda}_\mathbf{k}}\rangle$ represents a single photonic state with momentum $\mathbf{k}$, transverse polarization $\hat{\lambda}_\mathbf{k}$ and frequency $\omega_\mathbf{k}$. In (3.14), the coupling Hamiltonian $H_{\mathrm{pl-ph}}$ is given by

$$\begin{aligned} H_{\mathrm{pl-ph}} = \mathrm{i}\hbar \sum_{n=1}^{2} \sum_{\tau,\sigma} \sum_{\mathbf{k},\hat{\lambda}_\mathbf{k}} \sqrt{\frac{\pi\omega_0^3 a^3}{\mathcal{V}\omega_\mathbf{k}}}\, \hat{\sigma}\cdot\hat{\lambda}_\mathbf{k} \left(u_{\tau,n}^\sigma + v_{\tau,n}^\sigma\right) \left(\beta_\tau^{\sigma\dagger} - \beta_\tau^\sigma\right) \left(a_\mathbf{k}^{\hat{\lambda}_\mathbf{k}} \mathrm{e}^{\mathrm{i}\mathbf{k}\cdot\mathbf{R}_n} + a_\mathbf{k}^{\hat{\lambda}_\mathbf{k}\,\dagger} \mathrm{e}^{-\mathrm{i}\mathbf{k}\cdot\mathbf{R}_n}\right) \\ + \pi\hbar\omega_0^2 \sum_{n=1}^{2} \sum_{\substack{\mathbf{k},\hat{\lambda}_\mathbf{k} \\ \mathbf{k}',\hat{\lambda}'_{\mathbf{k}'}}} \frac{\hat{\lambda}_\mathbf{k}\cdot\hat{\lambda}'_{\mathbf{k}'}}{\sqrt{\omega_\mathbf{k}\omega_{\mathbf{k}'}}} \left(a_\mathbf{k}^{\hat{\lambda}_\mathbf{k}} \mathrm{e}^{\mathrm{i}\mathbf{k}\cdot\mathbf{R}_n} + a_\mathbf{k}^{\hat{\lambda}_\mathbf{k}\,\dagger} \mathrm{e}^{-\mathrm{i}\mathbf{k}\cdot\mathbf{R}_n}\right) \left(a_{\mathbf{k}'}^{\hat{\lambda}'_{\mathbf{k}'}} \mathrm{e}^{\mathrm{i}\mathbf{k}'\cdot\mathbf{R}_n} + a_{\mathbf{k}'}^{\hat{\lambda}'_{\mathbf{k}'}\,\dagger} \mathrm{e}^{-\mathrm{i}\mathbf{k}'\cdot\mathbf{R}_n}\right), \end{aligned} \tag{3.15}$$

while $|\mathrm{vac}\rangle$ denotes the photonic vacuum state. The latter expression is obtained inserting the inverse transformation for the operators b_n^σ [64, 79]

$$b_n^\sigma = \sum_{\tau=\pm} \left(u_{\tau,n}^\sigma \beta_\tau^\sigma - v_{\tau,n}^\sigma \beta_\tau^{\sigma\dagger}\right) \tag{3.16}$$

into the quantized form of $\mathbf{\Pi}_n(\mathbf{R}_n)$ [$\propto (b_n^{\sigma\dagger} - b_n^\sigma)$, cf. Eq. (3.6)] and the expression for the vector potential (2.15), into Eq. (3.4). Eq. (3.15) describes therefore the coupling Hamiltonian $H_{\mathrm{pl-ph}}$ written in second quantization in the eigenbasis of the plasmonic system.

Inserting the Hamiltonian (3.15) into Eq. (3.14), one obtains for the second-order correction [64]

$$E_{n_\tau^\sigma}^{(2)} = \pi\hbar\omega_0^2\omega_\tau^\sigma \frac{a^3}{\mathcal{V}} \sum_{\mathbf{k},\hat{\lambda}_\mathbf{k}} \frac{|\hat{\sigma}\cdot\hat{\lambda}_\mathbf{k}|^2}{\omega_\mathbf{k}} \frac{(2n_\tau^\sigma + 1)\omega_\mathbf{k} - \omega_\tau^\sigma}{\omega_\tau^{\sigma\,2} - \omega_\mathbf{k}^2} \left[1 + \tau \mathrm{sgn}\{\eta^\sigma\} \cos(k_z d)\right], \tag{3.17}$$

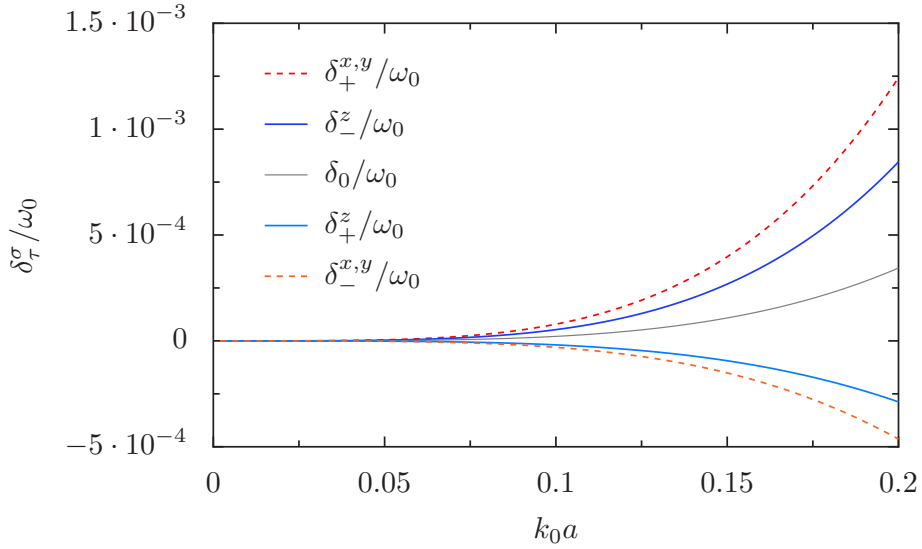

Figure 3.3: Radiative frequency shift for a homogeneous dimer (scaled by ω_0) as a function of the nanoparticle size. In the figure, the thin gray line represents the radiative shift of an isolated nanoparticle (see Fig. 2.4) while the colored lines show the radiative shift for a dimer [cf. Eq. (3.21)] with interparticle distance $d = 3a$. In the figure $\omega_c = c/a$. Figure adapted from Ref. [64].

with $k_z = \mathbf{k} \cdot \hat{z}$ and where the summation over the momenta $\mathbf{k}$ excludes the values for which $\omega_\tau^\sigma = \omega_\mathbf{k}$. Since the expression (3.17) diverges linearly, a regularization procedure (identical to the one used for the isolated nanoparticles [65,66]) is required to regularize Eq. (3.17). Such steps then yield the energy correction

$$\bar{E}_{n_\tau^\sigma}^{(2)} = \pi\hbar\omega_0^2\omega_\tau^{\sigma 2}\frac{a^3}{\mathcal{V}}\sum_{\mathbf{k},\hat{\lambda}_\mathbf{k}}\frac{|\hat{\sigma}\cdot\hat{\lambda}_\mathbf{k}|^2}{\omega_\mathbf{k}^2}\frac{(2n_\tau^\sigma+1)\omega_\tau^\sigma-\omega_\mathbf{k}}{\omega_\tau^{\sigma 2}-\omega_\mathbf{k}^2}\left[1+\tau\mathrm{sgn}\{\eta^\sigma\}\cos(k_z d)\right]. \tag{3.18}$$

Calculating the regularized energy difference between two consecutive plasmonic levels, one has $\bar{E}_{n_\tau^\sigma+1} - \bar{E}_{n_\tau^\sigma} = \hbar\bar{\omega}_\tau^\sigma$, with $\bar{\omega}_\tau^\sigma = \omega_\tau^\sigma + \delta_\tau^\sigma$. In the latter expression, the radiative frequency shift is given by

$$\delta_\tau^\sigma = 2\pi\hbar\omega_0^2\omega_\tau^{\sigma 3}\frac{a^3}{\mathcal{V}}\sum_{\mathbf{k},\hat{\lambda}_\mathbf{k}}\frac{|\hat{\sigma}\cdot\hat{\lambda}_\mathbf{k}|^2}{\omega_\mathbf{k}^2}\frac{1+\tau\mathrm{sgn}\{\eta^\sigma\}\cos(k_z d)}{\omega_\tau^{\sigma 2}-\omega_\mathbf{k}^2}. \tag{3.19}$$

One can carry out the summation over photon momenta in Eq. (3.19) by taking the continuous limit. Introducing the ultraviolet cut-off k_c (of the order of $1/a$) and using Eq. (2.27), one obtains for the shift

$$\delta_\tau^\sigma = \frac{\omega_0^2\omega_\tau^{\sigma 2}a^3}{(2\pi c)^2}\mathcal{P}\int_0^{k_c}\frac{\mathrm{d}k}{\omega_\tau^{\sigma 2}-(ck)^2}\int_0^\pi \mathrm{d}\theta\sin\theta\left[1+\tau\mathrm{sgn}\{\eta^\sigma\}\cos(kd\cos\theta)\right]\int_0^{2\pi}\mathrm{d}\varphi[1-(\hat{k}\cdot\hat{\sigma})^2]. \tag{3.20}$$

One can evaluate the integrals above to yield [64]

$$\delta_\tau^\sigma = \frac{\omega_\tau^{\sigma\,2}}{3\pi\omega_0}(k_0 a)^3 \ln\left(\frac{\omega_\mathrm{c}/\omega_\tau^\sigma + 1}{\omega_\mathrm{c}/\omega_\tau^\sigma - 1}\right) + \tau\frac{|\eta^\sigma|\omega_0\Omega}{\pi\omega_\tau^\sigma} g_\tau^\sigma, \tag{3.21}$$

where the expression for g_τ^σ is given in Eq. (B.2) in Appendix B, and where $\omega_\mathrm{c} = ck_\mathrm{c}$ denotes the cut-off frequency. The radiative shift of the hybridized plasmons δ_τ^σ is shown as a function of the radius a of the nanoparticles in Fig. 3.3 for all possible energy modes and polarization configurations.

One can see from the figure that the radiative shift displays different behaviors depending on the hybridized mode configurations. The collective plasmonic modes containing in-phase LSPs (with frequencies ω_-^z and $\omega_+^{x,y}$) show a frequency shift similar to the one of the single nanoparticle (see grey line in Fig. 3.3), corresponding to a blueshift of the frequencies. The out-of-phase modes (with frequencies ω_+^z and $\omega_-^{x,y}$) present however the opposite trend, that is a redshift of their frequencies due to the coupling to the photonic environment. Moreover, one can observe from the figure that the shift is larger for the transverse modes as compared to the longitudinal ones. Finally, one can show [64] that the radiative shift (3.21) scales with a^4 similarly to the isolated nanoparticle (cf. Sec. 2.4.1).

Radiative damping

In order to describe the radiative decay rate associated to the hybridized modes , we will rely on the work of Brandstetter-Kunc and coworkers and closely follow the procedures developed in Ref. [79].

Using a Fermi golden rule for the Hamiltonian (3.4), one obtains, for the radiative damping rate of the hybridized modes the result

$$\gamma_\tau^\sigma = \frac{2\pi}{\hbar^2}\sum_{\mathbf{k},\hat{\lambda}_\mathbf{k}} \left|\langle 0_\tau^\sigma, 1_\mathbf{k}^{\hat{\lambda}_\mathbf{k}}|H_\mathrm{pl-ph}|1_\tau^\sigma, \mathrm{vac}\rangle\right|^2 \delta(\omega_\tau^\sigma - \omega_\mathbf{k}). \tag{3.22}$$

Thus, substituting the expression (3.15) for the coupling Hamiltonian into the Fermi golden rule above yields

$$\gamma_\tau^\sigma = \frac{2\pi^2\omega_0^3 a^3}{\mathcal{V}}\sum_{\mathbf{k},\hat{\lambda}_\mathbf{k}} \frac{|\hat{\sigma}\cdot\hat{\lambda}_\mathbf{k}|^2}{\omega_\mathbf{k}} \left|\sum_{n=1}^{2}\left(u_{\tau,n}^\sigma + v_{\tau,n}^\sigma\right)\mathrm{e}^{-\mathrm{i}\mathbf{k}\cdot\mathbf{R}_n}\right|^2 \delta(\omega_\tau^\sigma - \omega_\mathbf{k}). \tag{3.23}$$

One may evaluate the above expression using Eq. (2.27) in the continuous limit $\mathcal{V} \to \infty$ [cf. Eq. (2.28)]. Moreover, using the explicit form of the Bogoliubov coefficients defined in Eq. (3.13) and assuming that the interparticle distance d is much smaller than the hybridized mode wavelength, one obtains for the radiative damping rate [80]

$$\gamma_\tau^\sigma = \frac{1}{2}\gamma_0\left(\frac{\omega_\tau^\sigma}{\omega_0}\right)^2 \left(1 + \tau\mathrm{sgn}\{\eta^\sigma\}\right)^2, \tag{3.24}$$

with $\tau = \pm 1$ and where γ_0, given in Eq. (1.7), is the radiative damping rate of the LSP in an iso-

lated nanoparticle. From Eq. (3.24), one can clearly identify two kinds of modes, namely the dark (with vanishing radiative losses) and bright (with non-zero damping rate) plasmonic modes. From the latter expression, we see that the configurations $\{\tau = +1, \sigma = z\}$ and $\{\tau = -1, \sigma = x, y\}$ correspond to dark modes. Using Eq. (3.12), we can identify these modes to the transverse low energy mode and longitudinal high energy one, respectively. With the energy diagram in Fig. 3.2, we can associate these two modes to the out-of-phase modes (represented by black arrows in the figure). These dark plasmons are immune to radiation losses due to the absence of coupling to the electromagnetic field (zero net dipole moment) and therefore long-lived as compared to the bright modes [79]. Consequently, one cannot excite or observe such modes with regular optical techniques. However, this drawback can be overcome using electron energy-loss spectroscopy (EELS) techniques to excite the dark plasmonic modes as presented in e.g., Refs. [123, 124]. The two remaining modes (with transverse high energy and longitudinal low energy) corresponding to in-phase oscillating LSPs, show a finite radiative damping rate [see Eq. (3.24)]. For large interparticle distances, both the transverse and longitudinal (bright) modes display a rate twice as large as the one of a single nanoparticle [see Eq. (3.24)]. Indeed, for such interparticle distance, the coupling frequency Ω is very small compared to ω_0 ($\Omega \simeq 0$) implying that the hybridized modes display a resonance frequency very close to ω_0 [cf. Eq. (3.12)]. In this particular case, the bright modes can then be seen as two decoupled aligned LSPs therefore emitting twice as much photons than a single plasmon. Moreover, the damping rate of the bright collective modes scales with the volume of the nanoparticles ($\propto a^3$) since such a rate is proportional to the radiative damping of a single nanoparticle which presents the same scaling with the radius a.

3.2.2 Electronic effects induced on the hybridized modes

Similarly to the photonic environment, the coupling between the plasmonic subsystem and the electronic relative coordinates gives rise to the Landau decay rate as well as an electronic frequency shift of the hybridized modes in the dimer. In the following, we will first present the procedure realized in Ref. [79] for obtaining the Landau damping and then we will evaluate the associated frequency shift. As a matter of fact, knowing the expression for the Landau damping reveals to be mandatory for calculating the electronic shift.

Landau damping

The second size-dependent damping mechanism responsible for the energy losses of the hybridized plasmons is the Landau damping. One may evaluate such a decay rate using a Fermi golden rule for the plasmon-electron coupling Hamiltonian (3.5). The Landau damping rate is thus given by

$$\Gamma_\tau^\sigma = \frac{2\pi}{\hbar^2} \sum_{n=1}^{2} \sum_{eh} |\langle 0_\tau^\sigma, eh_n | H_{\mathrm{pl-eh}} | 1_\tau^\sigma, \mu_n \rangle|^2 \, \delta(\omega_\tau^\sigma - \omega_{eh}), \tag{3.25}$$

where $|1_\tau^\sigma\rangle$ is an hybridized plasmonic state with energy ω_τ^σ and $|0_\tau^\sigma\rangle$ a state with no hybridized plasmon. In the latter equation, $|eh_n\rangle$ and $|\mu_n\rangle$ correspond to a state in the nanoparticle n with a single electron-hole pair with energy $\hbar\omega_{eh}$ and no such pair, respectively. Following now Ref. [79], one can show that the Hamiltonian (3.5) can be rewritten within the mean-field approximation

(providing that correlations between the electrons are negligible) as

$$H_{\mathrm{pl-eh}} = \sum_{n=1}^{2} \sum_{\sigma=x,y,z} \sum_{ij} \Lambda \left(b_n^\sigma + b_n^{\sigma\dagger} \right) \hat{\sigma} \cdot \mathbf{d}_{ij,n} c_{ni}^\dagger c_{nj}, \tag{3.26}$$

where the constant Λ was defined in Eq. (2.20). In Eq. (3.26), the operator $c_{ni}^\dagger$ (c_{ni}) creates (annihilates) an electron in a state $|ni\rangle$ with energy ϵ_{ni} in the self-consistent potential V (see Fig. 2.2) on the nanoparticle n. Similarly to the isolated nanoparticle one has

$$\mathbf{d}_{ij,n} = \langle ni|\mathbf{r}|nj\rangle. \tag{3.27}$$

Thus, using the expression (3.16) of the b_n^σ operators expressed in the eigenbasis of the plasmonic subsystem into the Hamiltonian (3.26), Eq. (3.25) simplifies to yield

$$\Gamma_\tau^\sigma = \sum_{n=1}^{2} |u_{\tau,n}^\sigma - v_{\tau,n}^\sigma|^2 \Sigma^\sigma(\omega_\tau^\sigma), \tag{3.28}$$

where the Bogoliubov coefficients and the function $\Sigma^\sigma(\omega)$ are given by Eqs. (3.13) and (2.35), respectively. One may directly evaluate the latter expression using the explicit form of the Bogoliubov coefficients as well as the one of the function $\Sigma^\sigma(\omega)$ which has been calculated in Appendix A [cf. Eq. (A.8)]. Therefore, the Landau damping rate for the hybridized plasmon reads

$$\Gamma_\tau^\sigma = \frac{3v_\mathrm{F}}{4a} \left(\frac{\omega_0}{\omega_\tau^\sigma} \right)^4 g\left(\frac{\hbar\omega_\tau^\sigma}{E_\mathrm{F}} \right), \tag{3.29}$$

where the function $g(\nu)$ is given in Eq. (A.10). Similarly to the isolated nanoparticle, the Landau damping scales with the inverse radius a of the clusters for both hybridized modes.

The scalings for the radiative ($\propto a^3$) and Landau ($\propto 1/a$) dampings imply, identically as for the isolated nanoparticle, the existence of an optimal radius a of the nanoparticles for which the losses are minimal for the bright modes. However, since the dark modes do not couple to light (and therefore do not radiate), only the Landau damping contributes to the energy losses of these modes and no optimal size exists in such case. For the dark plasmons, the larger the nanoparticles are, the less the losses are important. Note that the limit $a \to \infty$ which in principle minimizes the rate (3.29), cannot be taken here since such a limit would break the quasistatic approximation $k_0 a \ll 1$ in which the dimer is studied.

Electronic shift

The electronic energy shift arises from the coupling between the hybridized plasmons and the electronic bath (i.e., the relative coordinates). Assuming that the plasmonic subsystem is weakly coupled to the electronic system, the Laudau shift may be evaluated with a second-order non-degenerated perturbation theory in the coupling Hamiltonian (3.26). Thus, the second-order energy

correction arising from the plasmon-electron coupling reads

$$\mathcal{E}^{(2)}_{n^\sigma_\tau} = \frac{1}{\hbar}\sum_{n=1}^{2}\sum_{\substack{m^\sigma_\tau \\ (m^\sigma_\tau \neq n^\sigma_\tau)}}\sum_{eh}\frac{\left|\langle m^\sigma_\tau, eh_n|H_{\mathrm{pl-eh}}|n^\sigma_\tau,\mu_n\rangle\right|^2}{(n^\sigma_\tau - m^\sigma_\tau)\,\omega^\sigma_\tau - \omega_{eh_n}}. \tag{3.30}$$

Writing the Hamiltonian (3.26) in the basis of the eigenmodes with the inverse Bogoliubov transformation (3.16), and inserting Eq. (3.26) into Eq. (3.30), the electronic shift for the hybridized modes $\Delta^\sigma_\tau = (\mathcal{E}^{(2)}_{n^\sigma_\tau+1} - \mathcal{E}^{(2)}_{n^\sigma_\tau})/\hbar$ reads as

$$\Delta^\sigma_\tau = -\frac{2}{\hbar^2}\sum_{n=1}^{2}|u^\sigma_{\tau,n} - v^\sigma_{\tau,n}|^2\left(\sum_{eh}|\Lambda\hat{\sigma}\cdot\mathbf{d}_{eh}|^2\,\frac{\omega_{eh}}{\omega^2_{eh}-\omega^{\sigma 2}_\tau}\right), \tag{3.31}$$

where $\mathbf{d}_{eh,n}$ simplifies into $\mathbf{d}_{eh}$ defined in Eq. (2.21) since we consider identical nanoparticles. In Eq. (3.31), the term inside the brackets is formally equal (except for the mode frequency ω^σ_τ) to Eq. (2.45). Therefore, replacing the expressions of the Bogoliubov coefficients (3.13) into (3.31) yields for the electronic shift

$$\Delta^\sigma_\tau = \frac{1}{\pi}\frac{\omega_0}{\omega^\sigma_\tau}\mathcal{P}\int_{-\infty}^{+\infty}\mathrm{d}\omega\frac{\omega\Sigma^\sigma(\omega)}{(\omega^\sigma_\tau)^2-\omega^2}. \tag{3.32}$$

The integral in the latter equation can be performed in a similar fashion as the one detailed in Sec. 2.4.2 [see Eqs. (2.45) to (2.52)]. As done in Eq. (2.47), we first replace the lower boundary of the integral by a frequency cutoff yielding

$$\Delta^\sigma_\tau \simeq \frac{1}{\pi}\frac{\omega_0}{\omega^\sigma_\tau}\mathcal{P}\int_{\omega^\sigma_\tau-\eta\Gamma^\sigma_\tau}^{+\infty}\mathrm{d}\omega\frac{\omega\Sigma^\sigma(\omega)}{(\omega^\sigma_\tau)^2-\omega^2}. \tag{3.33}$$

In the equation above, we choose the cutoff for the integral in analogy of what have been done in Sec. 2.4.2 for the evaluation of the electronic shift in the isolated nanoparticle. The crucial difference is that the electron-hole pairs responsible for the electronic shift have a frequency close to the resonance frequency of the hybridized modes and not to the Mie frequency ω_0. We thus also substitute the associated damping rate Γ_0 in (2.47) by Γ^σ_τ in Eq. (3.33). We now evaluate the electronic shift (3.33) following closely the procedure exposed in Ref. [68]. We first substitute the expression (A.8) of $\Sigma^\sigma(\omega)$ into the integral considering the asymptotic expansion given in Eq. (2.48) (within the limit $E_\mathrm{F} \ll \hbar\omega^\sigma_\tau$) for the function $g(\nu)$. Performing these steps then gives

$$\Delta^\sigma_\tau = -\frac{8}{15\pi}\frac{3v_\mathrm{F}}{4a}\left(\frac{\omega_0}{\omega^\sigma_\tau}\right)^4 I\left(\frac{\hbar\omega^\sigma_\tau}{E_\mathrm{F}}, \eta\frac{\hbar\Gamma^\sigma_\tau}{E_\mathrm{F}}\right), \tag{3.34}$$

where the function $I(\xi,\alpha)$ is given by Eq. (2.50). Thus, substituting the expression for the function $I(\xi,\alpha)$ in the limit $\xi \gg \alpha$ given in Eq. (2.51) into Eq. (3.34) together with the expression (3.29) of

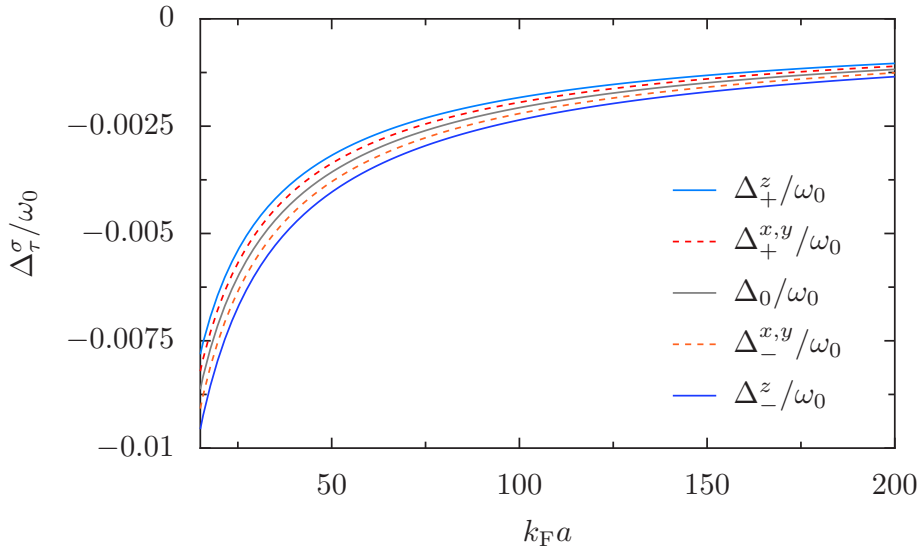

Figure 3.4: Landau frequency shift (3.35) of the hybridized plasmonic modes of a nanoparticle dimer as a function of the radius a. The grey line corresponding to the isolated nanoparticle case is plotted for comparison. In the figure, we have $d = 3a$, $\eta = 1/2$ and the relevant parameters for the silver nanoparticle (in vacuum), $\hbar\omega_0 = 2.6\,\mathrm{eV}$ and $E_\mathrm{F} = 5.5\,\mathrm{eV}$.

the Landau damping rate yields for the electronic shift

$$\Delta_\tau^\sigma = -\frac{3v_\mathrm{F}}{4a}\beth\left(\omega_\tau^\sigma\right), \tag{3.35}$$

where the function $\beth(\omega)$ was introduced in Eq. (2.53). Since the latter function is always positive, the electronic frequency shift corresponds to a redshift.

We plot in Fig. 3.4 the electronic frequency shifts Δ_τ^σ [Eq. (3.35)] associated with the hybridized plasmonic modes of a homogeneous silver nanoparticle dimer as a function of the (reduced) radius a of the nanoparticles. The separation between the two clusters is $d = 3a$ corresponding to a coupling frequency $\Omega = \omega_0/54$ [see Eq. (3.8)]. As can be seen from the figure, the absolute value of the shift for a given mode is larger for low energy modes for all nanoparticle sizes. Such behavior is opposite to the radiative shift which is quasi-identical for all hybridized modes for small-sized nanoparticles (see Fig. 3.3). Moreover, contrary to the radiative shift which correspond to a blueshift for the bright modes and to a redshift for the dark ones, the electronic shifts correspond to a redshift of the collective plasmon frequencies.

Experimental detection of the frequency shifts

In the following paragraph, we briefly discuss the proposal suggested by Downing and coworkers [64] that one can use to detect experimentally the radiative frequency shifts. We also complete the results shown in Ref. [64] by adding the electronic shift into the calculations to look for possible

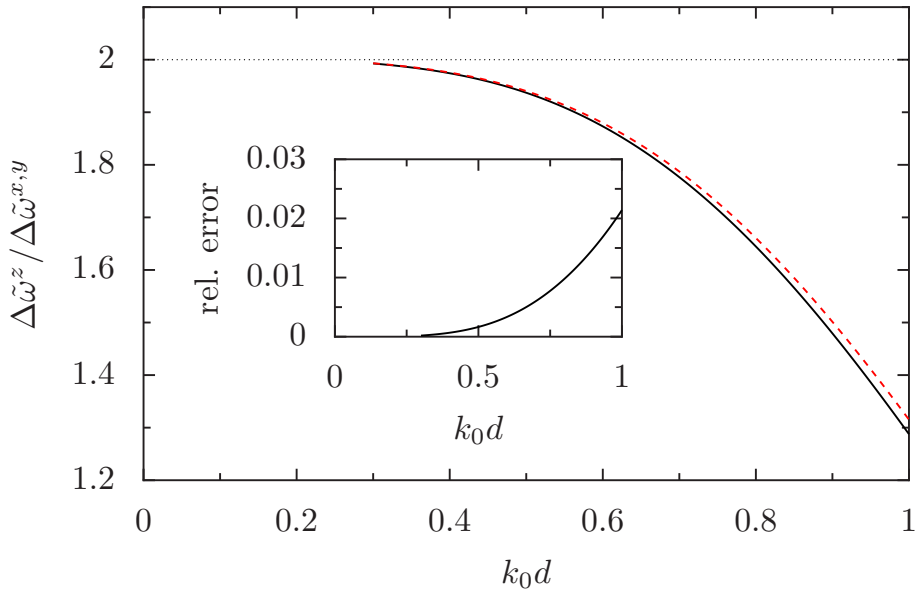

Figure 3.5: Comparison between the frequency ratio $\Delta\bar{\omega}^z/\Delta\bar{\omega}^{x,y}$ and $\Delta\tilde{\omega}^z/\Delta\tilde{\omega}^{x,y}$ as a function of the (reduced) interparticle distance. The red dashed line reproduces the results from Ref. [64] while the solid black line shows the same results including the Landau shifts Δ_τ^σ into the calculations. The dotted line corresponds to the same ratio without coupling to the environments. The inset shows the relative error between the black and red curves as a function of the nanoparticle separation d. In the figure, $d = 3a$.

modifications regarding their conclusions.

In their work, the authors of Ref. [64] proposed to evaluate the difference between the dark and bright mode frequency (which amounts to have $\bar{\omega}_\tau^\sigma = \omega_\tau^\sigma + \delta_\tau^\sigma$) $\Delta\bar{\omega}^\sigma = \bar{\omega}_+^\sigma - \bar{\omega}_-^\sigma$ for both transverse and longitudinal polarization and to calculate the ratio of the two quantities $\Delta\bar{\omega}^z/\Delta\bar{\omega}^{x,y}$. Using Eq. (3.12) for the eigenfrequencies of the hybridized modes in the limit $\Omega/\omega_0 \ll 1$, one has $\Delta\omega^z/\Delta\omega^{x,y} = 2$ in absence of any coupling to the environments. As shown in Ref. [64], neglecting the coupling to the electronic environment and considering only the radiative shift (3.21), the ratio displays a universal dependence with the interparticle distance d for any nanoparticle size a. Such ratio can be approximated by $\Delta\bar{\omega}^z/\Delta\bar{\omega}^{x,y} \simeq 2 - (k_0 d)^4$.

In order to check if including the Landau shift into the renormalized frequencies mentioned above affects the ratio $\Delta\bar{\omega}^z/\Delta\bar{\omega}^{x,y}$, we replace the radiative shift δ_τ^σ by the total shift $\delta_\tau^\sigma + \Delta_\tau^\sigma$ into the expression of $\bar{\omega}_\tau^\sigma$ where Δ_τ^σ is given by Eq. (3.35). We compare in Fig. 3.5 the results of Ref. [64] for the ratio as a function of the nanoparticle interdistance d and the same ratio including the Landau shift. The interparticle distance is $d = 3a$. In the figure, we only show the results for $k_0 a = 0.1$ but similar conclusions can be drawn for other nanoparticle sizes a. The red dashed line in Fig. 3.5 corresponds to the results of Ref. [64] while the black solid line to our corrected results which includes the electronic shift. The curves start from $d = 3a$ in order to remain consistent with the dipolar approximation. As it is clear from the figure, we see small deviations between the

two curves appearing for $k_0 d \gtrsim 0.5$. We plot in the inset of Fig. 3.5, the relative error $|(R_{\mathrm{Dow}} - R)/R_{\mathrm{Dow}}|$ as a function of the interparticle distance. In the latter expression R_{Dow} and R denote the ratio $\Delta\bar{\omega}^z/\Delta\bar{\omega}^{x,y}$ in the work of Downing *et al.* [64] and the same ratio $\Delta\tilde{\omega}^z/\Delta\tilde{\omega}^{x,y}$, (with $\tilde{\omega}_\tau^\sigma = \omega_\tau^\sigma + \delta_\tau^\sigma + \Delta_\tau^\sigma$) in the frame of this manuscript, respectively. As can be noted from the inset of the figure, including the coupling to the electronic environment does not affect significantly the universal behavior of the ratio $\Delta\bar{\omega}^z/\Delta\bar{\omega}^{x,y}$ emphasized in Ref. [64] with only a deviation of the order of 10^{-2}. Therefore, the proposal for the experimental detection of the radiative shift exposed in Ref. [64] still holds considering the plasmon-electron coupling in addition to the plasmon-photon one.

3.3 Extended metastructure: the nanoparticle chain

In order to exploit the collective plasmonic modes for applications (e.g., the propagation of light), one may extend the nanoparticle dimer concept to larger metastructures (single nanoparticles and dimers present as well appealing applications as emphasized in the Introduction of the manuscript). The natural extension of the plasmonic dimer in one dimension is the regular nanoparticle chain. In the present section, we review the essential modifications of the properties of the collective plasmonic modes hosted by simple chains of regularly-spaced spherical metallic nanoparticles as compared to the dimers. Such a review is based on Refs. [80, 135].

3.3.1 Model Hamiltonian

We consider a chain of identical spherical metallic nanoparticles (see Fig. 3.6) of radius a. In the chain the center of the nanoparticle n lies at the position $\mathbf{R}_n$ and the distance between two neighboring nanoparticles is denoted by$d$. In order to construct the Hamiltonian for the chain, one can readily generalize the Hamiltonian of the dimer (3.1) by extending the summation over the nanoparticles to $\mathcal{N}$ for the chain instead of 2 for the dimer [see, e.g., Eq. (3.7)]. Since we consider chain that are large with respect to the interparticle distance d, one needs to include the long-range nature of the quasistatic dipole-dipole interaction into the plasmonic Hamiltonian. In the second quantization formalism, the plasmonic Hamiltonian of the chain thus reads [135]

$$H_{\mathrm{pl}} = \sum_{\sigma=x,y,z} \left[\hbar\omega_0 \sum_{n=1}^{\mathcal{N}} b_n^{\sigma\dagger} b_n^\sigma + \frac{\hbar\Omega}{2} \sum_{\substack{n,m=1 \\ (n\neq m)}}^{\mathcal{N}} \frac{\eta^\sigma}{|n-m|^3} \left(b_n^\sigma + b_n^{\sigma\dagger}\right)\left(b_m^\sigma + b_m^{\sigma\,\dagger}\right) \right], \tag{3.36}$$

with n, m two integer numbers and where the frequencies ω_0 and Ω are defined in Eqs. (1.5) and (3.8), respectively. In the latter equation, the operator $b_n^{\sigma\dagger}$ (b_n^σ) creates (annihilates) a plasmon with polarization σ on the nanoparticle n and η^σ is defined in Eq. (2.31).

The plasmonic Hamiltonian above shows certain similarities with an electronic tight-binding Hamiltonian [107]. Indeed, the first term of (3.36) ($\propto b_n^{\sigma\dagger} b_n^\sigma$) is reminiscent of an on-site energy term which counts the number of LSPs on each individual nanoparticle. In addition, one can notice "hopping-like" terms ($\propto b_n^{\sigma\dagger} b_m^\sigma$) which annihilate an LSP on a site m while creating another

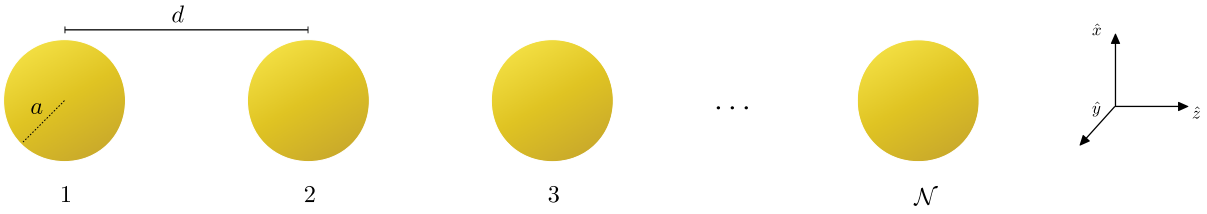

Figure 3.6: Sketch of a plasmonic chain constituted by $\mathcal{N}$ identical spherical metallic nanoparticles of radius a separated by an interparticle distance d. Figure reproduced from Ref. [135].

LSP on a site n (the reverse process is encoded into the Hermitian conjugate term $\propto b_n^\sigma {b_m^\sigma}^\dagger$). Despite these clear analogies, important differences between a tight-binding Hamiltonian and the expression (3.36) can be observed. First, the plasmonic Hamiltonian (3.36) describes bosons (i.e., plasmons) instead of fermions (i.e., electrons). Then, the dipole-dipole interactions between the LSPs are long-ranged ($\propto 1/d^3$) and polarization-dependent contrary to the hopping interaction which is isotropic and which decays with the interparticle distance exponentially. Moreover, one can note in (3.36) the presence of non-resonant terms ($\propto b_n^\sigma b_m^\sigma$ and $\propto {b_n^\sigma}^\dagger {b_m^\sigma}^\dagger$) which annihilate or create two LSPs on the sites n and m simultaneously. Such terms are required for evaluating the eigenstates of the plasmonic chain and therefore essential when calculating state-dependent quantities (e.g., the damping rates). Finally, since the chain is larger than the plasmonic resonance wavelength λ, the plasmons hosted by the chain suffer from retardation effects due to the interaction with the free photon field. Such effects are included in the model through the coupling between the plasmonic system and the photonic environment (see Sec. 3.3.2). One can readily generalize the Hamiltonians of the photonic and electronic environments $H_{\rm ph}$ and $H_{\rm eh}$ as well as the associated coupling Hamiltonians $H_{\rm pl-ph}$ and $H_{\rm pl-eh}$ for the chains. While $H_{\rm ph}$ is still given by Eq. (2.16)[1], the three remaining terms [i.e. $H_{\rm eh}$, $H_{\rm pl-ph}$ and $H_{\rm pl-eh}$, see Eq. (3.1)] can be straightforwardly obtained in second quantization from their counterparts introduced for the dimers. The Hamiltonian of the electronic environment is therefore given within a mean-field approximation by

$$H_{\rm eh} = \sum_{n=1}^{\mathcal{N}} \sum_i \epsilon_{ni} c_{ni}^\dagger c_{ni}, \tag{3.37}$$

where c_{ni} ($c_{ni}^\dagger$) annhilihilates (creates) an electron in the $n^{\rm th}$ nanoparticle associated with the one-body state $|ni\rangle$ with energy ϵ_{ni} in the self-consistent potential V of that nanoparticle. Such potential is assumed (similarly to Chapter 2) to be a spherically symmetric hard-wall potential [67]. Finally, the two coupling Hamiltonians read in second quantization

$$H_{\rm pl-ph} = {\rm i}\sqrt{\frac{\mathcal{N}_{\rm e}\hbar\omega_0 e^2}{2m_{\rm e}c^2}} \sum_{n=1}^{\mathcal{N}} \sum_\sigma \left({b_n^\sigma}^\dagger - b_n^\sigma\right) \hat{\sigma}\cdot\mathbf{A}(\mathbf{R}_n) + \frac{\mathcal{N}_{\rm e}e^2}{2m_{\rm e}c^2} \sum_{n=1}^{\mathcal{N}} \mathbf{A}^2(\mathbf{R}_n), \tag{3.38}$$

[1]Note that, since we consider interparticle separation distances much smaller than the wavelength associated with the LSP resonances, we neglect Umklapp processes in the photon-related Hamiltonians.

and

$$H_{\mathrm{pl-eh}} = \sum_{n=1}^{\mathcal{N}} \sum_{\sigma=x,y,z} \sum_{ij} \Lambda \left(b_n^\sigma + b_n^{\sigma\dagger} \right) \hat{\sigma} \cdot \mathbf{d}_{ij,n} c_{ni}^\dagger c_{nj}, \tag{3.39}$$

respectively. In Eq. (3.38), the vector potential $\mathbf{A}(\mathbf{R}_n)$ is given in Eq. (2.15). In Eq. (3.39), the quantities Λ and $\mathbf{d}_{ij,n}$ are defined in Eqs. (2.20) and (3.27), respectively.

Plasmonic eigenmodes

Identically to the plasmonic dimer, the basis formed by the operators b_n^σ do not constitute an eigenbasis of the plasmonic Hamiltonian (3.36). Therefore, one needs first to diagonalize such Hamiltonian in order to access the relevant quantities arising from the coupling to the environments. In the limit of a chain composed of an infinite number of nanoparticles ($\mathcal{N} \gg 1$), it is convenient to first express the Hamiltonian (3.36) into wavevector space using the Fourier transform

$$b_n^\sigma = \frac{1}{\sqrt{\mathcal{N}}} \sum_q \mathrm{e}^{\mathrm{i}nqd} b_q^\sigma, \tag{3.40}$$

where the operator b_q^σ annihilates a collective plasmonic mode with wavevector q and polarization σ within the chain while its adjoint $b_q^{\sigma\dagger}$ creates such a collective mode. Choosing periodic boundary conditions, the plasmonic wavevectors are quantized as $q = 2\pi p/\mathcal{N}d$ with $p \in [-\mathcal{N}/2, \mathcal{N}/2]$ an integer. Consequently, one obtains for the plasmonic Hamiltonian (3.36) [135]

$$H_{\mathrm{pl}} = \sum_{\sigma=x,y,z} \sum_q \left\{ \hbar\omega_0 b_q^{\sigma\dagger} b_q^\sigma + \frac{\hbar\Omega}{2} \left[f_q^\sigma b_q^{\sigma\dagger} \left(b_q^\sigma + b_{-q}^{\sigma\,\dagger} \right) + \mathrm{h.c.} \right] \right\}, \tag{3.41}$$

where the lattice sum is given by

$$f_q^\sigma = 2\eta^\sigma \sum_{n=1}^{\infty} \cos(nqd)/n^3 = \eta^\sigma [\mathrm{Li}_3(e^{\mathrm{i}qd}) + \mathrm{Li}_3(e^{-\mathrm{i}qd})]. \tag{3.42}$$

In the equation above, $\mathrm{Li}_s(z) = \sum_{n=1}^{\infty} z^n/n^s$ denotes the polylogarithm function. One can write the latter Hamiltonian into its diagonal form as

$$H_{\mathrm{pl}} = \sum_{\sigma=x,y,z} \sum_q \hbar\omega_q^\sigma \beta_q^{\sigma\dagger} \beta_q^\sigma, \tag{3.43}$$

with the help of a bosonic Bogoliubov transformation $\beta_q^\sigma = u_q^\sigma b_q^\sigma + v_q^\sigma b_{-q}^{\sigma\,\dagger}$ [80, 135]. The spectrum of the collective plasmons in Eq. (3.43) is then given by

$$\omega_q^\sigma = \omega_0 \sqrt{1 + 2\frac{\Omega}{\omega_0} f_q^\sigma}, \tag{3.44}$$

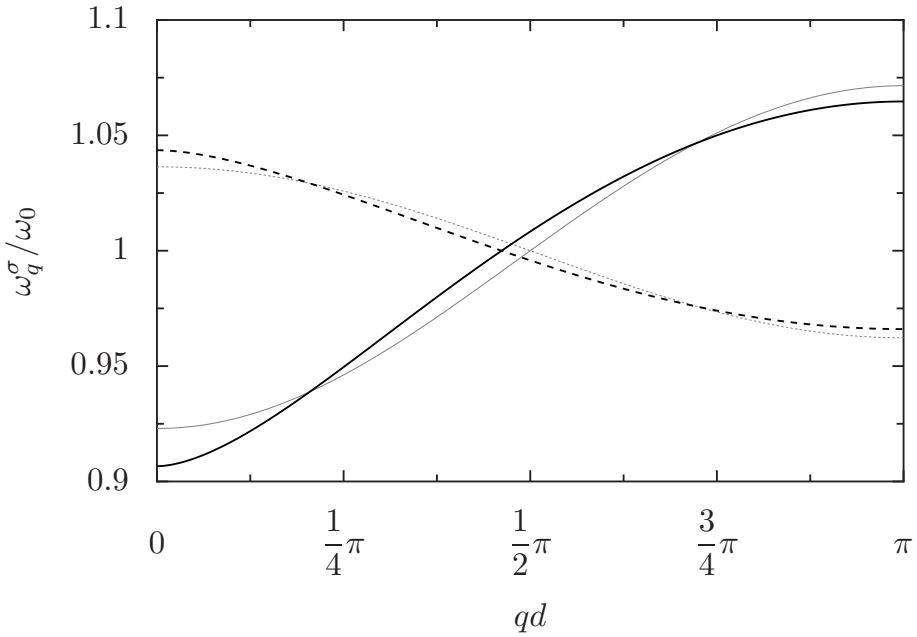

Figure 3.7: Dispersion relation of the plasmonic chain as a function of the (reduced) wavevector q. The solid (dashed) line corresponds to the longitudinal (transverse) collective modes considering the full quasi-static bandstructure (3.44). The grey thin lines show the dispersion relation in nearest-neighbor approximation for comparison. In the figure, $d = 3a$, corresponding to a coupling frequency $\Omega = \omega_0/54$.

while the Bogoliubov coefficients read

$$u_q^\sigma = \frac{\omega_q^\sigma + \omega_0}{2\sqrt{\omega_q^\sigma \omega_0}} \tag{3.45a}$$

and

$$v_q^\sigma = \frac{\omega_q^\sigma - \omega_0}{2\sqrt{\omega_q^\sigma \omega_0}}, \tag{3.45b}$$

respectively [80]. The quasistatic dispersion relation (3.44) for an infinite chain of nanoparticles is shown in Fig. 3.7 for both longitudinal and transverse collective modes as a function of the wavevector q. In the figure, the bandstructure in nearest-neighbor approximation is plotted for comparison.

Such dispersion relations take into account the long-range nature of the dipole-dipole interaction. Notice that one can access the nearest-neighbor coupling approximation by taking only the first term of the sum into the lattice sum f_q^σ. In such a case, which constitutes the framework of Ref. [80], the lattice sum reduces to $f_{q,\mathrm{nn}}^\sigma = 2\eta^\sigma \cos(qd)$ which modify only quantitatively the dispersion relation (3.44) as can be seen in Fig. 3.7. Although the chain is assumed to be infinite (with periodic boundary conditions), the plasmonic band structure presented above (see Fig. 3.7) does

not consider the retardation effects of the dipole-dipole interactions [4]. In order to take into account these effects, one needs to concentrate on the plasmon-photon coupling since the light-matter interaction Hamiltonian includes retardation effects [148, 154]. Indeed, in the Coulomb gauge, the Hamiltonian (3.38) describes (together with instantaneous processes[2]) fully-retarded transitions between plasmonic levels mediated by virtual photons. In order to account for such transitions in an open-quantum system framework, one needs to evaluate the second order energy corrections within a perturbation theory. As it will be presented in the following, such terms lead to frequency shifts resulting from the retardation effects induced by the electromagnetic interactions. In what follows, we review the properties arising from both the photonic and electronic environments.

3.3.2 Radiative frequency shift and linewidth of the collective plasmons

Identically to the simple nanostructures we discussed previously, the chain of nanoparticles exhibits a renormalization of the frequencies associated to the plasmonic eigenmodes of the system due to the coupling to the external photonic degrees of freedom. Such a coupling contributes as well to the total linewidth of the collective modes through the radiative decay rate.

Radiative frequency shifts and retardation effects

Following the prescription given in Ref. [135], one can evaluate by means of a second-order perturbation theory in the coupling Hamiltonian (3.38) the radiative frequency shifts associated with the collective plasmons. In order to access the radiative shift of a given plasmonic mode, one needs to evaluate the second-order energy correction $E^{(2)}_{n_q^\sigma}$ induced by the photonic environment to the mode energy. Taking only the corrections due to the photonic environments into account, the energy of a given plasmonic eigenmode is $E_{n_q^\sigma} = \hbar\omega_q^\sigma n_q^\sigma + E^{(1)}_{n_q^\sigma} + E^{(2)}_{n_q^\sigma}$, where $\hbar\omega_q^\sigma n_q^\sigma$ is the unperturbed energy of the mode. The number n_q^σ is a positive integer which identifies the number of excited plasmonic states in a given mode q with polarization σ. It can be shown [135] that the first order correction does not depend on the plasmonic number. Such a properties implies that one obtains the radiative shift by evaluating the quantity $\delta_q^\sigma = (E^{(2)}_{n_q^\sigma+1} - E^{(2)}_{n_q^\sigma})/\hbar$ where the second-order correction is given by [135]

$$E^{(2)}_{n_q^\sigma} = \pi\hbar\omega_0^2\omega_q^\sigma \frac{a^3}{\mathcal{V}} \sum_{\mathbf{k},\hat{\lambda}_\mathbf{k}} \frac{|\hat{\sigma}\cdot\hat{\lambda}_\mathbf{k}|^2}{\omega_\mathbf{k}} \left(\frac{n_q^\sigma |\mathcal{F}^-_{\mathbf{k},q}|^2}{\omega_q^\sigma - \omega_\mathbf{k}} - \frac{\left(n_q^\sigma + 1\right)|\mathcal{F}^+_{\mathbf{k},q}|^2}{\omega_q^\sigma + \omega_\mathbf{k}} \right). \tag{3.46}$$

In Eq. (3.46), the summation over the photonic wavevector $\mathbf{k}$ excludes the one for which $\omega_\mathbf{k} = \omega_q^\sigma$ and the array factor for the chain is given by

$$\mathcal{F}^\pm_{\mathbf{k},q} = \frac{\mathrm{e}^{\mp \mathrm{i}k_z d}}{\sqrt{\mathcal{N}}} \sum_{n=1}^{\mathcal{N}} \mathrm{e}^{\mathrm{i}n(q\pm k_z)d}. \tag{3.47}$$

In the continuum limit, the second-order energy correction diverges. Such a behavior can be overcome by introducing an ultraviolet cutoff k_c of the order of $1/a$. The frequency associated with

[2] The total contribution of the instantaneous processes coming from the vector potential is fully compensated by the one from the scalar potential [154] leading to a fully-retarded light-matter interaction Hamiltonian.

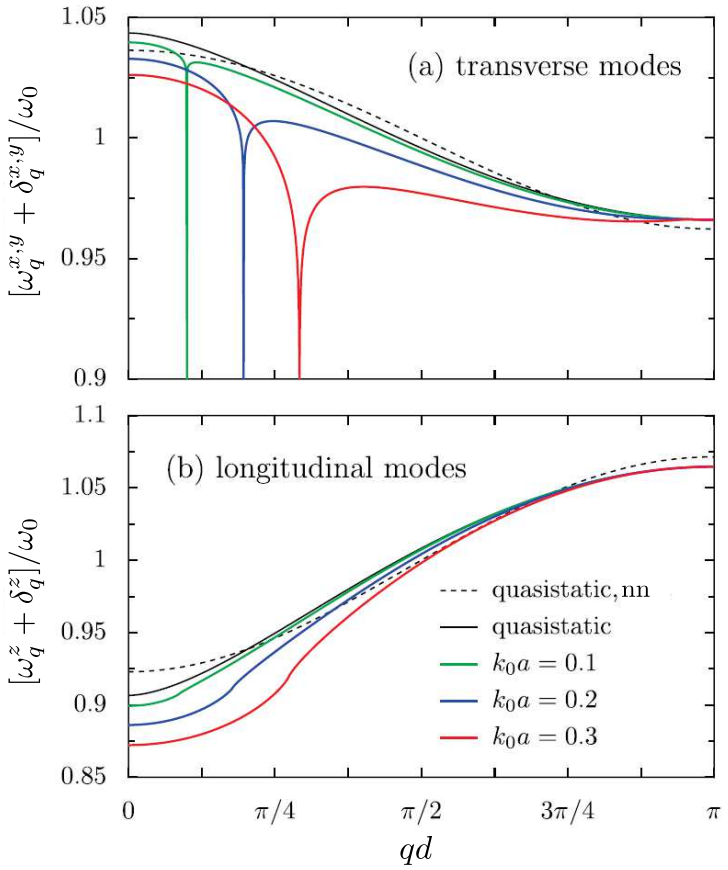

Figure 3.8: Plasmonic dispersion relations as a function of the (reduced) wavevector q for (a)–(c) transverse ($\sigma = x, y$) and (d)–(f) longitudinal ($\sigma = z$) polarizations. the solid black lines display the full quasistatic bandstructure while the dashed lines show the bandstructure accounting for the nearest-neighbor coupling only. Colored lines: fully-retarded plasmonic bandstructure $\omega_q^\sigma + \delta_q^\sigma$ including the radiative shift (3.50) for $k_0 a = 0.1$ (green lines), $k_0 a = 0.2$ (blue lines) and $k_0 a = 0.3$ (red lines). In the figure $d = 3a$ while the cutoff frequency is $\omega_c = c/a$. Figure adapted from Ref. [135].

such a cutoff corresponds to the one for which the dipole-dipole approximation breaks down. Note that, contrary to the isolated nanoparticle and the plasmonic dimer (cf. Secs. 2.4.1 and 3.2.1), the energy regularization procedure is not required to obtain meaningful results for the energy shift of the chain. Such an absence of the renormalization of the energy correction is reminiscent of the cooperative Lamb shift [152, 155] where such procedure is not needed as well. Taking the continuous limit [cf. (2.28)] in Eq. (3.46) together with the expression of the summation over the photon polarization (2.27) one obtains

$$\delta_q^\sigma = \frac{1}{8\pi^2 c}\omega_0^2 \omega_q^\sigma a^3 \mathcal{P} \int_0^{k_c} \mathrm{d}k\, k \int_0^\pi \mathrm{d}\theta \sin\theta \left(\frac{|\mathcal{F}^-_{\mathbf{k},q}|^2}{\omega_q^\sigma - ck} - \frac{|\mathcal{F}^+_{\mathbf{k},q}|^2}{\omega_q^\sigma + ck} \right) \int_0^{2\pi} \mathrm{d}\varphi [1 - (\hat{\sigma}\cdot\hat{k})^2]. \quad (3.48)$$

Taking the infinite chain limit, one has

$$|\mathcal{F}^{\pm}_{\mathbf{k},q}|^2 \simeq 2\pi\delta([q \pm k\cos\theta]d). \tag{3.49}$$

Replacing then the expressions of $|\mathcal{F}^{+}_{\mathbf{k},q}|^2$ and $|\mathcal{F}^{-}_{\mathbf{k},q}|^2$ into Eq. (3.48) together with (2.32), one can evaluate the remaining integrals to yield the radiative energy shifts

$$\delta^{\sigma}_{q} = \frac{\eta^{\sigma}}{2}\frac{\omega_0^2}{\omega_q^{\sigma}}\frac{q^2a^3}{d}\Theta(\omega_{\mathrm{c}} - c|q|)\left\{\ln\left(\frac{\omega_{\mathrm{c}}}{c|q|}\right) + \frac{1}{2}\left[1 + \mathrm{sgn}\{\eta^{\sigma}\}\left(\frac{\omega_q^{\sigma}}{cq}\right)^2\right]\ln\left(\frac{|(cq)^2 - \omega_q^{\sigma\,2}|}{\omega_{\mathrm{c}}^2 - \omega_q^{\sigma\,2}}\right)\right\}, \tag{3.50}$$

where $\omega_{\mathrm{c}} = ck_{\mathrm{c}}$. Such a shift adds up to the bare resonance frequency ω_q^{σ} to yield the renormalized frequencies of the plasmonic eigenmodes $\omega_q^{\sigma} + \delta_q^{\sigma}$. These frequencies are plotted as colored lines in Fig. 3.8 as a function of the wavevector q for an interparticle distance $d = 3a$, an ultraviolet cutoff frequency $\omega_{\mathrm{c}} = c/a$ and for different sizes of nanoparticle. In the figure, the transverse and longitudinal modes are plotted in the upper (a) and lower (b) panel, respectively.

One can directly observe from Fig. 3.8 that adding the radiative shift to the quasistatic resonance frequency ω_q^{σ} from Eq. (3.44) affects the dispersion relations differently depending of the polarization of the modes. The most striking difference is the existence of a logarithmic singularity appearing for the transverse modes. Such a cusp occurs at the crossing between the light cone $\omega = c|q|$ and the dispersion ω_q^{σ}. As can be seen from the figure, the plasmonic bandstructure is also altered in the vicinity of this crossing for the longitudinal modes (see lower panel in the figure) but in lesser proportion than the transverse ones. Interestingly, similar observations have been previously reported in several works (see e.g., [133, 134]) by means of complex computations of the fully-retarded solutions to Maxwell's equations.

We further show in Fig. 3.9 the comparison between the analytical (colored lines) and the numerical (colored dots) results for the radiative shift calculated in Ref. [135] as a function of the wavevector q. In the figure, the transverse modes are shown in panels (a)–(c) and the longitudinal ones in panels (d)–(f), respectively. The different panels correspond to $k_0a = 0.1$ [panels (a),(d)], $k_0a = 0.2$ [panels (b),(e)], and $k_0a = 0.3$ [panels (c),(f)]. As can be seen from the figure, the numerical results show a very good agreement with respect to the perturbative calculations developed above. In addition to provide fully analytical results, such a method gives meaningful results which do not require heavy computations. As such, we expect that employing similar methods for evaluating the radiative shifts in metasurfaces give relevant results as well.

Radiative losses

Following Ref. [80], the radiative damping rate can be evaluated by means of a Fermi golden rule for the plasmon-photon coupling Hamiltonian (3.38). Such a rate describing the relaxation of a given plasmonic mode (with wavevector q and polarization σ) into photons through spontaneous emission thus reads

$$\gamma_q^{\sigma} = 2\pi^2\omega_0^2\omega_q^{\sigma}\frac{a^3}{\mathcal{V}}\sum_{\mathbf{k},\hat{\lambda}_{\mathbf{k}}}\frac{|\hat{\lambda}_{\mathbf{k}}\cdot\hat{\sigma}|^2}{\omega_{\mathbf{k}}}|\mathcal{F}^{-}_{\mathbf{k},q}|^2\delta(\omega_q^{\sigma} - \omega_{\mathbf{k}}). \tag{3.51}$$

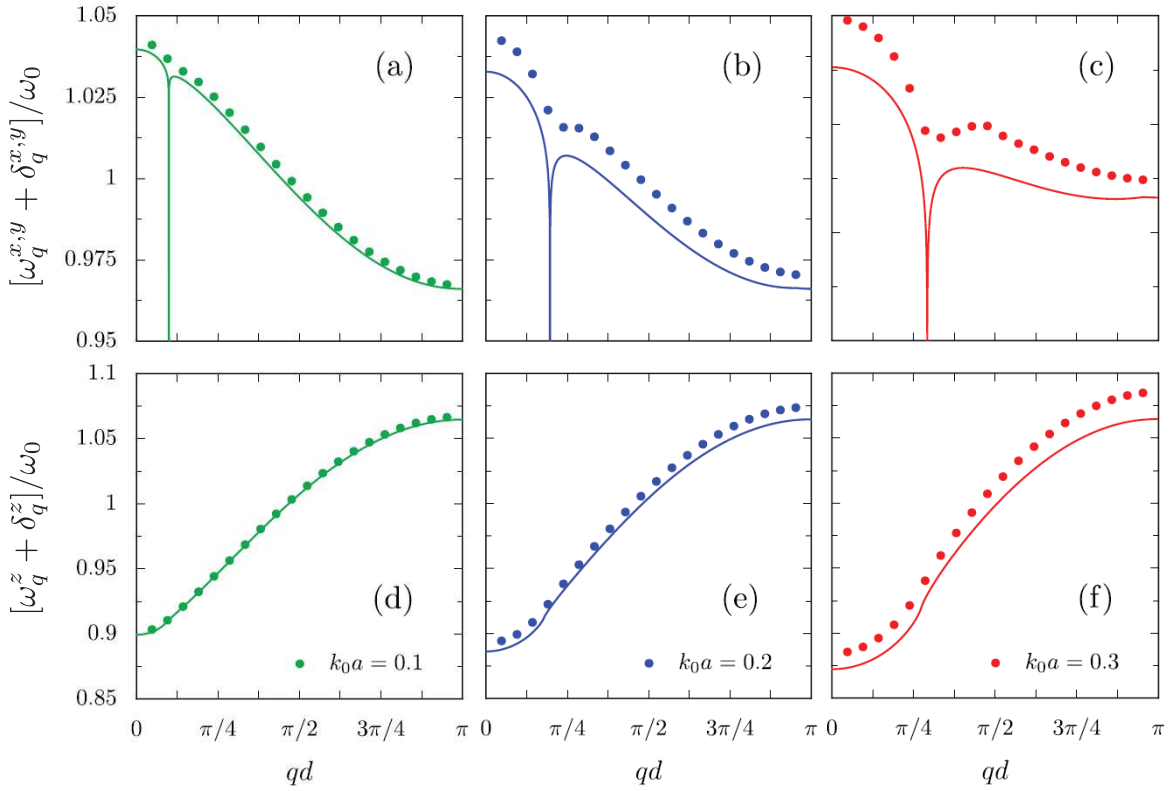

Figure 3.9: Plasmonic dispersion relations as a function of the (reduced) wavevector q for (a)–(c) transverse ($\sigma = x, y$) and (d)–(f) longitudinal ($\sigma = z$) polarizations. The dots are the fully-retarded numerical solutions to Maxwell's equations for nanoparticle sizes (a), (d) $k_0a = 0.1$ (green dots), (b), (e) $k_0a = 0.2$ (blue dots), (c), (f) $k_0a = 0.3$ (red dots). The solid lines show the analytical dispersion relations $\omega_q^\sigma + \delta_q^\sigma$ from Eqs. (3.44) and (3.50) for (a), (d) $k_0a = 0.1$ (green lines), (b), (e) $k_0a = 0.2$ (blue lines), (c), (f) $k_0a = 0.3$ (red lines). In the figure, $d = 3a$ while the cutoff frequency is $\omega_c = c/a$. Figure adapted from Ref. [135].

The summations in the latter equation can be readily replaced by integrals using Eq. (2.27) as well as the continuous limit, Eq. (2.28), to yield

$$\gamma_q^\sigma = \frac{\omega_0^2 \omega_q^\sigma}{2c^2 d} a^3 \int_{-\infty}^{+\infty} \mathrm{d}k \delta\left(\frac{\omega_q^\sigma}{c} - k\right) \int_0^\pi \mathrm{d}\theta \sin\theta \delta\left(\frac{q}{k} - \cos\theta\right) \int_0^{2\pi} \mathrm{d}\varphi [1 - (\hat{\sigma} \cdot \hat{\mathbf{k}})^2], \tag{3.52}$$

where $|F_{\mathbf{k},q}^-|^2$ is replaced by its $\mathcal{N} \gg 1$ limit [see Eq. (3.49)]. Using Eq. (2.32) to calculate directly the integral over the φ angle, the remaining integrals are easily evaluated and one obtains for the radiative damping decay rate [80, 135]

$$\gamma_q^\sigma = \frac{\pi \eta^\sigma}{2} \frac{\omega_0^2}{\omega_q^\sigma} \frac{q^2 a^3}{d} \Theta(\omega_q^\sigma - c|q|) \left[1 + \mathrm{sgn}\{\eta^\sigma\} \left(\frac{\omega_q^\sigma}{cq}\right)^2\right]. \tag{3.53}$$

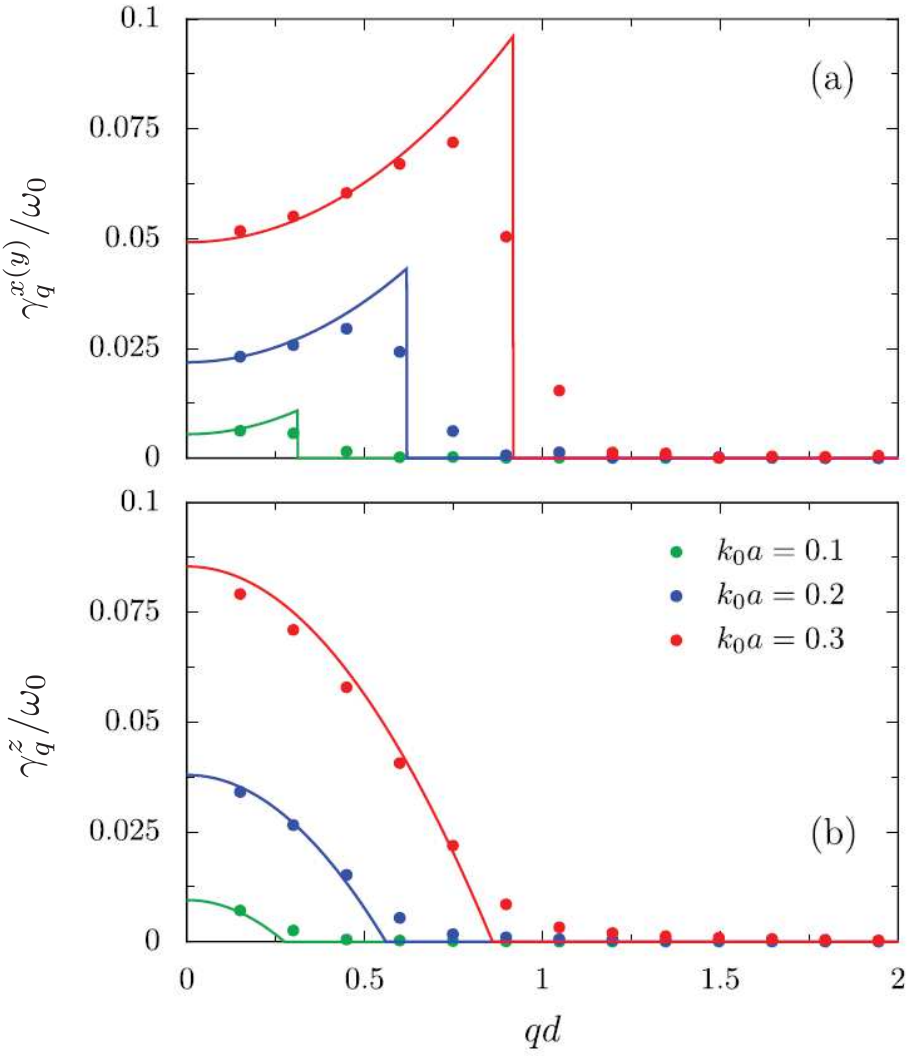

Figure 3.10: Radiative damping rate γ_q^σ (scaled by the Mie frequency ω_0) as a function of the wavevector q for (a) the longitudinal and (b) transverse modes. The colored lines are the results directly taken from Eq. (3.50) for $k_0a = 0.1$ (green lines), $k_0a = 0.2$ (blue lines) and $k_0a = 0.3$ (red lines). The dots are the fully-retard solutions obtained by solving numerically the Maxwell's equations for a chain of $\mathcal{N} = 20$ nanoparticles. In the figure, $d = 3a$. Figure adapted from Ref. [135].

The expression (3.53) is plotted in Fig. 3.10 as a function of the wavevector q for both transverse and longitudinal modes in panels (a) and (b), respectively. In the figure, different curves correspond respectively to $k_0a = 0.1$ (green lines), $k_0a = 0.2$ (blue lines) and $k_0a = 0.3$ (red lines). The figure displays as well the numerical solutions of the fully-retarded Maxwell's equations for a chain constituted by 20 nanoparticles. From the figure, one can clearly observe two distinct regimes for both

mode polarizations. Outside the light cone, i.e., for modes with wavelength smaller than $\sim 2\pi/k_0$ (corresponding to $q \gtrsim k_0$), the plasmonic modes are dark modes with vanishing damping rates. Such a behavior (well-reproduced by numerical calculations) arises from the destructive interferences between the isolated electric dipoles (i.e., the LSPs) inducing an absence of coupling with the light. In contrast, a majority of modes for both polarizations display a superradiant behavior, (i.e., $\gamma_q^\sigma > \gamma_0$) inside the light cone ($q \lesssim k_0$). Such large rates (up to several times γ_0) arise due to constructive interferences between the electric fields of the individuals LSPs hosted by the chain. One can however observe from the figure that the rate of the transverse modes increases (inside the light cone) as a function of the wavevector, while the longitudinal ones display an opposite tendency.

As we will see in Chapter 7, the situation shown in Eq. (3.53) and Fig. 3.10 for the chain will be strongly modified as soon as we consider extended two-dimensional metasurfaces. Indeed, in the case of metasurfaces (with arbitrary geometries), the collective plasmons polarized within the plane of the arrays (e.g., x– and y–directions) may possess an arbitrary in-plane polarization which is not necessarily along the σ–direction thus creating more complex cases to consider.

3.3.3 Landau damping and electronic-induced frequency shift

Identically to the previous plasmonic structures we depicted in this manuscript (i.e., single nanoparticles and dimers), the coupling of the plasmonic system to the electronic environment induces a shift of the resonance frequency ω_q^σ and opens a decay channel for the relaxation of the plasmonic eigenmodes. As mentioned in Chapters 1 and 2, the contribution to the total linewidth arising from such a coupling is linked to a non-radiative (Landau) process. In what follows, we review the procedure given in Refs. [80, 135] one may use in order to evaluate the Landau decay rate. We here point out that in Ref. [80], the calculations are performed for a chain of finite length but the procedure remains unchanged (only the details in the calculation are modified). We finally conclude this section by discussing the procedure we employ to evaluate the electronic shift of the collective plasmons.

Landau damping

The second mode-dependent damping mechanism inducing the collective plasmon decay is the Landau damping (similarly to the plasmonic dimer). Such a decay rate can be obtained with a Fermi golden rule for the plasmon-electron coupling Hamiltonian (3.39). Going to wavevector space [using the Fourier decomposition of the b_n^σ operators, cf. (3.40)] and expressing the operators b_q^σ as a function of the operators β_q^σ with $b_q^\sigma = u_q^\sigma \beta_q^\sigma - v_q^\sigma {\beta_{-q}^\sigma}^\dagger$ where the Bogoliubov coefficients u_q^σ and v_q^σ are given in Eq. (3.45), one gets for the Landau damping rate

$$\Gamma_q^\sigma = |u_q^\sigma - v_q^\sigma|^2 \Sigma^\sigma(\omega_q^\sigma), \tag{3.54}$$

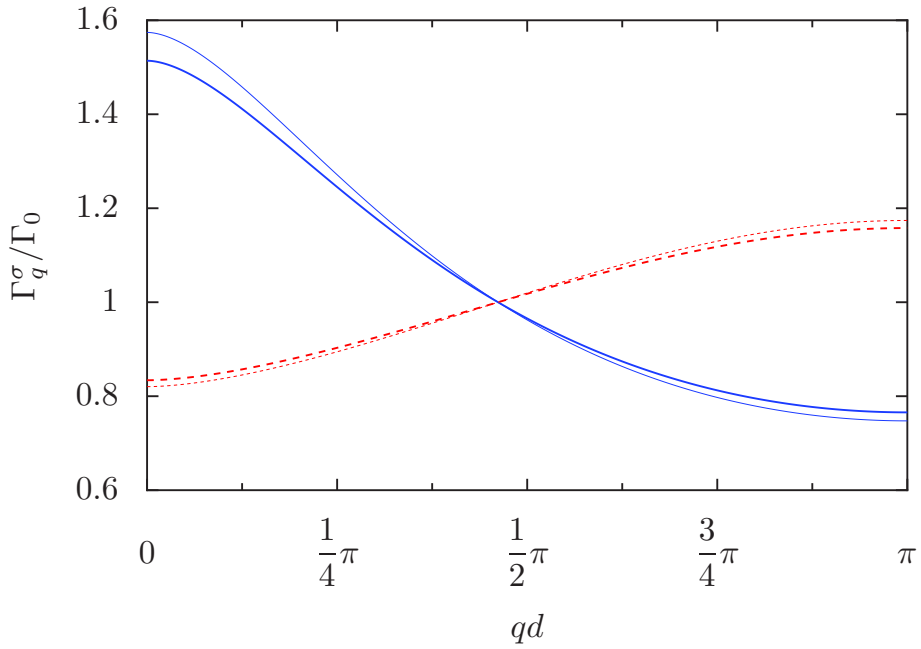

Figure 3.11: Landau damping rate (scaled by the rate of an isolated nanoparticle (3.55)) of an infinite chain of nanoparticles as a function of the wavevector q for transverse (red dashed lines) and longitudinal (blue solid lines) modes. The thick (thin) lines correspond to $\hbar\omega_0/E_\mathrm{F} = 0.5$ ($\hbar\omega_0/E_\mathrm{F} = 1$). In the figure, the interparticle distance is $d = 3a$.

where the function $\Sigma^\sigma(\omega)$ is given in Eq. (2.35). The latter expression can be readily evaluated using Eq. (A.8) together with Eq. (3.45) to yield

$$\Gamma_q^\sigma = \frac{3v_\mathrm{F}}{4a}\left(\frac{\omega_0}{\omega_q^\sigma}\right)^4 g\left(\frac{\hbar\omega_q^\sigma}{E_\mathrm{F}}\right), \tag{3.55}$$

where $g(\nu)$ is given in Eq. (A.10). Figure 3.11 shows the results of the Landau damping rate (3.55) for both polarizations (transverse and longitudinal) as a function of the wavevector q inside the half first Brillouin zone ($q \in [0, \pi/d]$). These rates, scaled by the Landau damping of an isolated nanoparticle [cf. Eq. (2.37)], are plotted for different values of the parameter $\hbar\omega_0/E_\mathrm{F}$ (thick lines: $\hbar\omega_0/E_\mathrm{F} = 0.5$, thin lines: $\hbar\omega_0/E_\mathrm{F} = 1$) and for an interparticle distance $d = 3a$. As can be seen from the expression (3.55), the general form of the damping rate is reminiscent of the one of the hybridized modes of the plasmonic dimer (3.29) where the frequency of the dimer eigenmodes are replaced by those of the chain. Therefore, the Landau damping rate scales with the inverse radius a of the nanoparticle similarly to the Landau losses of the dimer. Moreover, comparing the dispersion relations in Fig. 3.7 with the Landau damping (3.55) plotted in Fig. 3.11, one immediately observes that the more the plasmonic modes are energetic, the less their energy is dissipated through electron-hole pair creations.

Frequency shift induced by the electronic degrees of freedom

The plasmonic frequencies ω_q^σ experience an electronic shift in addition to the radiative one [cf. Eq. (3.50)] calculated in the previous section (cf. Sec. 3.3.2). In contrast to the radiative renormalization of the plasmonic frequencies which provides essential features incorporated into the light-matter interaction (i.e., the retardation effects) and which are not accessible without using this perturbation theory in the frame of an open-quantum system, the electronic shift only corresponds to a global redshift of the plasmonic dispersion relations.

Using second-order perturbation theory for the plasmon-electron coupling Hamiltonian (3.39) together with the Fourier transform and the inverse Bogoliubov transformation for the b_q^σ operators, one obtains for the electronic (or Landau) shift

$$\Delta_q^\sigma = |u_q^\sigma - v_q^\sigma|^2 \times \left(\frac{-2}{\hbar^2} \sum_{eh} |\Lambda \hat{\sigma} \cdot \mathbf{d}_{eh,n}|^2 \, \frac{\omega_{eh}}{\omega_{eh}^2 - \omega_q^{\sigma 2}} \right). \tag{3.56}$$

Since the matrix elements $\mathbf{d}_{eh,n}$ are identical for all n, the term in parenthesis reduces to Eq. (2.45) where ω_0 is replaced by ω_q^σ. Following the procedure used in Sec. 3.2.2 [cf. Eqs (3.32)–(3.35)] to evaluate the electronic shift Δ_τ^σ of the hybridized plasmonic modes, the latter equation reads

$$\Delta_q^\sigma = -\frac{3v_\mathrm{F}}{4a} \beth \left(\omega_q^\sigma \right), \tag{3.57}$$

where $\beth(\omega)$ is defined in Eq. (2.53). Note that we used the definition of the Bogoliubov coefficients u_q^σ and v_q^σ [cf. Eq. (3.45)] into (3.56) to get the final form in Eq. (3.57). Such a shift scales with the inverse radius of the nanoparticles and corresponds to a redshift of the frequency in a similar way as the isolated nanoparticle and the plasmonic dimer.

3.3.4 Spectral response of the plasmonic chain

The relevant quantity characterizing the collective plasmons resonances within metastructures is the spectral response which can be obtained experimentally. Assuming that a given plasmonic collective mode is excited (optically or with EELS methods) within the chain of nanoparticles, the total spectral response $\mathcal{A}_q^\sigma(\omega)$ of such a mode will thus be measured as a Lorentzian line shape. Therefore, we assume the spectral function to have a Breit-Wigner form as

$$\mathcal{A}_q^\sigma(\omega) \propto \frac{1}{\left(\omega - \tilde{\omega}_q^\sigma\right)^2 + \left(\gimel_q^\sigma/2\right)^2}. \tag{3.58}$$

In the latter expression, $\tilde{\omega}_q^\sigma = \omega_q^\sigma + \delta_q^\sigma + \Delta_q^\sigma$ and $\gimel_q^\sigma = \gamma_q^\sigma + \Gamma_q^\sigma + \gamma_\mathrm{O}$ are the renormalized frequency and the total damping rate of the plasmonic modes, respectively. Here γ_O arises from the intrinsic absorption losses of the metal (dominated by electon-phonon interactions at room temperature). Equipped with the expressions of the frequency shifts (3.50) and (3.57) as well as those of the damping rates (3.53) and (3.55), one can compute analytically the total spectral function for the whole plasmonic band structure of the chain. We show in Fig. 3.12 the normalized spectral function of a plasmonic chain of Ag nanoparticles for the transverse and longitudinal collective modes for

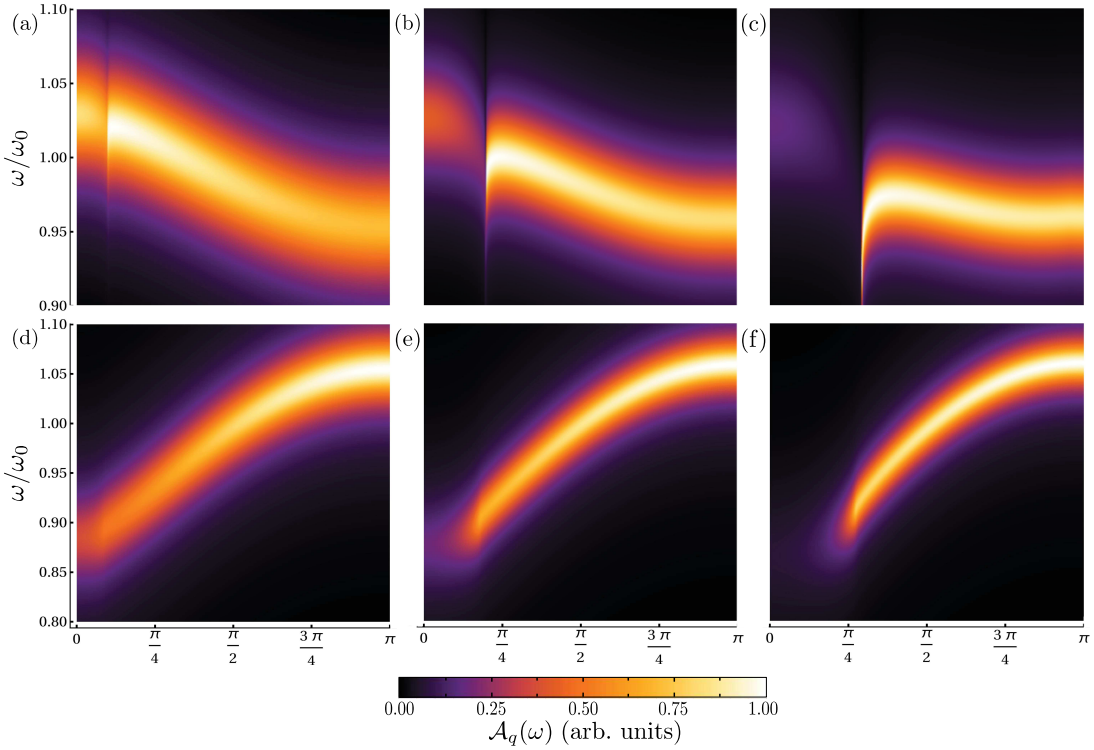

Figure 3.12: Total spectral function (3.58) (in arbitrary units) for an infinite plasmonic chain composed of spherical Ag nanoparticles of radius a for (a)–(c) transverse and (d)–(f) longitudinal plasmonic modes. The panels (a),(d), (b),(e) and (c),(f) correspond respectively to a size of nanoparticles of $k_0a = 0.1$, $k_0a = 0.2$ and $k_0a = 0.3$. In the figure, we choose $\hbar\omega_0/E_{\rm F} = 0.47$, $\omega_0/ck_{\rm F} = 1.1 \times 10^{-3}$ (corresponding to Ag nanoparticles)and $\gamma_{\rm O}/\omega_0 = 0.027$ which is extracted from the experiments of Ref. [156]. Moreover, the interparticle distance is $d = 3a$.

various nanoparticle sizes. In the figure the panels (a)–(c) and (d)–(f) depict the expression (3.58) for the transverse ($\sigma = x, y$) and longitudinal ($\sigma = z$) plasmonic modes, respectively. The panels (a),(d), (b),(e) and (c),(f) correspond respectively to $k_0a = 0.1$, $k_0a = 0.2$ and $k_0a = 0.3$. In Fig. 3.12, we used for the total renormalized frequency and the total damping rate entering (3.58), the parameters $\hbar\omega_0/E_{\rm F} = 0.47$ and $\omega_0/ck_{\rm F} = 1.1 \times 10^{-3}$ corresponding to silver nanoparticles (placed in vacuum) separated by a distance $d = 3a$. Moreover, we have $\gamma_{\rm O}/\omega_0 = 0.027$ for the Ohmic damping rate.[3] From the figure, we clearly observe in the absorption two distinct regimes for both polarizations. Such regimes are a direct consequence of plasmonic properties induced by the coupling with the photonic environment (i.e., the radiative frequency shift and radiative damping).

For the transverse modes [panels (a)–(c)], we immediately notice the divergence which occurs at the crossing between the quasistatic dispersion relations and the light cone similarly to the renormalized plasmonic frequencies $\omega_q^z + \delta_q^z$ (see Fig. 3.8 in Sec. 3.3.2). Inside the light cone, the width

[3]This particular value corresponding to silver is extracted from the experiments of Ref. [156].

of the Lorentzian becomes larger as the size of the nanoparticles increases. Such a dependence is due to the scaling of the radiative damping rate with the volume of the nanoparticle. Additionally, we can also distinguish [e.g., in panel (c)] that such a width also increases as the wavevector approaches the light cone. These effects are directly related to the behavior of the radiative damping of the transverse modes as a function of the wavevector [see Fig. 3.10(a)]. Conversely, outside the light cone, the width of the absorption reduces as a function of the nanoparticle size and shows almost no variations across the rest of the Brillouin zone. Indeed, outside the light cone, only the non-radiative processes contributes to the total damping rate. Since the Ohmic losses are not affected by the radius a, the absorption depends on the $1/a$ scaling of the Landau damping alone.

The longitudinal modes ($\sigma = z$) in panels (d)–(f) show a spectral function with a similar scaling with the nanoparticle size a as those presented above for $\sigma = x, y$. Aside the absence of a singularity (identically as for the radiative shifts) for the longitudinal modes, we note [see Fig. 3.12(f)] the slight reduction of the width close to the light cone limit. Such a behavior is due to the profile of the radiative damping (3.53) for $\sigma = z$ [see Fig. 3.10(b)].

In conclusion, Figure 3.12 shows that one may experimentally resolve the fully-retarded plasmonic dispersion relation of chains of silver nanoparticles for all polarizations providing optical techniques using oil immersion objectives (see e.g., Ref. [88]) to image the band structure outside the light cone.[4] In the figure, taking a radius $a \simeq 15.2\,\mathrm{nm}$ (corresponding to panels (b),(e) in Fig. 3.12 where $k_0 a = 0.2$) should thus give good experimental results for chains of Ag nanoparticles.

3.4 Conclusion for Chapter 3

In this chapter, we have reviewed the principal results obtained in an open-quantum system framework discussed in Refs. [64, 79, 80, 135] about plasmonic simple one-dimensional metastructures composed of spherical metallic nanoparticles. Focusing first on nanoparticle dimers, we have provided the fully quantized Hamiltonian of the plasmonic dimer. In particular, neglecting the proximity effects (multipolar and tunneling effects), we have given the plasmonic Hamiltonian as well as the two Hamiltonians corresponding to the coupling to the photonic and electronic environments. Then, we have introduced the hybridized plasmonic modes, which are the eigenmodes of the plasmonic Hamiltonian, with the help of a bosonic Bogoliubov transformation. Such modes are referred to as bright or dark modes. While the latter does not display a net dipole moment at infinity therefore not coupling to the light, the former presents a net dipole moment.

Next, we gave the key steps one can perform to derive the photonic induced effects for the hybridized modes, i.e., the radiative shift and radiative linewidth. Importantly, the radiative shift may be positive (corresponding to a blue shift) or negative (corresponding to a redshift) and scales with the volume of the nanoparticle. Moreover, we have seen that, compared to the single nanoparticle case, the dimers exhibit dark modes which do not couple to light and thus do note radiate in the far field. The bright modes show however larger radiative damping rates as the individual LSPs interfere constructively.

[4] Alternatively, EELS techniques could also allow for a measurement of the plasmonic bandstructure outside the light cone.

To conclude the section about plasmonic dimers, we have reviewed the calculations for the Landau damping rate. Such a damping rate of the hybridized modes was calculated similarly as done for the isolated nanoparticle and display only quantitative modifications as compared to the simple plasmonic modes. Furthermore, one can note that both damping mechanisms show similar scalings with the nanoparticle size ($\propto a^3$ for the radiative losses and $1/a$ for the Landau ones) for the single nanoparticle and the plasmonic dimer. Then, we evaluated the second frequency shift arising from the coupling of the plasmonic subsystem to the electronic environment. Such a contribution is always negative and scales with the inverse radius of the nanoparticles (up to a logarithmic factor). Importantly, we also verified that, considering the total shift $\delta_\tau^\sigma + \Delta_\tau^\sigma$ into the renormalized eigenfrequencies instead of only the radiative shift does not modify the conclusions presented in Ref. [64].

In the second part of this chapter, we have concentrated on one-dimensional simple chains of nanoparticles. We have first presented the total Hamiltonian of the chain with an identical procedure as used for the plasmonic Hamiltonian of the dimer. We have seen that the Hamiltonian (3.36) shows similarities (e.g., on-site energy and hopping-like terms) with electronic tight-binding Hamiltonians. Eq. (3.36) shows however important differencies such as the polarization of the modes. Then, we have given the expression of the plasmonic eigenmodes as well as the corresponding eigenstates using a Bogoliubov transformation in the wavevector space following the prescription of Ref. [80]. From this Hamiltonian description, we have then reviewed the principal results concerning the frequency shifts and the energy damping rates induced on the plasmonic eigenmodes of the chain by the photonic and electronic environments.

The frequency shifts can be evaluated with a second-order perturbation theory for the two different coupling Hamiltonians. Contrary to the Landau shift which presents analogous expressions as the electronic shift of the plasmonic dimer, the frequency renormalization due to the photonic environment shows new features as compared to the two nanostructures studied previously, that is the retardation effects included into the light-matter interaction since the nanoparticles within the chain may be spread by a distance of the order of $1/k_0$, breaking the quasistatic limit. We have then presented the procedure one can perform to evaluate the damping rates of the plasmonic excitations using Fermi's golden rules for both coupling Hamiltonians (3.38) and (3.39). In contrast with the eigenmodes of the plasmonic dimer which exhibit dark and bright modes for both transverse and longitudinal polarization, the radiative damping rate of the collective plasmons of the chain behaves differently depending of the polarization. Importantly though, only the eigenmodes with a wavevector q inside the light cone (with dispersion $\omega = c|q|$) can emit photons leading to a vanishing rate outside this region. We finally concluded this section by briefly giving the expression for the Landau damping which is reminiscent of the one of the hybridized modes of the dimer. Note that both damping rates are proportional to those of the single nanoparticle hence showing the same scaling (with the volume and the inverse size for the radiative and Landau damping, respectively). We have finally computed the spectral function (assumed to have a Breit-Wigner form) associated with the collective plasmons hosted by chains of nanoparticles within the first Brillouin zone. We showed that for nanoparticle sizes close to $15\,\mathrm{nm}$, one can measure an spectral signal with an appreciable width (since the damping is sufficiently low).

All the properties of the collective plasmons discussed in this chapter are strongly related to the dimensionality of the underlying structures which support them. In the reminder of this manuscript,

we will concentrate on metastructures with larger dimensionality.[5] In the next chapter we will develop our model to study the collective plasmonic modes of two dimensional metastructures with arbitrary geometries. Indeed, due to their two-dimensional nature, these metasurfaces offer a richer scope of interesting topological properties (such as Dirac-like bosons in honeycomb lattices [108, 109, 139]) than in simple chains of nanoparticles (note however that such pseudo-relativistic plasmons have been predicted in bipartite chains of nanoparticles [136]).

[5] This work will only focus on two-dimensional structures and will not consider three-dimensional objects composed of nanoparticles. As a matter of fact, in such a situation, the light-matter interaction cannot be considered as a small perturbation and a full polaritonic description of the system needs to be conducted [157, 158].

Chapter 4

Modeling plasmonic metasurfaces: an open-quantum system approach

In this chapter, we introduce our theoretical framework that will serve us to investigate the properties of the collective plasmonic modes in arbitrary periodic metasurfaces. Using similar methods as discussed in the previous chapters, we will derive the Hamiltonian characterizing the dipolar plasmonic modes hosted by generic two-dimensional arrays of metallic nanoparticles. Considering that, these bosonic modes are weakly coupled to the external photonic and electronic degrees of freedom, we will treat the plasmonic system as an open-quantum system. In a second section, we present the procedure we use to diagonalize exactly the plasmonic Hamiltonian (written in the wavevector space). Such a procedure, based on Bogoliubov transformations and the Heisenberg equation of motion, allows to unveil analytic expressions for the plasmonic eigenquantities. We then conclude the present chapter by discussing the polarization of the collective plasmonic modes.

4.1 Model Hamiltonian

We consider an assembly of identical spherical metallic nanoparticles of radius a forming a two-dimensional metastructure. Since our model aims to describe any geometries for such periodic metasurfaces, we will in the following focus on structures constituted by arbitrary Bravais lattices with a basis. Similarly to the previous chapters, we consider noble-metal nanoparticles placed in vacuum and further neglect the screening effects due to the core electrons. Within these approximations, each nanoparticle hosts three degenerate localized surface plasmons polarized in the x, y and z-direction with resonance frequency ω_0, the Mie frequency introduced in Eq. (1.5). We show in Figure 4.1, the general sketch of such two-dimensional lattice. In order to study non-Bravais plasmonic lattices (e.g., the honeycomb lattice), we first characterize the arbitrary structure by a set of vectors $\mathbf{R} = n\mathbf{t}_1 + m\mathbf{t}_2$ forming a Bravais lattice. Here, $\mathbf{t}_1$ and $\mathbf{t}_2$ are the primitive lattice vectors and where $n \in [0, \mathcal{N}_1]$ and $m \in [0, \mathcal{N}_2]$ are integer numbers with $\mathcal{N}_1$ and $\mathcal{N}_2$ the number of unit cells in the $\mathbf{t}_1$ and $\mathbf{t}_2$ directions, respectively. The full array is composed of $\mathcal{S}$ sublattices and the nanoparticles belonging to the sublattice $s = 1, \ldots, \mathcal{S}$ are located at $\mathbf{R}_s = \mathbf{R} + \mathbf{d}_s$ where $\mathbf{d}_s$ is the vector connecting the sublattice s to the vectors $\mathbf{R}$. By convention, we set $\mathbf{d}_1 = 0$ in the remainder of the manuscript.

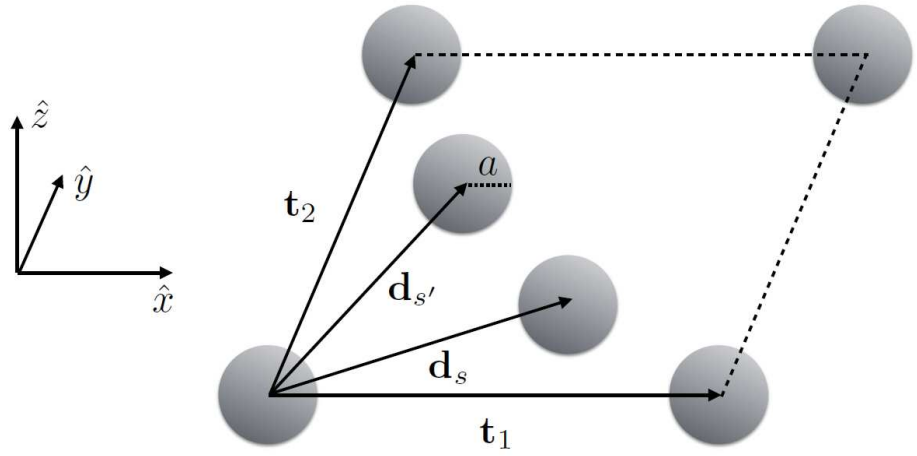

Figure 4.1: Sketch of the primitive cell of a generic two-dimensional array of identical spherical metallic nanoparticles with radius a forming a Bravais lattice with a basis. In the figure, $\mathbf{t}_1$ and $\mathbf{t}_2$ are the primitive vectors of the Bravais lattice and $\mathbf{d}_s$ ($s = 1, \ldots, \mathcal{S}$) are the vectors forming the basis. By convention, $\mathbf{d}_1 = 0$.

The plasmons supported by the nanoparticles interact with their neighbors through Coulomb interactions. Focusing on the regime $3a \lesssim d \ll k_0^{-1}$, with d the center-to-center nearest-neighbor interparticle distance, the dominant interaction between two nanoparticles is the near-field quasistatic dipole-dipole interaction (similarly to plasmonic dimers and chains, cf. Chapter 3). As introduced in the previous chapters, such an interaction, which scales as $1/d^3$ and depends strongly on the polarization of the individual plasmons, gives rise to collective plasmonic modes which extend over the whole metasurface. Identically to individual LSPs, the collective plasmons supported by the metasurface are coupled to both a photonic and an electronic environment. The collective modes are indeed coupled through the light-matter interactions to vacuum electromagnetic modes giving rise to finite radiative lifetimes as well as radiative frequency shifts. Moreover, such plasmonic modes are coupled to electron-hole excitations inside the nanoparticles, leading to a nonradiative energy dissipation (i.e., the Landau damping) and an additional frequency renormalization.

Considering the number of plasmonic degrees of freedom to be much smaller than those of the environments, we study the plasmonic metasurface in an open-quantum system framework. Within such a scheme, the total Hamiltonian describing the full system reads as

$$H = H_{\mathrm{pl}} + H_{\mathrm{ph}} + H_{\mathrm{eh}} + H_{\mathrm{pl-ph}} + H_{\mathrm{pl-eh}}. \tag{4.1}$$

As detailed in the following sections, the first term of the r.h.s. of Eq. (4.1) accounts only for the plasmonic degrees of freedom obtained by separating the center-of-mass and relative coordinates of the electrons of the system (identically to the one presented in Chapter 2). In Eq. (4.1), the second and third terms correspond to the Hamiltonians of the photonic and electronic environments, respectively. Finally, as developed below, the two remaining terms of Eq. (4.1) arise from the coupling between the plasmonic sub-system and both of the environments.

4.1.1 The plasmonic Hamiltonian

Identically to the plasmonic chain, we write the plasmonic Hamiltonian as the summation of a non-interacting and an interacting term as

$$H_{\rm pl} = H_{\rm pl}^{0} + H_{\rm pl}^{\rm int}. \tag{4.2}$$

The non-interacting term $H_{\rm pl}^{0}$ which accounts for the contribution of each isolated plasmons supported by the nanoparticles belonging to the entire array reads

$$H_{\rm pl}^{0} = \sum_{s=1}^{\mathcal{S}} \sum_{\mathbf{R}_s} \sum_{\sigma=x,y,z} \left\{ \frac{[\Pi_s^{\sigma}(\mathbf{R}_s)]^2}{2\mathcal{N}_{\rm e} m_{\rm e}} + \frac{\mathcal{N}_{\rm e} m_{\rm e}}{2} \omega_0^2 \left[h_s^{\sigma}(\mathbf{R}_s)\right]^2 \right\}. \tag{4.3}$$

In Eq. (4.3), $h_s^{\sigma}(\mathbf{R}_s)$ corresponds to the σ-component of the displacement field associated with the dipole moment of a single plasmon ($h_s^{\sigma}(\mathbf{R}_s)$ accounts for the motion of the electronic center-of-mass located at $\mathbf{R}_s$ in the direction σ) reading

$$\mathbf{p}_s(\mathbf{R}_s) = -e\mathcal{N}_{\rm e} \sum_{\sigma=x,y,z} h_s^{\sigma}(\mathbf{R}_s)\hat{\sigma}, \tag{4.4}$$

and located at position $\mathbf{R}_s$. $\Pi_s^{\sigma}(\mathbf{R}_s)$ represents the momentum conjugated to the displacement field $h_s^{\sigma}(\mathbf{R}_s)$. The second term of (4.2), arising from the quasistatic dipole-dipole interactions, reads as

$$H_{\rm pl}^{\rm int} = \frac{1}{2} \sum_{ss'} \sum_{\substack{\mathbf{R}_s, \mathbf{R}'_{s'} \\ (\mathbf{R}_s \neq \mathbf{R}'_{s'})}} \frac{1}{|\mathbf{R}'_{s'} - \mathbf{R}_s|^3} \left\{ \mathbf{p}_s(\mathbf{R}_s) \cdot \mathbf{p}_{s'}(\mathbf{R}'_{s'}) - 3[\mathbf{p}_s(\mathbf{R}_s) \cdot \hat{n}][\mathbf{p}_{s'}(\mathbf{R}'_{s'}) \cdot \hat{n}] \right\}, \tag{4.5}$$

with $\hat{n} = (\mathbf{R}'_{s'} - \mathbf{R}_s)/|\mathbf{R}'_{s'} - \mathbf{R}_s|$ the unit vector connecting the nanoparticles located at $\mathbf{R}_s$ and $\mathbf{R}'_{s'}$, respectively. The factor $1/2$ in Eq. (4.5), is added to avoid the double-counting of the interactions between pairs of nanoparticles. Inserting (4.4) into (4.5) then yields

$$H_{\rm pl}^{\rm int} = \frac{(e\mathcal{N}_{\rm e})^2}{2} \sum_{ss'} \sum_{\mathbf{R}_s} \sum_{\substack{\boldsymbol{\rho}_{ss'} \\ (\boldsymbol{\rho}_{ss'} \neq 0)}} \sum_{\sigma\sigma'} \frac{1}{\rho_{ss'}^3} h_s^{\sigma}(\mathbf{R}_s) h_{s'}^{\sigma'}(\mathbf{R}_s + \boldsymbol{\rho}_{ss'}) [\delta_{\sigma\sigma'} - 3(\hat{\sigma} \cdot \hat{\rho}_{ss'})(\hat{\sigma}' \cdot \hat{\rho}_{ss'})]. \tag{4.6}$$

In the latter equation, we have defined $\boldsymbol{\rho}_{ss'} = \mathbf{R}'_{s'} - \mathbf{R}_s$. Such a quantity encapsulates the positions $\mathbf{R}'_{s'}$ of all nanoparticles neighboring the one located at $\mathbf{R}_s$ which allows us to change the summation over the positions $\mathbf{R}'_{s'}$ by a new one that runs over $\boldsymbol{\rho}_{ss'}$. Importantly, the vectors $\boldsymbol{\rho}_{ss'}$ link two nanoparticles which can belong to the same sublattice or to two different sublattices for the case of non-simple Bravais lattices (see Chapter 5). Moreover, exchanging the indices s and s' implies that $\boldsymbol{\rho}_{s's} = -\boldsymbol{\rho}_{ss'}$.

Second quantization procedure

Since our model aims to describe several purely quantum effects (e.g., the Landau damping) induced by the electronic environment, the plasmonic Hamiltonian (4.2) needs to be quantized. The

quantization is performed by introducing the bosonic operators

$$b_s^\sigma(\mathbf{R}_s) = \sqrt{\frac{\mathcal{N}_\mathrm{e} m_\mathrm{e}\omega_0}{2\hbar}} h_s^\sigma(\mathbf{R}_s) + \mathrm{i}\frac{\Pi_s^\sigma(\mathbf{R}_s)}{\sqrt{2\mathcal{N}_\mathrm{e} m_\mathrm{e}\hbar\omega_0}} \tag{4.7a}$$

and

$$b_s^{\sigma\dagger}(\mathbf{R}_s) = \sqrt{\frac{\mathcal{N}_\mathrm{e} m_\mathrm{e}\omega_0}{2\hbar}} h_s^\sigma(\mathbf{R}_s) - \mathrm{i}\frac{\Pi_s^\sigma(\mathbf{R}_s)}{\sqrt{2\mathcal{N}_\mathrm{e} m_\mathrm{e}\hbar\omega_0}}, \tag{4.7b}$$

where $b_s^\sigma(\mathbf{R}_s)$ [$b_s^{\sigma\dagger}(\mathbf{R}_s)$] annihilates [creates] an isolated plasmon polarized along the σ-direction on the nanoparticle belonging to a sublattice s and located at the position $\mathbf{R}_s$. Such ladder operators fulfill the usual bosonic commutation relations $[b_s^\sigma(\mathbf{R}_s), b_{s'}^{\sigma'\dagger}(\mathbf{R}'_{s'})] = \delta_{ss'}\delta_{\sigma\sigma'}\delta_{\mathbf{R}_s\mathbf{R}'_{s'}}$ and $[b_s^\sigma(\mathbf{R}_s), b_{s'}^{\sigma'}(\mathbf{R}'_{s'})] = [b_s^{\sigma\dagger}(\mathbf{R}_s), b_{s'}^{\sigma'\dagger}(\mathbf{R}'_{s'})] = 0$.

Using Eq. (4.7) into Eqs. (4.3) and (4.6), we thus obtain for the plasmonic Hamiltonian (4.2)

$$\begin{aligned} H_\mathrm{pl} = {} & \hbar\omega_0 \sum_s \sum_{\mathbf{R}_s} \sum_\sigma b_s^{\sigma\dagger}(\mathbf{R}_s) b_s^\sigma(\mathbf{R}_s) \\ & + \frac{\hbar\Omega}{2} \sum_{ss'} \sum_{\mathbf{R}_s} \sum_{\substack{\boldsymbol{\rho}_{ss'} \\ (\rho_{ss'}\neq 0)}} \sum_{\sigma\sigma'} \left(\frac{d}{\rho_{ss'}}\right)^3 [\delta_{\sigma\sigma'} - 3(\hat{\sigma}\cdot\hat{\rho}_{ss'})(\hat{\sigma}'\cdot\hat{\rho}_{ss'})] \\ & \times \left[b_s^\sigma(\mathbf{R}_s) + b_s^{\sigma\dagger}(\mathbf{R}_s)\right] \left[b_{s'}^{\sigma'}(\mathbf{R}_s + \boldsymbol{\rho}_{ss'}) + b_{s'}^{\sigma'\dagger}(\mathbf{R}_s + \boldsymbol{\rho}_{ss'})\right], \end{aligned} \tag{4.8}$$

with the coupling constant Ω given by Eq. (3.8) and where $\rho_{ss'}$ represents the norm of the vector $\boldsymbol{\rho}_{ss'}$. The latter Hamiltonian shows some similarities with a tight-binding Hamiltonian of an electronic two-dimensional system [107]. These similarities have been extensively discussed in Section 3.3.1 for the plasmonic Hamiltonian of a chain of nanoparticles. Identically to the Hamiltonian (3.36), the expression (4.8) displays as well important differences with respect to an electronic tight-binding Hamiltonian (e.g., the nature of the dipolar interaction as compared to the hopping amplitude and the interaction between the plasmons and the free photon field). Note that all these differences are fully presented in Sec. 3.3.1 for the one-dimensional case. However, since our model describes two-dimensional plasmonic systems, a crucial change appears in the expression (4.8) as compared to the one-dimensional Hamiltonian (3.36). Indeed, the two-dimensional nature of the system implies the appearance of a coupling between the single plasmons polarized within the plane of the metasurface terms [$\propto (\hat{x}\cdot\hat{\rho}_{ss'})(\hat{y}\cdot\hat{\rho}_{ss'})$ in Eq. (4.8)]. As we will see in Chapter 5, such in-plane modes lead in general to non-degenerate in-plane polarized collective modes resulting into three (for simple Bravais lattices) non-degenerate plasmonic bands. The aforementioned observation contrasts with the one-dimensional plasmonic chain where the transverse modes are fully degenerate (cf. Sec. 3.3.1).

4.1.2 Description of the environments in second quantization

We now turn to the description of the different environments to which the metasurface is coupled. Similarly to the previous section, we use a second quantization formalism to detail the two corre-

sponding coupling Hamiltonians. These photonic and electronic baths are described respectively by the second and third terms of the total Hamiltonian (4.1).

The photonic environment

The photonic bath is described by the term $H_{\rm ph}$ in Eq. (4.1). In the context of large metasurfaces we consider here, the vector potential $\mathbf{A}(\mathbf{r})$ given in Eq. (2.15) needs to be modified to account for the contributions of the photons of high energy in the first Brillouin zone. Thus, we first introduce the reciprocal vector $\mathbf{G} = n\mathbf{b}_1 + m\mathbf{b}_2$, where $\mathbf{b}_1$ and $\mathbf{b}_2$ are the two primitive lattice vectors in the reciprocal space and n and m are two integers. The vector potential is given by

$$\mathbf{A}(\mathbf{r}) = \sum_{\mathbf{k},\mathbf{G},\hat{\lambda}_{\mathbf{k}}} \sqrt{\frac{2\pi\hbar c^2}{\mathcal{V}\omega_{\mathbf{k},\mathbf{G}}}}\hat{\lambda}_{\mathbf{k}} \left(a_{\mathbf{k},\mathbf{G}}^{\hat{\lambda}_{\mathbf{k}}} \mathrm{e}^{\mathrm{i}(\mathbf{k}-\mathbf{G})\cdot\mathbf{r}} + a_{\mathbf{k},\mathbf{G}}^{\hat{\lambda}_{\mathbf{k}}\,\dagger} \mathrm{e}^{-\mathrm{i}(\mathbf{k}-\mathbf{G})\cdot\mathbf{r}} \right), \tag{4.9}$$

In Eq. (4.9), the operator $a_{\mathbf{k},\mathbf{G}}^{\hat{\lambda}_{\mathbf{k}}}$ ($a_{\mathbf{k},\mathbf{G}}^{\hat{\lambda}_{\mathbf{k}}\,\dagger}$) annihilates (creates) a photon with wavevector $\mathbf{k}$ in the first Brillouin zone, transverse polarization $\hat{\lambda}_{\mathbf{k}}$ and frequency $\omega_{\mathbf{k},\mathbf{G}} = c|\mathbf{k}-\mathbf{G}|$. In analogy with Eq. (2.16), the Hamiltonian associated with the photonic bath then reads

$$H_{\rm ph} = \sum_{\mathbf{k},\mathbf{G},\hat{\lambda}_{\mathbf{k}}} \hbar\omega_{\mathbf{k},\mathbf{G}} a_{\mathbf{k},\mathbf{G}}^{\hat{\lambda}_{\mathbf{k}}\,\dagger} a_{\mathbf{k},\mathbf{G}}^{\hat{\lambda}_{\mathbf{k}}}. \tag{4.10}$$

Nevertheless, for the purpose of obtaining analytical expressions for the photonic-induced quantities (cf. Chapter 6), we consider only the photons of minimal energy (i.e., for $\mathbf{G} = 0$) in the remainder of this manuscript. Therefore, the Hamiltonian (4.10) reduces to Eq. (2.16) given in Chapter 2.

The electronic environment

The electronic environment (i.e., the relative coordinate degrees of freedom) is taken into account through the third term $H_{\rm eh}$ of the Hamiltonian (4.1). With the center-of-mass and relative coordinate separation procedure [67, 118], such a term constitutes a direct generalization of Eq. (2.5) in the case of a metastructure. Similarly to the isolated nanoparticle, we neglect the correlations between the electrons (within each nanoparticle) and write, in second quantized form, the Hamiltonian of the electronic degrees of freedom within the mean-field approximation. Such a prescription thus yields

$$H_{\rm eh} = \sum_{s}\sum_{\mathbf{R}_s}\sum_{i} \epsilon_{\mathbf{R}_s i} c_{\mathbf{R}_s i}^{\dagger} c_{\mathbf{R}_s i}, \tag{4.11}$$

where the operator $c_{\mathbf{R}_s i}^{\dagger}$ ($c_{\mathbf{R}_s i}$) creates (annihilates) one single electronic state $|\mathbf{R}_s i\rangle$ with energy $\epsilon_{\mathbf{R}_s i}$ inside the nanoparticle located at $\mathbf{R}_s$ within the self-consistent potential $V_{\mathbf{R}_s}$. As we consider identical nanoparticles, the potential $V_{\mathbf{R}_s}$ reduces to V, the self-consistent potential of an isolated nanoparticle introduced in Sec. 2.2 and which we take as a hard-wall spherical potential.

4.1.3 The plasmon-bath coupling Hamiltonians

The two remaining terms of the Hamiltonian (4.1) encapsulate the coupling between the plasmonic system and the photonic and electronic baths, respectively. Identically to the electronic Hamiltonian (4.11) we derive each coupling Hamiltonians by generalizing to two dimensions their one-dimensional counterpart introduced for the plasmonic chain [see Eqs. (3.38) and (3.39) in Sec. 3.3.1]. Following such a prescription, we write the plasmon-photon coupling Hamiltonian $H_{\mathrm{pl-ph}}$ appearing into Eq. (4.1) in the dipolar approximation as

$$H_{\mathrm{pl-ph}} = \sum_{s} \sum_{\mathbf{R}_s} \left[\frac{e}{m_{\mathrm{e}} c} \mathbf{\Pi}_s(\mathbf{R}_s) \cdot \mathbf{A}(\mathbf{R}_s) + \frac{\mathcal{N}_{\mathrm{e}} e^2}{2 m_{\mathrm{e}} c^2} \mathbf{A}^2(\mathbf{R}_s) \right], \tag{4.12}$$

where the vector potential is defined in its quantized form in Eq. (2.15) and where the conjugate momentum $\mathbf{\Pi}_s(\mathbf{R}_s)$, using (4.7), is given by

$$\mathbf{\Pi}_s(\mathbf{R}_s) = \mathrm{i} \sqrt{\frac{\mathcal{N}_{\mathrm{e}} m_{\mathrm{e}} \hbar \omega_0}{2}} \sum_{\sigma} \hat{\sigma} \left[b_s^{\sigma\dagger}(\mathbf{R}_s) - b_s^{\sigma}(\mathbf{R}_s) \right]. \tag{4.13}$$

The second coupling Hamiltonian $H_{\mathrm{pl-eh}}$ introduced in Eq. (4.1) corresponds to the coupling between the electronic center-of-mass coordinates (i.e., the LSPs) and the relative ones. We write the Hamiltonian by generalizing the one corresponding to such a coupling in the case of a single particle (2.12) to two-dimensional metasurfaces. The coupling Hamiltonian thus reads as

$$H_{\mathrm{pl-eh}} = \Lambda \sum_{s} \sum_{\mathbf{R}_s} \sum_{\sigma} \sum_{ij} \left[b_s^{\sigma}(\mathbf{R}_s) + b_s^{\sigma\dagger}(\mathbf{R}_s) \right] \langle \mathbf{R}_s i | \sigma | \mathbf{R}_s j \rangle c^{\dagger}_{\mathbf{R}_s i} c_{\mathbf{R}_s j}, \tag{4.14}$$

where the constant Λ is given by Eq. (2.20).

4.2 Diagonalization of the plasmonic Hamiltonian

In order to make transparent the collective modes in the metasurface, we first diagonalize the plasmonic Hamiltonian (4.8).

4.2.1 Plasmonic Hamiltonian in wavevector space

Since we consider large arrays, it is convenient to treat the plasmonic Hamiltonian (4.8) within periodic boundary conditions and to move to wavevector space. We thus use the Fourier transform

$$b_s^{\sigma}(\mathbf{R}_s) = \frac{1}{\sqrt{\mathcal{N}}} \sum_{\mathbf{q}} \mathrm{e}^{\mathrm{i}\mathbf{q}\cdot\mathbf{R}_s} b_s^{\sigma}(\mathbf{q}), \tag{4.15a}$$

and

$$b_s^{\sigma\dagger}(\mathbf{R}_s) = \frac{1}{\sqrt{\mathcal{N}}} \sum_{\mathbf{q}} \mathrm{e}^{-\mathrm{i}\mathbf{q}\cdot\mathbf{R}_s} b_s^{\sigma\dagger}(\mathbf{q}), \tag{4.15b}$$

of the bosonic ladder operators $b_s^\sigma(\mathbf{R}_s)$ and $b_s^{\sigma\dagger}(\mathbf{R}_s)$ defined in Eq. (4.7). In Eq. (4.15), the operator $b_s^\sigma(\mathbf{q})$ [$b_s^{\sigma\dagger}(\mathbf{q})$] annihilates [creates] an isolated plasmon with a wavector $\mathbf{q}$ and polarized along the σ–direction on a nanoparticle belonging to the sublattice s, while $\mathcal{N} = \mathcal{N}_1\mathcal{N}_2 \gg 1$ denotes the total number of unit cells composing the lattice. Note that, in the latter equation, the wavevector $\mathbf{q}$ lives in a two-dimensional space similarly to the vector $\mathbf{R}_s$.

Inserting the expressions (4.15) into the plasmonic Hamiltonian (4.8) and making use of the relation $\sum_{\mathbf{qq}'} \exp[\mathrm{i}(\mathbf{q}-\mathbf{q}')\cdot\mathbf{R}_s] = \mathcal{N}\delta_{\mathbf{qq}'}$ [147], then leads to

$$\begin{aligned} H_{\mathrm{pl}} = \hbar\omega_0 \sum_{\mathbf{q}}\sum_{s}\sum_{\sigma} b_s^{\sigma\dagger}(\mathbf{q}) b_s^{\sigma}(\mathbf{q}) \\ + \frac{\hbar\Omega}{2}\sum_{\mathbf{q}}\sum_{ss'}\sum_{\sigma\sigma'}\left\{ f_{ss'}^{\sigma\sigma'}(\mathbf{q}) b_s^{\sigma\dagger}(\mathbf{q}) \left[b_{s'}^{\sigma'}(\mathbf{q}) + b_{s'}^{\sigma'\dagger}(-\mathbf{q}) \right] + \mathrm{h.c.} \right\}, \end{aligned} \tag{4.16}$$

where $\mathrm{h.c.}$ denotes the hermitian conjugate. In Eq. (4.16), the lattice sum

$$f_{ss'}^{\sigma\sigma'}(\mathbf{q}) = \sum_{\substack{\boldsymbol{\rho}_{ss'} \\ (\rho_{ss'}\neq 0)}} \left(\frac{d}{\rho_{ss'}}\right)^3 \mathrm{e}^{\mathrm{i}\mathbf{q}\cdot\boldsymbol{\rho}_{ss'}} [\delta_{\sigma\sigma'} - 3(\hat{\sigma}\cdot\hat{\rho}_{ss'})(\hat{\sigma}'\cdot\hat{\rho}_{ss'})] \tag{4.17}$$

takes into account the quasistatic dipole-dipole interaction between each pair of nanoparticles composing the metasurface. Such a function allows to investigate the effects of the long-range nature of the dipolar interaction on the collective plasmonic modes. Since we consider periodic boundary conditions, $f_{ss'}^{\sigma\sigma'}(\mathbf{q})$ is real for $s = s'$ due to the inversion symmetry of any Bravais lattices. Moreover, $f_{ss'}^{\sigma\sigma'}(\mathbf{q}) = [f_{s's}^{\sigma\sigma'}(\mathbf{q})]^*$ since we have $\boldsymbol{\rho}_{s's} = -\boldsymbol{\rho}_{ss'}$. In the remainder of this manuscript, we evaluate the lattice sum (4.17) numerically until satisfactory convergence is obtained.[1] Importantly, the plasmonic metasurfaces show (identically to the plasmonic chains, cf. Sec. 3.3.1) peculiar similarities with two-dimensional electronic systems since the Hamiltonian (4.16) resembles an electronic tight-binding Hamiltonian (written in wavevector space). Consequently, these similarities and more importantly, the differences (e.g., long-ranged anisotropic interactions and retardation effects) are those described in Section 3.3.1 for the chains of nanoparticles. Note however, that the lattice sum (4.17) is more complex that its equivalent for the chain [cf. Eq. (3.7)]. Such a complexity, e.g., the mixing of in-plane polarizations, originates from the dimensionality of the metasurfaces.

4.2.2 Diagonalization procedure

The plasmonic Hamiltonian (4.16) being quadratic, it can be diagonalized exactly. Such a procedure gives access to the collective plasmons which are the eigenmodes of the plasmonic system.

We perform the diagonalization of Eq. (4.16) by means of a bosonic Bogoliubov transformation. To this end, we introduce a new set of bosonic operators constructed as a linear combination of the

[1] Throughout this thesis, we calculate the lattice sums using a Python routine considering the interactions between the nanoparticles up to a distance of $300d$. Such an upper limit is chosen to ensure that for any array geometry, the relative difference between calculations with $n+1$ and n neighbors does not exceed 10^{-9}.

$b_s^\sigma(\mathbf{q})$ operators as

$$\beta_\tau^\varepsilon(\mathbf{q}) = \sum_{s=1}^{\mathcal{S}} \sum_{\sigma=x,y,z} \left[u_{\tau s}^{\varepsilon\sigma}(\mathbf{q}) b_s^\sigma(\mathbf{q}) + v_{\tau s}^{\varepsilon\sigma}(\mathbf{q}) b_s^{\sigma\dagger}(-\mathbf{q}) \right]. \tag{4.18}$$

The ladder operator above annihilates a collective plasmon with wavevector $\mathbf{q}$ in the band τ with polarization ε while its hermitian conjugate creates such a collective mode. We here point out that the polarization ε of the collective modes is, in general, a $\mathbf{q}$- and τ-dependent quantity [$\varepsilon \equiv \varepsilon_\tau(\mathbf{q})$] but we drop in the remainder of this work the both indices for notational simplicity.

In Eq. (4.18), $u_{\tau s}^{\varepsilon\sigma}(\mathbf{q})$ and $v_{\tau s}^{\varepsilon\sigma}(\mathbf{q})$ are complex coefficients which are determined imposing that H_{pl} is diagonal in this new basis, i.e.,

$$H_{\mathrm{pl}} = \sum_{\mathbf{q}} \sum_{\tau\varepsilon} H_\tau^\varepsilon(\mathbf{q}), \quad H_\tau^\varepsilon(\mathbf{q}) = \hbar\omega_\tau^\varepsilon(\mathbf{q}) \beta_\tau^{\varepsilon\dagger}(\mathbf{q}) \beta_\tau^\varepsilon(\mathbf{q}), \tag{4.19}$$

where $\omega_\tau^\varepsilon(\mathbf{q})$ is the collective plasmon dispersion relation. The Bogoliubov operators $\beta_\tau^\varepsilon(\mathbf{q})$ and $\beta_\tau^{\varepsilon\dagger}(\mathbf{q})$ act on an eigenstate $|n_\tau^\varepsilon(\mathbf{q})\rangle$ of the Hamiltonian $H_\tau^\varepsilon(\mathbf{q})$ corresponding to a collective plasmon in the band τ with wavevector $\mathbf{q}$ and polarization ε as $\beta_\tau^\varepsilon(\mathbf{q})|n_\tau^\varepsilon(\mathbf{q})\rangle = \sqrt{n_\tau^\varepsilon(\mathbf{q})}|n_\tau^\varepsilon(\mathbf{q})-1\rangle$ and $\beta_\tau^{\varepsilon\dagger}(\mathbf{q})|n_\tau^\varepsilon(\mathbf{q})\rangle = \sqrt{n_\tau^\varepsilon(\mathbf{q})+1}|n_\tau^\varepsilon(\mathbf{q})+1\rangle$, respectively. Here, $n_\tau^\varepsilon(\mathbf{q})$ is a non-negative integer.

Since the operators in (4.18) describe bosonic systems, they have to fulfill the usual bosonic commutation relations $[\beta_\tau^\varepsilon(\mathbf{q}), \beta_{\tau'}^{\varepsilon'\dagger}(\mathbf{q}')] = \delta_{\tau\tau'}\delta_{\varepsilon\varepsilon'}\delta_{\mathbf{q}\mathbf{q}'}$ and $[\beta_\tau^\varepsilon(\mathbf{q}), \beta_{\tau'}^{\varepsilon'}(\mathbf{q}')] = 0$. By substituting the expression (4.18) of these Bogoliubov operators into the commutation rules above, we then obtain the following conditions that the Bogoliubov coefficients need to fulfill. These relations read as

$$\sum_{s\sigma} \left[u_{\tau s}^{\varepsilon\sigma}(\mathbf{q}) u_{\tau' s}^{\varepsilon'\sigma *}(\mathbf{q}) - v_{\tau s}^{\varepsilon\sigma}(\mathbf{q}) v_{\tau' s}^{\varepsilon'\sigma *}(\mathbf{q}) \right] = \delta_{\tau\tau'}\delta_{\varepsilon\varepsilon'} \tag{4.20}$$

and

$$\sum_{s\sigma} \left[u_{\tau s}^{\varepsilon\sigma}(\mathbf{q}) v_{\tau' s}^{\varepsilon'\sigma *}(\mathbf{q}) - v_{\tau s}^{\varepsilon\sigma}(\mathbf{q}) u_{\tau' s}^{\varepsilon'\sigma *}(\mathbf{q}) \right] = 0, \tag{4.21}$$

where we have made use of the relations $u_{\tau s}^{\varepsilon\sigma *}(-\mathbf{q}) = u_{\tau s}^{\varepsilon\sigma}(\mathbf{q})$ and $v_{\tau s}^{\varepsilon\sigma *}(-\mathbf{q}) = v_{\tau s}^{\varepsilon\sigma}(\mathbf{q})$. Importantly, for $\tau = \tau'$ and $\varepsilon = \varepsilon'$, the expression (4.20) acts as a normalization condition for the Bogoliubov coefficients. Such a normalization condition reads

$$\sum_{s\sigma} \left[|u_{\tau s}^{\varepsilon\sigma}(\mathbf{q})|^2 - |v_{\tau s}^{\varepsilon\sigma}(\mathbf{q})|^2 \right] = 1 \tag{4.22}$$

We furthermore point out that such a condition reflects the bosonic nature of the plasmonic excitations. Indeed, in the case of fermionic pseudoparticles, the $-$ sign in Eq. (4.20) would be replaced by a $+$ sign. Such a difference has nevertheless important impact on the procedure we use to obtain the eigenvalues and eigenvectors numerically.

In order to extract the dispersion relation $\omega_\tau^\varepsilon(\mathbf{q})$ as well as the coefficients $u_{\tau s}^{\varepsilon\sigma}(\mathbf{q})$ and $v_{\tau s}^{\varepsilon\sigma}(\mathbf{q})$ introduced in (4.18), we apply the Heisenberg equation of motion for the Bogoliubov operator $\beta_\tau^\varepsilon(\mathbf{q})$ as

$$[\beta_\tau^\varepsilon(\mathbf{q}), H_{\mathrm{pl}}] = \hbar\omega_\tau^\varepsilon(\mathbf{q}) \beta_\tau^\varepsilon(\mathbf{q}). \tag{4.23}$$

We then substitute into Eq. (4.23) the expressions of the plasmonic Hamiltonian $H_{\rm pl}$ and of the operator $\beta_\tau^\varepsilon(\mathbf{q})$ given by Eqs. (4.16) and (4.18), respectively. We therefore obtain the relation

$$\begin{aligned}[\beta_\tau^\varepsilon(\mathbf{q}), H_{\rm pl}] &= \hbar\omega_0 \sum_{s\sigma} \left[u_{\tau s}^{\varepsilon\sigma}(\mathbf{q}) b_s^\sigma(\mathbf{q}) - v_{\tau s}^{\varepsilon\sigma}(\mathbf{q}) b_s^{\sigma\dagger}(-\mathbf{q}) \right] \\ &\quad + \hbar\Omega \sum_{\substack{s\sigma \\ s'\sigma'}} \left[u_{\tau s}^{\varepsilon\sigma}(\mathbf{q}) - v_{\tau s}^{\varepsilon\sigma}(\mathbf{q}) \right] f_{ss'}^{\sigma\sigma'}(\mathbf{q}) \left[b_{s'}^{\sigma'}(\mathbf{q}) + b_{s'}^{\sigma'\dagger}(-\mathbf{q}) \right] \\ &\stackrel{!}{=} \hbar\omega_\tau^\varepsilon(\mathbf{q}) \sum_{s\sigma} \left[u_{\tau s}^{\varepsilon\sigma}(\mathbf{q}) b_{s'}^{\sigma'}(\mathbf{q}) + v_{\tau s}^{\varepsilon\sigma}(\mathbf{q}) b_{s'}^{\sigma'\dagger}(-\mathbf{q}) \right], \end{aligned} \tag{4.24}$$

where we have used the identity $[f_{s's}^{\sigma\sigma'}(\mathbf{q})]^* = f_{ss'}^{\sigma\sigma'}(\mathbf{q})$. Rearranging the terms in Eq. (4.24) then yields the equality

$$\begin{aligned}&\sum_{s'\sigma'} \left\{ \left[\omega_0 - \omega_\tau^\varepsilon(\mathbf{q}) \right] u_{\tau s'}^{\varepsilon\sigma'}(\mathbf{q}) + \Omega \sum_{s\sigma} \left[u_{\tau s}^{\varepsilon\sigma}(\mathbf{q}) - v_{\tau s}^{\varepsilon\sigma}(\mathbf{q}) \right] f_{ss'}^{\sigma\sigma'}(\mathbf{q}) \right\} b_{s'}^{\sigma'}(\mathbf{q}) \\ &+ \sum_{s'\sigma'} \left\{ \left[-\omega_0 - \omega_\tau^\varepsilon(\mathbf{q}) \right] v_{\tau s'}^{\varepsilon\sigma'}(\mathbf{q}) + \Omega \sum_{s\sigma} \left[u_{\tau s}^{\varepsilon\sigma}(\mathbf{q}) - v_{\tau s}^{\varepsilon\sigma}(\mathbf{q}) \right] f_{ss'}^{\sigma\sigma'}(\mathbf{q}) \right\} b_{s'}^{\sigma'\dagger}(-\mathbf{q}) = 0. \end{aligned} \tag{4.25}$$

The equation above can thus only hold if the system of equations

$$\left[\omega_0 - \omega_\tau^\varepsilon(\mathbf{q}) \right] u_{\tau s}^{\varepsilon\sigma}(\mathbf{q}) + \Omega \sum_{s'\sigma'} \left[u_{\tau s'}^{\varepsilon\sigma'}(\mathbf{q}) - v_{\tau s'}^{\varepsilon\sigma'}(\mathbf{q}) \right] f_{s's}^{\sigma'\sigma}(\mathbf{q}) = 0 \tag{4.26a}$$

and

$$-\left[\omega_0 + \omega_\tau^\varepsilon(\mathbf{q}) \right] v_{\tau s}^{\varepsilon\sigma}(\mathbf{q}) + \Omega \sum_{s'\sigma'} \left[u_{\tau s'}^{\varepsilon\sigma'}(\mathbf{q}) - v_{\tau s'}^{\varepsilon\sigma'}(\mathbf{q}) \right] f_{s's}^{\sigma'\sigma}(\mathbf{q}) = 0 \tag{4.26b}$$

is fulfilled for all integer $s \in [1, \mathcal{S}]$ and all polarizations $\sigma = x, y, z$. Such a requirement leads to a $6\mathcal{S} \times 6\mathcal{S}$ eigensystem to solve. Due to the structure of the lattice sum $f_{ss'}^{\sigma\sigma'}(\mathbf{q})$ defined in Eq. (4.17) implying that $f_{ss'}^{xz} = f_{ss'}^{yz} = 0$, such an eigensystem can be decoupled into a block-diagonal matrix composed of a $4\mathcal{S} \times 4\mathcal{S}$ and a $2\mathcal{S} \times 2\mathcal{S}$ block, corresponding to the in-plane (IP) (with $\sigma = x, y$) and out-of-plane (OP) (with $\sigma = z$) polarized modes, respectively. Each block then yields a secular equation of order $2\mathcal{S}$ and $\mathcal{S}$ in $[\omega_\tau^\varepsilon(\mathbf{q})]^2$, respectively, which allows us to derive the quasistatic plasmonic bandstructure.

Practically, the system of equations (4.26) can be only used for systems with small number s of sublattices. Although Eq. (4.26) may provide a powerful tool to derive analytic expressions for all quantities depending on the eigenfrequencies and eigenmodes, solving analytically the above system become rapidly a formidable task and thus restricted to simple Bravais structures (e.g., square or hexagonal lattices) and to specific situations. Indeed, apart from the mathematical difficulty to solve (analytically) an eigensystem with large dimension ($\mathcal{S} = 3, 4$ for $\sigma = z$ and $\mathcal{S} = 2$ for $\sigma = x, y$, respectively), the size of a tractable eigensystem is theoretically limited by the order of its secular equation which cannot exceed an order of 4 since the Abel-Ruffini theorem states that no algebraic solutions can be found for general polynomial equations (with arbitrary coefficients) of degree 5 or higher. Even though the analytical resolution of Eq. (4.26) cannot be performed for arrays with $\mathcal{S} = 5$ sublattices, the mathematical difficulties one may encounter when dealing with

metasurfaces with smaller number of sublattices can be reduced. To do so, one may employ an alternative diagonalization procedure based on a perturbative approach. We provide such a procedure in Sec. D.

In the next chapter of this manuscript, we systematically derive analytically the quasistatic plasmonic dispersion relations $\omega_\tau^\varepsilon(\mathbf{q})$ and the associated Bogoliubov coefficients $u_{\tau s}^{\varepsilon\sigma}(\mathbf{q})$ and $v_{\tau s}^{\varepsilon\sigma}(\mathbf{q})$ whenever such a task remains tractable mathematically. Therefore, in the following, we treat analytically the out-of-plane polarized collective modes ($\varepsilon = z$) for Bravais ($\mathcal{S} = 1$) and bipartite ($\mathcal{S} = 2$) lattices. We further obtain analytic expressions for the latter quantities for in-plane polarized modes ($\varepsilon = \varepsilon_\parallel$) in Bravais lattices. In the remainder of the manuscript, the quantity $\varepsilon_\parallel$ denotes the in-plane polarization of the collective plasmon. Finally, Eq. (4.26) allows us to derive the plasmonic bandstructures analytically in specific cases that are for the out-of-plane modes of tripartite ($\mathcal{S} = 3$) lattices and in-plane modes in bipartite lattices assuming nearest-neighbors dipole-dipole coupling only.

In all the other cases we will treat in this thesis, the plasmonic bandstructures as well as the Bogoliubov coefficients are evaluated numerically. Although the latter quantities can be obtained by directly solving the system (4.26) together with the bosonic normalization conditions (4.20), we have chosen to use an alternative numerical algorithm based on the Cholesky decomposition [159, 160] in order to systematize the diagonalization procedure. Such an alternative also allows to include directly the bosonic normalization condition while solving the eigensystem. We provide the full algorithm in Appendix C.

Alternatively to the exact diagonalization given above, we may also employ a perturbative approach to obtain the plasmonic dispersion relations $\omega_\tau^\varepsilon(\mathbf{q})$ and the Bogoliubov coefficients $u_{\tau s}^{\varepsilon\sigma}(\mathbf{q})$ and $v_{\tau s}^{\varepsilon\sigma}(\mathbf{q})$. Such a procedure given in Appendix D, allows to evaluate separately the coefficients $u_{\tau s}^{\varepsilon\sigma}(\mathbf{q})$ and $v_{\tau s}^{\varepsilon\sigma}(\mathbf{q})$ in the regime $\Omega \ll \omega_0$.

4.3 Polarization of the plasmonic modes

One particular quantity depending on the Bogoliubov coefficients $u_{\tau s}^{\varepsilon\sigma}(\mathbf{q})$ and $v_{\tau s}^{\varepsilon\sigma}(\mathbf{q})$ provides a useful insight on the nature of the collective plasmons, that is the polarization angle $\phi_\tau^\varepsilon(\mathbf{q})$ of a given mode. Such a polarization corresponds to the projection of the total dipolar moment, $\propto \sum_\sigma [\beta_\tau^\varepsilon(\mathbf{q}) + \beta_\tau^{\varepsilon\dagger}(\mathbf{q})]\hat{\sigma}$ associated with the eigenstates to the wavevector $\mathbf{q}$ of the first Brillouin zone. To access the latter angle, we first introduce two vectors as

$$\mathbf{u}_\tau^\varepsilon(\mathbf{q}) = \begin{pmatrix} \sum_s u_{\tau s}^{\varepsilon x}(\mathbf{q}) \\ \sum_s u_{\tau s}^{\varepsilon y}(\mathbf{q}) \\ \sum_s u_{\tau s}^{\varepsilon z}(\mathbf{q}) \end{pmatrix} \tag{4.27a}$$

and

$$\mathbf{v}_\tau^\varepsilon(\mathbf{q}) = \begin{pmatrix} \sum_s v_{\tau s}^{\varepsilon x}(\mathbf{q}) \\ \sum_s v_{\tau s}^{\varepsilon y}(\mathbf{q}) \\ \sum_s v_{\tau s}^{\varepsilon z}(\mathbf{q}) \end{pmatrix}. \tag{4.27b}$$

The two vectors (4.27a) and (4.27b) can be seen as a result of the vector summation of each contribution $u_{\tau s}^{\varepsilon\sigma}(\mathbf{q})$ and $v_{\tau s}^{\varepsilon\sigma}(\mathbf{q})$ coming from the dipolar moments of the individual LSPs located on

sublattice s in each direction of space σ. The polarization angle $\phi_\tau^\varepsilon(\mathbf{q})$ thus corresponds to the angle between the wavevector $\mathbf{q}$ along which the collective plasmonic mode propagates and the orientation of its associated dipolar moment [which is collinear to the vector $\mathbf{u}_\tau^\varepsilon(\mathbf{q})$]. The angle $\phi_\tau^\varepsilon(\mathbf{q})$ is defined as [139]

$$\phi_\tau^\varepsilon(\mathbf{q}) = \arccos(|\hat{u}_\tau^\varepsilon(\mathbf{q}) \cdot \hat{q}|). \tag{4.28}$$

Note that the above definition of the polarization angle is not unique since one may substitute the Bogoliubov coefficient $\hat{u}_\tau^\varepsilon(\mathbf{q})$ by $\hat{v}_\tau^\varepsilon(\mathbf{q})$ in Eq. (4.28). In Chapter 5, we will give a brief example where this assumption can be verified using the plasmonic eigenstates associated to the square lattice which we evaluate analytically.

Importantly, the polarization angle (4.28) can take particular values corresponding to specific polarizations. In the case of the out-of-plane polarized modes ($\varepsilon = z$), we have necessarily $\phi_\tau^z(\mathbf{q}) = \pi/2$ as expected since we have simultaneously $u_{\tau s}^{zx}(\mathbf{q}) = u_{\tau s}^{zy}(\mathbf{q}) = 0$ and $q_z = 0$ so that the collective plasmons are purely transversely polarized. For the in-plane polarized modes ($\varepsilon = \varepsilon_\parallel$), the situation is more complex. Indeed, three different classes of polarization may appear for such modes. First, the angle (4.28) can be equal to $\pi/2$ corresponding to purely transverse polarized modes within the plane of the metasurface. Second, the modes can be purely longitudinally polarized (i.e. $\hat{u}_\tau^{\varepsilon_\parallel}(\mathbf{q})$ collinear to the wavevector $\mathbf{q}$) implying $\phi_\tau^{\varepsilon_\parallel}(\mathbf{q}) = 0$. Finally the situation for which $\phi_\tau^{\varepsilon_\parallel}(\mathbf{q}) \in]0, \pi/2[$ corresponds to modes with a mixed polarization which is neither transverse nor longitudinal (with respect to the wavevector $\mathbf{q}$).

4.4 Conclusion for Chapter 4

In this chapter, we have introduced our theoretical framework to study the collective plasmonic modes in generic two-dimensional metasurfaces constituted by a periodic assembly of spherical metallic nanoparticles. Toward this end, we have considered the arbitrary array composed of a Bravais lattice with a basis describing all kinds of periodic plasmonic metasurfaces. Then, similarly to the plasmonic chain [80, 135], we have used an approach based on the decomposition of the electronic degrees of freedom of each nanoparticle into center-of-mass and relative coordinates, in order to derived the Hamiltonian describing the plasmonic modes within the framework of an open-quantum system. We then wrote such a Hamiltonian, composed of on-site energy terms and a interaction ones (taking into account all dipole-dipole interactions between each pairs of nanoparticles) in the second quantization formalism using bosonic ladder operators.

Together with the plasmonic Hamiltonian $H_{\rm pl}$, we have also derived, in second quantized form, the two Hamiltonians characterizing the photonic and electronic baths to which the plasmonic system is coupled to. Finally, we have given the second quantized Hamiltonians corresponding to the couplings between the plasmonic modes and the two environments. Such coupling Hamiltonians are reminiscent of Eqs. (3.38) and (3.39) introduced in Sec. 3.3.1 since they amount for the generalization to two dimension of the plasmonic chain.

Then, we have presented the exact diagonalization procedure of the plasmonic Hamiltonian (4.8) with the help of a Bogoliubov transformation. Starting from the plasmonic Hamiltonian written in wavevector space, we have introduced new Bogoliubov bosonic operators (4.18) which diagonalize exactly $H_{\rm pl}$ [cf. Eq. (4.19)]. Afterwards, using the Heisenberg equation of motion for

the Bogoliubov operators, we have derived a system of equations leading to a $6\mathcal{S} \times 6\mathcal{S}$ eigensystem. Such a system, once solved, gives access to the dispersion relations and the plasmonic eigenstates which then can be used to evaluate the quantities induced by the various environments (i.e., damping rates and frequency shifts).

Finally, we have discussed the polarization of the collective plasmons for the out-of-plane and in-plane polarized modes. Such a quantity provides an interesting insight on the behavior of the plasmonic modes with respect to the photonic-induced processes (cf. Chapter 6).

Armed with the tools introduced in this chapter, we are now able to investigate the various properties of the collective plasmonic modes for specific arrays. In the following chapter, we will concentrate on the dispersion relations of simple Bravais, bipartite and tripartite lattices including the long-range quasistatic interactions only. The effects of the photonic and electronic baths on such dispersion relations will have their own dedicated chapters in the manuscript.

Chapter 5

Quasistatic plasmonic bandstructure

In this chapter, we concentrate on the quasistatic bandstructure of the plasmonic subsystem described by the Hamiltonian (4.16) for arbitrary two-dimensional metasurfaces. These dispersion relations are obtained by solving analytically (or numerically whenever it is necessary) the system of equations (4.26) introduced in Chapter 4. In particular, we study the influence of the long-range nature of the dipolar interactions responsible for the appearance of the collective modes with respect to the nearest-neighbor approximation. The first part of the chapter is dedicated to the study of simple Bravais lattices. We first develop general analytic results for the out-of-plane and in-plane modes which can be applied to any (2D) Bravais lattices. Then, we illustrate these results with various examples. The second section is devoted to bipartite lattices, while the last one to tripartite arrays. In both sections, we first present general results and then illustrate the results with well-known examples (honeycomb, Lieb and kagome lattices) presenting appealing topological properties.

5.1 Metasurfaces based on simple Bravais lattices

Before analyzing metasurfaces with more complex geometries, we begin this chapter by solving fully analytically the eigensystem (4.26) for simple Bravais lattices. Although such lattices do not present topological properties, they constitute a perfect playground to understand several crucial features arising from the long-range dipolar interactions.

5.1.1 Arbitrary Bravais lattices

As a starting point for studying the metasurfaces with arbitrary Bravais geometries, we consider the general lattice presented in Section 4.1 in the limit where the number of sublattices reduces to $\mathcal{S} = 1$. In such a situation, the sublattice indices s and s' as well as the band index τ are irrelevant and can then be dropped in the upcoming calculations. As stated in the previous chapter, the structure of the lattice sum (4.17) allows to fully decouple the out-of-plane and in-plane polarized modes. Therefore, we are able to derive the out-of-plane (in-plane) plasmonic eigenfrequencies and eigenvectors using the system of equation (4.26) for $\sigma = z$ ($\sigma = x, y$) only.

Derivation of the out-of-plane polarized collective plasmons

For $\mathcal{S} = 1$ and $\sigma = \varepsilon = z$, Eq. (4.26) reduces to a 2×2 eigensystem which we can solve fully analytically. Such an eigensystem reads

$$\boldsymbol{\mathcal{D}}_1^z(\mathbf{q}) \begin{pmatrix} u^{zz}(\mathbf{q}) \\ v^{zz}(\mathbf{q}) \end{pmatrix} = \begin{pmatrix} \varsigma^{zz}(\mathbf{q}) - \omega^z(\mathbf{q}) & -\Omega f^{zz}(\mathbf{q}) \\ \Omega f^{zz}(\mathbf{q}) & -\varsigma^{zz}(\mathbf{q}) - \omega^z(\mathbf{q}) \end{pmatrix} \begin{pmatrix} u^{zz}(\mathbf{q}) \\ v^{zz}(\mathbf{q}) \end{pmatrix} = 0 \tag{5.1}$$

where we have defined

$$\varsigma^{\sigma\sigma}(\mathbf{q}) = \omega_0 + \Omega f_{11}^{\sigma\sigma}(\mathbf{q}) \tag{5.2}$$

for $\sigma = x, y$ and z. In the latter equation, and in the remaining of this chapter, we denote $\boldsymbol{\mathcal{D}}_{\mathcal{S}}^{\varepsilon}(\mathbf{q})$ the matrix extracted from Eq. (4.26). Thus, for Eq. (5.1), we have $\mathcal{S} = 1$ and $\varepsilon = z$.

Then, evaluating $\mathrm{Det}[\boldsymbol{\mathcal{D}}_1^z(\mathbf{q})] = 0$ yields immediately [using Eq. (5.2)] the dispersion relation [161]

$$\omega^z(\mathbf{q}) = \omega_0 \sqrt{1 + 2\frac{\Omega}{\omega_0} f^{zz}(\mathbf{q})}. \tag{5.3}$$

The Bogoliubov coefficients $u^{zz}(\mathbf{q})$ and $v^{zz}(\mathbf{q})$ are straightforwardly calculated using (5.1) together with the normalization condition (4.20). For simple Bravais lattices, considering perpendicular polarized modes ($\sigma = z$) the condition (4.20) reduces to

$$|u^{zz}(\mathbf{q})|^2 - |v^{zz}(\mathbf{q})|^2 = 1. \tag{5.4}$$

Then, we notice that making use of Eq. (4.26), we have the relation

$$[\omega_0 - \omega^{\varepsilon}(\mathbf{q})]\, u_{\tau s}^{\varepsilon\sigma}(\mathbf{q}) = [\omega_0 + \omega^{\varepsilon}(\mathbf{q})]\, v_{\tau s}^{\varepsilon\sigma}(\mathbf{q}) \tag{5.5}$$

between the two Bogoliubov coefficients. In the present case, we use (5.5) within the limit $\mathcal{S} = 1$ and $\sigma = \varepsilon = z$. The latter relation can also be derived directly from the system (5.1). Finally, inserting (5.5) into (5.4) and choosing the positive root for $u^{zz}(\mathbf{q})$ gives for the coefficients

$$u^{zz}(\mathbf{q}) = \frac{\omega^z(\mathbf{q}) + \omega_0}{2\sqrt{\omega_0 \omega^z(\mathbf{q})}} \tag{5.6a}$$

and

$$v^{zz}(\mathbf{q}) = \frac{\omega^z(\mathbf{q}) - \omega_0}{2\sqrt{\omega_0 \omega^z(\mathbf{q})}}. \tag{5.6b}$$

Note that, we have to first order in the limit $\Omega \ll \omega_0$ (which constitutes our regime of interest) $\omega^z(\mathbf{q}) \simeq \omega_0 + \Omega f^{zz}(\mathbf{q})$ leading to $u^{zz}(\mathbf{q}) \simeq 1$ and $v^{zz}(\mathbf{q}) \simeq (\Omega/2\omega_0) f^{zz}(\mathbf{q})$. Such approximated results correspond exactly to those obtained with the diagonalization procedure of the plasmonic Hamiltonian (D.1) within a perturbative treatment (cf. Sec. D). Importantly, the "selection rules" which dictates that $u^{z\sigma}(\mathbf{q}) = v^{z\sigma}(\mathbf{q}) = 0$ for $\sigma = x, y$ imply that the polarization vector $\hat{u}^z(\mathbf{q})$ defined in Eq. (4.27a) is equivalent to $\hat{v}^z(\mathbf{q})$ [cf. Eq. (4.27b)] and reads, using the expression (5.6) for the Bogoliubov coefficients, $\hat{u}^z(\mathbf{q}) = (0, 0, 1)$ as expected. Consequently, the polarization angle

$\phi^z(\mathbf{q})$ [see Eq. (4.28)] takes the value

$$\phi^z(\mathbf{q}) = \pi/2 \tag{5.7}$$

corresponding indeed to purely transverse collective modes.

In-plane polarized collective plasmons

Since we consider two-dimensional arrays with arbitrary geometries, the coupling between the LSPs polarized within the plane ($\sigma = x, y$) leads to collective plasmon with mixed polarization (not necessarily along a particular axis σ) contrary to the out-plane modes. Therefore, we denote such in-plane polarization $\varepsilon_\parallel$. Applying Eq. (4.26) for $\mathcal{S} = 1$ and $\sigma = x, y$ thus yields the eigensystem

$$\boldsymbol{\mathcal{D}}_1^{\varepsilon_\parallel}(\mathbf{q}) \begin{pmatrix} u^{\varepsilon_\parallel x}(\mathbf{q}) \\ v^{\varepsilon_\parallel x}(\mathbf{q}) \\ u^{\varepsilon_\parallel y}(\mathbf{q}) \\ v^{\varepsilon_\parallel y}(\mathbf{q}) \end{pmatrix} = 0 \tag{5.8}$$

with

$$\boldsymbol{\mathcal{D}}_1^{\varepsilon_\parallel}(\mathbf{q}) = \begin{pmatrix} \varsigma^{xx}(\mathbf{q}) - \omega^{\varepsilon_\parallel}(\mathbf{q}) & -\Omega f^{xx}(\mathbf{q}) & \Omega f^{xy}(\mathbf{q}) & -\Omega f^{xy}(\mathbf{q}) \\ \Omega f^{xx}(\mathbf{q}) & -\varsigma^{xx}(\mathbf{q}) - \omega^{\varepsilon_\parallel}(\mathbf{q}) & \Omega f^{xy}(\mathbf{q}) & -\Omega f^{xy}(\mathbf{q}) \\ \Omega f^{xy}(\mathbf{q}) & -\Omega f^{xy}(\mathbf{q}) & \varsigma^{yy}(\mathbf{q}) - \omega^{\varepsilon_\parallel}(\mathbf{q}) & -\Omega f^{yy}(\mathbf{q}) \\ \Omega f^{xy}(\mathbf{q}) & -\Omega f^{xy}(\mathbf{q}) & \Omega f^{yy}(\mathbf{q}) & -\varsigma^{yy}(\mathbf{q}) - \omega^{\varepsilon_\parallel}(\mathbf{q}) \end{pmatrix}. \tag{5.9}$$

From the condition $\mathrm{Det}[\boldsymbol{\mathcal{D}}_1^{\varepsilon_\parallel}(\mathbf{q})] = 0$, we get the relation

$$\Big\{ [\omega^{\varepsilon_\parallel}(\mathbf{q})]^2 - \omega_0^2 - 2\omega_0 \Omega f^{xx}(\mathbf{q}) \Big\} \Big\{ [\omega^{\varepsilon_\parallel}(\mathbf{q})]^2 - \omega_0^2 - 2\omega_0 \Omega f^{yy}(\mathbf{q}) \Big\} = [2\omega_0 \Omega f^{xy}(\mathbf{q})]^2 \tag{5.10}$$

that the plasmonic eigenfrequencies $\omega^{\varepsilon_\parallel}(\mathbf{q})$ need to fulfill. From Eq. (5.10) being quadratic in $[\omega^{\varepsilon_\parallel}(\mathbf{q})]^2$, we obtain immediately the two (real) positive roots as [161]

$$\omega^{\varepsilon_\parallel,\pm}(\mathbf{q}) = \omega_0 \left\{ 1 + \frac{\Omega}{\omega_0} \left[f^{xx}(\mathbf{q}) + f^{yy}(\mathbf{q}) \pm \sqrt{[f^{xx}(\mathbf{q}) - f^{yy}(\mathbf{q})]^2 + 4\,[f^{xy}(\mathbf{q})]^2} \right] \right\}^{1/2}. \tag{5.11}$$

Notice that when $f^{xy}(\mathbf{q}) = 0$, we have $\varepsilon_{\parallel,\pm} = x, y$ (such a situation occurs for instance in the square lattice within the nearest-neighbor approximation). The Bogoliubov coefficients $u^{\varepsilon_\parallel \sigma}(\mathbf{q})$ and $v^{\varepsilon_\parallel \sigma}(\mathbf{q})$ (with $\sigma = x, y$) are obtained inserting Eq. (5.5) applied for $\sigma = x, y$ (and $\mathcal{S} = \tau = 1$) into (5.8) and using the normalization condition

$$|u^{\varepsilon_\parallel x}(\mathbf{q})|^2 + |u^{\varepsilon_\parallel y}(\mathbf{q})|^2 - |v^{\varepsilon_\parallel x}(\mathbf{q})|^2 - |v^{\varepsilon_\parallel y}(\mathbf{q})|^2 = 1. \tag{5.12}$$

Performing these steps thus yields, using the condition (5.10), the Bogoliubov coefficients

$$u^{\varepsilon_\parallel,\pm x}(\mathbf{q}) = \frac{\omega^{\varepsilon_\parallel,\pm}(\mathbf{q}) + \omega_0}{2\sqrt{\omega_0 \omega^{\varepsilon_\parallel,\pm}(\mathbf{q})}} \sqrt{\frac{\zeta_\pm^y(\mathbf{q})}{\zeta_\pm^x(\mathbf{q}) + \zeta_\pm^y(\mathbf{q})}}, \tag{5.13a}$$

$$u^{\varepsilon_{\parallel},\pm y}(\mathbf{q}) = \pm \mathrm{sgn}\left\{f^{xy}(\mathbf{q})\right\} \frac{\omega^{\varepsilon_{\parallel},\pm}(\mathbf{q}) + \omega_0}{2\sqrt{\omega_0 \omega^{\varepsilon_{\parallel},\pm}(\mathbf{q})}} \sqrt{\frac{\zeta_{\pm}^{x}(\mathbf{q})}{\zeta_{\pm}^{x}(\mathbf{q}) + \zeta_{\pm}^{y}(\mathbf{q})}}, \tag{5.13b}$$

and

$$v^{\varepsilon_{\parallel},\pm x}(\mathbf{q}) = \frac{\omega^{\varepsilon_{\parallel},\pm}(\mathbf{q}) - \omega_0}{2\sqrt{\omega_0 \omega^{\varepsilon_{\parallel},\pm}(\mathbf{q})}} \sqrt{\frac{\zeta_{\pm}^{y}(\mathbf{q})}{\zeta_{\pm}^{x}(\mathbf{q}) + \zeta_{\pm}^{y}(\mathbf{q})}}, \tag{5.14a}$$

$$v^{\varepsilon_{\parallel},\pm y}(\mathbf{q}) = \pm \mathrm{sgn}\left\{f^{xy}(\mathbf{q})\right\} \frac{\omega^{\varepsilon_{\parallel},\pm}(\mathbf{q}) - \omega_0}{2\sqrt{\omega_0 \omega^{\varepsilon_{\parallel},\pm}(\mathbf{q})}} \sqrt{\frac{\zeta_{\pm}^{x}(\mathbf{q})}{\zeta_{\pm}^{x}(\mathbf{q}) + \zeta_{\pm}^{y}(\mathbf{q})}}, \tag{5.14b}$$

where we have defined

$$\zeta_{\pm}^{\sigma}(\mathbf{q}) = \left[\omega^{\varepsilon_{\parallel},\pm}(\mathbf{q})\right]^2 - \omega_0^2 - 2\omega_0 \Omega f^{\sigma\sigma}(\mathbf{q}). \tag{5.15}$$

With the expression of the Bogoliubov coefficients (5.13), we may compute exactly the vector $\mathbf{u}^{\varepsilon_{\parallel}}$ given in Eq. (4.27a) which thus reads

$$\mathbf{u}^{\varepsilon_{\parallel},\pm} = \frac{\omega^{\varepsilon_{\parallel},\pm}(\mathbf{q}) + \omega_0}{2\sqrt{\omega_0 \omega^{\varepsilon_{\parallel},\pm}(\mathbf{q})}} \begin{pmatrix} \sqrt{\frac{\zeta_{\pm}^{y}(\mathbf{q})}{\zeta_{\pm}^{x}(\mathbf{q})+\zeta_{\pm}^{y}(\mathbf{q})}} \\ \pm \mathrm{sgn}\left\{f^{xy}(\mathbf{q})\right\} \sqrt{\frac{\zeta_{\pm}^{x}(\mathbf{q})}{\zeta_{\pm}^{x}(\mathbf{q})+\zeta_{\pm}^{y}(\mathbf{q})}} \\ 0 \end{pmatrix}. \tag{5.16}$$

Substituting the latter expression into Eq. (4.28) yields for the polarization angle for the in-plane polarized modes the general expression

$$\phi^{\varepsilon_{\parallel},\pm}(\mathbf{q}) = \arccos\left(\frac{q_x}{|\mathbf{q}|} \sqrt{\frac{\zeta_{\pm}^{y}(\mathbf{q})}{\zeta_{\pm}^{x}(\mathbf{q}) + \zeta_{\pm}^{y}(\mathbf{q})}} \pm \mathrm{sgn}\left\{f^{xy}(\mathbf{q})\right\} \frac{q_y}{|\mathbf{q}|} \sqrt{\frac{\zeta_{\pm}^{x}(\mathbf{q})}{\zeta_{\pm}^{x}(\mathbf{q}) + \zeta_{\pm}^{y}(\mathbf{q})}} \right), \tag{5.17}$$

where $\zeta_{\pm}^{\sigma}(\mathbf{q})$ is given in Eq. (5.15) for $\sigma = x, y$.

Importantly, the eigenfrequencies (5.3) [(5.11)], the associated Bogoliubov coefficients (5.6) [(5.13) and (5.14)] as well as the associated polarization angle (5.7) [(5.17)] for the out-of-plane [in-plane] polarized modes are valid for any two-dimensional simple Bravais lattices. Note that, according to the crystallography [162], only five different classes of Bravais lattices exist in two dimensions.[1]

5.1.2 The square lattice

As an illustration of application of the general method presented above for obtaining the quasistatic bandstructure of the plasmonic modes in generic Bravais lattices, we consider in the following the simple square lattice. The square lattice sketched in Fig. 5.1(a) is defined by the two lattice vectors $\mathbf{t}_1 = d(1,0)$ and $\mathbf{t}_2 = d(0,1)$. The corresponding first Brillouin zone, depicted in Fig. 5.1(b), has for reciprocal vectors $\mathbf{b}_1 = \frac{2\pi}{d}(1,0)$ and $\mathbf{b}_2 = \frac{2\pi}{d}(0,1)$. In the figure, the red bold lines in

[1] In two dimensions, the five classes of Bravais lattices are the oblique, the square, the centered-square, the rectangular and the hexagonal lattices.

the sketch of the first Brillouin zone highlight the high symmetry lines of the square lattice along which the plasmonic bandstructure is shown (identically to the electronic bandstructure in tight-binding systems [60]). Such dispersion relations are plotted for the square in Figs. 5.1(c) and 5.1(d) for the plasmonic modes polarized perpendicularly [Eq. (5.3)] and within the plane [Eq. (5.11)], respectively.[2]

Out-of-plane modes

As can be seen from Fig. 5.1(c), the plasmonic bandstructure considering only dipolar interactions between nearest neighbors (nn) in the lattice (dashed lines), for which the lattice sum (4.17) reduces to

$$f^{zz}_{\mathrm{nn}}(\mathbf{q}) = 2\left[\cos(q_x d) + \cos(q_y d)\right], \tag{5.18}$$

reproduced qualitatively the quasistatic dispersion $\omega^z(\mathbf{q})$ [Eq. (5.3)] (black lines) in most of the first Brillouin zone, except for wavevectors close to the Γ point. In such a region, we clearly observe a pronounced cusp appearing for the full quasistatic bandstructure. As we will see in the following, such a cusp is characteristic of the long-range nature of the quasistatic dipole-dipole interactions in two-dimensional systems.[3] Note that the dispersion relation within the nearest-neighbor approximation shows qualitatively the same dispersion as for electronic systems studied with tight-binding models.

In what follows, we present a method in order to explain the cusps appearing in the full quasistatic bandstructure in Fig. 5.1(c). Such a method is based on the mean-field approximation (mf) of the dipolar interactions between the individual LSPs in the lattice. Importantly, we do not average over the totality of the dipolar interactions since doing so would imply the loss of the specific geometry of the lattice we consider. To keep track of the lattice structure, we thus consider exactly the nearest-neighbor interactions and then average over the remaining interactions. To this end, we therefore split the lattice sum (4.17) into two terms as $f^{zz}(\mathbf{q}) \simeq f^{zz}_{\mathrm{nn}}(\mathbf{q}) + f^{zz}_{\mathrm{mf}}(\mathbf{q})$ where $f^{zz}_{\mathrm{nn}}(\mathbf{q})$ is defined in Eq. (5.18). The mean-field part is given by

$$f^{zz}_{\mathrm{mf}}(\mathbf{q}) = \int\limits_{\rho\geq\sqrt{2}d} \frac{\mathrm{d}^2\boldsymbol{\rho}}{d^2} \mathrm{e}^{\mathrm{i}\mathbf{q}\cdot\boldsymbol{\rho}} \left(\frac{d}{\rho}\right)^3. \tag{5.19}$$

In the latter equation, the quantity d^2 in the integrand accounts for the nanoparticle density while the lower limit of the integral arises from the minimal distance between the nanoparticles and their next-nearest-neighbors. Choosing polar coordinates and integrating over the angular degrees of freedom yields for (5.19)

$$f^{zz}_{\mathrm{mf}}(\mathbf{q}) = 2\pi|\mathbf{q}|d \int\limits_{\sqrt{2}|\mathbf{q}|d}^{+\infty} \mathrm{d}z \frac{J_0(z)}{z^2}, \tag{5.20}$$

[2] Within the figure (and all the others showing results within the first Brillouin zone), the high symmetry lines along which the bandstructures are shown, are in units of $|\mathbf{q}|d$.

[3] Indeed, several studies on plasmonic one-dimensional chains including the dipolar interactions beyond nearest neighbors did not reported such cusps (see e.g., Refs. [133, 135, 137]).

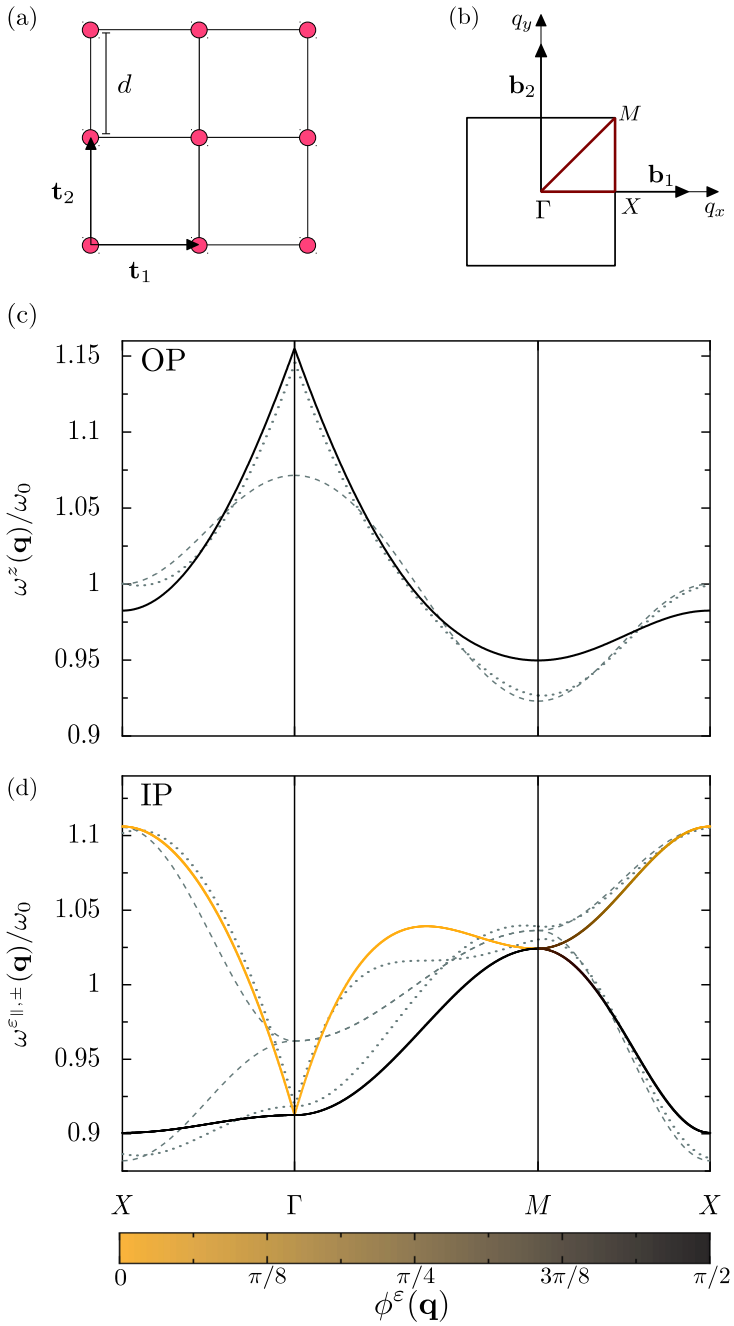

Figure 5.1: (a) Sketch of a square lattice with primitive lattice vectors $\mathbf{t}_1 = d\,(1,0)$ and $\mathbf{t}_2 = d\,(0,1)$. (b) Corresponding first Brillouin zone, with primitive reciprocal vectors $\mathbf{b}_1 = \frac{2\pi}{d}(1,0)$ and $\mathbf{b}_2 = \frac{2\pi}{d}(0,1)$. (c),(d) Quasistatic plasmonic dispersion relation as a function of the wavevector $\mathbf{q}$ (scaled with the interparticle distance d) along high-symmetry paths in the first Brillouin zone [cf. panel (b)] for (c) out-of-plane (OP) and (d) in-plane (IP) polarizations. The dashed and solid lines correspond, respectively, to nearest-neighbor and long-range couplings. The dotted lines correspond to the mean-field approximation discussed in the text. Color code of the solid lines: polarization angle (4.28). In the figure, the interparticle distance $d = 3a$ (corresponding to $\Omega = \omega_0/54$).

where $J_n(z)$ are the Bessel functions of the first kind. The remaining integral in Eq. (5.20) then yields

$$f^{zz}_{\mathrm{mf}}(\mathbf{q}) = 2\pi|\mathbf{q}|d\mathcal{F}\left(\sqrt{2}|\mathbf{q}|d\right), \tag{5.21}$$

with

$$\mathcal{F}(z) = -1 + J_1(z)\left[-1 + \frac{\pi}{2}z\mathbf{H}_0(z)\right] + J_0(z)\left[\frac{1}{z} + z - \frac{\pi}{2}z\mathbf{H}_1(z)\right]. \tag{5.22}$$

In Eq. (5.22), $\mathbf{H}_n(z)$ are the Struve functions. We thus obtain the quasistatic plasmonic dispersion within the mean-field approximation by substituting the results $f^{zz}_{\mathrm{nn}}(\mathbf{q})$ [Eq. (5.18)] and $f^{zz}_{\mathrm{mf}}(\mathbf{q})$ [Eq. (5.21)] for the lattice sum $f^{zz}(\mathbf{q}) \simeq f^{zz}_{\mathrm{nn}}(\mathbf{q}) + f^{zz}_{\mathrm{mf}}(\mathbf{q})$ into Eq. (5.3). In the vicinity of the Γ point ($|\mathbf{q}|d \ll 1$) and in the weak-coupling regime of interest ($\Omega \ll \omega_0$), we find

$$\omega^z(\mathbf{q}) \simeq \omega_0 + \Omega\left[4 + \sqrt{2}\pi - 2\pi|\mathbf{q}|d + \left(\frac{\pi}{\sqrt{2}} - 1\right)(|\mathbf{q}|d)^2\right] \tag{5.23}$$

so that a cusp appears in the dispersion (5.3). We plot in Fig. 5.1(c) the mean-field result for the dispersion (5.3) in grey dotted line. As can be seen from the figure, the mean-field approximation reproduces well the cusp in the vicinity of the Γ point where the dispersion is given by Eq. (5.23). In the rest of the first Brillouin zone, the approximate dispersion is dominated by the nearest-neighbor interactions [cf. Eq. (5.18)] since the mean-field part approaches zero for wavevectors away from the Γ point.

In-plane modes

We now turn to the discussion of the plasmonic modes polarized within the plane formed by the square lattice. The bandstructure (5.11) is plotted in Fig. 5.1(d) as solid lines. For comparison, we further plot the dispersion relation taking into account nearest-neighbor couplings only, for which the lattice sums in Eq. (5.11) are replaced by

$$f^{xx}_{\mathrm{nn}}(\mathbf{q}) = -4\cos(q_x d) + 2\cos(q_y d), \tag{5.24a}$$

$$f^{yy}_{\mathrm{nn}}(\mathbf{q}) = 2\cos(q_x d) - 4\cos(q_y d) \tag{5.24b}$$

and

$$f^{xy}_{\mathrm{nn}}(\mathbf{q}) = 0. \tag{5.24c}$$

In contrast to the out-of-plane modes [Fig. 5.1(c)], the long-range nature of the dipolar interaction has a more pronounced effect on the plasmonic bandstructure for in-plane polarized modes. For instance, the dipolar interaction lifts the degeneracy of the dispersion induced by the symmetry of the square lattice within the nearest-neighbor approximation along the ΓM direction of the first Brillouin zone. In addition, the long-range dipolar interaction leads to a cusp for the upper plasmonic band at the Γ point, while the lower band does not show such an effect.

In Fig. 5.1(d), the color code encodes the polarization angle (5.17) for the in-plane plasmonic modes. Along the high symmetry lines $X\Gamma$ and ΓM, we see that the collective plasmonic modes belonging to the upper [lower] band $\omega^{\varepsilon_\parallel,+}(\mathbf{q})$ [$\omega^{\varepsilon_\parallel,-}(\mathbf{q})$] are polarized longitudinally [transversely] to the high symmetry line along which the wavevector $\mathbf{q}$ is directed. As an illustration to this

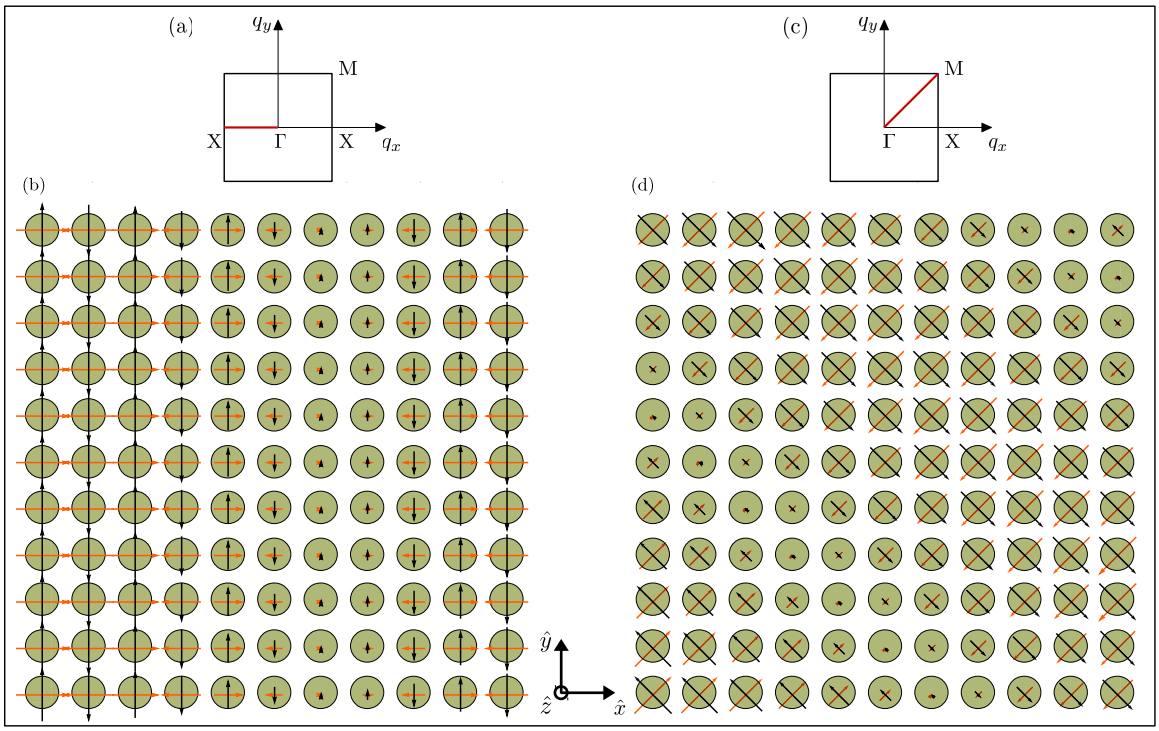

Figure 5.2: Localized surface plasmon orientations along the two high-symmetry axis for a square array of nanoparticles for a given mode $\mathbf{q}$. (a) First Brillouin zone with the $X\Gamma$ axis highlighted. (b) 11×11 portion of a 301×301 array (each grey sphere represent a nanoparticle). The arrows represent the orientation and the strength (i.e., length of the arrows) of each LSPs for a given mode $\mathbf{q} = (-2.89/d, 0)$ for the upper band $\omega^{\varepsilon_\parallel,+}$ in orange and the lower band $\omega^{\varepsilon_\parallel,-}$ in black. (c),(d) Same as panels (a),(b) for the ΓM direction for a mode $\mathbf{q} = (0.25/d, 0.25/d)$. In the figure, $d = 3a$.

phenomenon, we show in Fig. 5.2 the vectors $\mathbf{u}^{\varepsilon_\parallel,\pm}(\mathbf{q})$ [see Eq. (5.16)] in the special case of a square array (schematized by a 11×11 array) along the $X\Gamma$ [Fig. 5.2(a),(b)] and ΓM directions [Fig. 5.2(c),(d)] for an arbitrary mode $\mathbf{q}$, respectively. As can be seen from panel (b) the black arrows are all perpendicular to the $X\Gamma$ axis with different lengths (representing the strength of the oscillation of the isolated LSPs) while the orange arrows point along the axis. In panel (d), we see a similar behavior as in panel (b) as half of the modes (orange arrows) are tilted by 45° from the x-axis while the other half (black arrows) are all perpendicular to the orange arrows. Note that in Fig. 5.2(b) [Fig. 5.2(d)], we display the results for $\mathbf{q} = (-2.89/d, 0)$ [$(0.25/d, 0.25/d)$] along the $X\Gamma$ [ΓM] direction. For the lower symmetry axis MX, the polarization angle (5.17) can take all the values between 0 and $\pi/2$ so that the collective modes are of mixed type, neither longitudinal nor transverse. As we will see in Chapter 6, knowing the polarization of the modes may be helpful to determine the behavior of relevant properties such as the radiative shifts and decay rates.

As was done for the out-of-plane modes, in order to explain respectively the presence and the absence of a cusp in the upper and lower bands $\omega^{\varepsilon_\parallel,\pm}$, we treat (similarly as for the out-of-

plane modes) the lattice sums (4.17) entering the dispersion relations (5.11) within a mean-field approximation. Consequently, we write the lattice sums as $f^{\sigma\sigma'}(\mathbf{q}) \simeq f^{\sigma\sigma'}_{\mathrm{nn}}(\mathbf{q}) + f^{\sigma\sigma'}_{\mathrm{mf}}(\mathbf{q})$ with $\sigma, \sigma' = x, y$ and where the nearest-neighbor parts $f^{\sigma\sigma'}_{\mathrm{nn}}(\mathbf{q})$ are given in Eq. (5.24). We first consider the case $\sigma = \sigma'$ so that

$$f^{\sigma\sigma}_{\mathrm{mf}}(\mathbf{q}) = \int\limits_{\rho \geq \sqrt{2}d} \frac{\mathrm{d}^2\boldsymbol{\rho}}{d^2} \mathrm{e}^{\mathrm{i}\mathbf{q}\cdot\boldsymbol{\rho}} \left(\frac{d}{\rho}\right)^3 \left[1 - (\hat{\sigma}\cdot\hat{\rho})^2\right]. \tag{5.25}$$

Distinguishing the two cases $\sigma = x$ and $\sigma = y$, the latter equation yields

$$f^{xx}_{\mathrm{mf}}(\mathbf{q}) = d\int_{\sqrt{2}d}^{+\infty} \frac{\mathrm{d}\rho}{\rho^2} \int_0^{2\pi} \mathrm{d}\theta \exp[\mathrm{i}|\mathbf{q}|\rho\cos(\theta-\varphi)] \left(1 - 3\cos^2\theta\right) \tag{5.26a}$$

and

$$f^{yy}_{\mathrm{mf}}(\mathbf{q}) = d\int_{\sqrt{2}d}^{+\infty} \frac{\mathrm{d}\rho}{\rho^2} \int_0^{2\pi} \mathrm{d}\theta \exp[\mathrm{i}|\mathbf{q}|\rho\cos(\theta-\varphi)] \left(1 - 3\sin^2\theta\right), \tag{5.26b}$$

where θ and φ are the angles between the vector $\boldsymbol{\rho}$ and the x-axis and between the wavevector $\mathbf{q}$ and the x-axis, respectively. Evaluating the integrals over the angular coordinates in Eq. (5.26) yields

$$f^{xx}_{\mathrm{mf}}(\mathbf{q}) = 2\pi|\mathbf{q}|d\left[\left(1 - 3\cos^2\varphi\right)\int_{\sqrt{2}|\mathbf{q}|d}^{+\infty} \mathrm{d}z \frac{J_0(z)}{z^2} + 3\cos(2\varphi)\int_{\sqrt{2}|\mathbf{q}|d}^{+\infty} \mathrm{d}z \frac{J_1(z)}{z^3}\right] \tag{5.27a}$$

and

$$f^{yy}_{\mathrm{mf}}(\mathbf{q}) = 2\pi|\mathbf{q}|d\left[\left(1 - 3\sin^2\varphi\right)\int_{\sqrt{2}|\mathbf{q}|d}^{+\infty} \mathrm{d}z \frac{J_0(z)}{z^2} + 3\cos(2\varphi)\int_{\sqrt{2}|\mathbf{q}|d}^{+\infty} \mathrm{d}z \frac{J_1(z)}{z^3}\right]. \tag{5.27b}$$

The two remaining integrals in Eq. (5.27) are easily performed to yield the following compact form for the mean-field part of the lattice sum

$$f^{\sigma\sigma}_{\mathrm{mf}}(\mathbf{q}) = 2\pi|\mathbf{q}|d\left\{-\left(\frac{q_\sigma}{|\mathbf{q}|}\right)^2 \mathcal{F}\left(\sqrt{2}|\mathbf{q}|d\right) + \left[\left(\frac{q_\sigma}{|\mathbf{q}|}\right)^2 - \frac{1}{2}\right] \frac{J_1\left(\sqrt{2}|\mathbf{q}|d\right)}{(|\mathbf{q}|d)^2}\right\}, \quad \sigma = x, y, \tag{5.28}$$

with $q_x = |\mathbf{q}|\cos\varphi$ and $q_x = |\mathbf{q}|\sin\varphi$, respectively. The last lattice sum, i.e., $f^{xy}_{\mathrm{mf}}(\mathbf{q})$ reads

$$f^{xy}_{\mathrm{mf}}(\mathbf{q}) = d\int_{\sqrt{2}d}^{+\infty} \frac{\mathrm{d}\rho}{\rho^2} \int_0^{2\pi} \mathrm{d}\theta \exp[\mathrm{i}|\mathbf{q}|\rho\cos(\theta-\varphi)] \cos\theta\sin\theta \tag{5.29}$$

Performing the angular integration in the latter equation yields the simple form

$$f^{xy}_{\mathrm{mf}}(\mathbf{q}) = 3\pi|\mathbf{q}|d\sin(2\varphi) \int\limits_{\sqrt{2}|\mathbf{q}|d}^{+\infty} \mathrm{d}z \frac{J_2(z)}{z^2}. \tag{5.30}$$

Making use of the relation $J_0(z)+J_2(z)=2J_1(z)/z$ between the Bessel functions of the first kind, the equation above thus leads to

$$f_{\mathrm{mf}}^{xy}(\mathbf{q})=2\pi|\mathbf{q}|d\frac{q_xq_y}{|\mathbf{q}|^2}\left[-\mathcal{F}\left(\sqrt{2}|\mathbf{q}|d\right)+\frac{J_1\left(\sqrt{2}|\mathbf{q}|d\right)}{(|\mathbf{q}|d)^2}\right]. \tag{5.31}$$

Thus, substituting the results (5.28) and (5.31) into the lattice sums together with the nearest-neighbor contributions [Eq. (5.24)] gives the in-plane plasmonic dispersions $\omega^{\varepsilon_\parallel,\pm}(\mathbf{q})$ within the mean-field approximation. These approximate results are plotted as dotted lines in Fig. 5.1(d) for the in-plane modes. As can be seen in the figure, the dotted lines reproduce quite well the presence and absence of cusps in the vicinity of the center of the first Brillouin zone. In particular, for $|\mathbf{q}|d\ll 1$, the plasmonic dispersions (5.11) become in first order in $\Omega\ll\omega_0$

$$\omega^{\varepsilon_\parallel,+}\simeq\omega_0+\Omega\left(-2-\frac{\pi}{\sqrt{2}}+2\pi|\mathbf{q}|d\right) \tag{5.32a}$$

and

$$\omega^{\varepsilon_\parallel,-}\simeq\omega_0-\Omega\left(2+\frac{\pi}{\sqrt{2}}\right) \tag{5.32b}$$

so that a cusp appears on the upper band (5.32a) while no cusp is observed for the lower one (5.32b).

Some of the conclusions we have drawn for the square lattice are not specific to its geometry and can be drawn as well for other Bravais lattices and also for Bravais lattices with a basis (cf. Secs. 5.2 and 5.3).

5.1.3 Other simple Bravais lattices

In this section, we study two other simple Bravais lattices which possess high-symmetry axis (for their Brillouin zones), i.e., the rectangular and hexagonal lattices. We choose for the rectangular lattice the two lattice vectors $\mathbf{t}_1=d(1,0)$ and $\mathbf{t}_2=d(0,\frac{3}{2})$ plotted in Fig. 5.3(a). The corresponding first Brillouin zone defined by the two reciprocal primitive lattice $\mathbf{b}_1=\frac{2\pi}{d}(1,0)$ and $\mathbf{b}_2=\frac{4\pi}{3d}(0,1)$ is plotted in Fig. 5.3(b). The hexagonal lattice with $\mathbf{t}_1=d(1,0)$ and $\mathbf{t}_2=d(\frac{1}{2},\frac{\sqrt{3}}{2})$ is shown in panel (c) with its corresponding first Brillouin zone with $\mathbf{b}_1=\frac{2\pi}{\sqrt{3}d}(\sqrt{3},-1)$ and $\mathbf{b}_2=\frac{4\pi}{\sqrt{3}d}(0,1)$ in panel (d).

As for the square lattice, we show in Figs. 5.3(e) and 5.3(g) the quasistatic dispersion relation (5.3) while the panels (f) and (h) depict the corresponding in-plane bandstructure (5.11) for the rectangular and hexagonal lattices, respectively. The color code in the figure represents the polarization angle (4.28). Concerning the out-of-plane modes, we clearly observe the same features as for the square, i.e., the appearance of a cusp in the vicinity of the Γ point. In addition, away from the center of the Brillouin zone, the quasistatic bandstructure (black lines) is well reproduced by the nearest-neighbor approximation [see dashed lines in Figs. 5.3(e),(g)]. For in-plane polarized modes [Figs. 5.3(f) and (h)], some of the characteristics occurring for the square lattice can be observed for the rectangular and hexagonal lattices, such as the presence of a cusp for one of the band and no cusp for the other. Note that the full quasistatic bandstructures are qualitatively reproduced by the

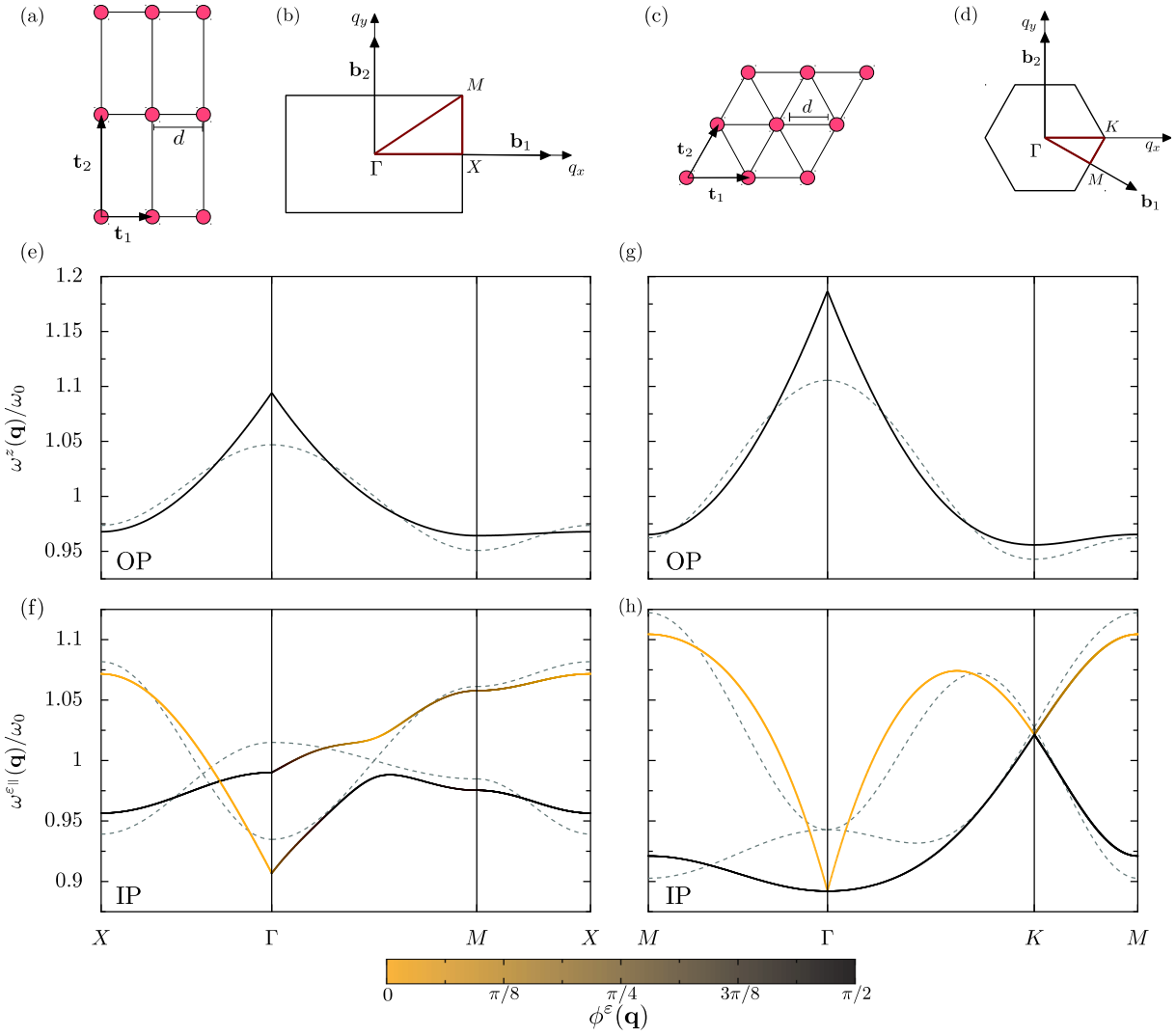

Figure 5.3: (a),(c) Sketch of (a) a rectangular lattice with primitive lattice vectors $\mathbf{t}_1 = d(1,0)$ and $\mathbf{t}_2 = d(0,\frac{3}{2})$ and (c) a hexagonal lattice with $\mathbf{t}_1 = d(1,0)$ and $\mathbf{t}_2 = d(\frac{1}{2},\frac{\sqrt{3}}{2})$. (b),(d) Corresponding first Brillouin zones, with (b) primitive reciprocal vectors $\mathbf{b}_1 = \frac{2\pi}{d}(1,0)$ and $\mathbf{b}_2 = \frac{4\pi}{3d}(0,1)$ and (d) $\mathbf{b}_1 = \frac{2\pi}{\sqrt{3}d}(\sqrt{3},-1)$ and $\mathbf{b}_2 = \frac{4\pi}{\sqrt{3}d}(0,1)$ (e)-(h) Quasistatic plasmonic bandstructure of (e),(f) the rectangular and (g),(h) the hexagonal lattices for (e),(g) out-of-plane (OP) and (f),(h) in-plane (IP) polarizations. The dashed and solid lines correspond, respectively, to nearest-neighbor and long-range couplings, and the color code represents the polarization angle (4.28). Same parameters as in Fig. 5.1.

nearest-neighbors approximation at the edges of the Brillouin zones. Importantly, in the case of the rectangular lattice, the collective plasmonic mode polarization angle $\phi^{\varepsilon_{\parallel},\pm}$ [cf. Eq. (5.17)] does not exhibit the same profile as for the square lattice [see Fig. 5.1(d)]. Indeed, we see in Fig. 5.3(f) that the collective modes show a mixed type polarization along the ΓM axis for rectangular lattices. Such a behavior stems from the lack of symmetries of the latter arrays with respect to the square and hexagonal ones. Note that for the high symmetry axis i.e., the $X\Gamma$-axis, the plasmonic modes are still purely longitudinal or transverse to the wavevector $\mathbf{q}$.

5.2 Bravais lattices with a basis of two

Since our model presented in Chapter 4 describes as well the plasmonic modes hosted by arrays of nanoparticles arranged into Bravais lattices with a basis, we now discuss the case of a basis of two. As for simple lattices, we may first evaluate several quantities in a very general case. We then illustrate our results with the example of the honeycomb lattice.

5.2.1 Arbitrary bipartite lattices

In the case of bipartite lattices ($\mathcal{S} = 2$), the system of equations (4.26) gives for the out-of-plane polarization ($\varepsilon = \sigma = z$) the 4×4 system

$$\boldsymbol{\mathcal{D}}_2^z(\mathbf{q}) \begin{pmatrix} u_{\tau 1}^{zz}(\mathbf{q}) \\ v_{\tau 1}^{zz}(\mathbf{q}) \\ u_{\tau 2}^{zz}(\mathbf{q}) \\ v_{\tau 2}^{zz}(\mathbf{q}) \end{pmatrix} = 0 \tag{5.33}$$

to solve. In the latter equation the matrix $\boldsymbol{\mathcal{D}}_2^z(\mathbf{q})$ is given by

$$\boldsymbol{\mathcal{D}}_2^z(\mathbf{q}) = \begin{pmatrix} \varsigma^{zz}(\mathbf{q}) - \omega_\tau^z(\mathbf{q}) & -\Omega f_{11}^{zz}(\mathbf{q}) & \Omega f_{12}^{zz*}(\mathbf{q}) & -\Omega f_{12}^{zz*}(\mathbf{q}) \\ \Omega f_{11}^{zz}(\mathbf{q}) & -\varsigma^{zz}(\mathbf{q}) - \omega_\tau^z(\mathbf{q}) & \Omega f_{12}^{zz*}(\mathbf{q}) & -\Omega f_{12}^{zz*}(\mathbf{q}) \\ \Omega f_{12}^{zz}(\mathbf{q}) & -\Omega f_{12}^{zz}(\mathbf{q}) & \varsigma^{zz}(\mathbf{q}) - \omega_\tau^z(\mathbf{q}) & -\Omega f_{11}^{zz}(\mathbf{q}) \\ \Omega f_{12}^{zz}(\mathbf{q}) & -\Omega f_{12}^{zz}(\mathbf{q}) & \Omega f_{11}^{zz}(\mathbf{q}) & -\varsigma^{zz}(\mathbf{q}) - \omega_\tau^z(\mathbf{q}) \end{pmatrix}, \tag{5.34}$$

where the lattice sums $f_{ss'}^{\sigma\sigma'}(\mathbf{q})$ are given by Eq. (4.17) while the quantity $\varsigma^{\sigma\sigma}(\mathbf{q})$ was introduced for the Bravais lattices in Eq. (5.2). The condition $\mathrm{Det}[\boldsymbol{\mathcal{D}}_2^z(\mathbf{q})] = 0$ thus yields the secular equation

$$[X_\tau^z(\mathbf{q})]^2 - 2\omega_0 X_\tau^z(\mathbf{q}) \left[\omega_0 + \Omega f_{11}^{zz}(\mathbf{q})\right] + \omega_0^2 \left\{\omega_0^2 + \omega_0 \Omega f_{11}^{zz}(\mathbf{q}) + 4\Omega^2 \left([f_{11}^{zz}(\mathbf{q})]^2 - |f_{12}^{zz}(\mathbf{q})|^2 \right)\right\} = 0, \tag{5.35}$$

with $X_\tau^z(\mathbf{q}) = [\omega_\tau^z(\mathbf{q})]^2$. Hence, solving Eq. (5.35) yields the two positive eigenfrquencies

$$\omega_\tau^z(\mathbf{q}) = \omega_0 \sqrt{1 + 2\frac{\Omega}{\omega_0}\left[f_{11}^{zz}(\mathbf{q}) + \tau |f_{12}^{zz}(\mathbf{q})|\right]}, \tag{5.36}$$

with $\tau = \pm 1$. Note that in the weak-coupling regime of interest $\Omega \ll \omega_0$, the latter equation reduces to $\omega_\tau^z(\mathbf{q}) \simeq \omega_0 + \Omega f_{11}^{zz}(\mathbf{q}) + \tau\Omega |f_{12}^{zz}(\mathbf{q})|$.

In the following, we evaluate the Bogoliubov coefficients $u^{zz}_{\tau s}(\mathbf{q})$ and $v^{zz}_{\tau s}(\mathbf{q})$ in Eq. (5.33) following a similar method as was done for the simple Bravais lattice in Sec. 5.1. First, applying the relation (5.5) for $\varepsilon = \sigma = z$ and $\mathcal{S} = 2$ allows us to write

$$v^{zz}_{\tau s}(\mathbf{q}) = \frac{\omega^z_\tau(\mathbf{q}) - \omega_0}{\omega^z_\tau(\mathbf{q}) + \omega_0} u^{zz}_{\tau s}(\mathbf{q}) \tag{5.37}$$

for $s = 1, 2$. Thus, using Eq. (5.37), the normalization condition (4.20) for $\mathcal{S} = 2$ and $\sigma = z$ gives

$$|u^{zz}_{\tau 1}(\mathbf{q})|^2 + |u^{zz}_{\tau 2}(\mathbf{q})|^2 = \frac{\left(\omega^z_\tau(\mathbf{q}) + \omega_0\right)^2}{4\omega_0\omega^z_\tau(\mathbf{q})}. \tag{5.38}$$

Substituting Eq. (5.37) for $s = 1, 2$ and using the expression (5.36) into the first line of Eq. (5.33) thus yields the phase relation

$$u^{zz}_{\tau 2}(\mathbf{q}) = \tau \frac{f^{zz}_{12}(\mathbf{q})}{|f^{zz}_{12}(\mathbf{q}|} u^{zz}_{\tau 1}(\mathbf{q}) \tag{5.39}$$

between the two coefficients. Replacing the latter equation into the condition (5.38) and choosing the arbitrary phase to be 1 for $u^{zz}_{\tau 1}(\mathbf{q})$ then gives the four Bogoliubov coefficients

$$u^{zz}_{\tau 1}(\mathbf{q}) = \frac{\omega^z_\tau(\mathbf{q}) + \omega_0}{2\sqrt{2\omega_0\omega^z_\tau(\mathbf{q})}}, \tag{5.40a}$$

$$u^{zz}_{\tau 2}(\mathbf{q}) = \tau \, \frac{f^{zz}_{12}(\mathbf{q})}{|f^{zz}_{12}(\mathbf{q})|} \, \frac{\omega^z_\tau(\mathbf{q}) + \omega_0}{2\sqrt{2\omega_0\omega^z_\tau(\mathbf{q})}}, \tag{5.40b}$$

and

$$v^{zz}_{\tau 1}(\mathbf{q}) = \frac{\omega^z_\tau(\mathbf{q}) - \omega_0}{2\sqrt{2\omega_0\omega^z_\tau(\mathbf{q})}}, \tag{5.41a}$$

$$v^{zz}_{\tau 2}(\mathbf{q}) = \tau \, \frac{f^{zz}_{12}(\mathbf{q})}{|f^{zz}_{12}(\mathbf{q})|} \, \frac{\omega^z_\tau(\mathbf{q}) - \omega_0}{2\sqrt{2\omega_0\omega^z_\tau(\mathbf{q})}}. \tag{5.41b}$$

As we will see in Chapter 6 in more details, the coefficients (5.40) and (5.41) play a crucial role for the nature of the collective modes and in particular, for distinguishing the bright and dark modes (see Sec. 6.1).

For the in-plane polarized modes, applying the system (4.26) for $\mathcal{S} = 2$ and $\sigma = x, y$ leads to an 8×8 eigensystem to solve. Consequently, the secular equation extracted from the matrix $\boldsymbol{\mathcal{D}}_2^{\varepsilon\parallel}(\mathbf{q})$ corresponds to a polynomial equation of the 4^{th} order in $[\omega^z_\tau(\mathbf{q})]^2$ to solve. Although it would be in principle possible to find analytically the roots for such a polynomial equation, the results we obtain would be of poor practical use due to the heavy calculations involved. Consequently, we solve numerically the eigensystem corresponding to the in-plane modes in bipartite lattices using the algorithm presented in Appendix C.

5.2.2 The honeycomb lattice

One of the bipartite lattice that has attracted a lot of attention these past fifteen years is the honeycomb lattice. In particular, our model allows to study the effects of the long-range dipolar interactions on the collective plasmonic modes within a similar formalism as done in Ref. [108, 109]. In the following, we thus apply our results for bipartite lattices presented in Sec. 5.2.1 to the special case of the honeycomb lattice. Such a lattice is formed by a hexagonal Bravais lattice with a basis of two. The primitive vectors of the array are $\mathbf{t}_1 = d(\sqrt{3}, 0)$ and $\mathbf{t}_2 = d(\frac{\sqrt{3}}{2}, \frac{3}{2})$, respectively while the basis vector linking the two sublattices is defined as $\mathbf{d}_2 = d(\frac{\sqrt{3}}{2}, \frac{1}{2})$. The lattice is sketched in Fig. 5.4(a) with its corresponding first Brillouin zone in panel (c). The latter is characterized by the primitive vectors $\mathbf{b}_1 = \frac{2\pi}{3d}(\sqrt{3}, -1)$ and $\mathbf{b}_2 = \frac{4\pi}{3d}(0, 1)$. The two plasmonic bands (5.36) corresponding to the out-of-plane collective modes are plotted in solid lines in Fig. 5.4(c). For comparison, we also show by dashed lines the quasistatic bandstructure with dipolar interactions between nearest neighbors only [108] for which we replace in Eq. (5.36) the lattice sums $f_{11}^{zz}(\mathbf{q})$ and $f_{12}^{zz}(\mathbf{q})$ by $f_{11,\mathrm{nn}}^{zz}(\mathbf{q}) = 0$ and $f_{12,\mathrm{nn}}^{zz}(\mathbf{q}) = \sum_{j=1}^{3} \mathrm{e}^{\mathrm{i}\mathbf{q}\cdot\mathbf{e}_j}$. In $f_{12,\mathrm{nn}}^{zz}(\mathbf{q})$, the vectors $\mathbf{e}_1 = \mathbf{d}_2 - \mathbf{t}_2$, $\mathbf{e}_2 = \mathbf{d}_2$, and $\mathbf{e}_3 = \mathbf{d}_2 - \mathbf{t}_1$ connect a lattice site belonging to the red sublattice in Fig. 5.4(a) to its three (blue) nearest neighbors.

Dirac Hamiltonian

From Fig. 5.4(c) we first observe that the Dirac point at the K point of the first Brillouin zone, located at $\mathbf{K} = \frac{4\pi}{3\sqrt{3}d}(1, 0)$ is not ruled out by long-range interactions. The latter statement can be verified by expanding the lattice sums in first order in $|\mathbf{k}|$, where $\mathbf{q} = \mathbf{K} + \mathbf{k}$ with $|\mathbf{k}| \ll |\mathbf{K}|$. Performing the expansions thus yields $f_{11}^{zz}(\mathbf{q}) \simeq f_{11}^{zz}(\mathbf{K}) \simeq -0.449$ and $f_{12}^{zz}(\mathbf{q}) \simeq -1.16\,(k_x + \mathrm{i}k_y)\,d$. Consequently, in the weak-coupling regime $\Omega \ll \omega_0$, we obtain for the dispersion relation (5.36)

$$\omega_\tau^z(\mathbf{k}) \simeq \omega_0 - \Omega|f_{11}^{zz}(\mathbf{K})| + \tau v^z|\mathbf{k}|. \tag{5.42}$$

corresponding to a conical dispersion. In the latter equation, the group velocity is given by $v^z = 1.16\Omega d$. Comparing the result (5.42) with the nearest-neighbor dispersion calculated in Ref. [108] given by $\omega_{\mathrm{nn},\tau}^z(\mathbf{k}) = \omega_0 + \tau v_{\mathrm{nn}}^z|\mathbf{k}|$ with $v_{\mathrm{nn}}^z = 3\Omega d/2$ we draw two conclusions. On the one hand, the intrasublattice coupling f_{11}^{zz} only induces an inconsequential redshift of the Dirac point frequency. On the other hand, the intersublattice coupling f_{12}^{zz} renormalizes the precise value of the group velocity.

Close to the K point, the Bogoliubov coefficients (5.41) are negligible as compared to the coefficients (5.40) so that we can disregard the former in our study of the dispersion relations. Note that, performing such a procedure amounts to take the rotating-wave approximation (see Appendix D) as done in Ref. [108]. Thus, close to the corner K of the first Brillouin zone, we may write an effective Hamiltonian in terms of the spinor operator $\Psi_{\mathbf{k}} = (b_1^z(\mathbf{k}), b_2^z(\mathbf{k}))$ as $H_{\mathrm{pl}}^{\mathrm{eff}} = \sum_{\mathbf{k}} \Psi_{\mathbf{k}}^\dagger \mathcal{H}_{\mathbf{k}}^{\mathrm{eff}} \Psi_{\mathbf{k}}$ where the Hamiltonian

$$\mathcal{H}_{\mathbf{k}}^{\mathrm{eff}} = [\hbar\omega_0 - \hbar\Omega|f_{11}^{zz}(\mathbf{K})|]\,\mathbb{1}_2 - \hbar v^z \boldsymbol{\sigma}\cdot\mathbf{k} \tag{5.43}$$

corresponds to a massless Dirac Hamiltonian. In the latter equation, $\mathbb{1}_n$ is the $n \times n$ identity matrix and $\boldsymbol{\sigma} = (\sigma_x, \sigma_y, \sigma_z)$ is the vector of Pauli matrices acting on the sublattice pseudospin $1/2$.

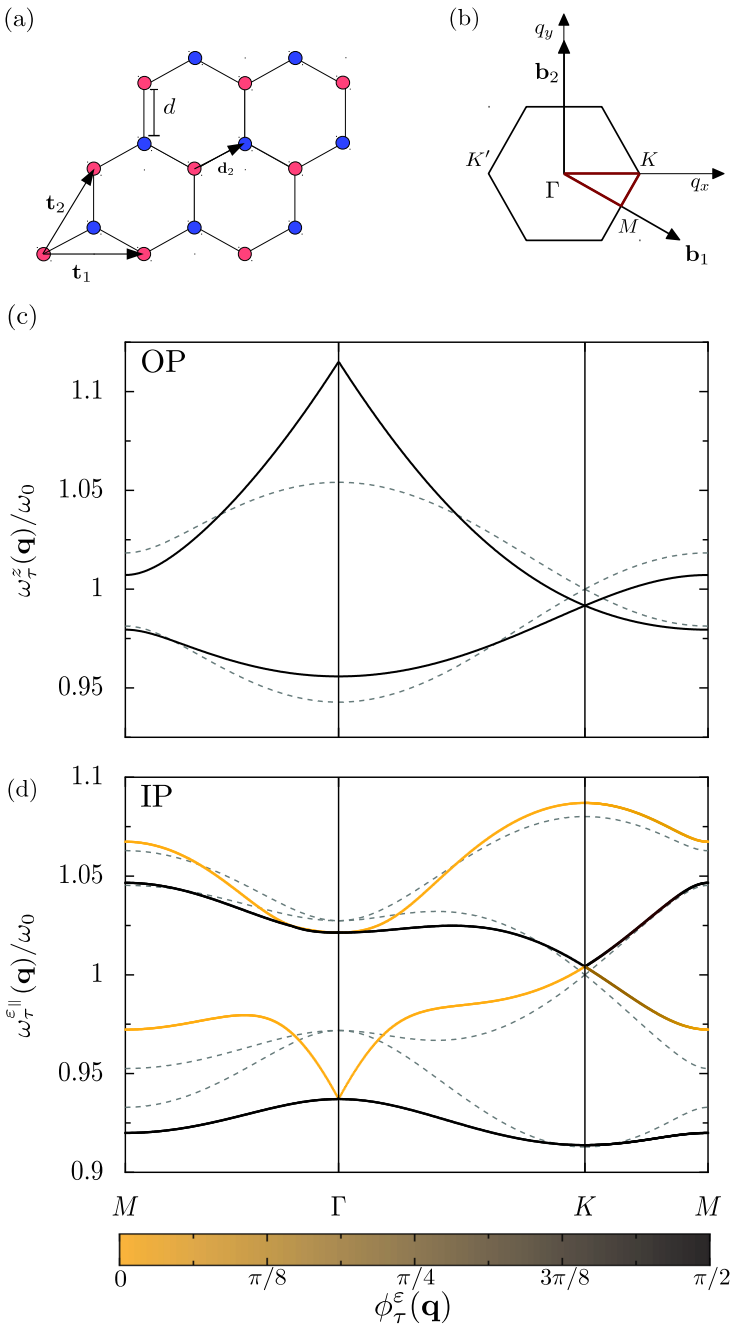

Figure 5.4: (a) Sketch of a honeycomb lattice with primitive lattice vectors $\mathbf{t}_1 = d(\sqrt{3}, 0)$ and $\mathbf{t}_2 = d(\frac{\sqrt{3}}{2}, \frac{3}{2})$, and basis vector $\mathbf{d}_2 = d(\frac{\sqrt{3}}{2}, \frac{1}{2})$). (b) Corresponding first Brillouin zone, with primitive reciprocal vectors $\mathbf{b}_1 = \frac{2\pi}{3d}(\sqrt{3}, -1)$ and $\mathbf{b}_2 = \frac{4\pi}{3d}(0, 1)$. (c),(d) Quasistatic plasmonic bandstructure for (c) out-of-plane (OP) and (d) in-plane (IP) polarizations. The solid lines correspond to the full quasistatic dispersion, and the color code to the polarization angle (4.28). The dashed lines correspond to the nearest-neighbor approximation. Same parameters as in Fig. 5.1.

Therefore, the long-range character of the dipole-dipole interactions does not rule out the massless Dirac nature of the plasmonic quasiparticles in the vicinity of the K point, and the nearest-neighbor approximation is sufficient in catching the relevant physics. Importantly, all the conclusions we have drawn in the vicinity of the K point apply as well to the inequivalent Dirac point located at K' in the first Brillouin zone [see Fig. 5.4(b)].

In addition to our study at the K point, we observe the appearance of a pronounced cusp at the Γ point for the upper ($\tau = +1$) band when taking into account all the quasistatic interactions. Such a cusp have been previously reported by Han *et al.* in Ref. [138] (see red lines in Fig. 1.12(c) in Chapter 1). Conversely, no cusp appears for the lower ($\tau = -1$) band. As we will see in Chapter 6, the latter modes correspond actually to dark plasmonic modes.

We now study the in-plane polarized plasmonic modes. We show in Fig. 5.4(d) the plasmonic bandstructure obtained numerically (using the algorithm presented in Appendix C) for $\sigma = x, y$ as solid lines. The color code in the figure indicating the polarization angle (4.28) reveals that two bands correspond to purely transverse plasmons, and two other bands to purely longitudinal plasmons along the high-symmetry axes $M\Gamma$ and ΓK. We also plot for comparison the dispersion relations with nearest-neighbors coupling only as dashed lines. In the latter case, the intrasublattice sums $f^{\sigma\sigma'}_{\mathrm{nn},11}(\mathbf{q})$ vanish so that the 8×8 eigensystem given by Eq. (4.26) can be solved analytically. Within the nearest-neighbor coupling approximation, solving the secular equation extracted from the 8×8 eigensystem yields the four dispersion relations

$$\omega^{\varepsilon_\parallel}_{\mathrm{nn},\tau}(\mathbf{q}) = \begin{cases} \omega_0 \left[1 + \sqrt{2}\dfrac{\Omega}{\omega_0}\sqrt{\mathcal{G}_1(\mathbf{q}) \pm \sqrt{\mathcal{G}_2(\mathbf{q})}}\right]^{1/2}, \\ \omega_0 \left[1 - \sqrt{2}\dfrac{\Omega}{\omega_0}\sqrt{\mathcal{G}_1(\mathbf{q}) \pm \sqrt{\mathcal{G}_2(\mathbf{q})}}\right]^{1/2}. \end{cases} \tag{5.44}$$

In the latter equation, we have defined the two functions

$$\mathcal{G}_1(\mathbf{q}) = |f^{xx}_{\mathrm{nn},12}(\mathbf{q})|^2 + |f^{yy}_{\mathrm{nn},12}(\mathbf{q})|^2 + 2|f^{xy}_{\mathrm{nn},12}(\mathbf{q})|^2 \tag{5.45}$$

and

$$\begin{aligned} \mathcal{G}_2(\mathbf{q}) = {} & \left[|f^{xx}_{\mathrm{nn},12}(\mathbf{q})|^2 - |f^{yy}_{\mathrm{nn},12}(\mathbf{q})|^2\right]^2 + 4|f^{xy}_{\mathrm{nn},12}(\mathbf{q})|^2 \left[|f^{xx}_{\mathrm{nn},12}(\mathbf{q})|^2 + |f^{yy}_{\mathrm{nn},12}(\mathbf{q})|^2\right] \\ & + 8\,\mathrm{Re}\left\{f^{xx}_{\mathrm{nn},12}(\mathbf{q}) f^{yy}_{\mathrm{nn},12}(\mathbf{q}) \left[f^{xy}_{\mathrm{nn},12}(\mathbf{q})\right]^{*2}\right\} \end{aligned} \tag{5.46}$$

where the intersublattice sums are given by

$$f^{xx}_{\mathrm{nn},12}(\mathbf{q}) = \mathrm{e}^{\mathrm{i}\mathbf{q}\cdot\mathbf{e}_1} - \frac{5}{4}(\mathrm{e}^{\mathrm{i}\mathbf{q}\cdot\mathbf{e}_2} + \mathrm{e}^{\mathrm{i}\mathbf{q}\cdot\mathbf{e}_3}), \tag{5.47a}$$

$$f^{yy}_{\mathrm{nn},12}(\mathbf{q}) = -2\mathrm{e}^{\mathrm{i}\mathbf{q}\cdot\mathbf{e}_1} + \frac{1}{4}(\mathrm{e}^{\mathrm{i}\mathbf{q}\cdot\mathbf{e}_2} + \mathrm{e}^{\mathrm{i}\mathbf{q}\cdot\mathbf{e}_3}) \tag{5.47b}$$

and

$$f^{xy}_{\mathrm{nn},12}(\mathbf{q}) = \frac{3\sqrt{3}}{4}(\mathrm{e}^{\mathrm{i}\mathbf{q}\cdot\mathbf{e}_3} - \mathrm{e}^{\mathrm{i}\mathbf{q}\cdot\mathbf{e}_2}). \tag{5.47c}$$

In Fig. 5.4(d), we see that the nearest-neighbors approximation used for Eq. (5.44) is sufficient to describe qualitatively the plasmonic dispersion relations, apart from the second less energetic band for wavevectors close to the Γ point, where a cusp appears in the full quasistatic bandstructure. Importantly, we notice the presence of two inequivalent conical intersections at the corner K and K' of the first Brillouin zone. Such intersections occur where the plasmonic modes are degenerate at energy $\hbar\omega_0$. For wavevectors $\mathbf{q}$ in the vicinity of the K point (i.e., $\mathbf{q} = \mathbf{K} + \mathbf{k}$ with $|\mathbf{k}| \ll |\mathbf{K}|$), we find for the second and third bands [see Fig. 5.4(d)] the dispersions

$$\omega^{\varepsilon_\parallel}_{\mathrm{nn},\tau}(\mathbf{k}) \simeq \omega_0 \pm \tau v^{\varepsilon_\parallel}_{\mathrm{nn}}|\mathbf{k}|, \tag{5.48}$$

where we have the group velocity $v^{\varepsilon_\parallel}_{\mathrm{nn}} = 9\Omega d/4$. The presence of such conical dispersions was already reported in Ref. [138] involving numerical solutions of Maxwell's equations. Consequently, we see that our transparent method allows us to obtain analytic solutions for describing such a complex structure which hosts Dirac-like bosonic quasiparticles.

Up to now, the lattices we have studied to illustrate the versatility of our model presented in Sec. 4.2 present a plasmonic bandstructure closely related to those calculated for their electronic counterparts. The only qualitative effects we may attribute so far to the long-range nature of the dipolar interactions are the appearance of the cusps for several plasmonic bands [see e.g., Figs. 5.1 and 5.4]. Importantly, the cusps existing within the quasistatic plasmonic dispersions are in fact "not physical" and arise due to the quasistatic calculations. We will see in Chapter 6 that taking into account the retardation effects of the dipolar interactions allow to regularize such cusps.

5.3 Tripartite lattices

As for the cases of the simple Bravais and bipartite lattices (cf. Secs. 5.1 and 5.2), some of the eigenquantities may me evaluated analytically for arbitrary tripartite lattices.

5.3.1 Case of arbitrary lattices

For tripartite lattices ($\mathcal{S} = 3$), the system of equation (4.26) leads to a 6×6 eigensystem for the out-of-plane polarized modes ($\varepsilon = z$). We can still extract from the latter system the eigenfrequencies analytically. However, we evaluate the corresponding Bogoliubov coefficients numerically. The secular equation obtained from the condition $\mathrm{Det}\,[\boldsymbol{\mathcal{D}}^z_3(\mathbf{q})] = 0$ reads

$$\begin{aligned}&[X^z_\tau(\mathbf{q})]^3 - 3\omega_0\left\{\omega_0 + 2\Omega f^{zz}_{11}(\mathbf{q})\right\}[X^z_\tau(\mathbf{q})]^2 + \omega_0^2\left\{3\omega_0^2 + 12\Omega f^{zz}_{11}(\mathbf{q})\varsigma^{zz}(\mathbf{q}) - 4\Omega^2\Sigma^{zz}(\mathbf{q})\right\}X^z_\tau(\mathbf{q})\\ &- \omega_0^6 - 6\omega_0^5\Omega f^{zz}_{11}(\mathbf{q}) - 12\omega_0^4\left[\Omega f^{zz}_{11}(\mathbf{q})\right]^2 - 8\omega_0^3\left[\Omega f^{zz}_{11}(\mathbf{q})\right]^3 + 4\omega_0^4\Omega^2\Sigma^{zz}(\mathbf{q})\\ &+ 8\omega_0^3\Omega^3 f^{zz}_{11}(\mathbf{q})\Sigma^{zz}(\mathbf{q}) - 16\omega_0^3\Omega^3\Pi^{zz}(\mathbf{q}) = 0.\end{aligned} \tag{5.49}$$

In the latter equation, we have defined the two quantities

$$\Sigma^{zz}(\mathbf{q}) = |f^{zz}_{12}(\mathbf{q})|^2 + |f^{zz}_{13}(\mathbf{q})|^2 + |f^{zz}_{23}(\mathbf{q})|^2 \tag{5.50a}$$

and

$$\Pi^{zz}(\mathbf{q}) = \mathrm{Re}\left\{f_{12}^{zz}(\mathbf{q}) f_{13}^{zz*}(\mathbf{q}) f_{23}^{zz}(\mathbf{q})\right\}. \tag{5.50b}$$

The equation (5.49) can be straightforwardly solved (see Appendix E for details) to yield the three positive roots for the plasmonic bands

$$\omega_\tau^z(\mathbf{q}) = \omega_0 \left\{1 + 2\frac{\Omega}{\omega_0}\left[f_{11}^{zz}(\mathbf{q}) + s_+(\mathbf{q}) + s_-(\mathbf{q})\right]\right\}^{1/2}, \tag{5.51a}$$

$$\omega_\tau^z(\mathbf{q}) = \omega_0 \left\{1 + \frac{\Omega}{\omega_0}\left[2f_{11}^{zz}(\mathbf{q}) - s_+(\mathbf{q}) - s_-(\mathbf{q}) \pm \mathrm{i}\sqrt{3}\Big(s_+(\mathbf{q}) - s_-(\mathbf{q})\Big)\right]\right\}^{1/2}, \tag{5.51b}$$

with (cf. Appendix E)

$$s_\pm(\mathbf{q}) = \left\{\Pi^{zz}(\mathbf{q}) \pm \mathrm{i}\sqrt{\left[\frac{\Sigma^{zz}(\mathbf{q})}{3}\right]^3 - \left[\Pi^{zz}(\mathbf{q})\right]^2}\right\}^{1/3}. \tag{5.52}$$

In the latter expression $\Sigma^{zz}(\mathbf{q})$ and $\Pi^{zz}(\mathbf{q})$ are given by Eqs. (5.50a) and (5.50b), respectively.

In the case of in-plane polarized modes ($\sigma = x, y$), the eigensystem obtained from Eq. (4.26) is solved numerically using the procedure presented in Appendix C.

5.3.2 The Lieb lattice

As a first example of tripartite lattices that can be described with our theory, we consider the Lieb lattice sketched in Fig. 5.5(a). Such a lattice is characterized by the primitive lattice vectors $\mathbf{t}_1 = d\,(2,0)$ and $\mathbf{t}_2 = d\,(0,2)$, and the basis vectors $\mathbf{d}_2 = \mathbf{t}_1/2$ and $\mathbf{d}_3 = \mathbf{t}_2/2$. The corresponding first Brillouin zone, with primitive reciprocal vectors $\mathbf{b}_1 = \frac{\pi}{d}(1,0)$ and $\mathbf{b}_2 = \frac{\pi}{d}(0,1)$ is shown in Fig. 5.5(b). Such a lattice (together with the kagome lattice discussed in Sec. 5.3.3) are best known to display conical dispersions together with a flat band in tight-binding models with nearest-neighbor interactions (see e.g., Refs. [140–144]). Consequently, it would be of interest to check whether or not these features survive in plasmonic metasurfaces. More precisely, we would like to study the influence of the long range nature of the dipolar interactions on such topological features occurring in the dispersion relation. In Fig. 5.5(c), we plot the full quasistatic plasmonic dispersion (5.51) for the out-of-plane modes in the Lieb lattice as solid lines. Similarly to the honeycomb case (see Fig. 5.4), we observe the presence of a cusp for the most energetic band in the vicinity of the center of the first Brillouin zone. The two remaining bands do not show such a cusp. For comparison, we also show as dashed lines the bandstructure considering only the nearest-neighbor dipolar interactions. In the latter approximation, the different lattice sums reduce to

$$f_{\mathrm{nn},12}^{zz}(\mathbf{q}) = 2\cos\left(q_x d\right), \tag{5.53a}$$

$$f_{\mathrm{nn},13}^{zz}(\mathbf{q}) = 2\cos\left(q_y d\right), \tag{5.53b}$$

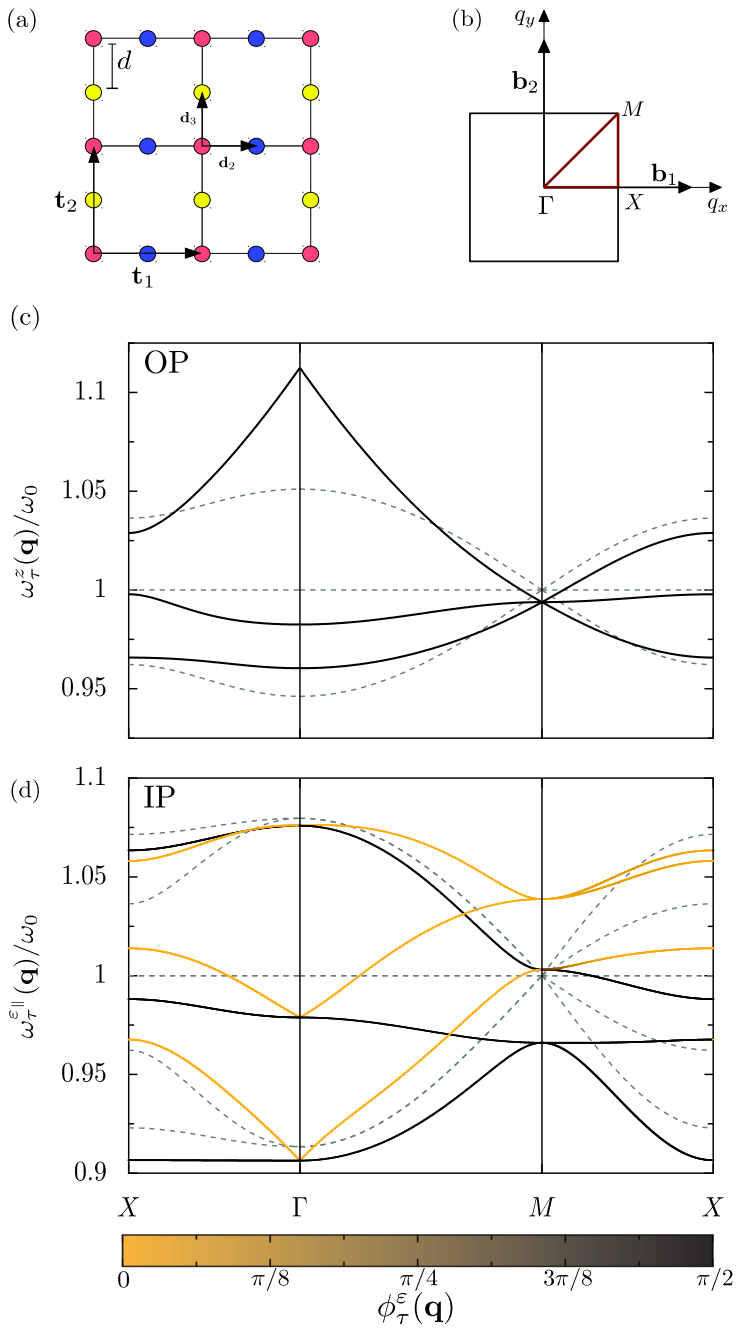

Figure 5.5: (a) Sketch of a Lieb lattice with primitive lattice vectors $\mathbf{t}_1 = d\,(2,0)$ and $\mathbf{t}_2 = d\,(0,2)$, and basis vectors $\mathbf{d}_2 = \mathbf{t}_1/2$ and $\mathbf{d}_3 = \mathbf{t}_2/2$. (b) Corresponding first Brillouin zone, with primitive reciprocal vectors $\mathbf{b}_1 = \frac{\pi}{d}(1,0)$ and $\mathbf{b}_2 = \frac{\pi}{d}(0,1)$. (c),(d) Quasistatic plasmonic bandstructure for (c) out-of-plane (OP) and (d) in-plane (IP) polarizations. The dashed and solid lines correspond, respectively, to nearest-neighbor and long-range couplings. Color code of the solid lines: polarization angle (4.28). Same parameters as in Fig. 5.1.

and

$$f^{zz}_{\mathrm{nn},11}(\mathbf{q}) = f^{zz}_{\mathrm{nn},23}(\mathbf{q}) = 0. \tag{5.53c}$$

Thus, replacing the lattice sums above into the expressions (5.50) allow us to get the plasmonic dispersions within the nearest-neighbors approximation. The plasmonic bandstructure leads to a flat band

$$\omega^{z}_{\mathrm{nn},\tau}(\mathbf{q}) = \omega_0 \tag{5.54a}$$

and to dispersive bands

$$\omega^{z}_{\mathrm{nn},\tau}(\mathbf{q}) = \omega_0 \left[1 \pm 4\frac{\Omega}{\omega_0}\sqrt{\cos^2(q_x d) + \cos^2(q_y d)}\right]. \tag{5.54b}$$

Expanding to first order in $|\mathbf{k}|$ the plasmonic bandstructure (5.54) with $\mathbf{q} = \mathbf{M}+\mathbf{k}$ (with $|\mathbf{k}| \ll |\mathbf{M}|$) in the vicinity of the M point [located at the corner of the first Brillouin zone at $\mathbf{M} = \frac{\pi}{2d}(1,1)$] leads to the conical dispersion $\omega^{z}_{\mathrm{nn},\tau}(\mathbf{k}) \simeq \omega_0 + \tau v^{z}_{\mathrm{nn}}|\mathbf{k}|$ where $v^{z}_{\mathrm{nn}} = 2\Omega d$ is the group velocity.

As can be seen from the dashed lines in Fig. 5.5(c), the nearest-neighbor approximation for plasmonic systems reproduces qualitatively the electronic bandstructure in tight-binding systems as expected. Indeed, we obtain a flat band (within the entire first Brillouin zone) as well as conical dispersions (at the M point). However, comparing the nearest-neighbor approximation (dashed lines) with the full quasistatic bandstructure (solid lines), we see that the topological features in Fig. 5.5(c) are not affected in a similar manner by the long-range nature of the dipolar interactions. Indeed, while the conical dispersion close to the M point is not ruled out by the long-range interactions (as is the case for the honeycomb array, see Sec. 5.2.2), the flat band is strongly reconstructed and becomes dispersive within the first Brillouin zone except at $\mathbf{M}$ where the band is only locally flat. In order to describe these features, we thus expand the lattice sums close to $\mathbf{M}$. With $\mathbf{q} = \mathbf{k} + \mathbf{M}$, to linear order in $|\mathbf{k}| \ll |\mathbf{M}|$ we find $f^{zz}_{ss}(\mathbf{q}) \simeq f^{zz}_{ss}(\mathbf{M}) \simeq -0.331$, $f^{zz}_{12}(\mathbf{k}) \simeq -1.65k_x d$, $f^{zz}_{13}(\mathbf{k}) \simeq -1.65k_y d$ and $f^{zz}_{23}(\mathbf{k}) \simeq 0$. With such approximated results, the dispersions (5.51) reduce to

$$\omega^{z}_{\tau}(\mathbf{k}) \simeq \omega_0 - \Omega|f^{zz}_{11}(\mathbf{M})| \tag{5.55a}$$

for the flat band and

$$\omega^{z}_{\tau}(\mathbf{k}) \simeq \omega_0 - \Omega|f^{zz}_{11}(\mathbf{M})| \pm v^{z}|\mathbf{k}| \tag{5.55b}$$

for the conical dispersions. In the latter equation, the renormalized group velocity reads $v^z = 1.65\Omega d$. Importantly, we notice that, likewise the honeycomb case (cf. Sec. 5.2.2), the effects of the long-range interactions on the conical dispersion are the modification of the group velocity v^z as well as a slight redshift of the frequency of the degeneracy point.

Effective Hamiltonian

Interestingly, we note some similarities between the conical dispersion in the vicinity of the M point for the Lieb lattice [Eq. (5.55)] and its equivalent for the honeycomb case [close to K point, cf. Eq. (5.42)]. From this observation, we write (within the rotating-wave approximation) the Hamiltonian corresponding to the out-of-plane plasmonic modes close to the M point in terms of the spinor operator $\Psi_{\mathbf{k}} = (b^{z}_{1}(\mathbf{q}), b^{z}_{2}(\mathbf{q}), b^{z}_{3}(\mathbf{q}))$. Within this notation, we have $H^{\mathrm{eff}}_{\mathrm{pl}} = \sum_{\mathbf{k}} \Psi^{\dagger}_{\mathbf{k}} \mathcal{H}^{\mathrm{eff}}_{\mathbf{k}} \Psi_{\mathbf{k}}$

where

$$\mathcal{H}_{\mathbf{k}}^{\text{eff}} = [\hbar\omega_0 - \hbar\Omega|f_{11}^{zz}(\mathbf{M})|]\,\mathbb{1}_3 - \hbar v^z \mathbf{S}\cdot\mathbf{k}. \tag{5.56}$$

In the latter equation, $\mathbf{S} = (S_x, S_y, S_z)$ corresponds to the vector of pseudospin-1 matrices (corresponding to the three inequivalent sublattices of the Lieb lattice). The three matrices are defined as

$$S_x = \begin{pmatrix} 0 & 1 & 0 \\ 1 & 0 & 0 \\ 0 & 0 & 0 \end{pmatrix} \quad S_y = \begin{pmatrix} 0 & 0 & 1 \\ 0 & 0 & 0 \\ 1 & 0 & 0 \end{pmatrix} \quad S_z = \begin{pmatrix} 0 & 0 & 0 \\ 0 & 0 & -\mathrm{i} \\ 0 & \mathrm{i} & 0 \end{pmatrix} \tag{5.57}$$

and fulfill the angular momentum algebra $[S_i, S_j] = i\epsilon_{ijk}S_k$, with ϵ_{ijk} the Levi-Civita symbol. The latter matrices, corresponding respectively to the Gell-Mann matrices λ_1, λ_4 and λ_7 [163], therefore correspond to a three-dimensional representation of the special unitary group $\mathrm{SU}(2)$. Importantly, these matrices do not form however a Clifford algebra (i.e., $\{S_i, S_j\} \neq 2\delta_{ij}\mathbb{1}_3$, with $\{A, B\}$ the anti-commutator between A and B). Consequently, the Hamiltonian (5.56) does not corresponds to a massless Dirac Hamiltonian [164] despite presenting a conical spectrum.

We finally show in Fig. 5.5(d) the plasmonic dispersion relations calculated numerically (see Appendix C for the in-plane polarized modes $\sigma = x, y$ as solid lines. The color code corresponds to the polarization angle (4.28) associated with the collective modes. We note that, similarly to the previous structures which have been studied in this manuscript, the plasmonic bands present well defined (transverse or longitudinal) polarization along the axis of high symmetries. Moreover, it is worth to emphasize that, along the highest symmetry lines of the first Brillouin zone, the number of transverse and longitudinal bands is equal to the number of sublattices if the array (e.g., three transverse and three longitudinal dispersions for the Lieb case). We further plot, for comparison, the numerical results with nearest-neighbor couplings only. We observe from the figure that for in-plane polarization, the long-range dipolar interactions completely reconstruct the plasmonic bandstructure. Notably, the topological features (flat bands and conical dispersions) occurring in the nearest-neighbors coupling approximation are not preserved when long-range interactions are included.

5.3.3 The kagome lattice

We conclude our analysis of tripartite plasmonic lattice by considering the kagome lattice. Such an array sketched in Fig. 5.6(a) is characterized by the primitive lattice vectors $\mathbf{t}_1 = d(2, 0)$ and $\mathbf{t}_2 = d(1, \sqrt{3})$ and the two basis vectors $\mathbf{d}_2 = \mathbf{t}_1/2$ and $\mathbf{d}_3 = \mathbf{t}_2/2$. Such an array is best known for its study within the field of frustrated magnets. Like the Lieb lattice the electronic bandstructure in tight-binding systems of the kagome lattice shows conical dispersions together with a flat band. The corresponding first Brillouin zone defined by the reciprocal vectors $\mathbf{b}_1 = \frac{\pi}{\sqrt{3}d}(\sqrt{3}, -1)$ and $\mathbf{b}_2 = \frac{2\pi}{\sqrt{3}d}(0, 1)$ is depicted in Fig. 5.6(b).

We plot the plasmonic dispersions (5.51) for the out-of plane polarized modes as solid lines in Fig. 5.6(c) for the kagome lattice. For comparison, we also show in the figure as dashed lines the bandstructure considering only the nearest-neighbor dipolar interactions. Within such an approximation, we have $f_{\text{nn},11}^{zz}(\mathbf{q}) = 0$ while the remaining lattice sums reduce to

$$f_{\text{nn},12}^{zz}(\mathbf{q}) = 2\cos(q_x d), \tag{5.58a}$$

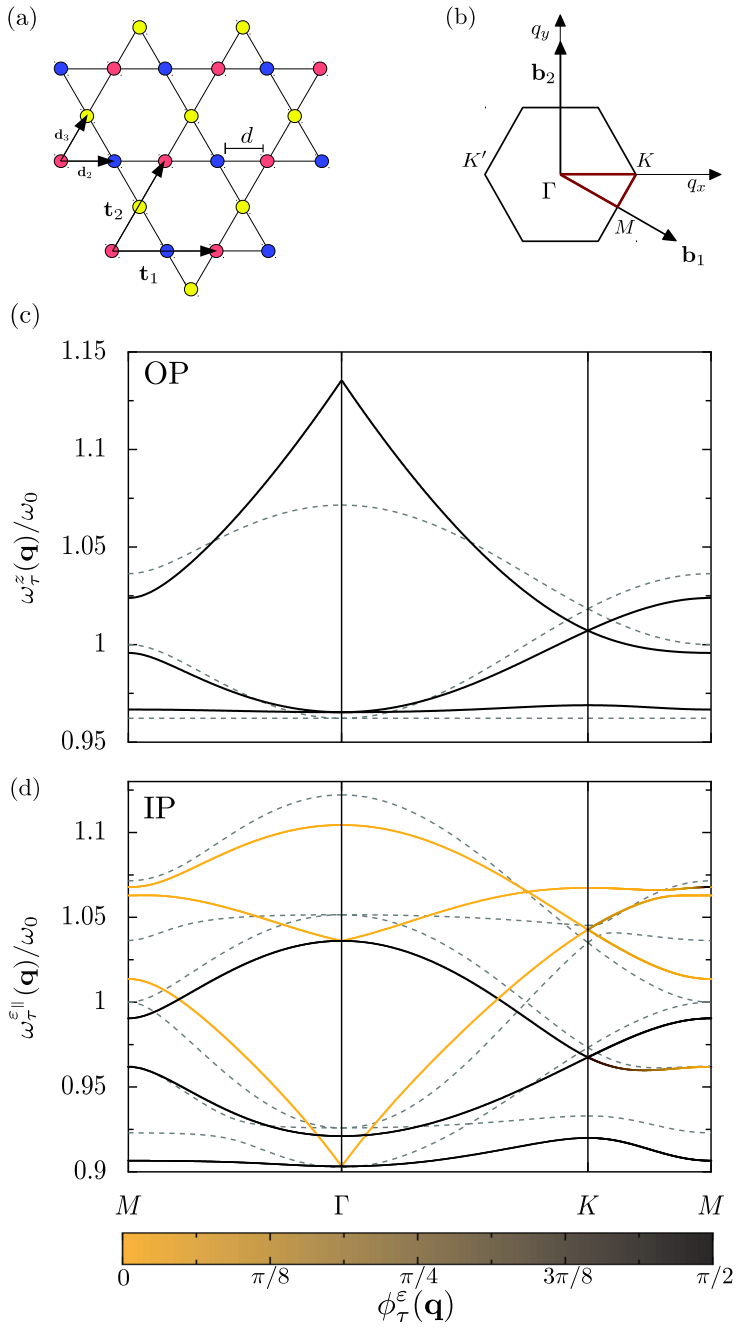

Figure 5.6: (a) Sketch of a kagome lattice with primitive lattice vectors $\mathbf{t}_1 = d\,(2,0)$ and $\mathbf{t}_2 = d\,(1,\sqrt{3})$, and basis vectors $\mathbf{d}_2 = \mathbf{t}_1/2$ and $\mathbf{d}_3 = \mathbf{t}_2/2$. (b) Corresponding first Brillouin zone, with primitive reciprocal vectors $\mathbf{b}_1 = \frac{\pi}{\sqrt{3}d}(\sqrt{3},-1)$ and $\mathbf{b}_2 = \frac{2\pi}{\sqrt{3}d}(0,1)$. (c),(d) Quasistatic plasmonic bandstructure for (c) out-of-plane (OP) and (d) in-plane (IP) polarizations. The dashed and solid lines correspond, respectively, to nearest-neighbor and long-range couplings. Color code of the solid lines: polarization angle (4.28). Same parameters as in Fig. 5.1.

$$f^{zz}_{\mathrm{nn},13}(\mathbf{q}) = 2\cos\left(\frac{[q_x+\sqrt{3}q_y]d}{2}\right), \tag{5.58b}$$

and

$$f^{zz}_{\mathrm{nn},23}(\mathbf{q}) = 2\cos\left(\frac{[q_x-\sqrt{3}q_y]d}{2}\right). \tag{5.58c}$$

Replacing the expressions for the lattice sums into the bandstructure (5.51) yields one flat band

$$\omega^z_{\mathrm{nn},\tau}(\mathbf{q}) = \omega_0\sqrt{1-4\frac{\Omega}{\omega_0}} \tag{5.59a}$$

and two dispersive bands

$$\omega^z_{\mathrm{nn},\tau}(\mathbf{q}) = \omega_0\sqrt{1+2\frac{\Omega}{\omega_0}\left[1\pm\sqrt{1+\Pi^{zz}(\mathbf{q})}\right]} \tag{5.59b}$$

forming a conical intersection at the corner $\mathbf{K} = \frac{2\pi}{3d}(1,0)$ of the first Brillouin zone. Note that we have used the relation $\Sigma^{zz}(\mathbf{q}) - \Pi^{zz}(\mathbf{q}) = 4$ [cf. Eq. (5.50)] to obtain the latter equation. Close to the K point (i.e., for $\mathbf{q} = \mathbf{K} + \mathbf{k}$ with $|\mathbf{k}| \ll |\mathbf{K}|$), the conical dispersions read

$$\omega^z_{\mathrm{nn},\tau}(\mathbf{k}) \simeq \omega_0 + \Omega \pm v^z_{\mathrm{nn}}|\mathbf{k}|, \tag{5.60}$$

with $v^z_{\mathrm{nn}} = \sqrt{3}\Omega d$ the group velocity. Comparing the solid and dashed lines in Fig. 5.6(c), we see that the conical dispersion is robust against long-range interactions. In contrast, the flat band becomes slightly dispersive, although much less than for the case of the Lieb lattice [compare with Fig. 5.5(c)]. We may understand these features by expanding the bandstructure close to the K point. Performing such a procedure thus gives for the non-dispersive band

$$\omega^z_{\tau}(\mathbf{k}) \simeq \omega_0 - \Omega[2 - |f^{zz}_{11}(\mathbf{K})|] \tag{5.61a}$$

and

$$\omega^z_{\tau}(\mathbf{k}) \simeq \omega_0 + \Omega[1 - 2|f^{zz}_{11}(\mathbf{K})|] \pm v^z|\mathbf{k}| \tag{5.61b}$$

for the conical intersection. In the latter equation, we have $f^{zz}_{11}(\mathbf{K}) = -0.291$ and $v^z = 1.49\Omega d$ for the lattice sum and the renormalized group velocity, respectively. Consequently, we see that the long-range quasistatic dipole-dipole interactions renormalize (similarly to the other cases we studied previously) the group velocity associated with the conical dispersion as compared to the nearest-neighbor approximation [cf. Eqs. (5.60) and (5.61b)]. In addition, the plasmonic bandstructure experiences a slight negative shift in energy at the level of the degeneracy point. Note finally that the full quasistatic bandstructure displays also a pronounced cusp close to the Γ point for the upper band while the two other bands do not show such a feature.

Finally, we show in Fig. 5.6(d) the bandstructure obtained by solving numerically the system of equations (4.26) for $\sigma = x, y$ as solid lines. We also plot the numerical results considering only nearest-neighbor couplings (dashed lines) for comparison. As can be seen from the figure, despite the fact that the long-range interactions reconstruct completely the quasistatic plasmonic bandstruc-

ture as compared to the nearest-neighbor result, the conical dispersions in the vicinity of the K and K' points of the first Brillouin zone for the kagome lattice remain qualitatively unaffected. We further note, using the polarization angle (4.28), the existence of purely longitudinal and transverse collective plasmonic modes along the axis of highest symmetries ($M\Gamma$ and ΓK axis).

5.4 Conclusion for Chapter 5

In this chapter we have studied plasmonic collective modes arising from the quasistatic dipole-dipole interactions within various metasurfaces. In order to illustrate the versatility of our method developed in Chapter 4, we have thus studied simple Bravais lattices as well as bipartite and tripartite lattices. We therefore evaluated analytically the general expressions for the plasmonic dispersion as well as the associated eigenstates whenever it is relevant in all the situations mentioned above (i.e., for a number of sublattices $\mathcal{S} = 1, 2$ and 3).

Moreover, we have critically studied the effects of the long-range dipolar interactions on the quasistatic plasmonic dispersion relations. In particular, we have compared these results (obtained analytically or numerically using the algorithm given in Appendix C) with those obtained using the nearest-neighbor approximation. For simple Bravais lattices, we have shown with fully analytical results that the long-range nature of the interactions does not modify qualitatively the results in nearest-neighbor approximation for out-of-plane polarized modes. To illustrate these statements, we have studied the square, the rectangular as well as the hexagonal lattices. The only significant modification that we have reported is the presence of a pronounced cusp in the vicinity of the center of the first Brillouin zone of the lattices we have considered. Such cusps are nevertheless not physical as we will show in the next chapter. We have explained the behavior of such cusps using a mean-field theory in the special case of the square lattice. The study of the in-plane polarized modes in simple Bravais lattices have revealed that the corresponding dispersion relations are more affected by the long-range interactions (lift of degeneracy for example) as compared to the nearest-neighbor coupling. In addition, we also used a mean-field theory (applied to the square lattice) to understand the presence and the absence of cusp observed in the bandstructures.

Then, we have analyzed the case of generic bipartite lattices for which we have calculated analytical expressions for the eigenquantities corresponding to the out-of-plane polarized modes. We have illustrated our general results for the honeycomb lattice. Importantly, we recovered with our transparent theory the numerical results reported by Han *et al.* on the subject. We have been able to demonstrate that the Dirac-like bosons hosted by the metasurface are not ruled out by the long-range interactions. We have shown that such interactions modify only quantitatively the dispersion relations. In addition, we provided details on the in-plane polarized modes within the honeycomb lattices.

The last part of this chapter was devoted to tripartite lattices. In particular, we derived the analytical expressions for the dispersion relations associated with the out-of-plane modes in generic tripartite lattices. We then applied these expressions to the special case of the Lieb and kagome lattices. Importantly, we showed that taking into account the interactions beyond nearest-neighbors affects qualitatively the flat band (existing in nearest-neighbors approximation) which become dispersive. We also studied these effects on the conical dispersions existing in those lattices. We

further calculated the plasmonic bandstructure for the in-plane modes and demonstrated that the long-ranged interactions fully reconstruct these dispersion relations (for both lattices).

Although the quasistatic results presented in this chapter allow us to describe efficiently several features concerning the collective plasmonic modes (e.g., the presence of Dirac-like bosons in the honeycomb lattices), they remain incomplete. Indeed, in order to be able to fully describe the plasmonic bandstructures in metasurfaces, we need to consider the fully-retarded dipolar interactions since we consider sufficiently large arrays. As a matter of fact, we will incorporate these retarded effects within a perturbative treatment of the plasmon-photon coupling Hamiltonian (4.12) in our open-quantum system approach. Chapter 6 will thus be dedicated to the effects induced on the plasmonic system by the photonic environments (i.e., the radiative frequency shift and linewidth). We will relegate to Chapter 7 the effects of the electronic bath, the other environment to which the plasmonic subsystem is coupled to.

Chapter 6

Photonic-induced effects on the collective plasmonic modes

In this chapter, we analyze the various effects induced by the photonic environment onto the quasistatic plasmonic bandstructures discussed in the previous chapter. In particular, we study the radiative linewidths arising from the light-matter coupling as well as the radiative frequency shifts experienced by the plasmonic modes that are due to retardation effects.

6.1 Radiative frequency shifts of the plasmonic bandstructure

We start the analysis of the effects of the photonic modes on the plasmonic subsystem by considering the radiative frequency shifts experienced by the plasmonic modes. Indeed, the photonic environment described by the Hamiltonian (2.16) modifies the quasistatic dispersion relations $\omega_\tau^\varepsilon(\mathbf{q})$ that we introduced in Chapter 5 through the plasmon-photon coupling Hamiltonian (4.12). Within an open-quantum system framework, we thus consider the plasmonic subsystem (4.19) to be weakly coupled to the photonic environment. Such a statement allows us to treat the Hamiltonian (4.12).

6.1.1 Radiative energy corrections within perturbation theory

Along the lines of Refs. [64, 135, 137] which considered one-dimensional systems, we treat the light-matter coupling Hamiltonian (4.12) to second order in standard nondegenerate perturbation theory. Within such a framework, the collective plasmon energy levels are given by

$$E_{n_\tau^\varepsilon(\mathbf{q})} = \hbar\omega_\tau^\varepsilon(\mathbf{q})n_\tau^\varepsilon(\mathbf{q}) + E^{(1)}_{n_\tau^\varepsilon(\mathbf{q})} + E^{(2)}_{n_\tau^\varepsilon(\mathbf{q})}. \tag{6.1}$$

In the latter equation, the first term represents the unperturbed energy of the plasmonic level $n_\tau^\varepsilon(\mathbf{q})$. The first order correction $E^{(1)}_{n_\tau^\varepsilon(\mathbf{q})}$ stems from the diamagnetic term (proportional to the vector potential squared) in the Hamiltonian (4.12) while the second-order one $E^{(2)}_{n_\tau^\varepsilon(\mathbf{q})}$ arises from the paramagnetic term [first term in the r.h.s. of Eq. (4.12)]. We emphasize the fact that the energy corrections arising in (6.1) are only related to the radiative environments. As we will see in the next chapter, supplementary energy corrections originate from the electronic environment. Following standard

quantum mechanics [147], the first and second order corrections to the unperturbed plasmonic levels are given by

$$E^{(1)}_{n^\varepsilon_\tau(\mathbf{q})} = \langle n^\varepsilon_\tau(\mathbf{q}), \mathrm{vac}|H_{\mathrm{pl-ph}}|n^\varepsilon_\tau(\mathbf{q}), \mathrm{vac}\rangle \tag{6.2}$$

and

$$E^{(2)}_{n^\varepsilon_\tau(\mathbf{q})} = \frac{1}{\hbar} \sum_{\substack{m^\varepsilon_\tau(\mathbf{q}),\mathbf{k},\hat{\lambda}_\mathbf{k} \\ [m^\varepsilon_\tau(\mathbf{q}) \neq n^\varepsilon_\tau(\mathbf{q})]}} \frac{\left|\langle m^\varepsilon_\tau(\mathbf{q}), 1^{\hat{\lambda}_\mathbf{k}}_\mathbf{k}|H_{\mathrm{pl-ph}}|n^\varepsilon_\tau(\mathbf{q}), \mathrm{vac}\rangle\right|^2}{[n^\varepsilon_\tau(\mathbf{q}) - m^\varepsilon_\tau(\mathbf{q})]\,\omega^\varepsilon_\tau(\mathbf{q}) - \omega_\mathbf{k}}, \tag{6.3}$$

respectively. In order to evaluate the two latter energies, we first need to rewrite the coupling Hamiltonian (4.12) in terms of the ladder operators $\beta^\varepsilon_\tau(\mathbf{q})$ associated with the plasmonic eigenmodes. Using the inverse Bogoliubov transformation

$$b^\sigma_s(\mathbf{q}) = \sum_{\tau\varepsilon} \left[u^{\varepsilon\sigma *}_{\tau s}(\mathbf{q})\beta^\varepsilon_\tau(\mathbf{q}) - v^{\varepsilon\sigma *}_{\tau s}(\mathbf{q})\beta^{\varepsilon\dagger}_\tau(-\mathbf{q})\right], \tag{6.4}$$

together with the ladder operators written in wavevector space [cf. Eq. (4.7)], we obtain for the plasmonic momentum

$$\mathbf{\Pi}_s(\mathbf{R}_s) = \mathrm{i}\sqrt{\frac{\mathcal{N}_\mathrm{e} m_\mathrm{e}\hbar\omega_0}{2\mathcal{N}}} \sum_{\mathbf{q},\sigma}\sum_{\tau,\varepsilon}\sum_{s,\mathbf{R}_s} \hat{\sigma}\mathrm{e}^{\mathrm{i}\mathbf{q}\cdot\mathbf{R}_s}\left[u^{\varepsilon\sigma *}_{\tau s}(\mathbf{q}) + v^{\varepsilon\sigma *}_{\tau s}(\mathbf{q})\right]\left[\beta^{\varepsilon\dagger}_\tau(-\mathbf{q}) - \beta^\varepsilon_\tau(\mathbf{q})\right]. \tag{6.5}$$

Then, substituting the latter expression into the light-matter coupling Hamiltonian (4.12) yields

$$\begin{aligned} H_{\mathrm{pl-ph}} = {} & \mathrm{i}\hbar \sum_{\mathbf{q},\sigma}\sum_{\tau,\varepsilon}\sum_{s,\mathbf{R}_s}\sum_{\mathbf{k},\hat{\lambda}_\mathbf{k}} \sqrt{\frac{\pi\omega_0^3 a^3}{\mathcal{V}\omega_\mathbf{k}}}\left(\hat{\sigma}\cdot\hat{\lambda}_\mathbf{k}\right)\mathrm{e}^{\mathrm{i}\mathbf{q}\cdot\mathbf{R}_s}[P^{\varepsilon\sigma}_{\tau s}(\mathbf{q})]^* \\ & \times\left[\beta^{\varepsilon\dagger}_\tau(-\mathbf{q}) - \beta^\varepsilon_\tau(\mathbf{q})\right]\left(a^{\hat{\lambda}_\mathbf{k}}_\mathbf{k}\mathrm{e}^{\mathrm{i}\mathbf{k}\cdot\mathbf{R}_s} + a^{\hat{\lambda}_\mathbf{k}\,\dagger}_\mathbf{k}\mathrm{e}^{-\mathrm{i}\mathbf{k}\cdot\mathbf{R}_s}\right) \\ & + \pi\hbar\omega_0^2\frac{a^3}{\mathcal{V}}\sum_{s,\mathbf{R}_s}\sum_{\substack{\mathbf{k},\hat{\lambda}_\mathbf{k} \\ \mathbf{k}',\hat{\lambda}_{\mathbf{k}'}}}\frac{\hat{\lambda}_\mathbf{k}\cdot\hat{\lambda}_{\mathbf{k}'}}{\sqrt{\omega_\mathbf{k}\omega_{\mathbf{k}'}}}\left(a^{\hat{\lambda}_\mathbf{k}}_\mathbf{k}\mathrm{e}^{\mathrm{i}\mathbf{k}\cdot\mathbf{R}_s} + a^{\hat{\lambda}_\mathbf{k}\,\dagger}_\mathbf{k}\mathrm{e}^{-\mathrm{i}\mathbf{k}\cdot\mathbf{R}_s}\right)\left(a^{\hat{\lambda}_{\mathbf{k}'}}_{\mathbf{k}'}\mathrm{e}^{\mathrm{i}\mathbf{k}'\cdot\mathbf{R}_s} + a^{\hat{\lambda}_{\mathbf{k}'}\,\dagger}_{\mathbf{k}'}\mathrm{e}^{-\mathrm{i}\mathbf{k}'\cdot\mathbf{R}_s}\right), \end{aligned} \tag{6.6}$$

where

$$P^{\varepsilon\sigma}_{\tau s}(\mathbf{q}) = u^{\varepsilon\sigma}_{\tau s}(\mathbf{q}) + v^{\varepsilon\sigma}_{\tau s}(\mathbf{q}). \tag{6.7}$$

Consequently, the first energy correction arising from the last term of the latter Hamiltonian reads

$$E^{(1)}_{n^\varepsilon_\tau(\mathbf{q})} = 2\pi\mathcal{S}\mathcal{N}\hbar\omega_0^2\frac{a^3}{\mathcal{V}}\sum_\mathbf{k}\frac{1}{\omega_\mathbf{k}}. \tag{6.8}$$

Importantly, the latter equation does not depend on the quantum number $n^\varepsilon_\tau(\mathbf{q})$ so that the first-order correction to the energy does not participate to the renormalization of the collective plasmon frequency, and merely represents an irrelevant global energy shift (proportional to the total number

$\mathcal{SN}$ of nanoparticles in the array) of the entire plasmonic bandstructure.

We obtain the second-order correction to the energy by substituting the Hamiltonian (6.6) into Eq. (6.3). This procedure thus yields

$$E^{(2)}_{n^{\varepsilon}_{\tau}(\mathbf{q})} = \pi\hbar\omega_0^3\frac{a^3}{\mathcal{V}}\sum_{\mathbf{k},\hat{\lambda}_{\mathbf{k}}}\frac{1}{\omega_{\mathbf{k}}}\left[\frac{n^{\varepsilon}_{\tau}(\mathbf{q})}{\omega^{\varepsilon}_{\tau}(\mathbf{q})-\omega_{\mathbf{k}}}\left|F^{-}_{\mathbf{k},\mathbf{q}}\sum_{s,\sigma}(\hat{\sigma}\cdot\hat{\lambda}_{\mathbf{k}})P^{\varepsilon\sigma}_{\tau s}(\mathbf{q})\mathrm{e}^{-\mathrm{i}(\mathbf{q}-\mathbf{k})\cdot\mathbf{d}_s}\right|^2 - \frac{n^{\varepsilon}_{\tau}(\mathbf{q})+1}{\omega^{\varepsilon}_{\tau}(\mathbf{q})+\omega_{\mathbf{k}}}\left|F^{+}_{\mathbf{k},\mathbf{q}}\sum_{s,\sigma}(\hat{\sigma}\cdot\hat{\lambda}_{\mathbf{k}})P^{\varepsilon\sigma}_{\tau s}(\mathbf{q})\mathrm{e}^{-\mathrm{i}(\mathbf{q}+\mathbf{k})\cdot\mathbf{d}_s}\right|^2\right], \tag{6.9}$$

where the term $P^{\varepsilon\sigma}_{\tau s}(\mathbf{q})$ is given in Eq. (6.7) and where we have defined the array factor as

$$F^{\pm}_{\mathbf{k},\mathbf{q}} = \frac{1}{\sqrt{\mathcal{N}}}\sum_{\mathbf{R}}\mathrm{e}^{\mathrm{i}(\mathbf{q}\pm\mathbf{k})\cdot\mathbf{R}}. \tag{6.10}$$

The radiative frequency shift associated to specific plasmonic eigenmode (with band index τ, polarization ε and wavevector $\mathbf{q}$), given by $\left[E_{n^{\varepsilon}_{\tau}(\mathbf{q})+1}-E_{n^{\varepsilon}_{\tau}(\mathbf{q})}\right]/\hbar-\omega^{\varepsilon}_{\tau}(\mathbf{q})$ thus reads

$$\delta^{\varepsilon}_{\tau}(\mathbf{q}) = \pi\hbar\omega_0^3\frac{a^3}{\mathcal{V}}\sum_{\mathbf{k},\hat{\lambda}_{\mathbf{k}}}\frac{1}{\omega_{\mathbf{k}}}\left[\frac{|F^{-}_{\mathbf{k},\mathbf{q}}|^2}{\omega^{\varepsilon}_{\tau}(\mathbf{q})-\omega_{\mathbf{k}}}\left|\sum_{s,\sigma}(\hat{\sigma}\cdot\hat{\lambda}_{\mathbf{k}})P^{\varepsilon\sigma}_{\tau s}(\mathbf{q})\mathrm{e}^{-\mathrm{i}(\mathbf{q}-\mathbf{k})\cdot\mathbf{d}_s}\right|^2 - \frac{|F^{+}_{\mathbf{k},\mathbf{q}}|^2}{\omega^{\varepsilon}_{\tau}(\mathbf{q})+\omega_{\mathbf{k}}}\left|\sum_{s,\sigma}(\hat{\sigma}\cdot\hat{\lambda}_{\mathbf{k}})P^{\varepsilon\sigma}_{\tau s}(\mathbf{q})\mathrm{e}^{-\mathrm{i}(\mathbf{q}+\mathbf{k})\cdot\mathbf{d}_s}\right|^2\right]. \tag{6.11}$$

The modulus-squared of the array factor $|F^{\pm}_{\mathbf{k},\mathbf{q}}|^2$ entering Eq. (6.11) can be straightforwardly evaluated using the expression $\mathbf{R}=n\mathbf{t}_1+m\mathbf{t}_2$ for the positions $\mathbf{R}$. Since we have $n\in[0,\mathcal{N}_1]$ and $m\in[0,\mathcal{N}_2]$, we have

$$|F^{\pm}_{\mathbf{k},\mathbf{q}}|^2 = \prod_{n=1}^{2}\frac{1}{\mathcal{N}_n}\frac{\sin^2\left([\mathcal{N}_n+1]\,(\mathbf{q}\pm\mathbf{k})\cdot\mathbf{t}_n/2\right)}{\sin^2\left([\mathbf{q}\pm\mathbf{k}]\cdot\mathbf{t}_n/2\right)}. \tag{6.12}$$

In the limit of large metasurfaces (i.e., for $\mathcal{N}_1\mathcal{N}_2\gg 1$), the latter equation has a very simple expression. Indeed, using the two relations [147]

$$\lim_{\varepsilon\to 0}\frac{\varepsilon}{\pi}\frac{\sin^2(x/\varepsilon)}{x}=\delta(x),\quad \lim_{x\to 0}\frac{x^2}{\sin^2(x)}=1, \tag{6.13}$$

we obtain for Eq. (6.12)

$$\begin{aligned}|F^{\pm}_{\mathbf{k},\mathbf{q}}|^2 &\simeq 4\pi^2\delta\left([\mathbf{q}\pm\mathbf{k}]\cdot\mathbf{t}_1\right)\delta\left([\mathbf{q}\pm\mathbf{k}]\cdot\mathbf{t}_2\right)\\ &= \frac{4\pi^2}{|\mathbf{t}_1\times\mathbf{t}_2|}\delta(q_x\pm k_x)\delta(q_y\pm k_y),\end{aligned} \tag{6.14}$$

since the lattice vectors are both lying within the plane of the metasurface. Using the definition

of the array factor (6.14) into Eq. (6.11) thus gives for the radiative frequency shift the general expression

$$\delta_\tau^\varepsilon(\mathbf{q}) = \pi\omega_0^3 \frac{a^3}{\mathcal{V}} \sum_{\mathbf{k},\hat{\lambda}_\mathbf{k}} \frac{\left|\sum_{s\sigma}(\hat{\sigma}\cdot\hat{\lambda}_\mathbf{k})P_{\tau s}^{\varepsilon\sigma}(\mathbf{q})\right|^2}{\omega_\mathbf{k}} \left[\frac{|F_{\mathbf{k},\mathbf{q}}^-|^2}{\omega_\tau^\varepsilon(\mathbf{q})-\omega_\mathbf{k}} - \frac{|F_{\mathbf{k},\mathbf{q}}^+|^2}{\omega_\tau^\varepsilon(\mathbf{q})+\omega_\mathbf{k}}\right]. \tag{6.15}$$

Importantly, the result above is valid for both in-plane and out-of-plane plasmon polarizations. Moreover, we emphasize that such a shift depends on the quasistatic plasmonic eigenstates through the dispersion $\omega_\tau^\varepsilon(\mathbf{q})$ as well as the Bogoliubov coefficients included in the factor $P_{\tau s}^{\varepsilon\sigma}(\mathbf{q})$ introduced in Eq. (6.7). Note finally that Eq. (6.15) scales with the volume of the nanoparticles ($\propto a^3$).

The general expression (6.15) may be written explicitly for particular plasmon polarizations. Therefore, in what follows we evaluate exactly the latter expression for both perpendicular and in-plane polarizations.

6.1.2 Radiative frequency shifts for out-of-plane polarized plasmonic modes

In order to evaluate explicitly the radiative shift (6.15), we first concentrate on the case of perpendicularly (with respect to the plane of the metasurfaces) polarized plasmonic modes. In such a case, we have $\sigma = \varepsilon = z$. Due to the internal structure of the Bogoliubov coefficients [through the lattice sums (4.17)], we can write a "selection rule" for the coefficient $P_{\tau s}^{\varepsilon\sigma}(\mathbf{q})$ in Eq. (6.7) implying that $P_{\tau s}^{z\sigma}(\mathbf{q}) = 0$ for $\sigma = x, y$ [see e.g., Eqs. (5.6) in Sec. 5.1.1]. Inserting the latter selection rule into the expression (6.15) yields for the radiative shift of the out-of-plane modes the expression

$$\delta_\tau^z(\mathbf{q}) = \pi\omega_0^3 \frac{a^3}{\mathcal{V}} \left|\sum_s P_{\tau s}^{zz}(\mathbf{q})\right|^2 \sum_{\mathbf{k},\hat{\lambda}_\mathbf{k}} \frac{(\hat{z}\cdot\hat{\lambda}_\mathbf{k})^2}{\omega_\mathbf{k}} \left[\frac{|F_{\mathbf{k},\mathbf{q}}^-|^2}{\omega_\tau^z(\mathbf{q})-\omega_\mathbf{k}} - \frac{|F_{\mathbf{k},\mathbf{q}}^+|^2}{\omega_\tau^z(\mathbf{q})+\omega_\mathbf{k}}\right]. \tag{6.16}$$

We may write the latter equation explicitly within the continuum limit using Eq. (2.28). Thus, within this approximation Eq. (6.16) reads

$$\delta_\tau^z(\mathbf{q}) \simeq \pi\omega_0^3 a^3 \left|\sum_s P_{\tau s}^{zz}(\mathbf{q})\right|^2 \mathcal{P}\int \frac{\mathrm{d}^3\mathbf{k}}{8\pi^3} \frac{1-(\hat{z}\cdot\hat{k})^2}{\omega_\mathbf{k}} \left[\frac{|F_{\mathbf{k},\mathbf{q}}^-|^2}{\omega_\tau^z(\mathbf{q})-\omega_\mathbf{k}} - \frac{|F_{\mathbf{k},\mathbf{q}}^+|^2}{\omega_\tau^z(\mathbf{q})+\omega_\mathbf{k}}\right]. \tag{6.17}$$

where we have used the relation (2.27) to perform the summation over the photon polarizations. Importantly, we do not need to introduce a cutoff frequency as done for plasmonic chains since the integral in Eq. (6.17) is convergent. Note that we have checked that, introducing a cutoff $k_\mathrm{c} \simeq 1/a$ does not modify importantly the results. We calculate the integral entering Eq. (6.17) in Cartesian coordinates. Indeed, for large metasurfaces, substituting the expression (6.14) for the array factors entering the radiative shift (6.17) allows to readily calculate the integrals over the in-plane photonic degrees of freedoms k_x and k_y. Consequently, writing the photon frequency as

$\omega_{\mathbf{k}} = c\sqrt{k_x^2 + k_y^2 + k_z^2}$, Eq. (6.17) reads as

$$\delta_\tau^z(\mathbf{q}) = \frac{\omega_0^3 a^3}{c|\mathbf{t}_1 \times \mathbf{t}_2|\omega_\tau^z(\mathbf{q})} \left| \sum_s P_{\tau s}^{zz}(\mathbf{q}) \right|^2 \mathcal{P} \int_0^{+\infty} \frac{\mathrm{d}z}{(1+z^2)^{3/2}} \left(\frac{1}{1-\alpha\sqrt{1+z^2}} - \frac{1}{1+\alpha\sqrt{1+z^2}} \right), \tag{6.18}$$

where $\alpha = c|\mathbf{q}|/\omega_\tau^z(\mathbf{q})$ and $z = k_z/|\mathbf{q}|$. The wavevector $\mathbf{q}$ (with $|\mathbf{q}|^2 = q_x^2 + q_y^2$) in the latter quantity arises from the integration over k_x and k_y implying the Dirac Delta distribution [cf. Eq. (6.14)]. Simplifying the term in parenthesis in Eq. (6.18) thus yield the compact form for the radiative shift

$$\delta_\tau^z(\mathbf{q}) = \frac{2\omega_0^3 a^3 |\mathbf{q}|}{|\mathbf{t}_1 \times \mathbf{t}_2| \left[\omega_\tau^z(\mathbf{q})\right]^2} \left| \sum_s P_{\tau s}^{zz}(\mathbf{q}) \right|^2 \mathcal{I}_1\left(\frac{c|\mathbf{q}|}{\omega_\tau^z(\mathbf{q})} \right). \tag{6.19}$$

In the equation above, the function $\mathcal{I}_1(\alpha)$ is given by

$$\mathcal{I}_1(\alpha) = \mathcal{P} \int_0^{+\infty} \frac{\mathrm{d}z}{(1+z^2)\left[1-\alpha^2(1+z^2)\right]} \tag{6.20}$$

with the parameter $\alpha > 0$ and is evaluated in Appendix F. Equipped with the general expression (F.8) of the function $\mathcal{I}_1(\alpha)$, we may now write the radiative shift for the out-of-plane collective modes. Substituting Eq. (F.8) with the definition of the parameter α into the expression (6.19) leads to the general expression

$$\delta_\tau^z(\mathbf{q}) = \frac{\pi\omega_0^3 a^3 |\mathbf{q}|}{|\mathbf{t}_1 \times \mathbf{t}_2| \left[\omega_\tau^z(\mathbf{q})\right]^2} \left| \sum_s P_{\tau s}^{zz}(\mathbf{q}) \right|^2 \left[1 - \frac{c|\mathbf{q}|}{\sqrt{(c|\mathbf{q}|)^2 - \left[\omega_\tau^z(\mathbf{q})\right]^2}} \Theta\Big(c|\mathbf{q}| - \omega_\tau^z(\mathbf{q})\Big) \right] \tag{6.21}$$

for the radiative shift. Importantly, the expression derived above is not periodic in reciprocal space. Such a lack of periodicity stems from the fact that we only consider the interactions between the plasmons and the photons for which the light cone belongs to the first Brillouin zone. Indeed, we should also take into account the interactions with the light cones originating from the other Brillouin zone (i.e., extended representation of the bandstructure) which contributes also to the radiative shift. Therefore, the results we show in the following must be taken with caution at the edges of the first Brillouin zones. Note finally that, such approximated results can be regularized by including the periodicity of the lattice into the photonic wavevector. To do so, one has to consider the array-periodic vector potential defined in Eq. (4.9) in the plasmon-photon coupling Hamiltonian (4.12) instead of the non-periodic one [cf. Eq. (2.15) we used for obtaining the radiative shift (6.21). Such a procedure implies however heavy computational calculations to deliver more accurate results (see Ref. [139]) so we do not show the corrected calculations in this thesis.

As an illustration of the frequency shift (6.21), we depict in panels (a)–(c) of Fig. 6.1 the plasmonic bandstructure for out-of-plane polarized modes $\omega_\tau^z(\mathbf{q}) + \delta_\tau^z(\mathbf{q})$ including Eq. (6.21) for (a) the square, (b) the rectangular and (c) the hexagonal lattices along the high symmetry lines of their respective first Brillouin zones. As can be seen for the square lattice in Fig. 6.1(a), the radiative frequency shift $\delta_\tau^z(\mathbf{q})$ induces an important modification of the quasistatic dispersion $\omega_\tau^z(\mathbf{q})$ which corresponds to purely transverse polarized modes. We observe a similar effect for other simple Bravais arrays presented in Chapter 5, i.e., for the rectangular [Fig. 6.1(b)] and hexagonal lattices

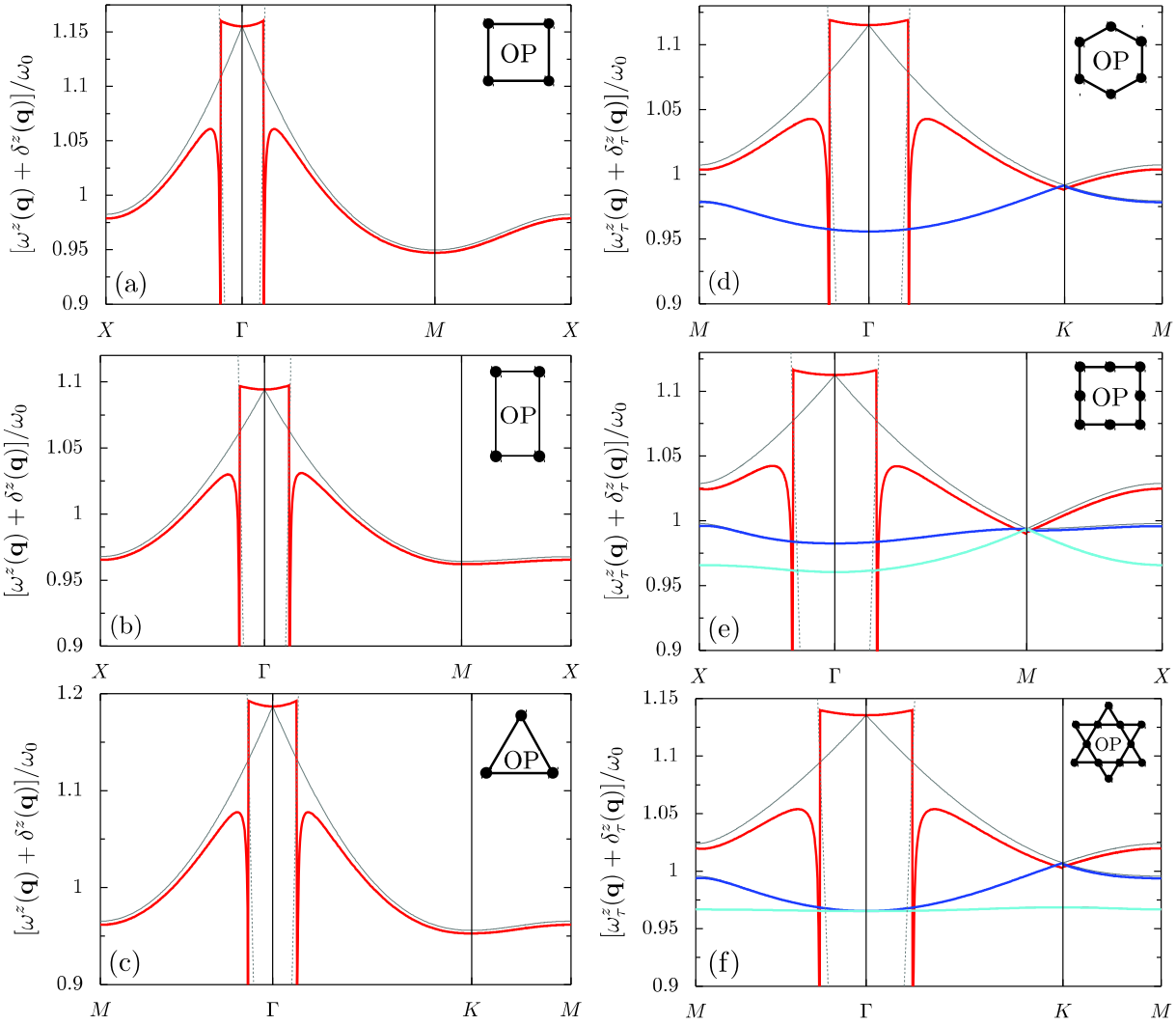

Figure 6.1: The colored lines display the plasmonic band structure $\omega_\tau^z + \delta_\tau^z(\mathbf{q})$ (scaled by ω_0) of the out-of-plane modes including retardation effects and the corresponding radiative frequency shift (6.21) for (a) the square, (b) the rectangular, (c) the hexagonal, (d) the honeycomb, (e) the Lieb and (f) the kagome lattices. For comparison purposes, the thin grey lines reproduce the corresponding quasistatic dispersion relations $\omega_\tau^z(\mathbf{q})$, while the dashed grey lines depict the light cone within each first Brillouin zones. In the figure, $d = 3a$ and $k_0 a = 0.15$.

[Fig. 6.1(c)]. Comparing the fully-retarded dispersion relation (red line) with the quasistatic [grey line in Fig. 6.1(a)], we first observe that the exact plasmonic dispersion diverges at the intersection of the quasistatic bandstructure with the light cone (dashed lines). Importantly, such a divergence was already reported in previous studies for the transverse plasmonic modes in one-dimensional chains using heavy computational calculations based on the fully retarded solutions of Maxwell's equations [133,134] as stated in the introduction of this thesis [see Fig. 1.11(a)]. These singularities are indeed similar to those found within a open-quantum system framework for plasmonic chains [135,137]. Consequently, we expect these features to be the signature of the retardation effects (as for the chains) within the full plasmonic bandstructure in metasurfaces. We here point out that the singularities observed in the dispersion relations showed in Fig. 6.1 arise from calculations based on a second-order perturbative treatment of the light-matter coupling. Therefore, important variations from the plasmon frequency ω_0 should be considered carefully. Interestingly, in contrast with one-dimensional systems for which the radiative shift (of the transverse modes) diverges logarithmically [cf. Eq. (3.50)], Eq. (6.21) behaves as an inverse square root close to the singularities.

Discussion concerning the cusp

As can be seen from Fig. 6.1(a), taking into account the radiative shift implies that the cusp appearing at the Γ point of the first Brillouin zone within the quasistatic approximation vanishes (compare the red and grey lines in the figure). Such a disappearance stems from the fact that accounting for the retardation effects allows to correct the results obtained within the quasistatic approximation. Indeed, when calculating the quasistatic bandstructure, we consider instantaneous interactions (i.e., the quasistatic dipole-dipole interactions) to be responsible for the collective plasmonic modes. Such instantaneous contributions [cf. Eq. (4.6)] to the plasmonic Hamiltonian $H_{\rm pl}$ [Eq. (4.2)] are in fact no longer valid for large metastructures for which the interactions between nanoparticles that are far apart are retarded since the condition $k_0 d \ll 1$ does not hold anymore. The quasistatic term is in reality counterbalanced exactly by the light-matter interactions encoded in the Hamiltonian (4.12). In fact, the light-matter interaction give rise to a fully retarded interacting term as well as an instantaneous contribution [154]. While the former corresponds to the real fully-retarded electromagnetic interactions, the latter cancels out exactly the quasistatic term in $H_{\rm pl}$, so that the Hamiltonian $H_{\rm pl} + H_{\rm pl-ph}$ accounts for fully-retarded contributions.

As an insight of this effect, we may study the radiative shift (6.21) in the vicinity of the Γ point for the square lattice [cf. Fig. 6.1(a)]. For $|\mathbf{q}|d \ll 1$, Eq. (6.21) reduces to

$$\delta^z(\mathbf{q}) \simeq 2\pi\Omega|\mathbf{q}|d + \mathcal{O}(|\mathbf{q}|d)^3, \tag{6.22}$$

in the regime of interest $\Omega \ll \omega_0$. As we can see from the expansion (6.22), the linear $|\mathbf{q}|$–dependance cancels out exactly the one of $\omega^z(\mathbf{q})$ in this regime of parameters [cf. Eq. (5.23)]. Consequently, we find for the fully-retarded dispersion

$$\omega^z(\mathbf{q}) + \delta^z(\mathbf{q}) \simeq \omega_0 + \Omega\left[4 + \sqrt{2}\pi + (|\mathbf{q}|d)^2\left(\frac{\pi}{\sqrt{2}} - 1\right)\right] \tag{6.23}$$

close to the Γ point, leading to a quadratic dependence on $|\mathbf{q}|d$ of the dispersion relation. The results

presented in Fig. 6.1(a) thus demonstrate that considering the retardation effects is crucial for the study of the collective plasmonic modes in metasurfaces of near-field-coupled nanoparticles, since the dispersion relations are qualitatively affected by the interactions with free photons. Such renormalization effects are more prominent in two-dimensional metamaterials than in one-dimensional plasmonic chains. Indeed, in one-dimensional plasmonic systems, apart from the divergence of the dispersion relation at the intersection with the light cone [see Fig. 3.8], the bandstructure is qualitatively unaffected by retardation effects [135, 137].

We now consider the fully-retarded dispersion relations including Eq. (6.21) for the out-of-plane polarized plasmonic modes within Bravais lattices with a basis. In Fig. 6.1, we show in panels (d)–(f), the full bandstructures $\omega_\tau^z(\mathbf{q}) + \delta_\tau^z(\mathbf{q})$ for (d) the honeycomb, (e) the Lieb and (f) the kagome lattices along the high symmetry lines of their respective first Brillouin zones. In Fig. 6.1(d), we plot the plasmonic bandstructure including retardation effects (colored lines) of the out-of-plane modes for the honeycomb lattice. For comparison purposes, we also show as grey lines the corresponding quasistatic bandstructure shown in Fig. 5.4(c). The upper band ($\tau = +1$) shows a similar profile as that of Fig. 6.1(a)–(c). It displays a divergence at the crossing between the light line (dashed line) and the quasistatic dispersion as well as the absence of a cusp at the Γ point. In contrast, the low energy band ($\tau = -1$) does not experience a noticeable (on the scale of the figure) renormalization induced by the light-matter coupling. Such modes are thus coined "dark" since they only weakly couple to light. In the case of the honeycomb lattice, we may understand this phenomenon by looking at the exact value of the coefficient $|\sum_s P_{\tau s}^{zz}(\mathbf{q})|^2$ appearing in the expression of the shift (6.21) using the expression of the Bogoliubov coefficients (5.40) and (5.41) calculated in Sec. 5.2.1. Thus, using Eqs. (5.40) and (5.41), the "brightness parameter" reads

$$\left|\sum_s P_{\tau s}^{zz}(\mathbf{q})\right|^2 = \frac{\omega_\tau^z(\mathbf{q})}{2\omega_0}\left|1 + \tau\frac{f_{12}^{zz}(\mathbf{q})}{|f_{12}^{zz}(\mathbf{q})|}\right|^2 \simeq \begin{cases} 2\omega_\tau^z(\mathbf{q})/\omega_0, & \tau = +1 \\ 0, & \tau = -1 \end{cases} \tag{6.24}$$

since the phase $f_{12}^{zz}(\mathbf{q})/|f_{12}^{zz}(\mathbf{q})|$ takes its values close to 1 as we have numerically checked. In a simple picture the dark modes can be seen as single LSPs oscillating out-of-phase within each unequivalent sublattices of the honeycomb lattice. Conversely, the plasmonic modes showing a significant coupling to light [red lines in Fig. 6.1(d)] are called "bright" modes. The latter modes correspond to LSP within each inequivalent sublattices oscillating in phase.

Importantly, the Dirac cone exhibited by the quasistatic bandstructure remains unaffected by the light-matter coupling since the Dirac point is situated outside the light cone within our regime of parameters. In Fig. 6.1(d), we nevertheless observe a slight mismatch between the two bands in the vicinity of the corner K of the first Brillouin zone. Such a mismatch originates from the non-periodicity of the radiative shift (6.21). Full polaritonic numerical calculations [139] has shown that taking the light-matter coupling exactly (and not perturbatively) allows for a full recovery of the conical dispersion. Consequently, the retardation effects do not affect the Dirac physics existing at the K point of the first Brillouin zone discussed in Sec. 5.2.2.

We finally show in panels (e) and (f) of Fig. 6.1 the fully-retarded dispersion relations of the out-of-plane plasmonic modes for the Lieb and kagome lattices, respectively. Along the lines of the above discussion on the honeycomb lattice, the most energetic bands in both cases (red lines) correspond to bright transverse collective plasmons and thus display a singularity at the crossing

between the light cone and their quasistatic dispersions as well as the absence of cusp at the Γ point of their respective first Brillouin zones. Moreover, the blue and cyan lines in both cases correspond to dark plasmonic modes. Similarly to Eq. (6.24), such an absence of interaction with the light can be understood by evaluating (numerically) the value of $|\sum_s P^{zz}_{\tau s}(\mathbf{q})|^2$ for the radiative shift. Note that in tripartite lattices the respective orientation of the isolated LSPs within each sublattices are less simple to explain as it is for bipartite lattices. In principle, one of the "dark" band corresponds to a fully vanishing coupling to light while the second one to a very weak (almost vanishing) coupling.

6.1.3 Radiative frequency shifts for in-plane polarized modes

We now treat the particular case of the radiative shifts associated with the plasmonic modes polarized within the plane of the metasurface for which the general expression (6.15) may be written explicitly. In order to derive such an analytic expression, we start from the general expression (6.15) derived in Sec. 6.1.1 with $\varepsilon = \varepsilon_\parallel$. Thus, we have the "selection rule" $P^{\varepsilon_\parallel z}_{\tau s}(\mathbf{q}) = 0$ for the coefficients (6.7) entering the radiative shift. Consequently, we write explicitly in the general expression (6.15), the summation over the plasmon polarization leading to

$$\delta^{\varepsilon_\parallel}_\tau(\mathbf{q}) = \pi\omega_0^3\frac{a^3}{\mathcal{V}}\sum_{\mathbf{k},\hat{\lambda}_\mathbf{k}}\frac{1}{\omega_\mathbf{k}}\left|\sum_s\left[(\hat{x}\cdot\hat{\lambda}_\mathbf{k})P^{\varepsilon_\parallel x}_{\tau s}(\mathbf{q}) + (\hat{y}\cdot\hat{\lambda}_\mathbf{k})P^{\varepsilon_\parallel y}_{\tau s}(\mathbf{q})\right]\right|^2 \times\left[\frac{|F^-_{\mathbf{k},\mathbf{q}}|^2}{\omega^\varepsilon_\tau(\mathbf{q})-\omega_\mathbf{k}} - \frac{|F^+_{\mathbf{k},\mathbf{q}}|^2}{\omega^\varepsilon_\tau(\mathbf{q})+\omega_\mathbf{k}}\right]. \tag{6.25}$$

In the latter equation, we write the term into squared brackets as

$$\left|\sum_s\left[(\hat{x}\cdot\hat{\lambda}_\mathbf{k})P^{\varepsilon_\parallel x}_{\tau s}(\mathbf{q}) + (\hat{y}\cdot\hat{\lambda}_\mathbf{k})P^{\varepsilon_\parallel y}_{\tau s}(\mathbf{q})\right]\right|^2 = \left|\hat{x}\cdot\hat{\lambda}_\mathbf{k}\right|^2\left|\sum_s P^{\varepsilon_\parallel x}_{\tau s}(\mathbf{q})\right|^2 + \left|\hat{y}\cdot\hat{\lambda}_\mathbf{k}\right|^2\left|\sum_s P^{\varepsilon_\parallel y}_{\tau s}(\mathbf{q})\right|^2 + 2(\hat{x}\cdot\hat{\lambda}_\mathbf{k})(\hat{y}\cdot\hat{\lambda}_\mathbf{k})\mathrm{Re}\left\{\sum_{ss'}P^{\varepsilon_\parallel x}_{\tau s}P^{\varepsilon_\parallel y}_{\tau s'}\right\}, \tag{6.26}$$

so that we can perform the summation over photonic polarizations [using Eq. (2.27)] into Eq. (6.25). We proceed with the evaluation of the summation over photonic wavevectors by going to the continuum limit (2.28) and performing directly the integral over the in-plane degrees of freedom k_x and k_y using the expression (6.14) for the array factor. Performing these steps yields for the radiative

shift of the in-plane modes (belonging to a given band τ) the expression

$$\delta_\tau^{\varepsilon_\parallel}(\mathbf{q}) \simeq \frac{2\omega_0^3 a^3 |\mathbf{q}|}{|\mathbf{t}_1 \times \mathbf{t}_2| \left[\omega_\tau^{\varepsilon_\parallel}(\mathbf{q})\right]^2} \mathcal{P} \int_0^{+\infty} \frac{\mathrm{d}z}{(1+z^2)\left[1-\alpha^2(1+z^2)\right]} \times \left\{ \left[\left(\frac{q_y}{|\mathbf{q}|}\right)^2 + z^2 \right] \left| \sum_s P_{\tau s}^{\varepsilon_\parallel x}(\mathbf{q}) \right|^2 + \left[\left(\frac{q_x}{|\mathbf{q}|}\right)^2 + z^2 \right] \left| \sum_s P_{\tau s}^{\varepsilon_\parallel y}(\mathbf{q}) \right|^2 - 2\frac{q_x q_y}{|\mathbf{q}|^2} \mathrm{Re}\left\{ \sum_{ss'} P_{\tau s}^{\varepsilon_\parallel x}(\mathbf{q}) P_{\tau s'}^{\varepsilon_\parallel y}(\mathbf{q}) \right\} \right\}, \tag{6.27}$$

where we have defined the parameters $\alpha = c|\mathbf{q}|/\omega_\tau^{\varepsilon_\parallel}(\mathbf{q})$ and $z = k_z/|\mathbf{q}|$. We then write, using $|\mathbf{q}|^2 = q_x^2 + q_y^2$, the latter equation as

$$\delta_\tau^{\varepsilon_\parallel}(\mathbf{q}) = \frac{2\omega_0^3 a^3 |\mathbf{q}|}{|\mathbf{t}_1 \times \mathbf{t}_2| \left[\omega_\tau^{\varepsilon_\parallel}(\mathbf{q})\right]^2} \left\{ \mathcal{I}_1(\alpha) \left[\left(\frac{q_y}{|\mathbf{q}|}\right)^2 \left| \sum_s P_{\tau s}^{\varepsilon_\parallel x}(\mathbf{q}) \right|^2 + \left(\frac{q_x}{|\mathbf{q}|}\right)^2 \left| \sum_s P_{\tau s}^{\varepsilon_\parallel y}(\mathbf{q}) \right|^2 - 2\frac{q_x q_y}{|\mathbf{q}|^2} \mathrm{Re}\left\{ \sum_{ss'} P_{\tau s}^{\varepsilon_\parallel x}(\mathbf{q}) P_{\tau s'}^{\varepsilon_\parallel y}(\mathbf{q}) \right\} \right] + \mathcal{I}_2(\alpha) \left[\left| \sum_s P_{\tau s}^{\varepsilon_\parallel x}(\mathbf{q}) \right|^2 + \left| \sum_s P_{\tau s}^{\varepsilon_\parallel y}(\mathbf{q}) \right|^2 \right] \right\}, \tag{6.28}$$

where the integral $\mathcal{I}_1(\alpha)$ is given by Eq. (F.8) and the function $\mathcal{I}_2(\alpha)$ is defined as

$$\mathcal{I}_2(\alpha) = \mathcal{P} \int_0^{+\infty} \frac{z^2 \mathrm{d}z}{(1+z^2)\left[1-\alpha^2(1+z^2)\right]}, \tag{6.29}$$

with $\alpha > 0$. The latter integral is evaluated in Appendix F. Thus, using the expressions for the functions $\mathcal{I}_1(\alpha)$ and $\mathcal{I}_2(\alpha)$ with $\alpha = c|\mathbf{q}|/\omega_\tau^{\varepsilon_\parallel}(\mathbf{q})$ [cf. Eqs. (F.8) and (F.11), respectively], the radiative shift of the in-plane polarized plasmonic modes finally reads

$$\delta_\tau^{\varepsilon_\parallel}(\mathbf{q}) = -\frac{\omega_0^3 a^3 |\mathbf{q}|}{|\mathbf{t}_1 \times \mathbf{t}_2| \left[\omega_\tau^{\varepsilon_\parallel}(\mathbf{q})\right]^2} \times \left\{ \left| \sum_s \left[\frac{q_x}{|\mathbf{q}|} P_{\tau s}^{\varepsilon_\parallel x}(\mathbf{q}) + \frac{q_y}{|\mathbf{q}|} P_{\tau s}^{\varepsilon_\parallel y}(\mathbf{q}) \right] \right|^2 \left[1 - \frac{c|\mathbf{q}|}{\sqrt{(c|\mathbf{q}|)^2 - \left[\omega_\tau^{\varepsilon_\parallel}(\mathbf{q})\right]^2}} \Theta\Big(c|\mathbf{q}| - \omega_{\varepsilon_\parallel}(\mathbf{q})\Big) \right] + \left(\left| \sum_s P_{\tau s}^{\varepsilon_\parallel x}(\mathbf{q}) \right|^2 + \left| \sum_s P_{\tau s}^{\varepsilon_\parallel y}(\mathbf{q}) \right|^2 \right) \frac{\left[\omega_\tau^{\varepsilon_\parallel}(\mathbf{q})\right]^2}{c|\mathbf{q}| \sqrt{(c|\mathbf{q}|)^2 - \left[\omega_\tau^{\varepsilon_\parallel}(\mathbf{q})\right]^2}} \Theta\Big(c|\mathbf{q}| - \omega_{\varepsilon_\parallel}(\mathbf{q})\Big) \right\}. \tag{6.30}$$

As an illustration, we display in Fig. 6.2, the fully-retarded dispersion relation of the in-plane plasmonic modes for the various metasurfaces discussed in Chapter 5. In each panel of the figure, we plot as grey lines their respective quasistatic bandstructures for comparison. The fully-retarded

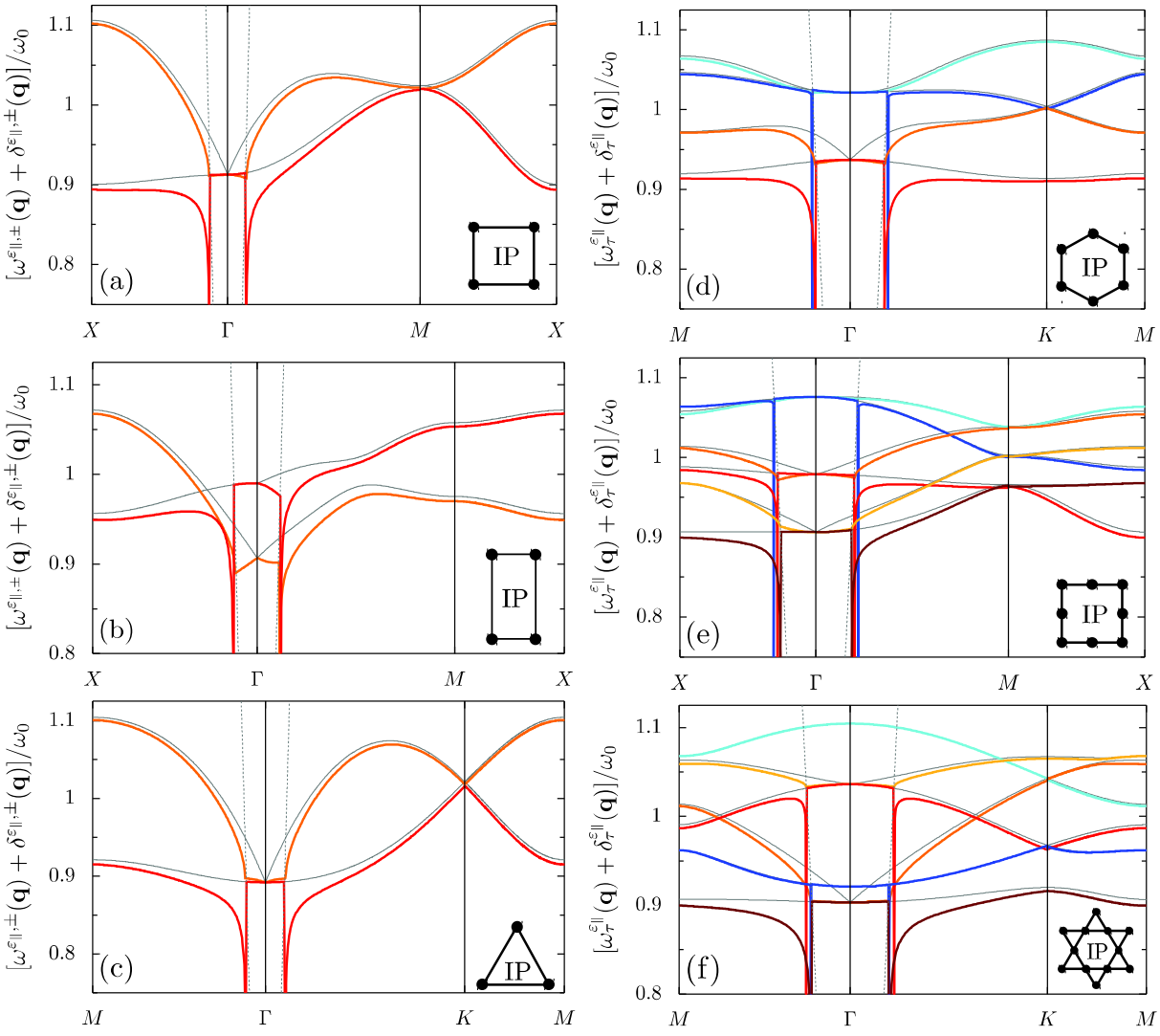

Figure 6.2: The colored lines display the plasmonic band structure $\omega_\tau^{\varepsilon\parallel} + \delta_\tau^{\varepsilon\parallel}(\mathbf{q})$ (scaled by ω_0) of the in-plane modes including retardation effects and the corresponding radiative frequency shift (6.30) for (a) the square, (b) the rectangular, (c) the hexagonal, (d) the honeycomb, (e) the Lieb and (f) the kagome lattices. For comparison purposes, the thin grey lines reproduce the corresponding quasistatic dispersion relations $\omega_\tau^{\bar{\varepsilon}\parallel}(\mathbf{q})$, while the dashed grey lines depict the light cone within each first Brillouin zones. Same parameters as in Fig. 6.1.

results showen in Fig. 6.2(a) correspond to those of the square lattice (see red and orange lines) and three important features appear when comparing them to the quasistatic ones. First, the low energy band (cf. red line) corresponding essentially to transverse modes [see Fig. 5.1(d)] present a singularity at the intersection of the quasistatic dispersion with the light cone. Conversely, the upper band (orange line), which corresponds mostly to longitudinal modes, does not show any singularity at the intersection with the light cone. Such an interesting feature is strongly reminiscent of what occurs in plasmonic chains for the longitudinal modes (see e.g., Refs. [133–135, 137]). Finally, the cusp appearing in the quasistatic dispersion relation in the vicinity of the Γ point is suppressed when considering the retardation effects. We explain the vanishing of the cusp for the in-plane polarized modes using the same arguments than for the case of the out-of-plane modes [cf. Sec. 6.1.2]. In other words, the cusps are not physical and arise from the quasistatic treatment which are corrected by the inclusion of the retardation effects.

Interestingly we notice that for the rectangular lattice shown in Fig. 6.2(b) the upper band also present a singularity along the ΓM axis while it is not the case for the other simple Bravais lattices [see Figs. 6.2(a),(c)]. We attribute this feature to the fact that along this particular axis, the rectangular lattice show less symmetries than along the $X\Gamma$ one and the modes are consequently not purely longitudinal [cf. Fig. 5.3(b)]. We can however draw identical conclusions as for the square case for the plasmonic modes in hexagonal lattices [Fig. 6.2(c)].

We finally present in panels (d)–(f) of Fig. 6.2, the fully-retarded dispersion relations corresponding of the in-plane modes for (d) the honeycomb, (e) the Lieb and (f) the kagome lattices. Within all this Bravais lattice with a basis, we notice that some of the bands display singularities at the intersection of the quasistatic dispersion relations with the light cones. Comparing Fig. 6.2 with the quasistatic bandstructrures of each lattices [cf. Figs. 5.4(d), 5.5(d) and 5.6(d)], we notice that such singularities are associated to transverse modes. Conversely, the bands which do not show such singularities correspond to longitudinally-polarized modes and do not display cusps (with respect to their quasistatic counterparts, cf. Chapter 5). In addition, the blue and cyan bands in the panels (d),(e) and (f) present only a weak coupling with the light and thus correspond to dark modes. However, we will see that these dark bands are associated to longitudinal and transverse modes similarly to the bright ones. Such a statement can be verified by analyzing simultaneously the polarization angle (4.28) of the modes alongside with their corresponding radiative shift to identify the polarization of the dark modes. Alternatively, we will show that in most of the situations, we may study the radiative linewidth for this purpose. Such a linewidth is the subject we will now discuss in the next section.

6.2 Radiative linewidths

We now concentrate on the second effect induced by the photonic bath onto the plasmonic subsystem, i.e., the radiative contribution to the finite linewidth of the collective modes (the remaining arises from non-radiative contributions). In what follows, we thus evaluate the radiative decay rate of the modes. To this end, we again treat the plasmon-photon coupling Hamiltonian (6.6) as a weak perturbation to the plasmonic subsystem $H_{\rm pl}$ (similarly as done for the radiative shift in Sec. 6.1). As for the radiative shift, we first derive a general analytical expression and then explicit it for out-of-plane and in-plane polarizations.

6.2.1 Fermi's golden rule for arbitrary polarization

In the weakly-coupling regime, the radiative decay rate of the plasmonic eigenmode $|1_\tau^\varepsilon(\mathbf{q})\rangle$ with band index τ, polarization ε and wavevector $\mathbf{q}$ is given by the Fermi golden rule

$$\gamma_\tau^\varepsilon(\mathbf{q}) = \frac{2\pi}{\hbar^2}\sum_{\mathbf{k},\hat{\lambda}_\mathbf{k}} \left|\langle 0_\tau^\varepsilon(\mathbf{q}), 1_\mathbf{k}^{\hat{\lambda}_\mathbf{k}}|H_{\mathrm{pl-ph}}|1_\tau^\varepsilon(\mathbf{q}), \mathrm{vac}\rangle\right|^2 \delta\left(\omega_\tau^\varepsilon(\mathbf{q}) - \omega_\mathbf{k}\right) \tag{6.31}$$

where the plasmon-photon coupling Hamiltonian $H_{\mathrm{pl-ph}}$ is given by Eq. (6.6). Writing explicitly the latter equation yields for the radiative decay rate

$$\gamma_\tau^\varepsilon(\mathbf{q}) = 2\pi^2\omega_0^3\frac{a^3}{\mathcal{V}}\sum_{\mathbf{k},\hat{\lambda}_\mathbf{k}}\frac{1}{\omega_\mathbf{k}}\left|F_{\mathbf{k},\mathbf{q}}^-\sum_{s\sigma}(\hat{\sigma}\cdot\hat{\lambda}_\mathbf{k})\mathrm{e}^{-\mathrm{i}(\mathbf{q}-\mathbf{k})\cdot\mathbf{d}_s}P_{\tau s}^{\varepsilon\sigma}(\mathbf{q})\right|^2\delta\left(\omega_\tau^\varepsilon(\mathbf{q})-\omega_\mathbf{k}\right), \tag{6.32}$$

where $P_{\tau s}^{\varepsilon\sigma}(\mathbf{q})$ is the coefficient given in Eq. (6.7) and $F_{\mathbf{k},\mathbf{q}}^-$ the array factor introduced in Eq. (6.10). In the large metasurface limit ($\mathcal{N}\gg 1$) the latter equation can be simplified using Eq. (6.14) to yield the general expression

$$\gamma_\tau^\varepsilon(\mathbf{q}) = 2\pi^2\omega_0^3\frac{a^3}{\mathcal{V}}\sum_{\mathbf{k},\hat{\lambda}_\mathbf{k}}\frac{|F_{\mathbf{k},\mathbf{q}}^-|^2}{\omega_\mathbf{k}}\left|\sum_{s\sigma}(\hat{\sigma}\cdot\hat{\lambda}_\mathbf{k})P_{\tau s}^{\varepsilon\sigma}(\mathbf{q})\right|^2\delta\left(\omega_\tau^\varepsilon(\mathbf{q})-\omega_\mathbf{k}\right). \tag{6.33}$$

The latter equation is valid for both out-of-plane and in-plane polarized plasmonic modes. Moreover, in a similar manner as done for the radiative frequency shifts, we may derive explicit results analytically for both of the aforementioned polarization of the modes.

6.2.2 Radiative linewidths associated with the out-of-plane polarized modes

In the particular case of plasmonic modes polarized perpendicularly to the plane of the metasurface ($\sigma=\varepsilon=z$), the general expression for the radiative decay rate (6.33) reduces to

$$\gamma_\tau^z(\mathbf{q}) = 2\pi^2\omega_0^3\frac{a^3}{\mathcal{V}}\left|\sum_s P_{\tau s}^{zz}(\mathbf{q})\right|^2\sum_{\mathbf{k},\hat{\lambda}_\mathbf{k}}\frac{|F_{\mathbf{k},\mathbf{q}}^-|^2}{\omega_\mathbf{k}}|\hat{z}\cdot\hat{\lambda}_\mathbf{k}|^2\delta\left(\omega_\tau^\varepsilon(\mathbf{q})-\omega_\mathbf{k}\right) \tag{6.34}$$

since $P_{\tau s}^{z\sigma}(\mathbf{q})=0$ for $\sigma=x,y$. We may write explicitly the latter expression using the continuum limit [cf. Eq. (2.28)] as well as Eq. (2.27) for the summation over photonic polarizations. Performing these steps thus yields the expression

$$\gamma_\tau^z(\mathbf{q}) \simeq \frac{\omega_0^3a^3}{4\pi}\left|\sum_s P_{\tau s}^{zz}(\mathbf{q})\right|^2\int\mathrm{d}^3\mathbf{k}\frac{|F_{\mathbf{k},\mathbf{q}}^-|^2}{\omega_\mathbf{k}}[1-(\hat{z}\cdot\hat{k})^2]\delta\left(\omega_\tau^\varepsilon(\mathbf{q})-\omega_\mathbf{k}\right). \tag{6.35}$$

Then, substituting the expression (6.14) into the latter equation and integrating over the photonic degrees of freedom k_x and k_y gives for the radiative damping

$$\begin{aligned}\gamma_\tau^z(\mathbf{q}) &= \frac{\pi\omega_0^3 a^3}{c|\mathbf{t}_1\times\mathbf{t}_2|\omega_\tau^z(\mathbf{q})}\left|\sum_s P_{\tau s}^{zz}(\mathbf{q})\right|^2 \int_{-\infty}^{+\infty}\frac{\mathrm{d}z}{(1+z^2)^{3/2}}\delta\left(1-\frac{c|\mathbf{q}|}{\omega_\tau^z(\mathbf{q})}\sqrt{1+z^2}\right)\\ &= \frac{\pi\omega_0^3 a^3}{c|\mathbf{t}_1\times\mathbf{t}_2|\omega_\tau^z(\mathbf{q})}\left|\sum_s P_{\tau s}^{zz}(\mathbf{q})\right|^2 \mathcal{K}_1\left(\frac{c|\mathbf{q}|}{\omega_\tau^z(\mathbf{q})}\right),\end{aligned} \tag{6.36}$$

with $z = k_z/|\mathbf{q}|$ and where the integral

$$\mathcal{K}_1(\alpha) = \int_{-\infty}^{+\infty}\frac{\mathrm{d}z}{(1+z^2)^{3/2}}\delta\left(1-\alpha\sqrt{1+z^2}\right)\Theta\left(1-\alpha\right) \tag{6.37}$$

is evaluated in Appendix F. Importantly in Eq. (6.37), only the plasmons with frequency $\omega_\tau^z(\mathbf{q})$ smaller than $\omega_\mathbf{k}$ (i.e., inside the light cone) can decay radiatively so that the constant $\alpha = c|\mathbf{q}|/\omega_\tau^z(\mathbf{q})$ is smaller than 1. Such a condition is thus taken into account by introducing a Heaviside-step function within the expression (6.37). Thus, inserting Eq. (F.14) into Eq. (6.36) we obtain for the radiative decay rate

$$\gamma_\tau^z(\mathbf{q}) = \frac{2\pi\omega_0^3 a^3 c|\mathbf{q}|^2}{|\mathbf{t}_1\times\mathbf{t}_2|\left[\omega_\tau^z(\mathbf{q})\right]^2}\left|\sum_s P_{\tau s}^{zz}(\mathbf{q})\right|^2 \frac{\Theta\left(\omega_\tau^z(\mathbf{q})-c|\mathbf{q}|\right)}{\sqrt{\left[\omega_\tau^z(\mathbf{q})\right]^2-(c|\mathbf{q}|)^2}}. \tag{6.38}$$

We plot in Fig. 6.3, the radiative decay rate (6.38) for the out-of-plane polarized modes of the square [panel (a)], the honeycomb [panel (b)] and the Lieb lattices [panel (c)] along the high symmetry lines connecting the Γ point of their respective first Brillouin zones. We do not show in the figure the results in the entire first Brillouin zones since the damping rate vanishes for wavevectors outside the light cone (i.e., $\mathbf{q} \gtrsim k_0$). This statement can be easily inferred from the Heaviside step function in Eq. (6.38). Morover, the results shown in Fig. 6.3 are scaled by the radiative decay rate of a single isolated nanoparticle γ_0 [see Eq. (1.7)].

For the square lattice [Fig. 6.3(a)], the plasmonic modes polarized perpendicularly to the plane of the array present a highly superradiant profile, i.e., $\gamma^z(\mathbf{q}) \gg \gamma_0$, inside of the light cone for wavevectors not too close to the center of the first Brillouin zone. In contrast, the decay rate vanishes outside the light cone. From the figure, we observe that the radiative decay rate $\gamma^z(\mathbf{q})$ increases rapidly as $\mathbf{q}$ moves away from the Γ point and diverges at the intersection of the quasistatic dispersion with the light cone. Such singularities are related to those we have reported in the fully-retarded dispersion relations (see Sec. 6.1). Importantly, similarly to the radiative shift, the divergences appear as a result of our perturbative calculations. Therefore, they should be renormalized by performing an exact treatment of the light-matter interaction. Interestingly, the superradiant behavior of the radiative damping rate observed in Fig. 6.3(a) is reminiscent to the one observed in one-dimensional chains (cf. Fig. 3.10 and e.g., Refs. [80, 133–135, 137]). In metasurfaces, such effects appear nevertheless to be much more prominent [$\gamma^z(\mathbf{q})$ takes very large values while in chains $\gamma_q^{x(y)}$ goes up to $5\gamma_0$, comparing the scales in Figs. 3.10 and 6.3], due to the enhanced constructive interferences between the the dipolar fields arising from each individual LSP.

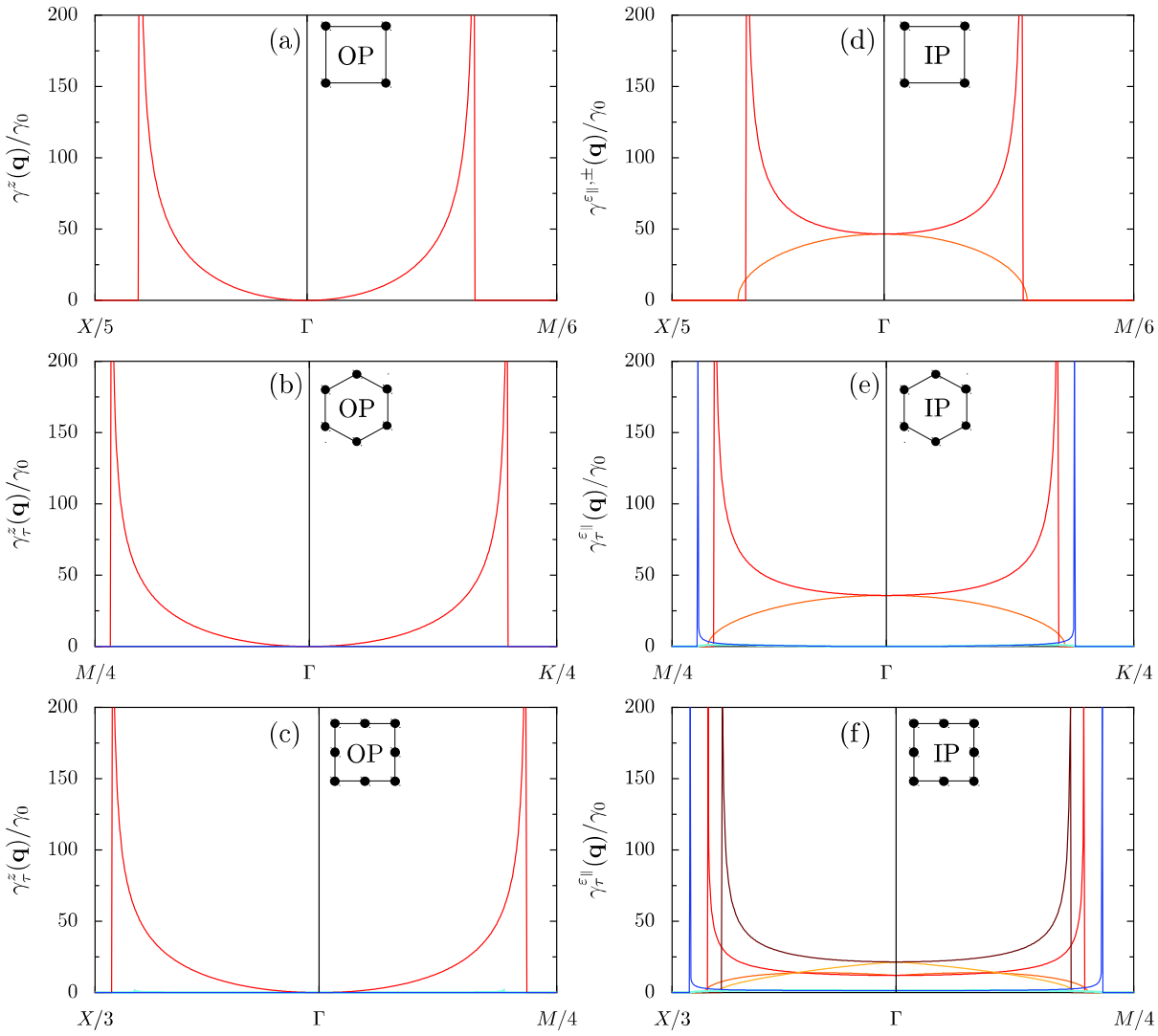

Figure 6.3: The colored lines display the radiative damping rate $\gamma_\tau^\varepsilon(\mathbf{q})$ from Eq. (6.33) [scaled by γ_0, cf. Eq. (1.7)] for (a),(d) the square, (b),(e) the honeycomb, and (c),(f) the Lieb lattices. Panels (a)–(c) [(d)–(f)] show the damping for the OP [IP] modes. Same parameters as in Fig. 6.1.

In panel (b) and (c) of Fig. 6.3, we plot the radiative damping rates (6.38) of the out-of-plane collective modes for the honeycomb and Lieb lattices, respectively. In both cases, the highest energetic band show a similar profile as that of Fig. 6.3(a). Indeed, in both panels the red lines present a superradiant regime which diverges at the crossing between the quasistatic dispersion relation and the light cone. However, the other band (blue and cyan lines) show the existence of subradiant modes (i.e., $\gamma_\tau^z(\mathbf{q}) \ll \gamma_0$) corresponding to dark modes. Indeed, those modes presenting near-zero radiative decay rates correspond to the one which are weakly coupled to light [cf. Fig. 6.1(d),(e)]. Note that we could have predicted such a behavior since the same "brightness parameter" $|\sum_s P_{\tau s}^{zz}(\mathbf{q})|^2$ already involved in the radiative shift (6.21) appears in the expression of the radiative decay rate (6.38).

6.2.3 Radiative linewidths for in-plane polarized modes

We now consider the case of the in-plane polarized modes ($\varepsilon = \varepsilon_\parallel$) for which we have the selection rule $P_{\tau s}^{\varepsilon_\parallel z}(\mathbf{q}) = 0$. Under these conditions we may thus rewrite the general expression (6.33) as

$$\gamma_\tau^{\varepsilon_\parallel}(\mathbf{q}) = 2\pi^2\omega_0^3\frac{a^3}{\mathcal{V}}\sum_{\mathbf{k},\hat{\lambda}_\mathbf{k}}\frac{|F^-_{\mathbf{k},\mathbf{q}}|^2}{\omega_\mathbf{k}}\left|\sum_s\left[(\hat{x}\cdot\hat{\lambda}_\mathbf{k})P_{\tau s}^{\varepsilon_\parallel x}(\mathbf{q}) + (\hat{y}\cdot\hat{\lambda}_\mathbf{k})P_{\tau s}^{\varepsilon_\parallel y}(\mathbf{q})\right]\right|^2\delta\left(\omega_\tau^{\varepsilon_\parallel}(\mathbf{q}) - \omega_\mathbf{k}\right), \tag{6.39}$$

where we have developed the summation over the plasmon polarization $\sigma = x, y$. In order to write explicitly the summation over the photonic degrees of freedom we proceed along the lines of the techniques we have employed for the radiative shift of the in-plane modes (see Sec. 6.1.3). Consequently, substituting the expression (6.26) for the term into the modulus squared in (6.39) and performing the summation over the photon polarization [using Eq. (2.27)] as well as going to the continuum limit with Eq. (6.14) for the array factor yields

$$\begin{aligned}\gamma_\tau^{\varepsilon_\parallel}(\mathbf{q}) \simeq{}& \frac{\pi\omega_0^3a^3}{c|\mathbf{t}_1\times\mathbf{t}_2|\omega_\tau^{\varepsilon_\parallel}(\mathbf{q})}\int_{-\infty}^{+\infty}\frac{\mathrm{d}z}{(1+z^2)^{3/2}}\delta\left(1-\alpha\sqrt{1+z^2}\right)\\
&\times\left\{\left[\left(\frac{q_y}{|\mathbf{q}|}\right)^2+z^2\right]\left|\textstyle\sum_s P_{\tau s}^{\varepsilon_\parallel x}(\mathbf{q})\right|^2+\left[\left(\frac{q_x}{|\mathbf{q}|}\right)^2+z^2\right]\left|\textstyle\sum_s P_{\tau s}^{\varepsilon_\parallel y}(\mathbf{q})\right|^2\right.\\
&\left.-2\frac{q_xq_y}{|\mathbf{q}|^2}\mathrm{Re}\left\{\textstyle\sum_{ss'}P_{\tau s}^{\varepsilon_\parallel x}(\mathbf{q})P_{\tau s'}^{\varepsilon_\parallel y}(\mathbf{q})\right\}\right\},\end{aligned} \tag{6.40}$$

with $\alpha = c|\mathbf{q}|/\omega_\tau^{\varepsilon_\parallel}(\mathbf{q})$ and $z = k_z/|\mathbf{q}|$. Rearranging the terms in the latter equation we then obtain

$$\begin{aligned}\gamma_\tau^{\varepsilon_\parallel}(\mathbf{q}) = \frac{\pi\omega_0^3a^3}{c|\mathbf{t}_1\times\mathbf{t}_2|\omega_\tau^{\varepsilon_\parallel}(\mathbf{q})}&\left\{\mathcal{K}_1(\alpha)\left[\left(\frac{q_y}{|\mathbf{q}|}\right)^2\left|\textstyle\sum_s P_{\tau s}^{\varepsilon_\parallel x}(\mathbf{q})\right|^2+\left(\frac{q_x}{|\mathbf{q}|}\right)^2\left|\textstyle\sum_s P_{\tau s}^{\varepsilon_\parallel y}(\mathbf{q})\right|^2\right.\right.\\
&\left.\left.-2\frac{q_xq_y}{|\mathbf{q}|^2}\mathrm{Re}\left\{\textstyle\sum_{ss'}P_{\tau s}^{\varepsilon_\parallel x}(\mathbf{q})P_{\tau s'}^{\varepsilon_\parallel y}(\mathbf{q})\right\}\right]+\mathcal{K}_2(\alpha)\left[\left|\textstyle\sum_s P_{\tau s}^{\varepsilon_\parallel x}(\mathbf{q})\right|^2+\left|\textstyle\sum_s P_{\tau s}^{\varepsilon_\parallel y}(\mathbf{q})\right|^2\right]\right\},\end{aligned} \tag{6.41}$$

where $\mathcal{K}_1(\alpha)$ is given in Eq. (6.37) and $\mathcal{K}_2(\alpha)$ is defined as

$$\mathcal{K}_2(\alpha) = \int_{-\infty}^{+\infty} \mathrm{d}z \frac{z^2}{(1+z^2)^{3/2}} \delta\left(1 - \alpha\sqrt{1+z^2}\right) \Theta\left(1-\alpha\right). \tag{6.42}$$

We here point out that, the inclusion of a Heaviside-step function in the latter integral $\mathcal{K}_2(\alpha)$ stems from similar considerations as for the decay rate associated with the out-of-plane modes (cf. Sec. 6.2.2). In order to evaluate Eq. (6.42), we proceed as for the integral $\mathcal{K}_1(\alpha)$ for which the explicit expression is given in Eq. (F.14). Following the procedure described in Appendix F [cf. Eqs. (F.12)–(F.14)], we obtain for Eq. (6.42)

$$\mathcal{K}_2(\alpha) = \frac{1-\alpha^2}{\alpha^2}\mathcal{K}_1(\alpha) = 2\sqrt{1-\alpha^2}\Theta\left(1-\alpha\right), \tag{6.43}$$

where we have used the expression (F.14) in the latter equation. Finally, substituting the expressions for $\mathcal{K}_1(\alpha)$ and $\mathcal{K}_2(\alpha)$ [given by Eqs. (F.14) and (6.43), respectively] we obtain for the radiative decay rate of the in-plane modes

$$\begin{aligned}\gamma_\tau^{\varepsilon\parallel}(\mathbf{q}) = &-\frac{2\pi\omega_0^3 a^3 c|\mathbf{q}|^2}{|\mathbf{t}_1\times\mathbf{t}_2|[\omega_\tau^{\varepsilon\parallel}(\mathbf{q})]^2} \frac{\Theta\left(\omega_\tau^{\varepsilon\parallel}(\mathbf{q}) - c|\mathbf{q}|\right)}{\sqrt{\left[\omega_\tau^{\varepsilon\parallel}(\mathbf{q})\right]^2 - (c|\mathbf{q}|)^2}} \left\{ \left| \sum_s \left[\frac{q_x}{|\mathbf{q}|} P_{\tau s}^{\varepsilon\parallel x}(\mathbf{q}) + \frac{q_y}{|\mathbf{q}|} P_{\tau s}^{\varepsilon\parallel y}(\mathbf{q}) \right] \right|^2 \right. \\ &\left. - \frac{\left[\omega_\tau^{\varepsilon\parallel}(\mathbf{q})\right]^2}{(c|\mathbf{q}|)^2} \left[\left| \sum_s P_{\tau s}^{\varepsilon\parallel x}(\mathbf{q}) \right|^2 + \left| \sum_s P_{\tau s}^{\varepsilon\parallel y}(\mathbf{q}) \right|^2 \right] \right\}. \end{aligned} \tag{6.44}$$

In Fig. 6.3(d)–(f), we exemplify the radiative damping rate for the in-plane polarized modes obtained above for the square [panel (d)], the honeycomb [panel (e)] and the Lieb lattices [panel (f)]. As can be seen from Fig. 6.3(d), the red line corresponding to the lower transverse plasmonic band in Fig. 5.1(d) [or Fig. 6.1(d)] displays singularities which coincide with those observed in Fig. 6.3(a). Notably, the decay rate for the in-plane modes is non-zero at the Γ point of the first Brillouin zone contrary to the case of out-of-plane modes [see Fig. 6.3(a)]. Conversely, the orange line in Fig. 6.3(d) which corresponds to the upper longitudinal band in Fig. 5.1(d) presents an opposite trend. Indeed, we observe that, starting from a non-zero offset, the radiative decay rate decreases until it reach zero as the wavevector $|\mathbf{q}|$ moves away from the center of the first Brillouin zone. Interestingly, such a behavior is strongly reminiscent of what occurs in plasmonic chains for transverse and longitudinal modes [80,133–135,137]. As a matter of fact, the radiative damping associated with the transverse and the longitudinal plasmonic modes in chains [see Figs. 3.10(a) and 3.10(b) for the transverse and longitudinal cases, respictively] exhibit similar trends as the in-plane polarized modes in metasurfaces. Note, nevertheless that the purely transverse in-plane modes in the metasurfaces display radiative decay rates which diverge close to the light cone. Concerning the honeycomb and Lieb lattices [Fig. 6.3(e) and (f), respectively], we draw the same conclusions concerning the bright modes (reddish lines) as that ones for the square lattice. Additionally, some of the bands (blue and cyan lines) display an almost vanishing decay rate, which is a signature of dark plasmonic modes. As for the out-of-plane modes (cf. Sec. 6.2.2), such an observation is

related to what occurs for the corresponding fully-retarded dispersion relations discussed in Sec. 6.1.

6.3 Conclusion for Chapter 6

In this chapter, we have evaluated the effects induced on the plasmonic quasistatic dispersion relations by the light-matter interaction, that is the radiative frequency shifts and radiative linewidths. Considering the plasmon-photon coupling Hamiltonian as a weak perturbation to the plasmonic subsystem, we have derived the associated frequency shifts as a second-order energy correction to the energy of the plasmonic levels. Importantly, the inclusion of such shifts is crucial as they arise from the fully-retarded dipolar interactions. As a matter of fact, taking into account the retardation effects modifies significantly the plasmonic bandstructures (for the bright modes). Interestingly, within our approximated perturbative treatment, we have managed to derive practical analytical expressions of the radiative shifts for both out-of-plane and in-plane polarized modes. Importantly, these expressions depend of the eigenstates (through the Bogoliubov coefficients) as well as the eigenfrequencies associated with the plasmonic modes.

With these results we have demonstrated that the influence of the retardation effects are strongly reminiscent of those in one-dimensional systems, although more prominent. Indeed, similarly to what occurs in plasmonic chains [80, 133–135, 137], the purely transverse polarized (bright) collective plasmons within metasurfaces exhibit a singularity at the intersection of the quasistatic dispersion with the light cone. Conversely, the purely longitudinal modes do not present such singularities when accounting for the retardation effects. Furthermore, we have proved that including the retardation effects correct some non-physical results arising from the instantaneous quasistatic contributions and thus comforting the importance of evaluating the retardation effects within large plasmonic metasurfaces.

In this chapter, we also evaluated general analytical expressions for the radiative decay rate associated with the out-of-plane and in-plane polarized modes using a Fermi golden rule. Similarly to the frequency shifts, we have shown that the radiative linewidths of the plasmonic modes hosted in metasurfaces show similar effects as those in plasmonic chains. In particular, for in-plane polarization, the rates associated with purely polarized modes display opposite trends as the wavevectors move away from the center of the Brillouin zones. In particular, the transverse modes show an increasing (divergent) decay rate as the wavevector $|\mathbf{q}|$ approaches the light cone while the longitudinal ones display a decreasing rate. Finally, we have demonstrated that in Bravais lattices with a basis, some plasmonic band, do not couple with the light corresponding to dark plasmonic modes which cannot be probed using optical methods.

Aside of the photonic environment, the electronic environment to which the plasmonic subsystem is coupled induces a finite linewidth and frequency shift which add up to those evaluated in this chapter. Importantly, as we have seen above, the plasmonic modes display a finite (radiative) linewidths within the light cone only. Consequently, the modes belonging to the bandstructure lying outside the light cone should present a linewidth arising from electronic and Ohmic contributions alone. The evaluation of such electronic damping rates is thus crucial for experimental purposes and the following chapter is therefore devoted to the effects of the electronic environment alone onto the quasistatic bandstructure.

Chapter 7

Effects of the electronic environment on the collective plasmonic excitations

This chapter is dedicated to the calculation of the electronic-induced quantities associated with the plasmonic bandstructure. As for the photonic environment, the electronic bath to which the plasmonic subsystem is coupled gives rise to electronic contributions to the finite linewidth and the frequency shift associated with the collective modes. In the following, we will derive analytical general expressions for both quantities in arbitrary two-dimensional metasurfaces.

7.1 Landau damping

In this section, we analyze in detail the Landau decay rate of the the plasmonic modes. Similarly as we have done for the radiative damping rate (see Sec. 6.2), we consider that the plasmonic subsystem is weakly coupled to the electronic bath. Consequently, we treat the system perturbatively.

7.1.1 Fermi golden rule

The Landau decay rate of a given plasmonic mode $|1^{\varepsilon}_{\tau}(\mathbf{q})\rangle$ with band index τ, polarization ε and wavevector $\mathbf{q}$ is given by the Fermi golden rule

$$\Gamma^{\varepsilon}_{\tau}(\mathbf{q}) = \frac{2\pi}{\hbar} \sum_{s,\mathbf{R}_s} \sum_{eh_{\mathbf{R}_s}} |\langle 0^{\varepsilon}_{\tau}(\mathbf{q}), eh_{\mathbf{R}_s}|H_{\mathrm{pl-eh}}|1^{\varepsilon}_{\tau}(\mathbf{q}), \mu_{\mathbf{R}_s}|\rangle|^2 \, \delta\left(\hbar\omega^{\varepsilon}_{\tau}(\mathbf{q}) - \epsilon_{e,\mathbf{R}_s} + \epsilon_{h,\mathbf{R}_s}\right), \qquad (7.1)$$

where the coupling Hamiltonian $H_{\mathrm{pl-eh}}$ is given by Eq. (4.14). In the equation above, we sum over the electron-hole pairs within each nanoparticle $eh_{\mathbf{R}_s}$ with energy $\epsilon_{e,\mathbf{R}_s} - \epsilon_{h,\mathbf{R}_s}$. In the equation above, $|\mu_{\mathbf{R}_s}\rangle$ and $|eh_{\mathbf{R}_s}\rangle$ correspond to the groundstate with no electron-hole pair and a single pair state inside the nanoparticle located at $\mathbf{R}_s$, respectively.

The plasmon-electron coupling Hamiltonian $H_{\mathrm{pl-eh}}$ entering Eq. (7.1) has to be expressed as a function of the operators $\beta^{\varepsilon}_{\tau}(\mathbf{q})$ given in Eq. (4.18). Thus, expressing the operators $b^{\sigma}_{s}(\mathbf{R}_s)$ into the wavevector-space [using Eq. (4.15)] together with the inverse Bogoliubov transformation (6.4) into

the Hamiltonian (4.14) yields

$$H_{\mathrm{pl-eh}} = \frac{\Lambda}{\sqrt{\mathcal{N}}} \sum_{s,\mathbf{R}_s} \sum_{\sigma} \sum_{i,j} \sum_{\mathbf{q}} \sum_{\tau,\varepsilon} \left\{ \mathrm{e}^{\mathrm{i}\mathbf{q}\cdot\mathbf{R}_s} [M_{\tau s}^{\varepsilon\sigma}(\mathbf{q})]^* \beta_\tau^\varepsilon(\mathbf{q}) + \mathrm{e}^{-\mathrm{i}\mathbf{q}\cdot\mathbf{R}_s} M_{\tau s}^{\varepsilon\sigma}(\mathbf{q}) \beta_\tau^{\varepsilon\dagger}(-\mathbf{q}) \right\} \times \langle \mathbf{R}_s i | \sigma | \mathbf{R}_s j \rangle c_{\mathbf{R}_s i}^\dagger c_{\mathbf{R}_s j}, \tag{7.2}$$

where the constant Λ is defined in Eq. (2.20) and where

$$M_{\tau s}^{\varepsilon\sigma}(\mathbf{q}) = u_{\tau s}^{\varepsilon\sigma}(\mathbf{q}) - v_{\tau s}^{\varepsilon\sigma}(\mathbf{q}). \tag{7.3}$$

Then, substituting the Hamiltonian (7.2) into the Fermi golden rule (7.1), we obtain for the Landau decay rate

$$\Gamma_\tau^\varepsilon(\mathbf{q}) = \frac{2\pi}{\hbar} \frac{\Lambda^2}{\mathcal{N}} \sum_{s,\mathbf{R}_s} \sum_{eh_{\mathbf{R}_s}} \left| \sum_\sigma [M_{\tau s}^{\varepsilon\sigma}(\mathbf{q})]^* \langle e_{\mathbf{R}_s} | \sigma | h_{\mathbf{R}_s} \rangle \right|^2 \delta\left(\hbar\omega_\tau^\varepsilon(\mathbf{q}) - \epsilon_{e,\mathbf{R}_s} + \epsilon_{h,\mathbf{R}_s}\right) \tag{7.4}$$

where the dipolar matrix elements are given by Eq. (2.22). Since we consider identical nanoparticles, the latter matrix elements are all the same so that $\langle e_{\mathbf{R}_s} | \sigma | h_{\mathbf{R}_s} \rangle$ can be replaced by $\langle e | \sigma | h \rangle$. Similarly the summation over the electron-hole pairs in the Fermi golden rule (7.4) transforms as $\sum_{eh_{\mathbf{R}_s}} \to \sum_{eh}$ yielding the result

$$\Gamma_\tau^\varepsilon(\mathbf{q}) = \frac{2\pi}{\hbar^2} \Lambda^2 \sum_s \sum_{eh} \left| \sum_\sigma [M_{\tau s}^{\varepsilon\sigma}(\mathbf{q})]^* \langle e | \sigma | h \rangle \right|^2 \delta\left(\omega_\tau^\varepsilon(\mathbf{q}) - \omega_{eh}\right), \tag{7.5}$$

where we performed the summation over the nanoparticle positions and where $\omega_{eh} = (\epsilon_e - \epsilon_h)/\hbar$.

7.1.2 Evaluation of the damping rate

Contrary to the radiative damping, the Landau decay rate can be directly evaluated for any polarization ε. To this end, we first expand the summation over the plasmon polarization σ yielding

$$\Gamma_\tau^\varepsilon(\mathbf{q}) = \frac{2\pi}{\hbar^2} \Lambda^2 \sum_s \sum_{eh} \left\{ \sum_\sigma |[M_{\tau s}^{\varepsilon\sigma}(\mathbf{q})]^* \langle e | \sigma | h \rangle|^2 + \sum_{\sigma,\sigma'} [M_{\tau s}^{\varepsilon\sigma}(\mathbf{q})]^* M_{\tau s}^{\varepsilon\sigma'}(\mathbf{q}) \langle e | \sigma | h \rangle \langle e | \sigma' | h \rangle^* \right\} \times \delta\left(\omega_\tau^\varepsilon(\mathbf{q}) - \omega_{eh}\right), \tag{7.6}$$

In the latter equation, we first concentrate on the second term inside the curvy brackets corresponding to the cross-polarized terms (those for which $\sigma \neq \sigma'$). To evaluate such a term, we go to the continuum limit to write explicitly the summation over the electronic degrees of freedom and use Eq. (A.1) for the single-particle density of states $\varrho(\epsilon)$ entering the resulting integral as was done in Chapter 2 for isolated nanoparticles. Note that the terms for which $\sigma = z$ and $\sigma' = x, y$ vanish due to the internal selection rules encoded within the matrix elements (2.22). Hence, we only have to calculate a single term (for which $\sigma = x$ and $\sigma' = y$). Therefore, using the selection rules over the

angular momentum, the cross-polarized term reads, within this procedure, as

$$\sum_{eh}\langle e|x|h\rangle\langle e|y|h\rangle^* = \mathrm{i}\int_{\max\{E_\mathrm{F},\hbar\omega_\tau^\varepsilon(\mathbf{q})\}}^{E_\mathrm{F}+\hbar\omega_\tau^\varepsilon(\mathbf{q})} \mathrm{d}\epsilon\left[\Lambda\mathcal{R}\Big(\epsilon,\epsilon-\hbar\omega_\tau^\varepsilon(\mathbf{q})\Big)\right]^2 \times\sum_{l=0}^{+\infty}\varrho_l(\epsilon)\left\{\sum_{m=-l}^{+l}\varrho_{l+1}\Big(\epsilon-\hbar\omega_\tau^\varepsilon(\mathbf{q})\Big)\left[\Big(\mathcal{A}_{l,l+1,1}^{m,m-1}\Big)^2-\Big(\mathcal{A}_{l,l+1,-1}^{m,m+1}\Big)^2\right] + \sum_{m=-l}^{+l}\varrho_{l-1}\Big(\epsilon-\hbar\omega_\tau^\varepsilon(\mathbf{q})\Big)\left[\Big(\mathcal{A}_{l,l-1,1}^{m,m-1}\Big)^2-\Big(\mathcal{A}_{l,l-1,-1}^{m,m+1}\Big)^2\right]\right\}. \tag{7.7}$$

In the equation above, $\varrho_l(\epsilon)$ is the momentum-dependent density-of-states introduced in Eq. (A.1) while the radial and angular parts of the electronic wavefunction are given in Eqs. (2.23) and (2.24), respectively. To proceed into the calculation of Eq. (7.7), we concentrate on the angular parts appearing in the two brackets of Eq. (7.7). Thus, using the explicit expression (2.24) for the four terms, we get for the summation over m the relation

$$\sum_{m=-l}^{+l}\left[\Big(\mathcal{A}_{l,l\pm1,1}^{m,m-1}\Big)^2-\Big(\mathcal{A}_{l,l\pm1,-1}^{m,m+1}\Big)^2\right] = \mp\sum_{m=-l}^{+l}\frac{m}{2l+1}=0, \tag{7.8}$$

so that Eq. (7.7) vanishes. We thus may write the general rule for the cross-polarized terms as

$$\sum_{m_e,m_h}\langle e|\sigma|h\rangle\langle h|\sigma'|e\rangle = 0 \tag{7.9}$$

for $\sigma\neq\sigma'$. Consequently, the Landau damping rate in Eq. (7.6) reduces to

$$\Gamma_\tau^\varepsilon(\mathbf{q}) = \sum_{s\sigma}|M_{\tau s}^{\varepsilon\sigma}(\mathbf{q})|^2\Sigma^\sigma\left(\omega_\tau^\varepsilon(\mathbf{q})\right), \tag{7.10}$$

where the function $\Sigma^\sigma(\omega)$ was introduced in Eq. (2.35) in Chapter 2. Due to the spherical symmetries of the electronic wavefunctions, we recall that we have $\Sigma^\sigma(\omega)=\Sigma(\omega)$ [cf. Eq. (2.36)] where the latter function is given in Eq. (A.8) for $\sigma=z$. Hence, Eq. (7.10) further simplifies to yield

$$\Gamma_\tau^\varepsilon(\mathbf{q}) = \frac{3v_\mathrm{F}}{4a}\sum_{s\sigma}|M_{\tau s}^{\varepsilon\sigma}(\mathbf{q})|^2\left(\frac{\omega_0}{\omega_\tau^\varepsilon(\mathbf{q})}\right)^3 g\left(\frac{\hbar\omega_\tau^\varepsilon(\mathbf{q})}{E_\mathrm{F}}\right), \tag{7.11}$$

where the function $g(\nu)$ is given in Eq. (A.10).

In Eq. (7.11), we can write explicitly the summation over the sublattices s and polarization σ. First, we expand the squared modulus in Eq. (7.11) using the definition (7.3) together with the relation between the coefficients $u_{\tau s}^{\varepsilon\sigma}(\mathbf{q})$ and $v_{\tau s}^{\varepsilon\sigma}(\mathbf{q})$ introduced in Eq. (5.5). Performing these steps yields the result

$$\sum_{s\sigma}|M_{\tau s}^{\varepsilon\sigma}(\mathbf{q})|^2 = \frac{4\omega_0^2}{\left(\omega_\tau^\varepsilon(\mathbf{q})+\omega_0\right)^2}\sum_{s\sigma}|u_{\tau s}^{\varepsilon\sigma}(\mathbf{q})|^2. \tag{7.12}$$

The latter equation can be further simplified using the normalization condition (4.20). Indeed, with

Eq. (5.5), the normalization condition can be rewritten as

$$\sum_{s\sigma}\left(|u_{\tau s}^{\varepsilon\sigma}(\mathbf{q})|^2-|v_{\tau s}^{\varepsilon\sigma}(\mathbf{q})|^2\right)=\frac{4\omega_0\omega_\tau^\varepsilon(\mathbf{q})}{\left(\omega_\tau^\varepsilon(\mathbf{q})+\omega_0\right)^2}\sum_{s\sigma}|u_{\tau s}^{\varepsilon\sigma}(\mathbf{q})|^2=1, \tag{7.13}$$

which yields the relation

$$\sum_{s\sigma}|u_{\tau s}^{\varepsilon\sigma}(\mathbf{q})|^2=\frac{\left(\omega_\tau^\varepsilon(\mathbf{q})+\omega_0\right)^2}{4\omega_0\omega_\tau^\varepsilon(\mathbf{q})}. \tag{7.14}$$

Consequently, inserting Eq. (7.14) into (7.12), the summation over the Bogoliubov coefficients reads as

$$\sum_{s\sigma}|M_{\tau s}^{\varepsilon\sigma}(\mathbf{q})|^2=\frac{\omega_0}{\omega_\tau^\varepsilon(\mathbf{q})}. \tag{7.15}$$

We thus obtain, using Eq. (7.15) into the expression (7.11), the analytical form for the Landau damping rate

$$\Gamma_\tau^\varepsilon(\mathbf{q})=\frac{3v_\mathrm{F}}{4a}\left(\frac{\omega_0}{\omega_\tau^\varepsilon(\mathbf{q})}\right)^4 g\left(\frac{\hbar\omega_\tau^\varepsilon(\mathbf{q})}{E_\mathrm{F}}\right), \tag{7.16}$$

which is valid for any polarization ε. To leading order in the coupling constant Ω, the Landau decay rate of the collective plasmonic modes scales as $1/a$, as it is the case for the single particle result (2.37). This is in contrast with the the radiative linewidth (see Sec. 6.1) which increases with the nanoparticle radius as a^3 [cf. Eq. (6.33)]. In addition, we note that the Landau damping only depends on the eigenfrquencies $\omega_\tau^\varepsilon(\mathbf{q})$ of the modes while the radiative damping depends on the Bogoliubov coefficients as well [through the coefficient $P_{\tau s}^{\varepsilon\sigma}(\mathbf{q})$ defined in Eq. (6.7)].

In Fig. 7.1, we illustrate the result derived in Eq. (7.16) for the special case of the out-of-plane modes in the honeycomb lattice. In the figure, we display the results scaled by the single-particle Landau damping linewidth Γ_0 given in Eq. (2.37). In the figure, the blue curve corresponds to the lower energy band in Fig. 5.4(c) while the red curve to the higher energy one. As can be seen from the figure, the higher the energy of the mode is, the lower its associated nonradiative Landau linewidth. This is reminiscent to what occurs for isolated nanoparticles [165]. We report from the figure variations going from -40% to $+20\%$ with respect to the Landau decay rate of the isolated nanoparticle. Such modifications are nevertheless of the order of Γ_0 in opposition to the radiative damping rates [see Eq. (6.33)] which diverge for transverse polarized modes close to the edges of the light cone. Importantly, in contrast with the radiative decay rate (6.33) studied in the previous chapter, the Landau damping is nonvanishing over the whole first Brillouin zone for any arrays. Therefore, it it crucial to take into account such a decay mechanism since it contributes (with the Ohmic losses) to the finite linewidth of the plasmonic modes outside the light cone. Such a linewidth is thus crucial to determine, especially for small nanoparticles (i.e., for $a<10\,\mathrm{nm}$).

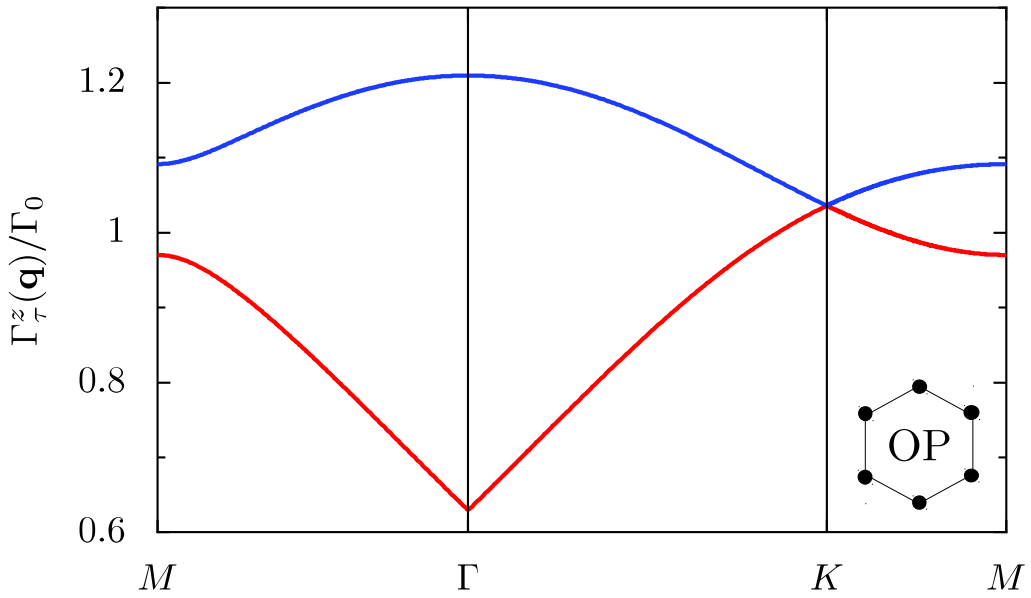

Figure 7.1: Landau damping linewidth (7.16) [scaled by the single-particle rate Γ_0, Eq. (2.37)] of the out-of-plane polarized modes in the honeycomb lattice. The blue (red) line corresponds to the decay rate associated with the lower (upper) plasmonic band in Fig. 5.4(c). In the figure, $d = 3a$ and $E_\mathrm{F} = 2\hbar\omega_0$.

7.2 Electronic-induced frequency shift

7.2.1 Second-order perturbation theory

We devote this section to the analytic calculation of the frequency shift induced by the electronic bath on the plasmonic collective modes. In a similar fashion as we took into account the retardation effects onto the plasmonic bandstructure (see Sec. 6.1), we consider that the plasmonic subsystem is weakly coupled to the relative electronic coordinates. Within this approximation, we thus treat the plasmon-electron coupling Hamiltonian (7.2) to second order in perturbative theory yielding for the collective plasmon energy levels $\hbar\omega^\varepsilon_\tau(\mathbf{q})n^\varepsilon_\tau(\mathbf{q}) + \mathcal{E}^{(1)}_{n^\varepsilon_\tau(\mathbf{q})} + \mathcal{E}^{(2)}_{n^\varepsilon_\tau(\mathbf{q})}$. In the latter expression, the different corrections $\mathcal{E}^{(i)}_{n^\varepsilon_\tau(\mathbf{q})}$ (with $i = 1, 2$) correspond to those induced only by the electronic environment. The two electronic contributions are thus given by

$$\mathcal{E}^{(1)}_{n^\varepsilon_\tau(\mathbf{q})} = \langle n^\varepsilon_\tau(\mathbf{q}), \mu_{\mathbf{R}_s} | H_{\mathrm{pl-eh}} | n^\varepsilon_\tau(\mathbf{q}), \mu_{\mathbf{R}_s} \rangle \tag{7.17a}$$

and

$$\mathcal{E}^{(2)}_{n^\varepsilon_\tau(\mathbf{q})} = \frac{1}{\hbar} \sum_{\substack{m^\varepsilon_\tau(\mathbf{q}),\mathbf{k},\hat{\lambda}_\mathbf{k} \\ [m^\varepsilon_\tau(\mathbf{q}) \neq n^\varepsilon_\tau(\mathbf{q})]}} \sum_{s,\mathbf{R}_s} \sum_{eh_{\mathbf{R}_s}} \frac{|\langle m^\varepsilon_\tau(\mathbf{q}), eh_{\mathbf{R}_s} | H_{\mathrm{pl-eh}} | n^\varepsilon_\tau(\mathbf{q}), \mu_{\mathbf{R}_s} \rangle|^2}{[n^\varepsilon_\tau(\mathbf{q}) - m^\varepsilon_\tau(\mathbf{q})]\,\omega^\varepsilon_\tau(\mathbf{q}) - \omega_{eh_{\mathbf{R}_s}}}, \tag{7.17b}$$

In Eq. (7.17), we sum over all the electron-hole pairs with energy $\hbar\omega_{eh_{\mathbf{R}_s}}$ in a given nanoparticle (located at $\mathbf{R}_s$). In analogy with the isolated nanoparticle case, the first order correction to the energy (7.17a) vanishes due to the selection rules encapsulated in the coupling Hamiltonian $H_{\mathrm{pl-eh}}$ [cf. Eq. (7.2)]. Inserting the expression (7.2) into Eq. (7.17b), the second-order correction reads as

$$\mathcal{E}^{(2)}_{n^{\varepsilon}_{\tau}(\mathbf{q})} = \frac{\Lambda^2}{\hbar\mathcal{N}} \sum_{s,\mathbf{R}_s} \sum_{eh_{\mathbf{R}_s}} \left[\frac{n^{\varepsilon}_{\tau}(\mathbf{q})}{\omega^{\varepsilon}_{\tau}(\mathbf{q}) - \omega_{eh_{\mathbf{R}_s}}} \left| \sum_{\sigma} \mathrm{e}^{-\mathrm{i}\mathbf{q}\cdot\mathbf{R}_s} M^{\varepsilon\sigma}_{\tau s}(\mathbf{q}) \langle e_{\mathbf{R}_s}|\sigma|h_{\mathbf{R}_s}\rangle \right|^2 \right.$$
$$\left. - \frac{n^{\varepsilon}_{\tau}(\mathbf{q}) + 1}{\omega^{\varepsilon}_{\tau}(\mathbf{q}) + \omega_{eh_{\mathbf{R}_s}}} \left| \sum_{\sigma} \mathrm{e}^{\mathrm{i}\mathbf{q}\cdot\mathbf{R}_s} \left[M^{\varepsilon\sigma}_{\tau s}(\mathbf{q})\right]^* \langle e_{\mathbf{R}_s}|\sigma|h_{\mathbf{R}_s}\rangle \right|^2 \right]. \tag{7.18}$$

Similarly to the Landau decay rate evaluated in Sec. 7.1, the indices $\mathbf{R}_s$ for the electron and hole states (as well as for the summation over the electron-hole pairs) may be dropped since all the nanoparticles are identical. Thus, the electronic shift $\Delta^{\varepsilon}_{\tau}(\mathbf{q}) = \mathcal{E}^{(2)}_{n^{\varepsilon}_{\tau}(\mathbf{q})+1} - \mathcal{E}^{(2)}_{n^{\varepsilon}_{\tau}(\mathbf{q})}]/\hbar$ reads

$$\Delta^{\varepsilon}_{\tau}(\mathbf{q}) = \frac{\Lambda^2}{\hbar^2} \sum_{s} \sum_{eh} \left[\frac{1}{\omega^{\varepsilon}_{\tau}(\mathbf{q}) - \omega_{eh}} \left| \sum_{\sigma} M^{\varepsilon\sigma}_{\tau s}(\mathbf{q}) \langle e|\sigma|h\rangle \right|^2 \right.$$
$$\left. - \frac{1}{\omega^{\varepsilon}_{\tau}(\mathbf{q}) + \omega_{eh}} \left| \sum_{\sigma} \left[M^{\varepsilon\sigma}_{\tau s}(\mathbf{q})\right]^* \langle e|\sigma|h\rangle \right|^2 \right]. \tag{7.19}$$

7.2.2 Evaluation of the electronic shift

In order to complete the evaluation of the electronic shift (7.19), we proceed along the lines of the method we used for the Landau damping. Thus, we first expand the summations over the polarizations σ in the two squared-modulus in Eq. (7.19). Then, using the relation (7.9) which allows us to simplify the cross-polarized terms, we write the frequency shift as

$$\Delta^{\varepsilon}_{\tau}(\mathbf{q}) = \frac{2\Lambda^2}{\hbar^2} \sum_{s} \sum_{eh} \sum_{\sigma} \left[\left| M^{\varepsilon\sigma}_{\tau s}(\mathbf{q}) \right|^2 \left| \langle e|\sigma|h\rangle \right|^2 \right] \frac{\omega_{eh}}{\left[\omega^{\varepsilon}_{\tau}(\mathbf{q})\right]^2 - \omega^2_{eh}}. \tag{7.20}$$

Along the lines of Ref. [67] and Chapter 2, we write the latter equation as

$$\Delta^{\varepsilon}_{\tau}(\mathbf{q}) = \sum_{s} \sum_{\sigma} \left| M^{\varepsilon\sigma}_{\tau s}(\mathbf{q}) \right|^2 \frac{1}{\pi} \mathcal{P} \int_{-\infty}^{+\infty} \mathrm{d}\omega \frac{\omega \Sigma^{\sigma}(\omega)}{\left[\omega^{\varepsilon}_{\tau}(\mathbf{q})\right]^2 - \omega^2}, \tag{7.21}$$

where $\Sigma^{\sigma}(\omega)$ by Eq. (2.36). Consequently, the radiative shift reads

$$\Delta^{\varepsilon}_{\tau}(\mathbf{q}) = \frac{\omega_0}{\omega^{\varepsilon}_{\tau}(\mathbf{q})} \frac{1}{\pi} \mathcal{P} \int_{-\infty}^{+\infty} \mathrm{d}\omega \frac{\omega \Sigma(\omega)}{\left[\omega^{\varepsilon}_{\tau}(\mathbf{q})\right]^2 - \omega^2}, \tag{7.22}$$

where we have used the relation (7.15) to simplify the summations over the s and σ indices. In order to proceed with the evaluation of Eq. (7.22) we first, in analogy to the single nanoparticle case (cf. Chapter 2), we replace the lower boundary in the integral by $\omega^{\varepsilon}_{\tau}(\mathbf{q}) - \eta\Gamma^{\varepsilon}_{\tau}(\mathbf{q})$ with η a

constant of the order of unity. Thus, the electronic shift is given by

$$\Delta_\tau^\varepsilon(\mathbf{q}) = \frac{\omega_0}{\omega_\tau^\varepsilon(\mathbf{q})}\frac{1}{\pi}\mathcal{P}\int_{\omega_\tau^\varepsilon(\mathbf{q})-\eta\Gamma_\tau^\varepsilon(\mathbf{q})}^{+\infty} \mathrm{d}\omega \frac{\omega\Sigma(\omega)}{\left[\omega_\tau^\varepsilon(\mathbf{q})\right]^2-\omega^2}, \tag{7.23}$$

Following the procedure presented in Refs. [67,68], we now evaluate the integral entering Eq. (7.23). Thus, we substitute into the integral (7.23) the expression (2.36) for the function $\Sigma(\omega)$ within the semi-classical limit, $k_\mathrm{F}a \gg 1$. Within such a limit, the function $g(\nu)$ entering (A.8) is given by Eq. (2.48) so that the electronic shift reads

$$\Delta_\tau^\varepsilon(\mathbf{q}) = -\frac{2v_\mathrm{F}}{5\pi a}\left(\frac{\omega_0}{\omega_\tau^\varepsilon(\mathbf{q})}\right)^4 I\left(\frac{\hbar\omega_\tau^\varepsilon(\mathbf{q})}{E_\mathrm{F}}, \eta\frac{\hbar\Gamma_\tau^\varepsilon(\mathbf{q})}{E_\mathrm{F}}\right), \tag{7.24}$$

where the function $I(\xi,\alpha)$ is given by Eq. (2.50). Then, using the expression (2.51) for $I(\xi,\alpha)$ in the limit $\xi \gg \alpha$, the electronic frequency shift is given by

$$\Delta_\tau^\varepsilon(\mathbf{q}) = -\frac{3v_\mathrm{F}}{4a}\beth\left(\omega_\tau^\varepsilon(\mathbf{q})\right). \tag{7.25}$$

In the latter equation, the function $\beth(\omega)$ is given in Eq. (2.53) and was introduced in Sec. 2.4.2 for the evaluation of the electronic shift associated with the LSP in isolated nanoparticles. The electronic shift (7.25) scales as $1/a$, up to a logarithmic correction [see Eq. (2.53)]. Therefore, such a frequency shift is mostly relevant for small nanoparticles as it the case for the Landau damping rate (7.16). In addition, the latter frequency shift involves only the plasmonic bandstructure $\omega_\tau^\varepsilon(\mathbf{q})$ associated with the plasmonic modes in contrast to the radiative frequency shifts [cf. Eqs. (6.21) and (6.30)] which depend on the eigenstates as well. We plot in Fig. 7.2 the results of Eq. (7.25) applied to the specific case of the out-of-plane polarized plasmonic modes in the honeycomb lattice. Similarly to Fig. 7.1, the red line in Fig. 7.2 corresponds to the upper band in Fig. 5.4(c), while the blue line to the lower band. In the figure, the results are scaled by the electronic shift $|\Delta_0|$ associated with a single nanoparticle [see Eq. (2.52)]. From the figure, we immediately notice that the electronic shift is negative in the entire first Brillouin zone thus corresponding to a global redshift of the plasmonic bandstructure. This is in contrast with the radiative frequency shift (6.15), whose sign is both depending on the wavevector and polarization of the modes (see Sec. 6.1). In addition, we see that such a shift is of the order of Δ_0 experiencing only variations between -30% to $+10\%$ for the choice of parameters in Fig. 7.2. Importantly, comparing the electronic and radiative shifts in Eqs. (7.25) and (6.21),(6.30), respectively, we point out that the electronic shifts do not affect qualitatively the plasmonic bandstructure contrary to the radiative ones which are a manifestation of the retardation effects (see Figs. 6.1 and 6.2). The only noticeable effect is that the higher the energy of the mode, the lower is its associated electronic shift. Such a conclusion is reminiscent of what occurs in isolated nanoparticles [165].

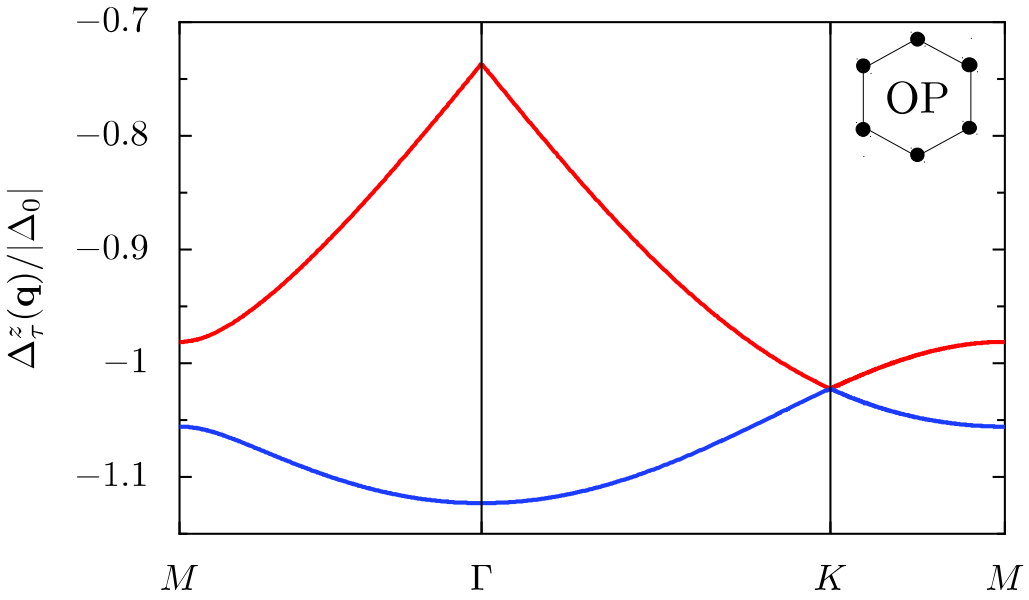

Figure 7.2: Electronic-induced frequency shift (7.25) [scaled by $|\Delta_0|$, see Eq. (2.52)] of the out-of-plane polarized modes in the honeycomb lattice. The red (blue) line corresponds to the frequency shift associated with the higher (lower) plasmonic band [see Fig. 5.4(c)]. In the figure, $d = 3a$, $E_\mathrm{F} = 2\hbar\omega_0$ and $k_\mathrm{F}a = 100$.

7.3 Conclusion for Chapter 7

In this chapter, we have evaluated the two principal quantities arising from the coupling of the plasmonic subsystem to the electronic bath, i.e., the Landau decay rate and the electronic frequency shift. Assuming a weak coupling between the plasmonic subsystem and the electronic bath we have calculated both quantities within a standard nondegenerate perturbation theory.

First, we have obtained the nonradiative Landau decay rate using a Fermi golden rule. From this general results we have derived a general analytic expression for the linewidth using semi-classical techniques as was done in Refs. [67, 68] for isolated nanoparticles. Importantly, we have shown that, contrary to the radiative linewidths discussed in Chapter 6, the expressions are valid for any plasmon polarization ε and are nonvanishing within the whole first Brillouin zone. This latter property is of prime relevance since it contributes to the linewidth of the plasmonic modes in the entire first Brillouin zone. Indeed, as emphasized in Chapter 6, the radiative damping can be zero for some plasmonic modes and vanishes outside the light cone. Moreover, we have demonstrated that, contrary to the radiative linewidth which scales with the volume of the nanoparticle ($\propto a^3$), the Landau damping rate goes as $1/a$. Consequently, it exists an optimal nanoparticle size for which the total linewidths of the collective modes are minimal, as it is the case for isolated nanoparticles (cf. Sec. 2.3). Such a fact may be crucial for the experimental detection of the collective modes.

In the second part of the chapter, we have considered the electronic frequency shift for which we have derived an analytical expression. As for the associated Landau damping, the expression

for the shift is valid for any polarization ε. In analogy with the single nanoparticle case, we have demonstrated that such a shift corresponds to a global redshift of the entire plasmonic bandstructure. This is in striking contrast with the radiative shift which encodes the retardation effects and thus modifies qualitatively the dispersion relation. The evaluation of the electronic shift is nevertheless crucial since it is significant (of the order of the shift of a isolated nanoparticle) for small-sized nanoparticles and thus relevant for experimental detection.

With the determination of the electronic-induced linewidths and frequency shifts as well as those arising from the coupling to the photonic bath presented in Chapter 6, we may now discuss the experimental observability of the plasmonic collective modes. This is the purpose of the next chapter of this thesis.

Chapter 8

Observability of the collective plasmons in metasurfaces

8.1 The spectral function

Typically, the dispersion relation associated with the collective plasmonic modes is probed with spectroscopy experiments. As we have mentioned in the introduction of this thesis (see Chapter 1), several kinds of experimental techniques can be used to obtained the spectral response of plasmonic metastructures. In particular, the most common technique amounts to probe the photoabsorption cross-section as a function of the exciting photon energy in order to partially reconstruct the band-structure (see e.g., Refs. [100, 166]). The main drawback of such a method is that it only allows to image the bandstructure within the light cone (since the wavevector of the light must be equal to the plasmonic wavevector $\mathbf{q}$), limiting its applicability. In addition, a non-zero coupling between the plasmons and the photon is required in photoabsorption experiments so that the dark plasmonic modes explored in Chapter 6 are difficult to access with such a technique. Alternatively, and to overcome the limits of the optical probing techniques, on may also use electrons in EELS experiments (whose techniques, employed to dimers [123, 124] and chains [126] may be employed for metasurfaces) to excite the plasmonic modes and then extract their dispersion relations within most of Brillouin zone.

The essential condition for an experimental observation of the plasmonic bandstructure is that the splitting between two plasmonic bands is sufficiently large with respect to their respective linewidths. This is required to be able to resolve individually the bands. One of the difficulties of imaging the fully-retarded plasmonic bandstructure presented in Chapters 6 and 7 within the entire first Brillouin zone is that one would have to combine both techniques discussed above to do so.

Let us for now assume that such constrains could be achieved experimentally. Thus, the typical spectral function resulting of the experiments would resemble the one of a standard absorption measurement (since both optical and EELS experiments are spectroscopic in nature). Consequently,

we assume for the total spectral response $\mathcal{A}(\omega, \mathbf{q})$ a Breit-Wigner form leading to

$$\mathcal{A}_{\mathrm{OP}}(\omega, \mathbf{q}) \propto \sum_{\tau} \frac{1}{\left[\omega - \tilde{\omega}_{\tau}^{z}(\mathbf{q})\right]^2 + \left[\beth_{\tau}^{z}(\mathbf{q})\right]^2} \tag{8.1a}$$

for the out-of-plane modes and

$$\mathcal{A}_{\mathrm{IP}}(\omega, \mathbf{q}) \propto \sum_{\tau} \frac{1}{\left[\omega - \tilde{\omega}_{\tau}^{\varepsilon\parallel}(\mathbf{q})\right]^2 + \left[\beth_{\tau}^{\varepsilon\parallel}(\mathbf{q})\right]^2} \tag{8.1b}$$

for the in-plane polarized modes, respectively. In Eq. (8.1), the renormalized frequency

$$\tilde{\omega}_{\tau}^{\varepsilon}(\mathbf{q}) = \omega_{\tau}^{\varepsilon}(\mathbf{q}) + \delta_{\tau}^{\varepsilon}(\mathbf{q}) + \Delta_{\tau}^{\varepsilon}(\mathbf{q}) \tag{8.2}$$

encapsulates the retardation effects through the radiative shift $\delta_{\tau}^{\varepsilon}(\mathbf{q})$ [cf. Eq. (6.15)] as well as the additional frequency redshift $\Delta_{\tau}^{\varepsilon}(\mathbf{q})$ [cf. Eq. (7.20)] induced on the plasmonic dispersion by the electronic environment. Additionally, the quantity $\beth_{\tau}^{\varepsilon}(\mathbf{q})$ entering the Lorentzian-shaped function $\mathcal{A}(\omega, \mathbf{q})$ in Eq. (8.1) amounts to the total linewidth and reads

$$\beth_{\tau}^{\varepsilon}(\mathbf{q}) = \gamma_{\tau}^{\varepsilon}(\mathbf{q}) + \Gamma_{\tau}^{\varepsilon}(\mathbf{q}) + \gamma_{\mathrm{O}}. \tag{8.3}$$

The latter linewidth includes three distinct contributions: (i) the radiative losses $\gamma_{\tau}^{\varepsilon}(\mathbf{q})$ evaluated in Chapter 6 and given by Eq. (6.33), (ii) the Landau damping $\Gamma_{\tau}^{\varepsilon}(\mathbf{q})$ given by Eq. (7.5) and (iii) the Ohmic losses, inherent to any (bulk) metals, characterized by the damping rate γ_{O}. We assume the latter contribution to be mode– and size–independent.

8.2 Results without Ohmic losses

8.2.1 Dependence of the spectral function on the nanoparticle size

As demonstrated in Chapters 6 and 7, the linewidths of the collective plasmonic modes vary as a function of the radius a of the nanoparticles composing the metasurfaces. Indeed, since the radiative damping scales as a^3, the dispersion relations may be difficult to resolve (inside the light cone) for large nanoparticles. Conversely, considering small nanoparticles would imply that the Landau decay rate (which scales as $1/a$) becomes important and would thus lower the experimental resolution. Consequently, we investigate in the following, the dependence of the bandstructure with the size of the nanoparticles within the whole Brillouin zone. As a simple example, we thus consider the case of the spectral function (8.1a) associated with the out-of-plane modes in a square lattice which we plot in Fig. 8.1 for different nanoparticle sizes. In the figure, we use the parameters $\hbar\omega_0 = 2.6\,\mathrm{eV}$ and $E_{\mathrm{F}} = 5.5\,\mathrm{eV}$, corresponding to silver nanoparticles [58] while the interparticle distance is $d = 3a$. In Fig. 8.1 the nanoparticle sizes are $k_0 a = 0.1$ [panel (a)], $k_0 a = 0.15$ [panel (b)], $k_0 a = 0.2$ [panel (c)] and $k_0 a = 0.3$ [panel (d)], respectively while the red dashed lines depict the light lines in each panels. As can be seen from Fig. 8.1, the more the size of the nanoparticles increases [going from panel (a) to (d)], the better one can resolve the plasmonic dispersion outside

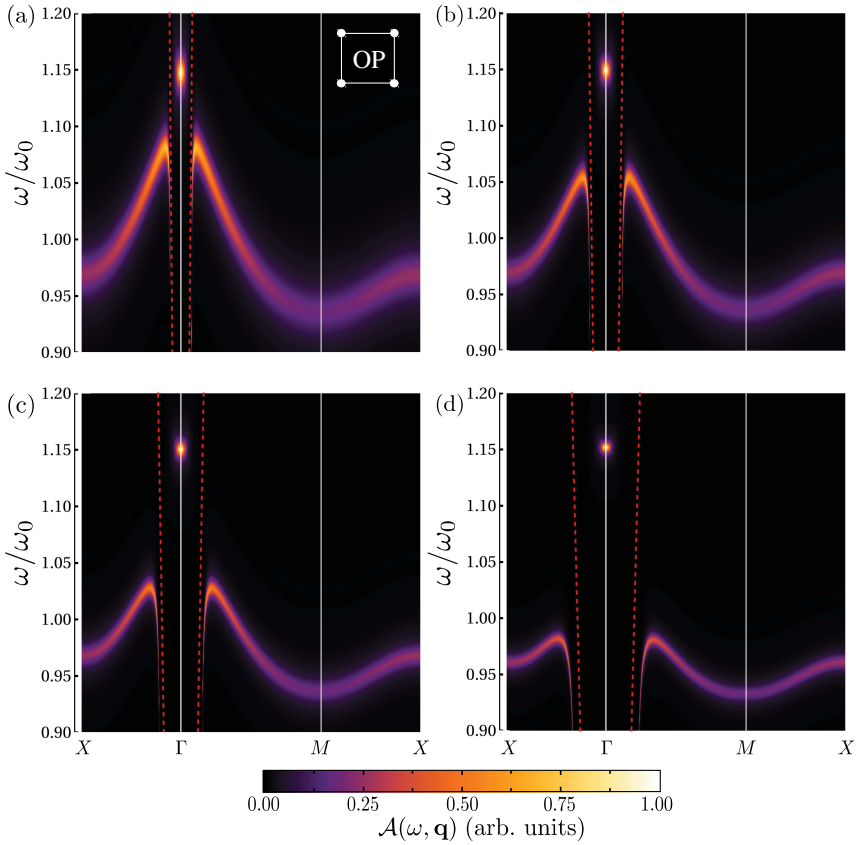

Figure 8.1: Spectral function (8.1) associated with the out-of-plane modes in a square lattice for different nanoparticle sizes. The figure displays the results for (a) $k_0 a = 0.1$, (b) $k_0 a = 0.15$, (c) $k_0 a = 0.2$ and (d) $k_0 a = 0.3$. In the figure, the red dashed lines correspond to the light cone and we choose the parameters $\hbar\omega_0/E_\mathrm{F} = 0.47$ and $k_0/k_\mathrm{F} = 1.1 \times 10^{-3}$, corresponding to silver nanoparticles. In addition, we take $d = 3a$ which gives $\Omega = \omega_0/54$ and neglect the Ohmic losses γ_O entering the total linewidth (8.3).

the light cone due to the scaling of the Landau damping (which is here the only mechanism giving the finite linewidth of plasmonic modes). However, for a size of $k_0 a = 0.3$ [see Fig. 8.1(d)] for which we observe the best resolution, the bandstructure experiences a pronounced distortion [with respect to the corresponding quasistatic dispersion shown in Fig. 5.1(c)] as the light cone becomes larger thus affecting a more important part of the plasmonic dispersion since the dipolar approximation ($k_0 d \ll 1$) used for our model starts to break down. Note that the light cone expands as the nanoparticle size increases. This behavior stems from the fact that we plot the plasmonic dispersions as a function of the parameter $\mathbf{q}d$ so that the light cone $\omega = c|\mathbf{q}|$, scales as $1/k_0 d$ in Fig. 8.1. In addition, for large radius a the bandstructure within the light cone is almost not resolved due to the contribution of the radiative damping. Conversely, for small nanoparticles i.e., for $k_0 a = 0.1$ [see panel (a)], the linewidth of the plasmonic dispersion is significant thus limiting the experimen-

tal resolution for plasmonic bands which are not well separated (e.g., as in the honeycomb and Lieb lattices). Consequently, we choose the size $k_0 a = 0.15$ for the nanoparticles in order to study the spectral function (8.1) associated with the plasmonic dispersion relations in the square, the honeycomb and the Lieb lattices. Indeed, such a value allows for a good compromise to resolve the bandstructures in the whole Brillouin zone.

8.2.2 General results

We now consider the case where we neglect the Ohmic losses $\gamma_{\rm O}$ entering the total linewidth (8.3). Such a limit allows to grasp the essential features which appear into the full plasmonic bandstructure probed with spectroscopic experiments. Consequently, we show in Fig. 8.2 the spectral function (8.1) for both the out-of-plane and in-plane polarized plasmonic modes for the square, the honeycomb, and the Lieb lattices along the high symmetry lines of their respective first Brillouin zone as a function of the frequency ω. Based on our analysis of Sec. 8.2.1, we have chosen in the figure $k_0 a = 0.15$ in order to be able to resolve efficiently the plasmonic bandstructures over their entire first Brillouin zones (and especially in the vicinity of the degeneracy points). The latter parameter corresponds to a nanoparticle radius $a = 11\,\mathrm{nm}$. Moreover, we choose the same parameters of Fig. 8.1 corresponding to silver nanoparticles. As can be seen in Fig. 8.2(a), which displays $\mathcal{A}(\omega, \mathbf{q})$ (without Ohmic losses) for the out-of-plane modes in the square lattice, the spectral function reproduces well the fully-retarded dispersion relation shown in Fig. 6.1(a). Such an effect can be explained by the fact that the electronic shift $\Delta^z(\mathbf{q})$ [cf. Eq. (7.20)] entering Eq. (8.2) only induces a finite $\mathbf{q}$-dependent redshift of the bandstructure. In the figure, we clearly identify two distinct profiles corresponding to wavevectors inside ($|\mathbf{q}| \lesssim k_0$) and outside ($|\mathbf{q}| \gtrsim k_0$) the light cone. Within the light cone, the total linewidth (8.3) is highly dominated by the radiative decay rate $\gamma^z(\mathbf{q})$ [cf. Eq. (6.38) and Fig. 6.3(a)], so that it is difficult to resolve properly the plasmonic dispersion relation. Indeed, as we move away from the center of the first Brillouin zone towards the edges of the light cone, the linewidth becomes so large that the bandstructure appears completely blurred. However, outside the light cone, only the Landau damping $\Gamma^z(\mathbf{q})$ [cf. Eq. (7.16)] contributes to the total linewidth of the spectral function, allowing for a clear resolution of the plasmonic band. We here point out that the good resolution we show in the figure is highly dependent of our choice for the nanoparticle size a. Indeed, similarly to the discussion of Sec. 8.2.1, we could increase the resolution outside the light cone by considering larger nanoparticle. Nevertheless, such a possibility remains limited by the dipolar approximation $a \ll k_0^{-1}$ we employ throughout the thesis as illustrated in Fig. 8.1(d) for the square lattice.

We plot in panel (b) and (c) of Fig. 8.2 the spectral function (8.1a) corresponding to out-of-plane polarized modes for the honeycomb and Lieb lattices, respectively. In both cases, we report a similar trend as that of Fig. 8.2(a). Indeed, the entire bandstructure is clearly resolved outside of the light cone in both Figs. 8.2(b) and 8.2(c), while the upper bands inside the light cone exhibit a rather large linewidth (arising from the large radiative contributions). However, we see that the lower bands for both the honeycomb and Lieb lattices are still well resolved inside the light cone. Indeed, the dispersion relations correspond to dark plasmonic modes [see the blue line in Fig. 6.3(b) and the cyan and blue lines in Fig. 6.3(c)] and only the Landau decay rate contributes to the observed linewidths.

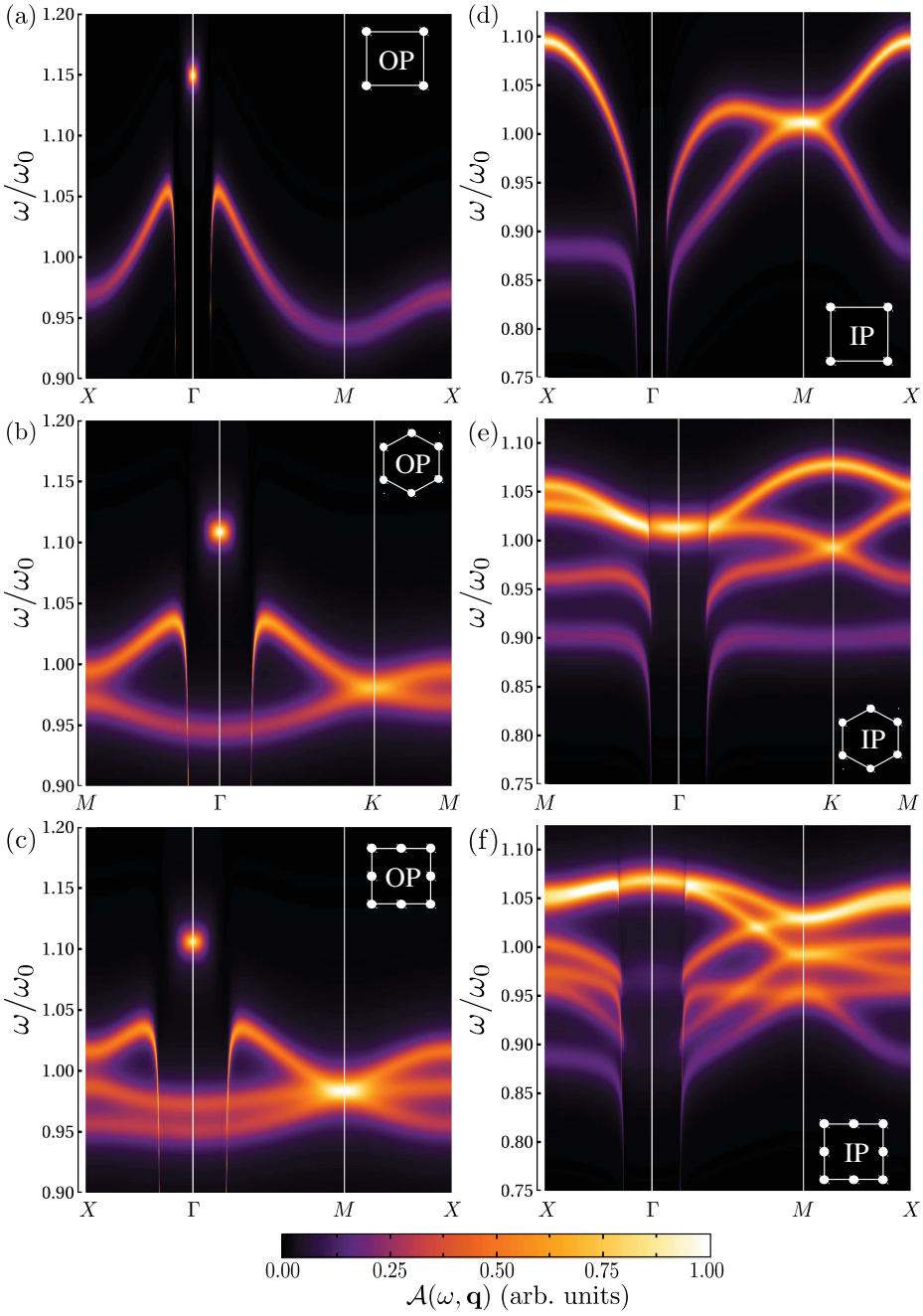

Figure 8.2: Spectral function (8.1) for (a),(d) the square, (b),(e) the honeycomb and (c),(f) the Lieb lattices. The results for the out-of-plane (in-plane) polarized modes are shown in panels (a)–(c) [(d)–(f)]. Same parameters as in Fig. 8.1 for a size of $k_0 a = 0.15$. The Ohmic losses γ_O entering the full linewidth (8.3) are neglected.

Finally, in panels (d)–(f) of Fig. 8.2, we display the spectral function (8.1b) associated with the in-plane plasmonic modes for (d) the square, (e) the honeycomb and (f) the Lieb lattices, respectively. Analyzing the different figures, we draw similar conclusions as those presented above for the out-of-plane modes. Indeed, while all the plasmonic bands are clearly visible outside the light cone, they are essentially not resolvable within the light cone unless they correspond to dark modes which do not couple to light.

8.3 Effects of the Ohmic losses on the bandstructure

In this section, we finally study for completeness the spectral functions as done in the previous section but including the Ohmic losses. Our goal is to determine the influence on these inherent losses on the experimental observability of the plasmonic dispersion relations. Therefore, we show in Fig. 8.3 the spectral functions associated with the lattices studied in the previous section, including into the total linewidth (8.3) the Ohmic contribution $\gamma_{\mathrm{O}} = 70\,\mathrm{meV}/\hbar$. The latter value was extracted from the experiments of Ref. [156] on silver clusters. In the figure, the panels (a)–(c) display the out-of-plane modes while the panels (d)–(f), the in-plane polarized ones. In the figure the results correspond to (a),(d) the square, (b),(e) the honeycomb, and (c),(f) the Lieb lattices, respectively. We immediately notice that the increased linewidth induced by the Ohmic losses results in a global resolution of the spectral function which is significantly lower than the one shown in Fig. 8.2. As a result, several plasmonic bands cannot be distinguished properly as it is the case for the out-of-plane plasmonic modes in the honeycomb and Lieb lattices in the vicinity of the corners of their respective first Brillouin zones for instance. Despite this lack of resolution, within the regime of parameters used in Fig. 8.3, the linewidth of the majority of the plasmonic bands remains sufficiently small to allow for an experimental detection. Note that the bright modes suffer from the same resolution issue as the one discussed in Sec. 8.2 for wavevectors within the light cone [see e.g., the two bands corresponding to the in-plane polarized modes in the square lattice in Fig. 8.3(d)].

Importantly, several experimental techniques exist in order to suppress or reduce the effects of the Ohmic losses. For instance, one may embed the metasurfaces in a gain media materials [49, 167–169] or design the nanoparticles with a metallic core coated by a gain medium [170]. Both techniques should help to diminish the influence of the Ohmic losses on the spectral functions and thus improve the experimental observability.

8.4 Conclusion for Chapter 8

In this chapter, we have addressed the issue of the experimental detection of the collective plasmonic modes within the metasurfaces. Assuming a Breit-Wigner form for the experimental response of the system, we have computed the spectral function one may obtain in typical spectroscopic measurements.

Since we have derived analytically all the quantities entering such Lorentzian-shaped functions (i.e., the quasistatic dispersions, the frequency shifts, and the linewidths), we have been able to study the effects of each contributions on the spectral function separately. Thus, neglecting first

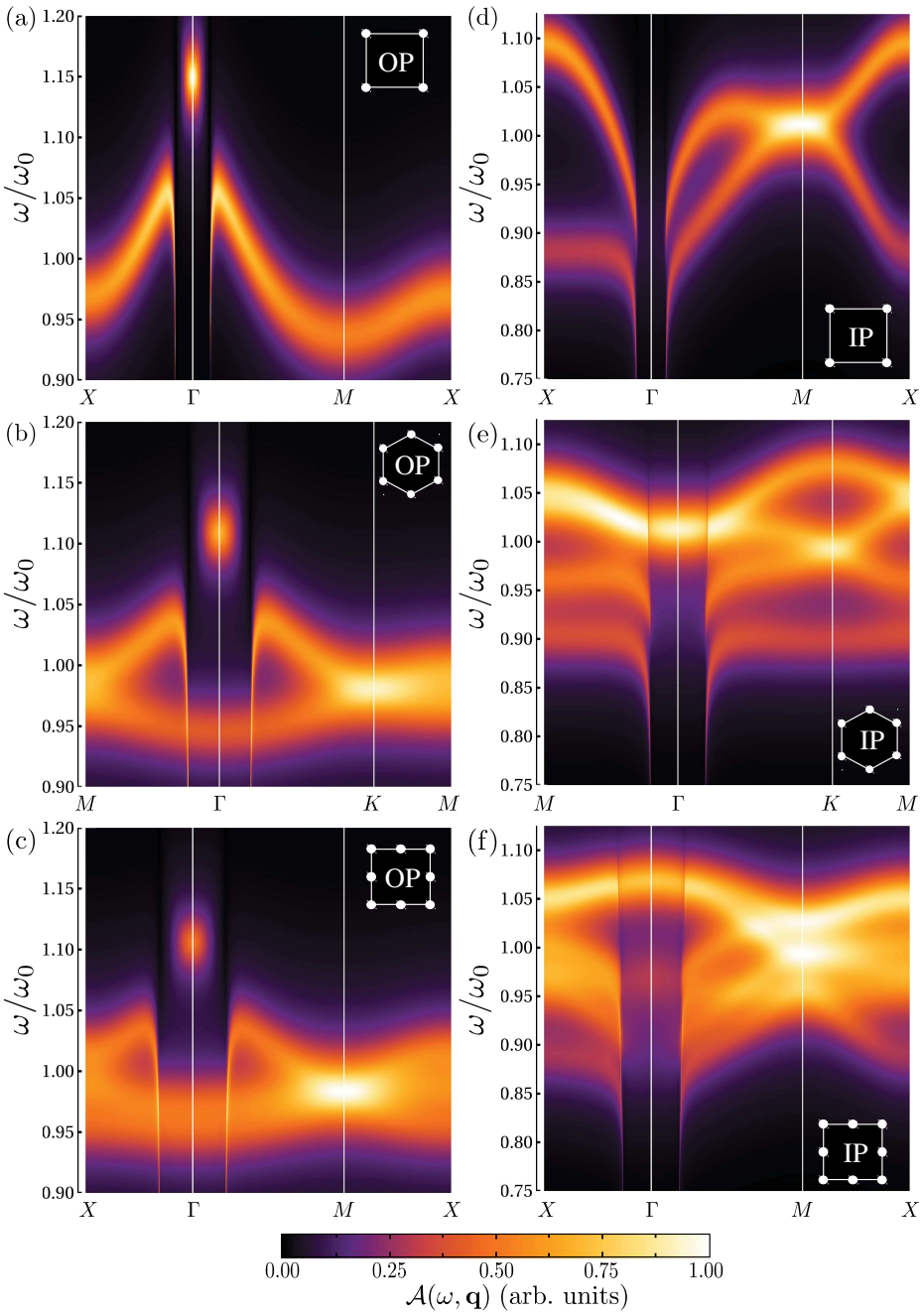

Figure 8.3: Spectral function (8.1) for (a),(d) the square, (b),(e) the honeycomb and (c),(f) the Lieb lattices. The results for the out-of-plane (in-plane) polarized modes are shown in panels (a)–(c) [(d)–(f)]. The Ohmic losses $\gamma_O = 0.027\omega_0$ entering the total damping rate (8.3) and corresponding to Ag [156] are taken into account. The other parameters are the same as in Fig. 8.2.

the Ohmic losses, we have determined that for a particular set of parameters one could image a large majority of the plasmonic bands with a rather good resolution. Importantly, our study showed that it would be preferable to employ EELS detection experiments since a significant part of the bandstructure lies outside the light cone and is thus not accessible with regular optical techniques. In addition, the bands corresponding to the dark plasmonic modes only couple weakly to the light and thus can be difficult to probe optically.

We further included the Ohmic absorption losses within the spectral function. As expected, this additional contribution to the total linewidth blur a significant part of the plasmonic bandstructures. Importantly, we have reported that, taking into account the Ohmic losses reduced in particular the resolution at the corner of the Brillouin zone where the conical dispersions lie. Consequently, it would be necessary to employ experimental methods to reduce such effects in order to resolve the topological plasmons existing within particular metasurfaces.

Chapter 9

Concluding remarks

9.1 General conclusion

In this thesis, we have studied the collective plasmonic excitations in generic two-dimensional metamaterials based on spherical metallic nanoparticles. We have focused on the particular case of near-field coupled nanoparticles, i.e., in the regime $3a \lesssim d \ll k_0^{-1}$. We have developed an analytical theory able to describe the principal properties of such collective modes within general lattices.

We have assumed that the size of the nanoparticles are much smaller than the wavelength associated with their resonance frequency so that each nanoparticle host three degenerate dipolar collective modes, i.e., the localized surface plasmons. Within the near-field limit we have restricted to, these plasmons thus interact with each others through fully-retarded dipole-dipole Coulomb interactions giving rise to the collective plasmons. To study the properties of these modes, we have employed an open-quantum system framework. Such an approach has indeed proven to provide very good insight on the dynamics of the plasmonic excitations in isolated nanoparticles [67,68,74,165] and simple one-dimensional arrays of nanoparticles [64, 79, 80, 135]. The open-quantum system method is standard when one aims to study an excited system exposed to dissipation channels into some environments.

For plasmonic metasurfaces, there are two environments to which the plasmonic modes are coupled and may decay: a photonic and an electronic environment. To access the dynamics of the collective plasmons, we have decomposed the many-body electronic Hamiltonian into electronic center-of-mass and relative coordinates within each nanoparticle. With this picture, the center of masses thus describe the isolated LSPs which couple to each other while the relative coordinates correspond to an *internal* environment into which the plasmons dissipate their energy. The quasistatic dipole-dipole coupling between the LSPs gives rise to the plasmonic collective modes. To complete our approach, we have added the second *external* photonic environment to which the plasmons are coupled (incorporated in this manner the retardation effects and the additional decay channels), using standard quantum optical calculations in the Coulomb gauge.

We have then applied our methods to arbitrary two-dimensional lattices which we characterized by Bravais lattices with a basis. In this context, we have constructed the Hamiltonian corresponding to the purely plasmonic excitations within such structures in a similar manner as those employed

for one-dimensional arrays. The Hamiltonian we obtained was divided into five distinct terms: one describing the plasmonic subsystem, two others describing respectively the photonic and electronic environments, and finally two terms corresponding to the coupling between the plasmonic excitations and each individual environment. Importantly, as our theory aimed at describing quantum effects induced by the electronic (internal) environment, we have quantized our Hamiltonian in the wavevector space. In momentum space, the characteristics of the quasistatic dipolar interactions are encoded within a single parameter: the lattice sum. The latter parameter constitutes one of the principal differences distinguishing the Hamiltonian of the plasmonic system with respect to a tight-binding Hamiltonian describing electronic systems.

From this description, we have then proposed an exact diagonalization of the Hamiltonian associated to the plasmonic modes to unveil the quasistatic eigenmodes properties. To perform such a diagonalization, we have introduced a bosonic Bogoliubov transformation. This linear combination of ladder operators associated with the single LSPs allowed us to characterize efficiently the plasmonic eigenstates. From the Heisenberg equation of motion applied to the new bosonic operators we have thus derived a system of equations allowing to find analytically the eigenfrequencies and the eigenstates of the plasmonic system. In particular, the case of arbitrary simple Bravais lattices was solved fully analytically.

Moreover, we have finally presented an alternative method for obtaining the plasmonic eigenstates based on a perturbation theory. The latter framework could be of interest for obtaining analytical solutions for complicated structures as the number of variables in the equations to obtain is divided by two (from $6\mathcal{S}$ to $3\mathcal{S}$. In addition, we have also provided within our theory a way to evaluate the polarization of the plasmonic collective modes. Such polarization has appeared to be strongly related to the photonic-induced quantities.

Within our model, we have extensively studied different kinds of lattices that are the simple Bravais, the bipartite and tripartite lattices, respectively. For each type of lattices, we have derived analytical solutions for the eigenfrequencies and eigenstates for out-of-plane and in-plane polarized plasmonic modes, whenever the results were tractable (i.e., when the obtained results were sufficiently compact to provide practical expressions). For the cases where no analytic solutions were obtainable, we have solved the eigensystems numerically. In particular, we have analyzed in detail the quasistatic plasmonic bandstructure for the square lattice since the case for simple Bravais lattices is fully analytically tractable. For this lattice, we have explained, using a mean-field theory, the pronounced cusps appearing in the full quasistatic dispersion relations in the vicinity of the center of the first Brillouin zone. We have checked that others Bravais lattices (i.e., the rectangular and hexagonal ones) depict similar features.

We have then applied our model to specific lattices presenting interesting topological features in electronic tight-binding systems, that are: the honeycomb, the Lieb and kagome lattices. Importantly, we have proven that the long-range dipolar interaction do not rule out the Dirac-like plasmons which were demonstrated to exist in honeycomb lattices [108, 109] in the vicinity of the K and K' points of the first Brillouin zone. The only noticeable effects of the long-range interactions as compared to the nearest-neighbor approximation is a slight shift of the bandstructure accompanied by a renormalization of the group velocity associated with the conical dispersion. In the case of the Lieb and the kagome lattices, we have showed that the effects of the long range interactions are much more important since they modify heavily the bandstructure obtained in the

nearest-neighbor approximation. In particular, the flat bands appearing in the dispersion relations within the latter approximation become only locally flat at the corners of the first Brillouin zones.

We have then tackled the problem of evaluating the quantities induced by the environments. To this end, we have used a perturbation theory assuming weak coupling between the plasmonic subsystems and the baths. Importantly, the use of such a perturbation theory has allowed us to take analytically into account the retardation effects arising from the electromagnetic interactions. Building onto what has been done for one-dimensional arrays, we have derived a general analytical expression for the radiative shifts arising from the retardation effects and valid for any collective plasmon polarizations and lattice geometries. In particular, we have derived expressions for the radiative shifts of the out-of-plane and in-plane polarized plasmonic modes which depend only on the eigenfrequencies and the eigenstates of the plasmonic subsystem. Importantly, we have demonstrated that taking into account the retardation effects leads to similar effects as reported for one-dimensional plasmonic arrays, that is the appearance of singularities at the intersection of the quasistatic bandstructures with the light cone. These effects are however largely more prominent in two-dimensional arrays and thus crucial to consider. In addition, the inclusion of the retarded effects have shown to suppress the cusps appearing in the dispersion relations which correspond in fact to instantaneous contributions to the plasmonic bandstructures. Moreover, we have demonstrated the existence of dark plasmonic modes which only couple weakly to light within metasurfaces. These modes can be predicted using a parameter which depends only on the Bogoliubov coefficients extracted from the eigensystem.

Using a Fermi golden rule, we have also evaluated the radiative decay rate of the plasmonic modes. Similarly to the radiative shifts, we have obtained analytical expression for such a rate for out-of-plane and in-plane polarization. We have further demonstrated that within the light cone, the LSPs interfere constructively giving rise to highly superradiant eigenstates. Conversely, some of the eigenstates correspond to dark modes with subradiant profiles which can be predicted similarly as to the radiative shift. For the radiative linewidths, the profile are reminiscent of those theorized in plasmonic chains [80, 135] but are much more pronounced.

In this thesis, we have also evaluated the effects of the electronic environment onto the plasmonic system. Using semi-classical tools [67,68,71,74], we have derived both the Landau linewidth and the electronic frequency shift. Within a perturbation theory, we have thus demonstrated that these purely quantum effects are crucial to consider since they constitute the predominant contributions for both the linewidths and the frequency shifts for small nanoparticles (of about few nanometers in size). Interestingly, we have further showed that the electronic-induced properties are always present contrary to the photonic induced ones which may vanish (i.e., for dark modes).

Our transparent analytical theory allowed us to compute the spectral function of the plasmonic modes. Indeed, with the expression of the total linewidths as well as of the frequency shifts, we have provided comprehensive informations about the possibility to resolve spectroscopically the plasmonic modes within the metasurfaces. Finally, within this framework, we have shown that the use of gain-medium for the experiments would be of interest. Indeed, depending of the absorption losses inherent of the metal, we have demonstrated that the splitting between the plasmonic bands would not be sufficient to resolve properly the dispersion relations and in particular those where lie the topological plasmonic states.

9.2 Future perspectives

In this final section, we provide an outlook for our work as well as some future perspectives which would be of interest for improving our theory. Indeed, the model we have developed in this thesis is based on several approximations which restrict its field of application. These restrictions can be examined separately.

Already at the level of the isolated nanoparticles constituting the lattices, we have treated the plasmonic excitation within the jellium model (i.e., mean-field treatment). A way to relax such an approximation for smaller nanoparticles would be to diagonalize exactly the many-body electronic Hamiltonian numerically. Concerning the collective plasmonic modes, we have considered the quasistatic dipole-dipole Coulomb interactions to be the principal contribution to the creation of these modes. In particular, we have restricted ourselves to interparticle distances not too small wit respect to the nanoparticle radius . Thus, it would be of interest to relax such an approximation and evaluate the effects of the multipolar contributions to the collective plasmonic modes. In addition, for closely packed nanoparticles, the presence of so-called *charge transfer plasmons* [117,171–173] (i.e., created by the tunneling of the electrons between the nanoparticules) has been reported. Thus, it would be interesting to investigate their influence on the plasmonic bandstructures.

Concerning the effects of the photonic environment, several improvements can be made as well. The principal limitations of our solutions for the linwidths and frequency shifts arise from our perturbative treatment. For the photonic-induced quantities, such an approximated theory implies that the important singularities we report in this thesis are not physical. To avoid such issues, we could evaluate in specific situations the deviation between our perturbative results and the numerical solutions of Maxwell's equation. We could employ the scheme used in Refs. [133,135] for instance. Moreover, in this thesis we have considered the plasmonic modes to be fully separated from the photonic ones. In principle, in the strong-coupling regime, the light degrees of freedoms couple to the plasmonic ones creating hybridized modes: the so-called *polaritons*. Considering the latter quasiparticles as the eigenmodes of the systems as in Ref. [139], should allow to correct some aberrations, i.e., the abrupt modifications of the plasmonic bandstructure arising in the vicinity of the light cone. Indeed, within this regions, the eigenmodes are of polritonic nature rather than plasmonic. These polaritonic modes can be obtained by diagonalizing the full Hamiltonian which include the plasmonic and photonic parts as well as their coupling. Such a diagonalization presented in Ref. [139] can be conducted along the lines of what we present in this thesis (i.e., using a Bogoliubov transformation). Finally, in our work, we only consider the interaction between the plasmons and the light originating from the first Brillouin zone of the lattice under consideration. As suggested in Chapter 6, such a restriction implies two effects. On the one hand the expressions for the linewidth and the frequency do not present the same periodicity as the lattice. On the other hand, such an approximation suppresses the contributions originating from the other Brillouin zones. These contributions become important for the modes existing at the corners of the first Brillouin zone so that the results we show in the manuscript are not fully reliable in these regions [e.g., the absence of the conical dispersion at the K point in the honeycomb lattice, see Fig. 6.1(d)]. One could take into account these various contributions of the light cones by using a photonic wavevector with the periodicity of the lattice instead of the one we have employed for our calculations. Using this formalism corrects indeed the mismatch we observe in the corner of the

first Brillouin zone (as reported in Ref. [139] for the honeycomb lattice) but comes with the cost of numerical calculations since the summations over the reciprocal lattice vectors require a large number of terms to converge properly.

In addition to relax the assumptions we have made for our work we could also try to provide a more quantitative theory. In this context, several improvements are interesting and would lead to a better agreement between the future experimental measurements and our theory. As a first, rather simple addition, we could include the spill-out effect within the plasmon resonance frequency which would lead to an additional redshift of the later frequency. Then, we also may add the effects of a substrate in our theory. Accounting for the substrate may be done in various ways. The more simplistic one is to consider an embedding homogeneous dielectric matrix which will screen the plasmonic resonance frequency. We can also consider a more advanced technique by combining the previous proposition with a more precise calculation of the effects of the substrate. In this case, the substrate can be seen as a collection of image dipoles to the dipolar LSPs. The LSPs interact with each other as well as with the image dipole moments within the substrate through quasistatic dipole-dipole interactions. Taking into account these additional charges should renormalize the different lattice sums appearing in the plasmonic bandstructures. Importantly, evaluating the influence of a dielectric environment would also imply to modify the light-matter interaction. In particular, one would have to modify the vector potential entering the plasmon-photon coupling Hamiltonian. We also expect this to induce only a quantitative renormalization of the bandstructure. Finally, we have considered fully identical nanoparticles and regular lattices within our model. In principle, the samples exhibit a slight deviation between the various nanoparticle sizes or separations. To include these experimental parameters, we could consider the nanoparticle size a and the interparticle separation d to by Gaussian distributed around a precise value. Thus, all the related quantities (e.g., the resonance and coupling frequencies) would have a finite standard-deviation attached to them. The drawback of such a procedure is that it would probably require a full numerical treatment to be fruitful.

More generally, we could also include in our model a way to diversify its applicability. To do so, several leads can be considered. First, we could extend our model to non spherical nanoparticles. Although it would once again required some numerical calculations (due to the lack of spherical symmetry), it would be interesting to treat the case of elongated nanorods which host orientated plasmonic modes (instead of three degenerate ones). Indeed, with elongated dipoles, we could shape the form of the plasmonic bandstructures (see Ref. [108, 109]). Furthermore, we could also considered arrays with non-periodic lattices or different kinds of nanoparticles within the lattices (e.g., including silver and gold nanoparticle within the same array).

Finally, we would like also to study the propagation of the plasmonic modes within the lattice when excited by a external electric field. In particular, it would be interesting to study the effects of the topological modes (such as the Dirac-like plasmons in the honeycomb lattice) onto the propagation. During the thesis,[1] we have started to study such a propagation. Based on the formalism of the reduced density matrix in the Lindblad form, we have derived the expression for the time-evolution of the dipole moments bared by each nanoparticle within a honeycomb lattice. It would be of prime interest to complete our analysis and investigate the behavior of a single plasmonic mode. In particular, we would like to study extensively the effects of the Dirac-like modes in a

[1] Not included in the manuscript.

honeycomb lattice or the locally flat bands in the Lieb lattice on the propagation of the collective plasmons. Indeed, the latter could be very interesting in the prospect of "stocking" the light at sub-wavelength scales.

Appendix A

Semiclassical derivation of the function $\sum^{\sigma}(\omega)$

In this appendix, we present the procedure one can use to evaluate the function $\Sigma^{\sigma}(\omega)$ defined in Eq. (2.35) following Ref. [67]. Due to the spherical symmetry of the system, $\Sigma^{\sigma}(\omega)$ is isotropic implying that one only requires to calculate the function for the special case $\sigma = z$. Introducing the single-particle density of states $\varrho(\epsilon)$ with energy ϵ which can be decomposed into fixed-angular momentum components

$$\varrho(\epsilon) = \sum_{l=0}^{\infty} \sum_{m=-l}^{+l} \varrho_l(\epsilon), \tag{A.1}$$

Eq. (2.35) can be rewritten as [67]

$$\Sigma^{z}(\omega) = \frac{4\pi}{\hbar} \Lambda^2 \sum_{l,l'} \sum_{m,m'} \int_{\max\{E_{\mathrm{F}}, \hbar\omega\}}^{E_{\mathrm{F}}+\hbar\omega} \mathrm{d}\epsilon \varrho_l(\epsilon) \varrho_{l'}(\epsilon - \hbar\omega) \left| \hat{z} \cdot \mathbf{d}_{eh} \right|^2 . \tag{A.2}$$

In Eq. (A.2), a factor of 2 was added to take into account the spin degeneracy. Then, using the expression of $\hat{z} \cdot \mathbf{d}_{eh}$ [see Eq. (2.22)], using the selection rules $l' = l \pm 1$ and $m = m'$ (corresponding to $\sigma = z$) encapsulated in Eq. (2.24), one can write for Eq. (A.2)

$$\begin{aligned} \Sigma^{z}(\omega) = \frac{4\pi}{\hbar} & \int_{\max\{E_{\mathrm{F}}, \hbar\omega\}}^{E_{\mathrm{F}}+\hbar\omega} \mathrm{d}\epsilon \left[\Lambda \mathcal{R}(\epsilon, \epsilon - \hbar\omega) \right]^2 \\ & \times \sum_{l=0}^{\infty} \sum_{m=-l}^{-l} \varrho_l(\epsilon) \left[\left(\mathcal{A}^{m,m}_{l,l+1,0} \right)^2 \varrho_{l+1}(\epsilon - \hbar\omega) + \left(\mathcal{A}^{m,m}_{l,l-1,0} \right)^2 \varrho_{l-1}(\epsilon - \hbar\omega) \right] . \end{aligned} \tag{A.3}$$

Then, one performs the summation over the quantum number m for $\aleph = 0$ which gives

$$\sum_{m=-l}^{+l} \left(\mathcal{A}^{m,m}_{l,l+1,0}\right)^2 = \frac{l+1}{3},$$
$$\sum_{m=-l}^{+l} \left(\mathcal{A}^{m,m}_{l,l-1,0}\right)^2 = \frac{l}{3}. \tag{A.4}$$

Thus, substituting Eq. (A.4) into (A.3) one obtains

$$\Sigma^z(\omega) = \frac{4\pi}{3\hbar} \int_{\max\{E_\mathrm{F},\hbar\omega\}}^{E_\mathrm{F}+\hbar\omega} \mathrm{d}\epsilon \left[\Lambda \mathcal{R}(\epsilon, \epsilon-\hbar\omega)\right]^2 \sum_{l=0}^{\infty} \varrho_l(\epsilon) \left[(l+1)\varrho_{l+1}(\epsilon-\hbar\omega) + l\varrho_{l-1}(\epsilon-\hbar\omega)\right]. \tag{A.5}$$

One next evaluates the density of states with fixed angular momentum $\varrho_l(\epsilon)$ with the help of semi-classical techniques [174, 175]. In such a framework, the leading order in $\hbar$ of the density of states $\varrho_l(\epsilon)$ is given by [72, 74]

$$\varrho_l(\epsilon) \simeq \frac{\sqrt{2m_\mathrm{e}a^2\epsilon/\hbar^2 - (l+1/2)^2}}{2\pi\epsilon}. \tag{A.6}$$

Then, inserting Eq. (A.6) together with Eq. (2.23) into the expression of $\Sigma^z(\omega)$ in (A.5) leads to

$$\Sigma^z(\omega) = \frac{8\pi}{3\hbar m_\mathrm{e}^2\omega^4}\frac{\Lambda^2}{a^2} \int_{\max\{E_\mathrm{F},\hbar\omega\}}^{E_\mathrm{F}+\hbar\omega} \mathrm{d}\epsilon \int_0^{l_\mathrm{max}} \mathrm{d}l \left[l\sqrt{\epsilon(\epsilon-\hbar\omega)}\sqrt{\frac{2m_\mathrm{e}a^2\epsilon}{\hbar^2} - l^2}\sqrt{\frac{2m_\mathrm{e}a^2(\epsilon-\hbar\omega)}{\hbar^2} - l^2}\right]. \tag{A.7}$$

In the latter equation the limit $l \gg 1$ has been taken since one is interested in high-energy limit in the semi-classical approximation. Such a restriction allows to replace the summation by an integral with upper limit $l_\mathrm{max} = 2m_\mathrm{e}a^2(\epsilon-\hbar\omega)/\hbar^2$, and to take $l \simeq l+1$. The equation (A.7) can finally be rewritten in a more compact form as

$$\Sigma^z(\omega) = \frac{3v_\mathrm{F}}{4a}\left(\frac{\omega_0}{\omega}\right)^3 g\left(\frac{\hbar\omega}{E_\mathrm{F}}\right), \tag{A.8}$$

where the function $g(\nu)$ is given by

$$g(\nu) = \frac{2}{\nu} \int_{\max\{1,\nu\}}^{1+\nu} \mathrm{d}x \int_0^{x-\nu} \mathrm{d}y \sqrt{(x-y)(x-y-\nu)}. \tag{A.9}$$

The integral above can be easily to yield [67, 71, 74, 149]

$$g(\nu) = \frac{1}{3\nu}\left[(1+\nu)^{3/2} - (1-\nu)^{3/2}\right] + \frac{\nu}{4}\left(\sqrt{1+\nu} - \sqrt{1-\nu} - \nu\ln\nu\right)$$
$$+ \frac{\nu}{2}\left[\left(1+\frac{\nu}{2}\right)\ln\left(\sqrt{1+\nu}-1\right) - \left(1-\frac{\nu}{2}\right)\ln\left(1-\sqrt{1-\nu}\right)\right], \tag{A.10a}$$

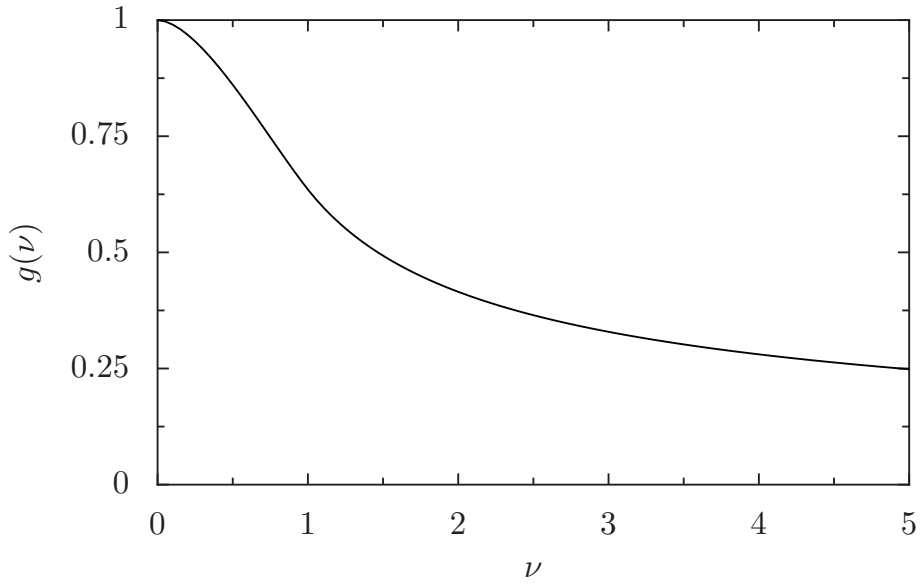

Figure A.1: Plot of the function $g(\nu)$ defined in Eq. A.10.

for $\nu \leqslant 1$ and

$$g(\nu) = \frac{1}{3\nu}\left(1+\nu\right)^{3/2} + \frac{\nu}{4}\left(\sqrt{1+\nu} - \ln\nu\right) + \frac{\nu}{2}\left[\left(1+\frac{\nu}{2}\right)\ln\left(\sqrt{1+\nu}-1\right) - \frac{\nu}{2}\ln\sqrt{\nu}\right], \tag{A.10b}$$

for $\nu > 1$. The function $g(\nu)$ given in Eq. (A.10) is a smooth decreasing function of its argument ν that we plot in Fig. A.1. Thus, the Landau damping decay rate [see e.g. Eq. (2.37)] for which the function $g(\nu)$ enters, decreases slowly as the ratio between the Mie frequency ω_0 and the Fermi energy $E_{\rm F}$ increases.

Appendix B

Explicit expressions of some of the functions used in the main text

In this appendix, we provide details concerning various functions and quantities appearing in the main text. In particular, we concentrate on the functions implied in the frequency shifts of the plasmonic excitations of isolated nanoparticles and the plasmonic dimers discussed in Chapters 2 and 3, respectively. In the following, we first present the function $\beth(\omega)$ introduced for the derivation of the Landau shift for the single nanoparticles in Sec. 2.4.2. Then, we briefly discuss the quantity g_τ^σ used for the radiative shift of the hybridized plasmons hosted by the nanoparticle dimers (see Sec. 3.2.1).

B.1 The function $\beth(\omega)$

We here describe the function $\beth(\omega)$ we evaluated in Eq. (2.53) for the electronic shift of collective plasmonic modes [see e.g., Eq. (3.34)]. In the figure, we show the function $\beth(\omega)$ for different nanoparticle sizes. The solid black line corresponds to $k_{\rm F}a = 50$ while the dashed and dotted ones to $k_{\rm F}a = 200$ and 300, respectively. In the figure, we choose the patameters $\eta = 0.5$, $\hbar\omega_0 = 1$ and $\hbar\omega_0/E_{\rm F} = 1/2$. We see that the function is a decreasing smooth function of the frequency ω within the range to which the collective mode resonance frequencies typically lie. The function $\beth(\omega)$ plotted in Fig. B.1 depends of the size of the nanoparticle. Importantly, since the function is proportional to $1/\omega^4$ up to a logarithmic factor [see Eq. (2.53)], the smaller the frequency is, the larger the value of $\beth(\omega)$.

B.2 The quantity g_τ^σ introduced for the radiative shift of the dimers

We begin this appendix by deriving the quantity g_τ^σ appearing in Sec. 3.2.1 for the evaluation of the radiative frequency shifts of the plasmonic hybridized modes of nanoparticle dimers. In the main

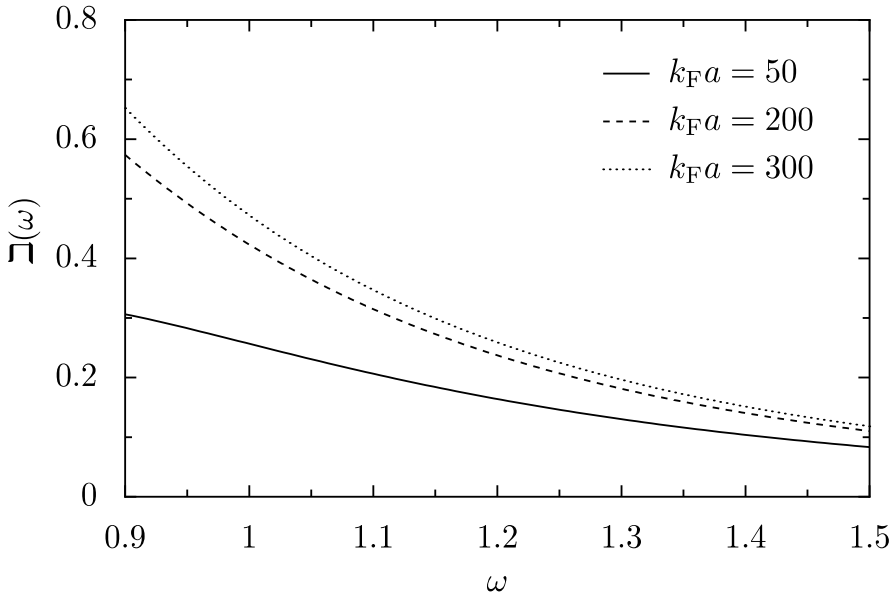

Figure B.1: Plot of the function $\beth(\omega/\omega_0)$ defined in Eq. (2.53) for different nanoparticle sizes. The solid, dashed and dotted lines correspond respectively to $k_{\rm F}a = 50, 200$ and 300. In the figure, we have $\eta = 1/2$ and $\hbar\omega_0 = 1$ and $\hbar\omega_0/E_{\rm F} = 1/2$.

text, this quantity is defined as an integral in Eq. (3.21) which can be written as

$$g_\tau^\sigma = \xi^4 \mathcal{P} \int_0^\alpha \frac{\mathrm{d}x}{x(\xi^2 - x^2)} \left[\left(1 + \mathrm{sgn}\{\eta^\sigma\} - \frac{2}{x^2} \right) \sin(x) + \frac{2}{x} \cos(x) \right], \tag{B.1}$$

where η^σ is related to the polarization of the plasmonic modes. In the main text we have $\xi = \omega_\tau^\sigma d/c$ and $\alpha = \omega_{\rm c} d/c$, entering Eq. (B.1). The latter integral can be straightforwardly evaluated to yield [64]

$$\begin{aligned} g_\tau^\sigma = & \left(\frac{k_\tau^\sigma}{k_{\rm c}} \right)^2 [\sin(k_{\rm c}d) - k_{\rm c}d\cos(k_{\rm c}d)] - \left[2f_\tau^\sigma + (k_\tau^\sigma d)^2 \right] \mathrm{Si}(k_{\rm c}d) \\ & + \sum_{\zeta=\pm} \{ r_\tau^\sigma \mathrm{Si}([k_{\rm c} + \zeta k_\tau^\sigma]d) - \zeta s_\tau^\sigma \mathrm{Ci}([k_{\rm c} + \zeta k_\tau^\sigma]d) \}. \end{aligned} \tag{B.2}$$

In the latter expression,

$$\mathrm{Si}(z) = \int_0^z \mathrm{d}t \frac{\sin t}{t} \tag{B.3a}$$

and

$$\mathrm{Ci}(z) = -\int_z^\infty \mathrm{d}t \frac{\cos t}{t} \tag{B.3b}$$

are the sine and cosine integrals, respectively, and one has

$$f_\tau^\sigma = 1 - \frac{(k_\tau^\sigma d)^2}{2}\left[1 + \mathrm{sgn}\{\eta^\sigma\}\right], \tag{B.4a}$$

$$r_\tau^\sigma = f_\tau^\sigma \sin(k_\tau^\sigma d) + k_\tau^\sigma d \sin(k_\tau^\sigma d), \tag{B.4b}$$

and

$$s_\tau^\sigma = f_\tau^\sigma \cos(k_\tau^\sigma d) - k_\tau^\sigma d \cos(k_\tau^\sigma d), \tag{B.4c}$$

with $k_\tau^\sigma = \omega_\tau^\sigma / c$ and $k_\mathrm{c} = \omega_\mathrm{c}/c$, respectively.

Appendix C

Diagonalization of a generic quadratic bosonic system

We present in this appendix the method we use to diagonalize numerically the plasmonic Hamiltonian (4.16) introduced in Chapter 4. Such a procedure which uses the Cholesky decomposition of the plasmonic Hamiltonian (written in its matrix form) is derived directly from the work of Colpa [159] for the diagonalization of generic quadratic bosonic Hamiltonians. Note that an alternative derivation of the same problem was also proposed in the work of Tsallis [176]. In what follows, we present in a first part the general method described in Ref. [159] for the diagonalization and give a practical example in the second section of this appendix to illustrate such a method.

C.1 General diagonalization algorithm

As a starting point of the algorithm, we consider the plasmonic Hamiltonian $H_{\rm pl}$ written in Fourier space [cf. Eq. (4.16)]. The first step is to write such a Hamiltonian in Bogoliubov-de Gennes (BdG) form as

$$H_{\rm pl} = \frac{1}{2}\sum_{\mathbf{q}} \begin{pmatrix} \mathbf{b}_{\mathbf{q}}^{\dagger} & \mathbf{b}_{-\mathbf{q}} \end{pmatrix} \cdot \boldsymbol{\mathcal{H}}_{\mathbf{q}} \cdot \begin{pmatrix} \mathbf{b}_{\mathbf{q}} \\ \mathbf{b}_{-\mathbf{q}}^{\dagger} \end{pmatrix}, \tag{C.1}$$

In the latter equation, the quantity

$$\mathbf{b}_{\mathbf{q}}^{\dagger} \equiv \left\{ \left[b_1^{x\dagger}(\mathbf{q}), b_1^{y\dagger}(\mathbf{q}), b_1^{z\dagger}(\mathbf{q}) \right], \ldots, \left[b_{\mathcal{S}}^{x\dagger}(\mathbf{q}), b_{\mathcal{S}}^{y\dagger}(\mathbf{q}), b_{\mathcal{S}}^{z\dagger}(\mathbf{q}) \right] \right\} \tag{C.2}$$

corresponds to the $3\mathcal{S}$ row vector constituted by all the individual bosonic creation operators $b_s^{\sigma\dagger}(\mathbf{q})$. Note that $\mathbf{b}_{-\mathbf{q}}$ account for the same kind of row vector implying that $\begin{pmatrix} \mathbf{b}_{\mathbf{q}}^{\dagger} & \mathbf{b}_{-\mathbf{q}} \end{pmatrix}$ is a $6\mathcal{S}$ row vector. In addition we have

$$\begin{pmatrix} \mathbf{b}_{\mathbf{q}} \\ \mathbf{b}_{-\mathbf{q}}^{\dagger} \end{pmatrix} = \left[\begin{pmatrix} \mathbf{b}_{\mathbf{q}}^{\dagger} & \mathbf{b}_{-\mathbf{q}} \end{pmatrix} \right]^{\dagger}. \tag{C.3}$$

Since $H_{\rm pl}$ in Eq. (C.1) is Hermitian, the BdG Hamiltonian $\boldsymbol{\mathcal{H}}_{\mathbf{q}}$ possesses the same property implying that

$$\boldsymbol{\mathcal{H}}_{\mathbf{q}} = \begin{pmatrix} \boldsymbol{\mathcal{A}}_{\mathbf{q}} & \boldsymbol{\mathcal{B}}_{\mathbf{q}} \\ \boldsymbol{\mathcal{B}}^{*}_{-\mathbf{q}} & \boldsymbol{\mathcal{A}}^{*}_{-\mathbf{q}} \end{pmatrix}. \tag{C.4}$$

In Eq. (C.4), $\boldsymbol{\mathcal{A}}_{\mathbf{q}}$ and $\boldsymbol{\mathcal{B}}_{\mathbf{q}}$ are two $3\mathcal{S} \times 3\mathcal{S}$ square matrices, so that $\boldsymbol{\mathcal{H}}_{\mathbf{q}}$ corresponds to a $6\mathcal{S} \times 6\mathcal{S}$ matrix. The latter Hamiltonian is then diagonalized as

$$\boldsymbol{\mathcal{H}}^{\rm D}_{\mathbf{q}} = \boldsymbol{\mathcal{T}}_{\mathbf{q}}{}^{\dagger} \boldsymbol{\mathcal{H}}_{\mathbf{q}} \boldsymbol{\mathcal{T}}_{\mathbf{q}} = \begin{pmatrix} \boldsymbol{\mathcal{E}}_{\mathbf{q}} & \mathbf{0}_{3\mathcal{S}} \\ \mathbf{0}_{3\mathcal{S}} & \boldsymbol{\mathcal{E}}_{-\mathbf{q}} \end{pmatrix}, \tag{C.5}$$

where $\boldsymbol{\mathcal{E}}_{\mathbf{q}}$ and $\boldsymbol{\mathcal{E}}_{-\mathbf{q}}$ are two diagonal matrices whose diagonal elements correspond to the collective plasmon eigenvalues. In the latter equation, $\mathbf{0}_{3\mathcal{S}}$ is a $3\mathcal{S} \times 3\mathcal{S}$ square null matrix and $\boldsymbol{\mathcal{T}}_{\mathbf{q}}$ represents the transformation matrix which diagonalizes the BdG Hamiltonian. Such a matrix satisfies the relation

$$\begin{pmatrix} \mathbf{b}^{\dagger}_{\mathbf{q}} & \mathbf{b}_{-\mathbf{q}} \end{pmatrix} = \begin{pmatrix} \boldsymbol{\beta}^{\dagger}_{\mathbf{q}} & \boldsymbol{\beta}_{-\mathbf{q}} \end{pmatrix} \boldsymbol{\mathcal{T}}_{\mathbf{q}}{}^{\dagger}, \tag{C.6}$$

where the row vector $\boldsymbol{\beta}^{\dagger}_{\mathbf{q}}$ is given by

$$\boldsymbol{\beta}^{\dagger}_{\mathbf{q}} \equiv \left\{ \left[\beta^{\varepsilon_{\parallel,1}\,\dagger}_{\tau_1}(\mathbf{q}), \beta^{\varepsilon_{\parallel,2}\,\dagger}_{\tau_1}(\mathbf{q}), \beta^{z\,\dagger}_{\tau_1}(\mathbf{q}) \right], \ldots, \left[\beta^{\varepsilon_{\parallel,1}\,\dagger}_{\tau_{\mathcal{S}}}(\mathbf{q}), \beta^{\varepsilon_{\parallel,2}\,\dagger}_{\tau_{\mathcal{S}}}(\mathbf{q}), \beta^{z\,\dagger}_{\tau_{\mathcal{S}}}(\mathbf{q}) \right] \right\}. \tag{C.7}$$

In Eq. (C.7), the operators $\beta^{\varepsilon\,\dagger}_{\tau}(\mathbf{q})$ are the collective plasmons creation oparators given in Eq. (4.18) in the main text. In Eq (C.7), the indices $\varepsilon_{\parallel,1}$, $\varepsilon_{\parallel,2}$ and z are the different values of the collective mode polarizations ε while the subscripts τ_s (with $s \in [1, \ldots, \mathcal{S}]$) account for the plasmonic band index.

Due to the requirement that the Hamiltonian $H_{\rm pl}$ obeys bosonic statistic, the matrix $\boldsymbol{\mathcal{T}}_{\mathbf{q}}$ which diagonalizes $\boldsymbol{\mathcal{H}}_{\mathbf{q}}$ is a para-unitary matrix instead of a unitary one (as for the regular diagonalization of fermionic systems). Such para-unitary condition implies that the matrix $\boldsymbol{\mathcal{T}}_{\mathbf{q}}$ obeys the rules

$$\boldsymbol{\mathcal{T}}_{\mathbf{q}}{}^{\dagger} \boldsymbol{\mathcal{J}} \boldsymbol{\mathcal{T}}_{\mathbf{q}} = \boldsymbol{\mathcal{J}}, \qquad \boldsymbol{\mathcal{T}}_{\mathbf{q}}\, \boldsymbol{\mathcal{J}} \boldsymbol{\mathcal{T}}_{\mathbf{q}}{}^{\dagger} = \boldsymbol{\mathcal{J}} \tag{C.8}$$

where $\boldsymbol{\mathcal{J}}$ is a $6\mathcal{S} \times 6\mathcal{S}$ diagonal matrix given by

$$\boldsymbol{\mathcal{J}} = \boldsymbol{\sigma}_z \otimes \mathbb{1}_{3\mathcal{S}}. \tag{C.9}$$

Here, $\boldsymbol{\sigma}_z$ stands for the third Pauli matrix. In order to construct the transformation matrix, we then follow closely the algorithm given in Ref. [159]. Thus, we first construct the matrix $\boldsymbol{\mathcal{K}}_{\mathbf{q}}$ as $\boldsymbol{\mathcal{H}}_{\mathbf{q}} = \boldsymbol{\mathcal{K}}^{\dagger}_{\mathbf{q}} \boldsymbol{\mathcal{K}}_{\mathbf{q}}$ using a PYTHON routine with the module NUMPY. Then, we build a new matrix using the matrix $\boldsymbol{\mathcal{K}}_{\mathbf{q}}$ we have just obtained. Such a matrix reads as

$$\boldsymbol{\mathcal{W}}_{\mathbf{q}} \equiv \boldsymbol{\mathcal{K}}_{\mathbf{q}}\, \boldsymbol{\mathcal{J}} \boldsymbol{\mathcal{K}}_{\mathbf{q}}{}^{\dagger}. \tag{C.10}$$

The latter matrix is then diagonalized using a regular diagonalization routine (we used in our case

the subroutine *numpy.linalg.eig()* included in PYTHON) yielding

$$\boldsymbol{\mathcal{U}}_{\mathbf{q}}{}^{\dagger}\boldsymbol{\mathcal{W}}_{\mathbf{q}}\,\boldsymbol{\mathcal{U}}_{\mathbf{q}} \;=\begin{pmatrix}\boldsymbol{\mathcal{E}}_{\mathbf{q}} & \mathbf{0}_{3\mathcal{S}}\\ \mathbf{0}_{3\mathcal{S}} & -\boldsymbol{\mathcal{E}}_{-\mathbf{q}}\end{pmatrix}. \tag{C.11}$$

The matrices $\boldsymbol{\mathcal{E}}_{\mathbf{q}}$ and $\boldsymbol{\mathcal{E}}_{-\mathbf{q}}$ appearing in the expression above are the same as those introduced in Eq. (C.5). Importantly, such a matrix $\boldsymbol{\mathcal{E}}_{\mathbf{q}}$ corresponds to the eigenvalues of the BdG Hamiltonian $\boldsymbol{\mathcal{H}}_{\mathbf{q}}$. Note that in Eq. (C.11), the two matrices $\boldsymbol{\mathcal{E}}_{\mathbf{q}}$ and $-\boldsymbol{\mathcal{E}}_{-\mathbf{q}}$ constitute $3\mathcal{S}$ pairs of positive and negative eigenvalues. Practically, however, we only have to consider the positive eigenvalues as the eigenfrequencies of the plasmonic system. Such a restriction stems from the necessity for eigenenergies to be positive in physical systems. Equipped with the transformation matrix $\boldsymbol{\mathcal{U}}_{\mathbf{q}}$ and the matrix of eigenvalues we can finally build the transformation matrix $\boldsymbol{\mathcal{T}}_{\mathbf{q}}$ (which diagonalizes $\boldsymbol{\mathcal{H}}_{\mathbf{q}}$) as

$$\boldsymbol{\mathcal{T}}_{\mathbf{q}}{}^{-1} = \boldsymbol{\mathcal{K}}_{\mathbf{q}}^{-1}\boldsymbol{\mathcal{U}}_{\mathbf{q}} \;\cdot\begin{pmatrix}\boldsymbol{\mathcal{E}}_{\mathbf{q}}^{1/2} & \mathbf{0}_{3\mathcal{S}}\\ \mathbf{0}_{3\mathcal{S}} & \boldsymbol{\mathcal{E}}_{-\mathbf{q}}^{1/2}\end{pmatrix}. \tag{C.12}$$

The matrix $\boldsymbol{\mathcal{T}}_{\mathbf{q}}$ above thus contains the Bogoliubov coefficients $u_{\tau s}^{\varepsilon\sigma}(\mathbf{q})$ and $v_{\tau s}^{\varepsilon\sigma}(\mathbf{q})$ introduced in Chapter 4 in the main text for the exact diagonalization. Note that within such an algorithm, the Bogoliubov coefficients are completely encoded into the first $3\mathcal{S}$ rows of $\boldsymbol{\mathcal{T}}_{\mathbf{q}}$ since the values within the rest of the rows are fully redundant with the first rows (similarly to the eigenvalues $\boldsymbol{\mathcal{E}}_{\mathbf{q}}$). As a supplementary procedure, one may also check that the transformation matrix fulfills the relation

$$\boldsymbol{\mathcal{H}}_{\mathbf{q}}\boldsymbol{\mathcal{T}}_{\mathbf{q}} = \boldsymbol{\mathcal{J}}\boldsymbol{\mathcal{T}}_{\mathbf{q}}\begin{pmatrix}\boldsymbol{\mathcal{E}}_{\mathbf{q}} & \mathbf{0}_{3\mathcal{S}}\\ \mathbf{0}_{3\mathcal{S}} & -\boldsymbol{\mathcal{E}}_{-\mathbf{q}}\end{pmatrix}. \tag{C.13}$$

which ensures that $\boldsymbol{\mathcal{T}}_{\mathbf{q}}$ is, as expected, a para-unitary matrix.

C.2 Practical example

In this section, we give more insight on the use of the algorithm presented above using a explicit example. As extensively discussed in Chapter 5, we are able to derive analytic expressions for the eigenfrequencies and Bogoliubov coefficients in specific metasurfaces (e.g. for $\mathcal{S}$ small). Importantly, as emphasized in Sec. 4.2, the inherent structure of the functions $f_{ss'}^{\sigma\sigma'}(\mathbf{q})$ [cf. Eq. (4.17)] allows to fully decouple the modes polarized out of the plane ($\sigma = z$) from those within the plane ($\sigma = x, y$) in the plasmonic Hamiltonian (4.16). Consequently, identical treatment can be perform to the diagonalization algorithm enabling to treat separately the out-of-plane and in-plane collective modes. Therefore, as an illustration of the method presented in the previous section, we choose to study the out-of-plane plasmonic modes in bipartite lattices (i.e., $\mathcal{S} = 2$ and $\sigma = z$). With such

parameters, expanding the summation in (4.16) yields

$$
\begin{aligned}
H_{\mathrm{pl}} = \hbar\omega_0 \sum_{\mathbf{q}} \left[b_1^{z\dagger}(\mathbf{q}) b_1^z(\mathbf{q}) + b_2^{z\dagger}(\mathbf{q}) b_2^z(\mathbf{q}) \right] \\
+ \frac{\hbar\Omega}{2} \sum_{\mathbf{q}} \Big\{ f_{11}^{zz}(\mathbf{q}) b_1^{z\dagger}(\mathbf{q}) \left[b_1^z(\mathbf{q}) + b_1^{z\dagger}(-\mathbf{q}) \right] + f_{12}^{zz}(\mathbf{q}) b_1^{z\dagger}(\mathbf{q}) \left[b_2^z(\mathbf{q}) + b_2^{z\dagger}(-\mathbf{q}) \right] \\
+ [f_{12}^{zz}(\mathbf{q})]^* b_2^{z\dagger}(\mathbf{q}) \left[b_1^z(\mathbf{q}) + b_1^{z\dagger}(-\mathbf{q}) \right] + f_{22}^{zz}(\mathbf{q}) b_2^{z\dagger}(\mathbf{q}) \left[b_2^z(\mathbf{q}) + b_2^{z\dagger}(-\mathbf{q}) \right] + \mathrm{h.c.} \Big\}. \quad \text{(C.14)}
\end{aligned}
$$

From the equation above, we thus build the corresponding BdG Hamiltonian using expression (C.1). Such a step then leads to the matrix

$$
\boldsymbol{\mathcal{H}}_{2,\mathbf{q}}^z = \hbar \begin{pmatrix}
\omega_0 + \Omega f_{11}^{zz}(\mathbf{q}) & \Omega f_{12}^{zz}(\mathbf{q}) & \Omega f_{11}^{zz}(\mathbf{q}) & \Omega f_{12}^{zz}(\mathbf{q}) \\
\Omega [f_{12}^{zz}(\mathbf{q})]^* & \omega_0 + \Omega f_{11}^{zz}(\mathbf{q}) & \Omega [f_{12}^{zz}(\mathbf{q})]^* & \Omega f_{11}^{zz}(\mathbf{q}) \\
\Omega f_{11}^{zz}(\mathbf{q}) & \Omega f_{12}^{zz}(\mathbf{q}) & \omega_0 + \Omega f_{11}^{zz}(\mathbf{q}) & \Omega f_{12}^{zz}(\mathbf{q}) \\
\Omega [f_{12}^{zz}(\mathbf{q})]^* & \Omega f_{11}^{zz}(\mathbf{q}) & \Omega [f_{12}^{zz}(\mathbf{q})]^* & \omega_0 + \Omega f_{11}^{zz}(\mathbf{q})
\end{pmatrix}. \quad \text{(C.15)}
$$

Let us choose arbitrarily the values $\hbar\omega_0 = 1, \hbar\Omega = 1/4, f_{11}^{zz}(\mathbf{q}) = -1/4$ and $f_{12}^{zz}(\mathbf{q}) = -\mathrm{i}/4$ for the purpose of this example. Therefore Eq. (C.15) leads to a 4×4 matrix given by

$$
\boldsymbol{\mathcal{H}}_{2,\mathbf{q}}^z = \begin{pmatrix}
0.9375 & -0.0625\mathrm{i} & -0.0625 & -0.0625\mathrm{i} \\
0.0625\mathrm{i} & 0.9375 & 0.0625\mathrm{i} & -0.0625 \\
-0.0625 & -0.0625\mathrm{i} & 0.9375 & -0.0625\mathrm{i} \\
0.0625\mathrm{i} & -0.0625 & 0.0625\mathrm{i} & 0.9375
\end{pmatrix}. \quad \text{(C.16)}
$$

The corresponding matrix originating from the Cholesky decomposition reads (using a PYTHON routine)

$$
\boldsymbol{\mathcal{K}}_{2,\mathbf{q}}^z = \begin{pmatrix}
0.9682 & -0.0645\mathrm{i} & -0.0645 & -0.0645\mathrm{i} \\
0 & 0.9660 & 0.0690\mathrm{i} & -0.0690 \\
0 & 0 & 0.9636 & -0.0741\mathrm{i} \\
0 & 0 & 0 & 0.9607
\end{pmatrix}. \quad \text{(C.17)}
$$

With the matrix $\boldsymbol{\mathcal{K}}_{2,\mathbf{q}}^z$ we then compute the matrix $\boldsymbol{\mathcal{W}}_{2,\mathbf{q}}^z$ using Eq. (C.10) (note that we used the definition $\boldsymbol{\mathcal{J}}_2 = \boldsymbol{\sigma}_z \otimes \mathbb{1}_2$ in the present case). Diagonalizing the matrix $\boldsymbol{\mathcal{W}}_{2,\mathbf{q}}^z$ (using the routine $numpy.linalg.eig()$ included in the NUMPY package in PYTHON [177]) yields the diagonal matrix of eigenvalues

$$
\boldsymbol{\mathcal{E}}_{\mathbf{q}} = \begin{pmatrix}
1 & 0 & 0 & 0 \\
0 & \sqrt{3}/2 & 0 & 0 \\
0 & 0 & -1 & 0 \\
0 & 0 & 0 & -\sqrt{3}/2
\end{pmatrix} \quad \text{(C.18)}
$$

so that the matrix $\boldsymbol{\mathcal{E}}_{2,\mathbf{q}}$ corresponds to the 2×2 matrix

$$
\boldsymbol{\mathcal{E}}_{2,\mathbf{q}} = \begin{pmatrix}
1 & 0 \\
0 & \sqrt{3}/2
\end{pmatrix}. \quad \text{(C.19)}
$$

Finally, with the equations (C.17), (C.19) together with the matrix $\boldsymbol{\mathcal{U}}^{z}_{2,\mathbf{q}}$ obtained from $\boldsymbol{\mathcal{W}}^{z}_{2,\mathbf{q}}$, we may compute the transformation matrix

$$\boldsymbol{\mathcal{T}}^{z}_{2,\mathbf{q}} = \begin{pmatrix} -\mathrm{i}/\sqrt{2} & 0.7089\mathrm{i} & 0 & 0.0509\mathrm{i} \\ 1/\sqrt{2} & 0.7089 & 0 & 0.0509 \\ 0 & 0.0509\mathrm{i} & -\mathrm{i}/\sqrt{2} & 0.7089\mathrm{i} \\ 0 & 0.0509 & 1/\sqrt{2} & 0.7089 \end{pmatrix}. \tag{C.20}$$

The matrix $\boldsymbol{\mathcal{T}}^{z}_{2,\mathbf{q}}$ then diagonalizes the Hamiltonian $\boldsymbol{\mathcal{H}}^{z}_{2,\mathbf{q}}$ as

$$\boldsymbol{\mathcal{T}}^{z}_{2,\mathbf{q}}{}^{\dagger} \boldsymbol{\mathcal{H}}^{z}_{2,\mathbf{q}} \, \boldsymbol{\mathcal{T}}^{z}_{2,\mathbf{q}} = \begin{pmatrix} 1 & 0 & 0 & 0 \\ 0 & \sqrt{3}/2 & 0 & 0 \\ 0 & 0 & 1 & 0 \\ 0 & 0 & 0 & \sqrt{3}/2 \end{pmatrix} \tag{C.21}$$

We have checked that the transformation matrix (C.20) verifies the relations (C.8) and (C.13) as required. Within the matrix $\boldsymbol{\mathcal{T}}^{z}_{2,\mathbf{q}}$, the Bogoliubov coefficients $u^{zz}_{\tau s}(\mathbf{q})$ and $v^{zz}_{\tau s}(\mathbf{q})$ are given in the first two columns since they are associated with the positive eigenvalues (the two others are associated with the negative eigenvalues). Moreover, the first and second columns give the coefficients for the band index $\tau = +1$ and $\tau = -1$, respectively. Finally, the two first rows contain the coefficients $u^{zz}_{\tau 1}(\mathbf{q})$ and $v^{zz}_{\tau 1}(\mathbf{q})$, respectively while the two last rows the same coefficients for $s = 2$.

Appendix D

Perturbative treatment of the plasmonic Hamiltonian: an alternative diagonalization

In this appendix, we provide an other method one may employ to derive the dispersion relations and the Bogoliubov coefficients of the plasmonic Hamiltonian (4.16) (see Sec. 4.2). Indeed, alternatively to the exact diagonalization of the plasmonic Hamiltonian (4.16) presented in Chapter 4, we can also treat the latter Hamiltonian within a perturbation theory since for all practical purposes the coupling constant $\Omega \ll \omega_0$ [see Eq. (3.8)]. Such a procedure may be appropriate in various cases since it reduces the dimension of the eigensystem one needs to solve by two. In the approximate treatment of the plasmonic Hamiltonian (4.16) presented below, we treat the nonresonant [$\propto b_s^{\sigma\dagger}(\mathbf{q})b_{s'}^{\sigma'\dagger}(\mathbf{q})$] terms perturbatively, while the resonant ones [$\propto b_s^{\sigma\dagger}(\mathbf{q})b_{s'}^{\sigma'}(\mathbf{q})$] are diagonalized exactly. We thus split the Hamiltonian (4.16) into two parts,

$$H_{\rm pl} = H_{\rm pl}^{(0)} + H_{\rm pl}^{(1)}. \tag{D.1}$$

In the equation above, the rotating-wave, resonant Hamiltonian $H_{\rm pl}^{(0)}$ reads as

$$H_{\rm pl}^{(0)} = \hbar\omega_0 \sum_{\mathbf{q}} \sum_{s} \sum_{\sigma} b_s^{\sigma\dagger}(\mathbf{q}) b_s^{\sigma}(\mathbf{q}) + \frac{\hbar\Omega}{2} \sum_{\mathbf{q}} \sum_{ss'} \sum_{\sigma\sigma'} \left[f_{ss'}^{\sigma\sigma'}(\mathbf{q}) b_s^{\sigma\dagger}(\mathbf{q}) b_{s'}^{\sigma'}(\mathbf{q}) + \text{h.c.} \right], \tag{D.2}$$

while the nonresonant part is

$$H_{\rm pl}^{(1)} = \frac{\hbar\Omega}{2} \sum_{\mathbf{q}} \sum_{ss'} \sum_{\sigma\sigma'} \left[f_{ss'}^{\sigma\sigma'}(\mathbf{q}) b_s^{\sigma\dagger}(\mathbf{q}) b_{s'}^{\sigma'\dagger}(-\mathbf{q}) + \text{h.c.} \right]. \tag{D.3}$$

In order to treat the nonresonant Hamiltonian (D.3) perturbatively, we first decompose the eigenfrequencies $\omega_\tau^\varepsilon(\mathbf{q})$ and the Bogoliubov operators $\beta_\tau^\varepsilon(\mathbf{q})$ entering the diagonal form (4.19) into

$$\omega_\tau^\varepsilon(\mathbf{q}) = \omega_\tau^{\varepsilon(0)}(\mathbf{q}) + \omega_\tau^{\varepsilon(1)}(\mathbf{q}), \tag{D.4a}$$

and

$$\beta_\tau^\varepsilon(\mathbf{q}) = \beta_\tau^{\varepsilon(0)}(\mathbf{q}) + \beta_\tau^{\varepsilon(1)}(\mathbf{q}). \tag{D.4b}$$

Here, the frequencies $\omega_\tau^{\varepsilon(0)}(\mathbf{q})$ and the operators

$$\beta_\tau^{\varepsilon(0)}(\mathbf{q}) = \sum_{s\sigma} \tilde{u}_{\tau s}^{\varepsilon\sigma}(\mathbf{q}) b_s^\sigma(\mathbf{q}) \tag{D.5}$$

diagonalize the resonant part of (D.1), i.e.,

$$H_{\mathrm{pl}}^{(0)} = \sum_{\mathbf{q}} \sum_{\tau\varepsilon} \hbar\omega_\tau^{\varepsilon(0)}(\mathbf{q}) {\beta_\tau^{\varepsilon(0)}}^\dagger(\mathbf{q}) \beta_\tau^{\varepsilon(0)}(\mathbf{q}). \tag{D.6}$$

Substituting (D.5) into the usual bosonic commutation rules then leads to the normalization condition

$$\sum_{s\sigma} \tilde{u}_{\tau s}^{\varepsilon\sigma}(\mathbf{q}) \tilde{u}_{\tau' s}^{\varepsilon'\sigma *}(\mathbf{q}) = \delta_{\tau\tau'}\delta_{\varepsilon\varepsilon'}. \tag{D.7}$$

We then treat the terms $\omega_\tau^{\varepsilon(1)}(\mathbf{q})$ and the operators

$$\beta_\tau^{\varepsilon(1)}(\mathbf{q}) = \sum_{s\sigma} \tilde{v}_{\tau s}^{\varepsilon\sigma}(\mathbf{q}) {b_s^\sigma}^\dagger(-\mathbf{q}) \tag{D.8}$$

perturbatively in the Heisenberg equation of motion (4.23). Solving the resulting expression order by order then yields the two equations of motion

$$\left[\beta_\tau^{\varepsilon(0)}(\mathbf{q}), H_{\mathrm{pl}}^{(0)}\right] = \hbar\omega_\tau^{\varepsilon(0)}(\mathbf{q}) \beta_\tau^{\varepsilon(0)}(\mathbf{q}) \tag{D.9}$$

and

$$\left[\beta_\tau^{\varepsilon(0)}(\mathbf{q}), H_{\mathrm{pl}}^{(1)}\right] + \left[\beta_\tau^{\varepsilon(1)}(\mathbf{q}), H_{\mathrm{pl}}^{(0)}\right] = \hbar\omega_\tau^{\varepsilon(1)}(\mathbf{q}) \beta_\tau^{\varepsilon(0)}(\mathbf{q}) + \hbar\omega_\tau^{\varepsilon(0)}(\mathbf{q}) \beta_\tau^{\varepsilon(1)}(\mathbf{q}). \tag{D.10}$$

Inserting Eqs. (D.2) and (D.5) into (D.9) then directly yields the relation

$$\left[\omega_0 - \omega_\tau^{\varepsilon(0)}(\mathbf{q})\right] \tilde{u}_{\tau s}^{\varepsilon\sigma}(\mathbf{q}) + \Omega \sum_{s'\sigma'} \tilde{u}_{\tau s'}^{\varepsilon\sigma'}(\mathbf{q}) f_{s's}^{\sigma'\sigma}(\mathbf{q}) = 0. \tag{D.11}$$

The latter expression represents a $3\mathcal{S} \times 3\mathcal{S}$ block-diagonal system which, once solved, gives access to the unperturbed eigenfrequencies $\omega_\tau^{\varepsilon(0)}(\mathbf{q})$ and Bogoliubov coefficients $\tilde{u}_{\tau s}^{\varepsilon\sigma}(\mathbf{q})$. Similarly, substituting the expressions (D.2) and (D.3) for the plasmonic Hamiltonian and Eqs. (D.5) and (D.8)

for the Bogoliubov operators into Eq. (D.10) then gives the identity

$$\begin{aligned}\left[\beta_\tau^{\varepsilon(0)}(\mathbf{q}), H_{\mathrm{pl}}^{(1)}\right] + \left[\beta_\tau^{\varepsilon(1)}(\mathbf{q}), H_{\mathrm{pl}}^{(0)}\right] &= \hbar\omega_0 \sum_{\substack{s\sigma \\ s'\sigma'}} \tilde{v}_{\tau s}^{\varepsilon\sigma}(\mathbf{q})\delta_{ss'}\delta_{\sigma\sigma'} b_{s'}^{\sigma'\dagger}(-\mathbf{q}) \\ &\quad + \hbar\Omega \sum_{\substack{s\sigma \\ s'\sigma'}} \left[\tilde{u}_{\tau s}^{\varepsilon\sigma}(\mathbf{q}) - \tilde{v}_{\tau s}^{\varepsilon\sigma}(\mathbf{q})\right] f_{ss'}^{\sigma\sigma'}(\mathbf{q}) b_{s'}^{\sigma'\dagger}(-\mathbf{q}) \\ &\stackrel{!}{=} \hbar\omega_\tau^{\varepsilon(1)}(\mathbf{q}) \sum_{\substack{s\sigma \\ s'\sigma'}} \tilde{u}_{\tau s}^{\varepsilon\sigma}(\mathbf{q})\delta_{ss'}\delta_{\sigma\sigma'} b_{s'}^{\sigma'}(\mathbf{q}) \\ &\quad + \hbar\omega_\tau^{\varepsilon(0)}(\mathbf{q}) \sum_{\substack{s\sigma \\ s'\sigma'}} \tilde{v}_{\tau s}^{\varepsilon\sigma}(\mathbf{q})\delta_{ss'}\delta_{\sigma\sigma'} b_{s'}^{\sigma'\dagger}(-\mathbf{q}) \end{aligned} \tag{D.12}$$

to be fulfilled. Identifying the different terms in the latter expression then leads to a vanishing first-order energy correction, i.e., $\omega_\tau^{\varepsilon(1)} = 0$ and to the following $3\mathcal{S} \times 3\mathcal{S}$ system of equations

$$\left[\omega_0 - \omega_\tau^{\varepsilon(0)}(\mathbf{q})\right] \tilde{v}_{\tau s}^{\varepsilon\sigma}(\mathbf{q}) + \Omega \sum_{s'\sigma'} \left[\tilde{u}_{\tau s'}^{\varepsilon\sigma'}(\mathbf{q}) - \tilde{v}_{\tau s'}^{\varepsilon\sigma'}(\mathbf{q})\right] f_{s's}^{\sigma'\sigma}(\mathbf{q}) = 0. \tag{D.13}$$

Solving the system above with Eq. (D.11) then gives access to the coefficients $\tilde{v}_{\tau s}^{\varepsilon\sigma}(\mathbf{q})$ and thus finalizes the approximate diagonalization procedure.

Appendix E

General solutions for cubic polynomial equations

In this appendix, we provide insight on the method we employ to evaluate analytically the plasmonic dispersion relations for tripartite lattices in Sec. 5.3. Such a method is the so-called *Cardan method* that we followed from Ref. [178]. The secular equation (5.49) for the out-of-plane polarized plasmonic modes in tripartite lattices may be written in the simple form

$$\left[X_\tau^z(\mathbf{q})\right]^3 + a_2\left[X_\tau^z(\mathbf{q})\right]^2 + a_1 X_\tau^z(\mathbf{q}) + a_0 = 0 \tag{E.1}$$

where we identify the coefficients a_n ($n = 0, 1, 2$) entering Eq. (E.1) to be

$$\begin{cases} a_2 = -3\omega_0\left\{\omega_0 + 2\Omega f_{11}^{zz}(\mathbf{q})\right\} \\ a_1 = \omega_0^2\left\{3\omega_0^2 + 12\Omega f_{11}^{zz}(\mathbf{q})\varsigma^{zz}(\mathbf{q}) - 4\Omega^2\Sigma^{zz}(\mathbf{q})\right\} \\ a_0 = -\omega_0^6 - 6\omega_0^5\Omega f_{11}^{zz}(\mathbf{q}) - 12\omega_0^4\left[\Omega f_{11}^{zz}(\mathbf{q})\right]^2 - 8\omega_0^3\left[\Omega f_{11}^{zz}(\mathbf{q})\right]^3 + 4\omega_0^4\Omega^2\Sigma^{zz}(\mathbf{q}) \\ \qquad +8\omega_0^3\Omega^3 f_{11}^{zz}(\mathbf{q})\Sigma^{zz}(\mathbf{q}) - 16\omega_0^3\Omega^3\Pi^{zz}(\mathbf{q}). \end{cases} \tag{E.2}$$

In the expression above, $\varsigma^{zz}(\mathbf{q})$ is given in Eq. (5.2) while $\Sigma^{zz}(\mathbf{q})$ and $\Pi^{zz}(\mathbf{q})$ are defined in Eqs. (5.50a) and (5.50b), respectively. Following Ref. [178], we then evaluate the two coefficients p and r as

$$p = \frac{1}{3}a_1 - \frac{1}{9}a_2^2 = -\frac{4}{3}\left(\omega_0\Omega\right)^2\Sigma^{zz}(\mathbf{q}) \tag{E.3a}$$

and

$$r = \frac{1}{6}(a_1 a_2 - 3a_0) - \frac{1}{27}a_2^3 = \left(\omega_0\Omega\right)^3\Pi^{zz}(\mathbf{q}). \tag{E.3b}$$

From the latter coefficients, we write the discriminant for Eq. (E.1) as

$$\Delta = p^3 + r^2 = 64\left(\omega_0\Omega\right)^6\left\{\left[\Pi^{zz}(\mathbf{q})\right]^2 - \left[\frac{\Sigma^{zz}(\mathbf{q})}{3}\right]^3\right\}. \tag{E.4}$$

According to the Cardan method, the nature of the three solutions of Eq. (E.1) depends on the sign of the discriminant Δ. If Δ is positive, the roots correspond to a pair of conjugate complex root accompanied with one real root. In the case where Δ vanishes, all the roots are real with at least two identical ones. Finally, in the irreducible case $\Delta < 0$, all the roots are real. Since the solutions of the secular equation (5.49) we are looking for correspond to eigenfrequencies, the latter discriminant has to be negative to ensure that all the roots are real. Following exactly the procedure described in Ref. [178], we then calculate the quantities

$$s_1 = \left[r + \sqrt{\Delta}\right]^{1/3} \tag{E.5a}$$

and

$$s_2 = \left[r - \sqrt{\Delta}\right]^{1/3} \tag{E.5b}$$

which read

$$s_n = 2\omega_0\Omega\left\{\Pi^{zz}(\mathbf{q}) + (3-2n)\mathrm{i}\sqrt{\left[\frac{\Sigma^{zz}(\mathbf{q})}{3}\right]^3 - \left[\Pi^{zz}(\mathbf{q})\right]^2}\right\}^{1/3} = 2\omega\Omega s_{\pm}(\mathbf{q}), \tag{E.6}$$

for $n = 1, 2$. In the latter equation, $s_{\pm}(\mathbf{q})$ is given by Eq. (5.52) in the main text. Finally, substituting (E.6) into the general expressions for the roots of a cubic equation [178]

$$z_1 = (s_1 + s_2) - \frac{a_2}{3}, \tag{E.7a}$$

$$z_2 = -(s_1 + s_2) - \frac{a_2}{3} + \mathrm{i}\frac{\sqrt{3}}{2}(s_1 - s_2), \tag{E.7b}$$

and

$$z_2 = -(s_1 + s_2) - \frac{a_2}{3} - \mathrm{i}\frac{\sqrt{3}}{2}(s_1 - s_2), \tag{E.7c}$$

yields the plasmonic dispersions (5.51) in Sec. 5.3.1 [note that such dispersions corresponds to the positive roots associated to $X^z_\tau(\mathbf{q}) = [\omega^z_\tau(\mathbf{q})]^2$ in Eq. (5.49)].

Appendix F

Evaluation of the integrals appearing in the calculation of the photonic-induced quantities

In this appendix, we provide the detailed calculations of the integrals $\mathcal{I}_n(\alpha)$, $\mathcal{J}(\beta)$ and $\mathcal{K}_n(\alpha)$ (with $n = 1, 2$) which are involved in the evaluation of the radiative frequency shifts and radiative linewidths discussed in Chapter 6. The first section of this appendix is dedicated to the integrals $\mathcal{I}_1(\alpha)$, $\mathcal{I}_2(\alpha)$ and $\mathcal{J}(\beta)$ appearing in calculations of the shifts. The second part of the Appendix is dedicated to the integrals $\mathcal{K}_1(\alpha)$ and $\mathcal{K}_2(\alpha)$ arising in the evaluation of the radiative damping.

F.1 Evaluation of the integrals implied in the evaluation of the radiative shifts

We first consider the integral $\mathcal{I}_1(\alpha)$ given in Eq. (6.20) introduced for the radiative shifts of the collective plasmonic modes with out-of-plane polarization. To proceed with the evaluation of Eq. (6.20), we first split the integral into two parts as

$$\mathcal{I}_1(\alpha) = \mathcal{P}\int_0^{+\infty} \mathrm{d}z \left[\frac{1}{1+z^2} - \frac{\alpha^2}{\alpha^2(z^2+1)-1}\right]. \tag{F.1}$$

While the first integral in the r.h.s. of Eq. (F.1) can be straightforwardly calculated, the second integral must be carefully carried out due to the value of α. For calculation purpose, we may thus rewrite the latter equation as

$$\mathcal{I}_1(\alpha) = \frac{\pi}{2} - \mathcal{J}(\beta), \tag{F.2}$$

where we have defined the function $\mathcal{J}(\beta)$ as

$$\mathcal{J}(\beta) = \mathcal{P}\int_0^{+\infty} \frac{\mathrm{d}z}{z^2+\beta}. \tag{F.3}$$

In the latter integral, we have the parameter $\beta = (\alpha^2 - 1)/\alpha^2$, where α is the parameter entering the radiative shift (6.18). Therefore we have to treat three distinct cases for β: (i) $\beta > 0$ (i.e., $\alpha > 1$) corresponding to plasmonic modes lying outside the light cone, (ii) $\beta < 0$ ($0 < \alpha < 1$) for modes inside the light cone and (iii) $\beta = 0$ ($\alpha = 1$) corresponding to the light line.

We start by evaluating the simplest case where $\beta = 0$. In this limit, we have directly for $\mathcal{J}(\beta)$

$$\mathcal{J}(0) = \lim_{\varepsilon \to 0} \int_{\varepsilon}^{+\infty} \frac{\mathrm{d}z}{z^2} = \lim_{\varepsilon \to 0} \frac{1}{\varepsilon} \to +\infty. \tag{F.4}$$

The second case for which $\beta > 0$ can be straightforwardly solved using the Residue theorem as

$$\mathcal{J}(\beta > 0) = \int_{-\infty}^{+\infty} \frac{\mathrm{d}z}{\left(z + \mathrm{i}\sqrt{\beta}\right)\left(z - \mathrm{i}\sqrt{\beta}\right)} = \frac{\pi}{2\sqrt{\beta}}. \tag{F.5}$$

In order to treat the remaining case, $\beta < 0$, we write $\beta = -\gamma^2$ so that $\gamma = \sqrt{1 - \alpha^2}/\alpha$ is defined positive. Therefore, the function $\mathcal{J}(\beta)$ may be rewritten as

$$\mathcal{J}(\beta) = \mathcal{P} \int_0^{+\infty} \frac{\mathrm{d}z}{z^2 - \gamma^2} = \lim_{z_\mathrm{m} \to +\infty} \frac{1}{2\gamma} \int_0^{z_\mathrm{m}} \left(\frac{1}{z - \gamma} - \frac{1}{z + \gamma} \right). \tag{F.6}$$

The equation above can be now readily evaluated using standard integration techniques yielding the simple result

$$\mathcal{J}(\beta < 0) = \frac{1}{2\gamma} \lim_{z_\mathrm{m} \to +\infty} \ln \left(\frac{z_\mathrm{m} - \gamma}{z_\mathrm{m} + \gamma} \right) = 0. \tag{F.7}$$

In conclusion, using Eqs. (F.4), (F.5) and (F.7) into the expression (F.2) yields for the function $\mathcal{I}_1(\alpha)$ the final result

$$\mathcal{I}_1(\alpha) = \begin{cases} \dfrac{\pi}{2}, & 0 < \alpha < 1 \\ \dfrac{\pi}{2} \left(1 - \dfrac{\alpha}{\sqrt{\alpha^2 - 1}} \right), & \alpha > 1. \end{cases} \tag{F.8}$$

The integral $\mathcal{I}_2(\alpha)$ given in Eq. (6.29) appears for the case of the radiative shift associated with the in-plane polarized modes. Similarly to the integral $\mathcal{I}_1(\alpha)$ we first split Eq. (6.29) into two parts as

$$\mathcal{I}_2(\alpha) = \mathcal{P} \int_0^{+\infty} \mathrm{d}z \left[-\frac{1}{1 + z^2} + \frac{\alpha^2 - 1}{\alpha^2(z^2 + 1) - 1} \right]. \tag{F.9}$$

While the first term in the latter equation can be readily calculated, we may rewrite the Eq. (F.9) in terms of the function $\mathcal{J}(\beta)$ defined in Eq. (F.3) as

$$\mathcal{I}_2(\alpha) = -\frac{\pi}{2} + \beta \mathcal{J}(\beta), \tag{F.10}$$

with $\beta = (\alpha^2 - 1)/\alpha^2$. The above equation can be directly evaluated using Eqs. (F.4), (F.5) and

(F.7) for the integral $\mathcal{J}(\beta)$. The integral $\mathcal{I}_2(\alpha)$ thus reads

$$\mathcal{I}_2(\alpha) = \frac{\pi}{2}\left[-1 + \frac{\sqrt{\alpha^2-1}}{\alpha}\Theta(\alpha-1)\right]. \tag{F.11}$$

F.2 Evaluation of the integrals implied in the evaluation of the radiative linewidths

In this section, we calculate the integral $\mathcal{K}_1(\alpha)$ appearing in the derivation of the radiative damping decay rates discussed in Chapter 6. The integral (6.37) given in Eq. (6.37) can be easily performed using the relation [147]

$$\int_{-\infty}^{+\infty} h(z)\delta\left(f(z)\right)\mathrm{d}z = \int_{-\infty}^{+\infty} h(z)\sum_{z_0}\frac{\delta(z-z_0)}{|f'(z_0)|}, \tag{F.12}$$

where z_0 are the zero of the function $f(z)$ and $f'(z)$ is the derivative of the function with respect to z. We then use the relation (F.12) for the integral $\mathcal{K}_1(\alpha)$ [see Eq. (6.37)] where the function $f(z)$ entering Eq. (F.12) is given by $f(z) = 1 - \alpha\sqrt{1+z^2}$. From this definition, we thus get

$$f(z) = 0 \Rightarrow z_0 = \pm\frac{\sqrt{1-\alpha^2}}{\alpha}, \tag{F.13a}$$

so that

$$f'(z) = -\frac{\alpha z}{\sqrt{1+z^2}} \Rightarrow f'(z_0) = \mp\alpha\sqrt{1-\alpha^2} \tag{F.13b}$$

Thus, substituting the relation (F.12) with the results (F.13) into the integral (6.37) we obtain

$$\mathcal{K}_1(\alpha) = \frac{2\alpha^2}{\sqrt{1-\alpha^2}}\Theta\left(1-\alpha\right). \tag{F.14}$$

Bibliography

[1] J. H. Relethford, *The Human Species: An Introduction to Biological Anthropology* (McGraw-Hill, US, 2012), 9th ed.

[2] Aristophanes, *The Clouds* (eBook, First play 424 BC), [Translation to english W. J. Hickie (2001)].

[3] L. Landau and E. Lifshitz, *Mechanics* (Pergamon, Oxford, 1976).

[4] J. D. Jackson, *Classical electrodynamics* (John Wiley & Sons, 1998), 3rd ed.

[5] D. J. Griffiths, *Introduction to Electrodynamics* (Addison-Wesley, 1998), 3rd ed.

[6] M. Born and E. Wolf, *Principles of Optics* (University Press, Cambridge, 1999), 7th ed.

[7] V. G. Veselago, *The electrodynamics of substances with simultaneously negative values of* ϵ *and* μ, Sov. Phys. Usp. **10**, 509 (1968).

[8] D. F. Sievenpiper, M. E. Sickmiller, and E. Yablonovitch, *3D wire mesh photonic crystals*, Phys. Rev. Lett. **76**, 2480 (1996).

[9] J. B. Pendry, A. J. Holden, D. J. Robbins, and W. J. Stewart, *Low frequency plasmons in thin-wire structures*, J. Phys: Condens. Matter **10**, 4785 (1998).

[10] R. A. Shelby, D. R. Smith, and S. Schultz, *Experimental verification of a negative index of refraction*, Science **292**, 77 (2001).

[11] J. B. Pendry, *Negative refraction makes a perfect lens*, Phys. Rev. Lett. **85**, 3966 (2000).

[12] J. B. Pendry, A. J. Holden, D. J. Robbins, and W. J. Stewart, *Magnetism from conductors and enhanced nonlinear phenomena*, IEEE Trans. on Microwave Theory and Techniques **47**, 2075 (1999).

[13] D. R. Smith, W. J. Padilla, D. C. Vier, S. C. Nemat-Nasser, and S. Schultz, *Composite medium with simultaneously negative permeability and permittivity*, Phys. Rev. Lett. **84**, 4184 (2000).

[14] R. A. Shelby, D. R. Smith, S. C. Nemat-Nasser, and S. Schultz, *Microwave transmission through a two-dimensional, isotropic, left-handed metamaterial*, Appl. Phys. Lett. **78**, 489 (2001).

[15] N. Fang, H. Lee, C. Sun, and X. Zhang, *Sub-diffraction-limited optical imaging with a silver superlens*, Science **308**, 534 (2005).

[16] R. P. Feynman, M. Sands, and R. B. Leighton, *The Feynman Lectures on Physics, Vol. I: The New Millennium Edition: Mainly Mechanics, Radiation, and Heat* (Basic Books; 50th New Millennium ed., 2011).

[17] J. Li and C. T. Chan, *Double-negative acoustic metamaterial*, Phys. Rev. E **70**, 055602 (2004).

[18] N. Fang, D. Xi, J. Xu, M. Ambati, W. Srituravanich, C. Sun, and X. Zhang, *Ultrasonic metamaterials with negative modulus*, Nat. Mater. **5**, 452 (2006).

[19] Y. Ding, Z. Liu, C. Qiu, and J. Shi, *Metamaterial with simultaneously negative bulk modulus and mass density*, Phys. Rev. Lett. **99**, 093904 (2007).

[20] M. Yang, G. Ma, Z. Yang, and P. Sheng, *Coupled membranes with doubly negative mass density and bulk modulus*, Phys. Rev. Lett. **110**, 134301 (2013).

[21] T. Brunet, A. Merlin, B. Mascaro, K. Zimny, J. Leng, O. Poncelet, C. Aristégui, and O. Mondain-Monval, *Soft 3D acoustic metamaterial with negative index*, Nat. Mater. **14**, 384 (2014).

[22] G. Ma and P. Sheng, *Acoustic metamaterials: From local resonances to broad horizons*, Sci. Adv. **2** (2016).

[23] Y. Wu, Y. Lai, and Z.-Q. Zhang, *Elastic metamaterials with simultaneously negative effective shear modulus and mass density*, Phys. Rev. Lett. **107**, 105506 (2011).

[24] X. Zhou, X. Liu, and G. Hu, *Elastic metamaterials with local resonances: an overview*, Theor. Appl. Mech. Lett. **2**, 041001 (2012).

[25] J. H. Oh, H. M. Seung, and Y. Y. Kim, *Doubly negative isotropic elastic metamaterial for sub-wavelength focusing: Design and realization*, J. Sound Vib. **410**, 169 (2017).

[26] S. Zhang, L. Yin, and N. Fang, *Focusing ultrasound with an acoustic metamaterial network*, Phys. Rev. Lett. **102**, 194301 (2009).

[27] J. Zhu, J. Christensen, J. Jung, L. Martin-Moreno, X. Yin, L. Fok, X. Zhang, and F. J. Garcia-Vidal, *A holey-structured metamaterial for acoustic deep-subwavelength imaging*, Nat. Phys. **7**, 52 (2010).

[28] F. Lemoult, M. Fink, and G. Lerosey, *Acoustic resonators for far-field control of sound on a subwavelength scale*, Phys. Rev. Lett. **107**, 064301 (2011).

[29] F. Lemoult, N. Kaina, M. Fink, and G. Lerosey, *Wave propagation control at the deep sub-wavelength scale in metamaterials*, Nat. Phys. **9**, 55 (2012).

[30] H. Jia, M. Ke, R. Hao, Y. Ye, F. Liu, and Z. Liu, *Subwavelength imaging by a simple planar acoustic superlens*, Appl. Phys. Lett. **97**, 173507 (2010).

[31] C. M. Park, J. J. Park, S. H. Lee, Y. M. Seo, C. K. Kim, and S. H. Lee, *Amplification of acoustic evanescent waves using metamaterial slabs*, Phys. Rev. Lett. **107**, 194301 (2011).

[32] J. J. Park, C. M. Park, K. J. B. Lee, and S. H. Lee, *Acoustic superlens using membrane-based metamaterials*, Appl. Phys. Lett. **106**, 051901 (2015).

[33] N. Meinzer, W. L. Barnes, and I. R. Hooper, *Plasmonic meta-atoms and metasurfaces*, Nat. Photon. **8**, 889 (2014).

[34] W. Wang, M. Ramezani, A. I. Väkeväinen, P. Törmä, J. G. Rivas, and T. W. Odom, *The rich photonic world of plasmonic nanoparticle arrays*, Mater. Today **21**, 303 (2018).

[35] V. G. Kravets, A. V. Kabashin, W. L. Barnes, and A. N. Grigorenko, *Plasmonic surface lattice resonances: A review of properties and applications*, Chem. Rev. **118**, 5912 (2018).

[36] S. A. Cummer, J. Christensen, and A. Alú, *Controlling sound with acoustic metamaterials*, Nat. Rev. Mater. **1**, 16001 (2016).

[37] A. A. Zadpoor, *Mechanical meta-materials*, Mater. Horiz. **3**, 371 (2016).

[38] N. Yu, P. Genevet, M. A. Kats, F. Aieta, J.-P. Tetienne, F. Capasso, and Z. Gaburro, *Light propagation with phase discontinuities: Generalized laws of reflection and refraction*, Science **334**, 333 (2011).

[39] D. Schurig, J. J. Mock, B. J. Justice, S. A. Cummer, J. B. Pendry, A. F. Starr, and D. R. Smith, *Metamaterial electromagnetic cloak at microwave frequencies*, Science **314**, 977 (2006).

[40] P. Moitra, Y. Yang, Z. Anderson, I. I. Kravchenko, D. P. Briggs, and J. Valentine, *Realization of an all-dielectric zero-index optical metamaterial*, Nat. Photon. **7**, 791 (2013).

[41] L. Zigoneanu, B.-I. Popa, and S. A. Cummer, *Three-dimensional broadband omnidirectional acoustic ground cloak*, Nat. Mater. **13**, 352 (2014).

[42] N. Stenger, M. Wilhelm, and M. Wegener, *Experiments on elastic cloaking in thin plates*, Phys. Rev. Lett. **108**, 014301 (2012).

[43] S. Brûlé, E. H. Javelaud, S. Enoch, and S. Guenneau, *Experiments on seismic metamaterials: Molding surface waves*, Phys. Rev. Lett. **112**, 133901 (2014).

[44] R.-M. Ma, X. Yin, R. F. Oulton, V. J. Sorger, and X. Zhang, *Multiplexed and electrically modulated plasmon laser circuit*, Nano Lett. **12**, 5396 (2012).

[45] W. Zhou, M. Dridi, J. Y. Suh, C. H. Kim, D. T. Co, M. R. Wasielewski, G. C. Schatz, and T. W. Odom, *Lasing action in strongly coupled plasmonic nanocavity arrays*, Nat. Nanotechnol. **8**, 506 (2013).

[46] M. T. Hill and M. C. Gather, *Advances in small lasers*, Nat. Photon. **8**, 908 (2014).

[47] A. Yang, T. B. Hoang, M. Dridi, C. Deeb, M. H. Mikkelsen, G. C. Schatz, and T. W. Odom, *Real-time tunable lasing from plasmonic nanocavity arrays*, Nat. Commun. **6**, 6939 (2015).

[48] F. Fan, S. Turkdogan, Z. Liu, D. Shelhammer, and C. Z. Ning, *A monolithic white laser*, Nat. Nanotechnol. **10**, 796 (2015).

[49] S. A. Maier, *Plasmonics : Fundamentals and Applications* (Springer, 2007).

[50] E. Hao and G. C. Schatz, *Electromagnetic fields around silver nanoparticles and dimers*, J. Chem. Phys. **120**, 357 (2004).

[51] R. Adato, A. A. Yanik, J. J. Amsden, D. L. Kaplan, F. G. Omenetto, M. K. Hong, S. Erramilli, and H. Altug, *Ultra-sensitive vibrational spectroscopy of protein monolayers with plasmonic nanoantenna arrays*, Proc. Natl. Acad. of Sci. **106**, 19227 (2009).

[52] P. Offermans, M. C. Schaafsma, S. R. K. Rodriguez, Y. Zhang, M. Crego-Calama, S. H. Brongersma, and J. Gómez Rivas, *Universal scaling of the figure of merit of plasmonic sensors*, ACS Nano **5**, 5151 (2011).

[53] K. Vynck, D. Felbacq, E. Centeno, A. I. Căbuz, D. Cassagne, and B. Guizal, *All-dielectric rod-type metamaterials at optical frequencies*, Phys. Rev. Lett. **102**, 133901 (2009).

[54] D. Felbacq, B. Guizal, G. Bouchitté, and C. Bourel, *Resonant homogenization of a dielectric metamaterial*, Microw. Opt. Technol. Lett. **51**, 2695 (2009).

[55] I. Staude and J. Schilling, *Metamaterial-inspired silicon nanophotonics*, Nature Photon. **11**, 274 (2017).

[56] W. A. de Heer, *The physics of simple metal clusters: experimental aspects and simple models*, Rev. Mod. Phys. **65**, 611 (1993).

[57] M. Brack, *The physics of simple metal clusters: self-consistent jellium model and semiclassical approaches*, Rev. Mod. Phys. **65**, 677 (1993).

[58] U. Kreibig and M. Vollmer, *Optical properties of metal clusters* (Springer-Verlag, Berlin, 1995).

[59] G. Mie, *Beiträge zur Optik trüber Medien, speziell kolloidaler Metallösungen*, Ann. Phys. **330**, 377 (1908).

[60] N. Ashcroft and N. Mermin, *Solid State Physics* (Academic Press, Orlando, 1976).

[61] C. Sönnichsen, T. Franzl, T. Wilk, G. von Plessen, and J. Feldmann, *Plasmon resonances in large noble-metal clusters*, New J. Phys. **4**, 93 (2002).

[62] V. Halté, J. Guille, J.-C. Merle, I. Perakis, and J.-Y. Bigot, *Electron dynamics in silver nanoparticles: Comparison between thin films and glass embedded nanoparticles*, Phys. Rev. B **60**, 11738 (1999).

[63] J.-Y. Bigot, V. Halté, J.-C. Merle, and A. Daunois, *Electron dynamics in metallic nanoparticles*, Chem. Phys. **251**, 181 (2000).

[64] C. A. Downing, E. Mariani, and G. Weick, *Radiative frequency shifts in nanoplasmonic dimers*, Phys. Rev. B **96**, 155421 (2017).

[65] H. A. Bethe, *The electromagnetic shift of energy levels*, Phys. Rev. **72**, 339 (1947).

[66] P. W. Milonni, *The quantum vacuum : an introduction to quantum electrodynamics* (Academic Press, London, 1994).

[67] G. Weick, G.-L. Ingold, R. A. Jalabert, and D. Weinmann, *Surface plasmon in metallic nanoparticles: Renormalization effects due to electron-hole excitations*, Phys. Rev. B **74**, 165421 (2006).

[68] G. Weick, Ph.D. thesis, Université Louis Pasteur, Strasbourg and Universität Augsburg (2006).

[69] A. Kawabata and R. Kubo, *Electronic properties of fine metallic particles. II. Plasma resonance absorption*, J. Phys. Soc. Jap. **21**, 1765 (1966).

[70] R. Ruppin and H. Yatom, *Size and shape effects on the broadening of the plasma resonance absorption in metals*, Phys. Stat. Solidi B. **74**, 647 (1976).

[71] C. Yannouleas and R. Broglia, *Landau damping and wall dissipation in large metal clusters*, Ann. Phys. **217**, 105 (1992).

[72] R. A. Molina, D. Weinmann, and R. A. Jalabert, *Oscillatory size dependence of the surface plasmon linewidth in metallic nanoparticles*, Phys. Rev. B **65**, 155427 (2002).

[73] R. A. Molina, D. Weinmann, and R. A. Jalabert, *Oscillatory behavior and enhancement of the surface plasmon linewidth in embedded noble metal nanoparticles*, Eur. Phys. J. D **24**, 127 (2003).

[74] G. Weick, R. A. Molina, D. Weinmann, and R. A. Jalabert, *Lifetime of the first and second collective excitations in metallic nanoparticles*, Phys. Rev. B **72**, 115410 (2005).

[75] G. Weick, G.-L. Ingold, D. Weinmann, and R. A. Jalabert, *Sidebands in the light absorption of driven metallic nanoparticles*, Eur. Phys. J. D **44**, 359 (2007).

[76] M. L. Brongersma, J. W. Hartman, and H. A. Atwater, *Electromagnetic energy transfer and switching in nanoparticle chain arrays below the diffraction limit*, Phys. Rev. B **62**, R16356 (2000).

[77] S. Y. Park and D. Stroud, *Surface-plasmon dispersion relations in chains of metallic nanoparticles: An exact quasistatic calculation*, Phys. Rev. B **69**, 125418 (2004).

[78] S. A. Maier, P. G. Kik, H. A. Atwater, S. Meltzer, E. Harel, B. E. Koel, and A. A. G. Requicha, *Local detection of electromagnetic energy transport below the diffraction limit in metal nanoparticle plasmon waveguides*, Nat. Mater. **2**, 229 (2003).

[79] A. Brandstetter-Kunc, G. Weick, D. Weinmann, and R. A. Jalabert, *Decay of dark and bright plasmonic modes in a metallic nanoparticle dimer*, Phys. Rev. B **91**, 035431 (2015), **92**, 199906(E) (2015).

[80] A. Brandstetter-Kunc, G. Weick, C. A. Downing, D. Weinmann, and R. A. Jalabert, *Nonradiative limitations to plasmon propagation in chains of metallic nanoparticles*, Phys. Rev. B **94**, 239902 (2016).

[81] M. Decker, M. W. Klein, M. Wegener, and S. Linden, *Circular dichroism of planar chiral magnetic metamaterials*, Opt. Lett. **32**, 856 (2007).

[82] W. Wu, E. Kim, E. Ponizovskaya, Y. Liu, Z. Yu, N. Fang, Y. Shen, A. Bratkovsky, W. Tong, C. Sun, et al., *Optical metamaterials at near and mid-IR range fabricated by nanoimprint lithography*, Appl. Phys. A **87**, 143 (2007).

[83] M. C. Gwinner, E. Koroknay, L. Fu, P. Patoka, W. Kandulski, M. Giersig, and H. Giessen, *Periodic large-area metallic split-ring resonator metamaterial fabrication based on shadow nanosphere lithography*, Small **5**, 400 (2009).

[84] G. Vecchi, V. Giannini, and J. Gómez Rivas, *Shaping the fluorescent emission by lattice resonances in plasmonic crystals of nanoantennas*, Phys. Rev. Lett. **102**, 146807 (2009).

[85] A. E. Nikolaenko, F. De Angelis, S. A. Boden, N. Papasimakis, P. Ashburn, E. Di Fabrizio, and N. I. Zheludev, *Carbon nanotubes in a photonic metamaterial*, Phys. Rev. Lett. **104**, 153902 (2010).

[86] W. Zhou and T. W. Odom, *Tunable subradiant lattice plasmons by out-of-plane dipolar interactions*, Nat. Nanotechnol. **6**, 423 (2011).

[87] M. Decker, N. Feth, C. M. Soukoulis, S. Linden, and M. Wegener, *Retarded long-range interaction in split-ring-resonator square arrays*, Phys. Rev. B **84**, 085416 (2011).

[88] A. D. Humphrey and W. L. Barnes, *Plasmonic surface lattice resonances on arrays of different lattice symmetry*, Phys. Rev. B **90**, 075404 (2014).

[89] K. Y. Bliokh, F. J. Rodríguez-Fortuño, F. Nori, and A. V. Zayats, *Spin–orbit interactions of light*, Nat. Photon. **9**, 796 (2015).

[90] T. Chervy, S. Azzini, E. Lorchat, S. Wang, Y. Gorodetski, J. A. Hutchison, S. Berciaud, T. W. Ebbesen, and C. Genet, *Room temperature chiral coupling of valley excitons with spin-momentum locked surface plasmons*, ACS Photonics **5**, 1281 (2018).

[91] V. G. Kravets, F. Schedin, and A. N. Grigorenko, *Extremely narrow plasmon resonances based on diffraction coupling of localized plasmons in arrays of metallic nanoparticles*, Phys. Rev. Lett. **101**, 087403 (2008).

[92] Y. Chu, E. Schonbrun, T. Yang, and K. B. Crozier, *Experimental observation of narrow surface plasmon resonances in gold nanoparticle arrays*, Appl. Phys. Lett. **93**, 181108 (2008).

[93] B. Auguié and W. L. Barnes, *Collective resonances in gold nanoparticle arrays*, Phys. Rev. Lett. **101**, 143902 (2008).

[94] G. Lozano, D. J. Louwers, S. R. K. Rodríguez, S. Murai, O. T. A. Jansen, M. A. Verschuuren, and J. Gómez Rivas, *Plasmonics for solid-state lighting: enhanced excitation and directional emission of highly efficient light sources*, Light: Sci. Appl. **2**, e66 (2013).

[95] B. Gallinet and O. J. F. Martin, *Refractive index sensing with subradiant modes: A framework to reduce losses in plasmonic nanostructures*, ACS Nano **7**, 6978 (2013).

[96] J. Stehr, J. Crewett, F. Schindler, R. Sperling, G. von Plessen, U. Lemmer, J. Lupton, T. Klar, J. Feldmann, A. Holleitner, et al., *A low threshold polymer laser based on metallic nanoparticle gratings*, Adv. Mater. **15**, 1726 (2003).

[97] I. D. W. Samuel, E. B. Namdas, and G. A. Turnbull, *How to recognize lasing*, Nat. Photon. **3**, 546 (2009).

[98] M. P. van Exter, V. T. Tenner, F. van Beijnum, M. J. A. de Dood, P. J. van Veldhoven, E. J. Geluk, and G. W. 't Hooft, *Surface plasmon dispersion in metal hole array lasers*, Opt. Express **21**, 27422 (2013).

[99] F. van Beijnum, P. J. van Veldhoven, E. J. Geluk, M. J. A. de Dood, G. W. 't Hooft, and M. P. van Exter, *Surface plasmon lasing observed in metal hole arrays*, Phys. Rev. Lett. **110**, 206802 (2013).

[100] A. H. Schokker and A. F. Koenderink, *Lasing at the band edges of plasmonic lattices*, Phys. Rev. B **90**, 155452 (2014).

[101] J.-P. Martikainen, M. O. J. Heikkinen, and P. Törmä, *Condensation phenomena in plasmonics*, Phys. Rev. A **90**, 053604 (2014).

[102] T. K. Hakala, A. J. Moilanen, A. I. Väkeväinen, R. Guo, J.-P. Martikainen, R. H. T. Daskalakis, K. S. and, A. Julku, J.-P. Törmä, P. Martikainen, M. O. J. Heikkinen, and P. Törmä, *Bose-Einstein condensation in a plasmonic lattice*, Nat. Phys. **14**, 739 (2018).

[103] N. Yu, F. Aieta, P. Genevet, M. A. Kats, Z. Gaburro, and F. Capasso, *A broadband, background-free quarter-wave plate based on plasmonic metasurfaces*, Nano Lett. **12**, 6328 (2012).

[104] F. Aieta, P. Genevet, M. A. Kats, N. Yu, R. Blanchard, Z. Gaburro, and F. Capasso, *Aberration-free ultrathin flat lenses and axicons at telecom wavelengths based on plasmonic metasurfaces*, Nano Lett. **12**, 4932 (2012).

[105] X. Chen, L. Huang, H. Mühlenbernd, G. Li, B. Bai, Q. Tan, G. Jin, C.-W. Qiu, S. Zhang, and T. Zentgraf, *Dual-polarity plasmonic metalens for visible light*, Nat. Commun. **3**, 1198 (2012).

[106] L. Huang, X. Chen, H. Mühlenbernd, H. Zhang, S. Chen, B. Bai, Q. Tan, G. Jin, K.-W. Cheah, C.-W. Qiu, et al., *Three-dimensional optical holography using a plasmonic metasurface*, Nat. Commun. **4**, 2808 (2013).

[107] G. Grosso and G. Pastori Parravicini, *Solid State Physics* (Academic Press, Oxford, 2014).

[108] G. Weick, C. Woollacott, W. L. Barnes, O. Hess, and E. Mariani, *Dirac-like plasmons in honeycomb lattices of metallic nanoparticles*, Phys. Rev. Lett. **110**, 106801 (2013).

[109] T. J. Sturges, C. Woollacott, G. Weick, and E. Mariani, *Dirac plasmons in bipartite lattices of metallic nanoparticles*, 2D Mater. **2**, 014008 (2015).

[110] A. H. Castro Neto, F. Guinea, N. M. R. Peres, K. S. Novoselov, and A. K. Geim, *The electronic properties of graphene*, Rev. Mod. Phys. **81**, 109 (2009).

[111] R. Ruppin, *Surface modes of two spheres*, Phys. Rev. B **26**, 3440 (1982).

[112] J. M. Gérardy and M. Ausloos, *Absorption spectrum of clusters of spheres from the general solution of Maxwell's equations. IV. Proximity, bulk, surface, and shadow effects (in binary clusters)*, Phys. Rev. B **27**, 6446 (1983).

[113] P. Nordlander, C. Oubre, E. Prodan, K. Li, and M. I. Stockman, *Plasmon hybridization in nanoparticle dimers*, Nano Lett. **4**, 899 (2004).

[114] C. Dahmen, B. Schmidt, and G. von Plessen, *Radiation damping in metal nanoparticle pairs*, Nano Lett. **7**, 318 (2007).

[115] G. Bachelier, I. Russier-Antoine, E. Benichou, C. Jonin, N. Del Fatti, F. Vallée, and P.-F. Brevet, *Fano profiles induced by near-field coupling in heterogeneous dimers of gold and silver nanoparticles*, Phys. Rev. Lett. **101**, 197401 (2008).

[116] J. Zuloaga, E. Prodan, and P. Nordlander, *Quantum description of the plasmon resonances of a nanoparticle dimer*, Nano Lett. **9**, 887 (2009).

[117] R. Esteban, A. G. Borisov, P. Nordlander, and J. Aizpurua, *Bridging quantum and classical plasmonics with a quantum-corrected model*, Nat. Commun. **3**, 825 (2012).

[118] L. G. Gerchikov, C. Guet, and A. N. Ipatov, *Multiple plasmons and anharmonic effects in small metallic clusters*, Phys. Rev. A **66**, 053202 (2002).

[119] H. Tamaru, H. Kuwata, H. T. Miyazaki, and K. Miyano, *Resonant light scattering from individual Ag nanoparticles and particle pairs*, Appl. Phys. Lett. **80**, 1826 (2002).

[120] W. Rechberger, A. Hohenau, A. Leitner, J. Krenn, B. Lamprecht, and F. Aussenegg, *Optical properties of two interacting gold nanoparticles*, Opt. Commun. **220**, 137 (2003).

[121] P. K. Jain, W. Huang, and M. A. El-Sayed, *On the universal scaling behavior of the distance decay of plasmon coupling in metal nanoparticle pairs: A plasmon ruler equation*, Nano Lett. **7**, 2080 (2007).

[122] P. Olk, J. Renger, M. T. Wenzel, and L. M. Eng, *Distance dependent spectral tuning of two coupled metal nanoparticles*, Nano Lett. **8**, 1174 (2008).

[123] M.-W. Chu, V. Myroshnychenko, C. H. Chen, J.-P. Deng, C.-Y. Mou, and F. J. García de Abajo, *Probing bright and dark surface-plasmon modes in individual and coupled noble metal nanoparticles using an electron beam*, Nano Lett. **9**, 399 (2009).

[124] A. L. Koh, K. Bao, I. Khan, W. E. Smith, G. Kothleitner, P. Nordlander, S. A. Maier, and D. W. McComb, *Electron Energy-Loss Spectroscopy (EELS) of surface plasmons in single silver nanoparticles and dimers: influence of beam damage and mapping of dark modes*, ACS Nano **3**, 3015 (2009).

[125] P. K. Jain and M. A. El-Sayed, *Plasmonic coupling in noble metal nanostructures*, Chem. Phys. Lett. **487**, 153 (2010).

[126] S. J. Barrow, D. Rossouw, A. M. Funston, G. A. Botton, and P. Mulvaney, *Mapping bright and dark modes in gold nanoparticle chains using electron energy loss spectroscopy*, Nano Lett. **14**, 3799 (2014).

[127] M. Quinten, A. Leitner, J. R. Krenn, and F. R. Aussenegg, *Electromagnetic energy transport via linear chains of silver nanoparticles*, Opt. Lett. **23**, 1331 (1998).

[128] J. R. Krenn, A. Dereux, J. C. Weeber, E. Bourillot, Y. Lacroute, J. P. Goudonnet, G. Schider, W. Gotschy, A. Leitner, F. R. Aussenegg, et al., *Squeezing the optical near-field zone by plasmon coupling of metallic nanoparticles*, Phys. Rev. Lett. **82**, 2590 (1999).

[129] S. A. Maier, M. L. Brongersma, P. G. Kik, and H. A. Atwater, *Observation of near-field coupling in metal nanoparticle chains using far-field polarization spectroscopy*, Phys. Rev. B **65**, 193408 (2002).

[130] D. Solis Jr., B. Willingham, S. L. Nauert, L. S. Slaughter, J. Olson, P. Swanglap, A. Paul, W.-S. Chang, and S. Link, *Electromagnetic energy transport in nanoparticle chains via dark plasmon modes*, Nano Lett. **12**, 1349 (2012).

[131] A. Apuzzo, M. Février, R. Salas-Montiel, A. Bruyant, A. Chelnokov, G. Lérondel, B. Dagens, and S. Blaize, *Observation of near-field dipolar interactions involved in a metal nanoparticle chain waveguide*, Nano Lett. **13**, 1000 (2013).

[132] S. A. Maier, P. G. Kik, and H. A. Atwater, *Optical pulse propagation in metal nanoparticle chain waveguides*, Phys. Rev. B **67**, 205402 (2003).

[133] W. H. Weber and G. W. Ford, *Propagation of optical excitations by dipolar interactions in metal nanoparticle chains*, Phys. Rev. B **70**, 125429 (2004).

[134] D. S. Citrin, *Coherent excitation transport in metal-nanoparticle chains*, Nano Lett. **4**, 1561 (2004).

[135] C. A. Downing, E. Mariani, and G. Weick, *Retardation effects on the dispersion and propagation of plasmons in metallic nanoparticle chains*, J. Phys: Condens. Matter **30**, 025301 (2018).

[136] C. A. Downing and G. Weick, *Topological collective plasmons in bipartite chains of metallic nanoparticles*, Phys. Rev. B **95**, 125426 (2017).

[137] C. A. Downing and G. Weick, *Topological plasmons in dimerized chains of nanoparticles: robustness against long-range quasistatic interactions and retardation effects*, Eur. Phys. J. B **91**, 253 (2018).

[138] D. Han, Y. Lai, J. Zi, Z.-Q. Zhang, and C. T. Chan, *Dirac spectra and edge states in honeycomb plasmonic lattices*, Phys. Rev. Lett. **102**, 123904 (2009).

[139] C.-R. Mann, T. J. Sturges, G. Weick, W. L. Barnes, and E. Mariani, *Manipulating type-I and type-II Dirac polaritons in cavity-embedded honeycomb metasurfaces*, Nat. Commun. **9**, 2194 (2018).

[140] D. L. Bergman, C. Wu, and L. Balents, *Band touching from real-space topology in frustrated hopping models*, Phys. Rev. B **78**, 125104 (2008).

[141] H.-M. Guo and M. Franz, *Topological insulator on the kagome lattice*, Phys. Rev. B **80**, 113102 (2009).

[142] C. Weeks and M. Franz, *Topological insulators on the Lieb and perovskite lattices*, Phys. Rev. B **82**, 085310 (2010).

[143] M. Niţă, B. Ostahie, and A. Aldea, *Spectral and transport properties of the two-dimensional Lieb lattice*, Phys. Rev. B **87**, 125428 (2013).

[144] G. Palumbo and K. Meichanetzidis, *Two-dimensional Chern semimetals on the Lieb lattice*, Phys. Rev. B **92**, 235106 (2015).

[145] W. Kohn, *Cyclotron resonance and de Haas-van Alphen oscillations of an interacting electron gas*, Phys. Rev. **123**, 1242 (1961).

[146] G. D. Mahan, *Many-Particle Physics* (Springer, 2000), 3rd ed.

[147] C. Cohen-Tannoudji, B. Diu, and F. Laloë, *Quantum Mechanics* (Wiley, 1991).

[148] G. Grynberg, A. Aspect, and C. Fabre, *Introduction to Quantum Optics: From the Semi-classical Approach to Quantized Light* (University Press, Cambridge, 2010).

[149] G. Weick and D. Weinmann, *Lifetime of the surface magnetoplasmons in metallic nanoparticles*, Phys. Rev. B **83**, 125405 (2011).

[150] W. E. Lamb and R. C. Retherford, *Fine structure of the hydrogen atom by a microwave method*, Phys. Rev. **72**, 241 (1947).

[151] A. Brandstetter-Kunc, Ph.D. thesis, Université de Strasbourg (2016).

[152] M. O. Scully, *Collective Lamb shift in single photon Dicke superradiance*, Phys. Rev. Lett. **102**, 143601 (2009).

[153] R. Röhlsberger, K. Schlage, B. Sahoo, S. Couet, and R. Rüffer, *Collective Lamb shift in single-photon superradiance*, Science **328**, 1248 (2010).

[154] D. Craig and T. Thirunamachandran, *Molecular Quantum Electrodynamics* (Academic Press, London, 1984).

[155] R. Friedberg, S. Hartmann, and J. Manassah, *Frequency shifts in emission and absorption by resonant systems ot two-level atoms*, Phys. Rep. **7**, 101 (1973).

[156] K.-P. Charlé, W. Schulze, and B. Winter, *The size dependent shift of the surface plasmon absorption band of small spherical metal particles*, Z. Phys. D **12**, 471 (1989).

[157] G. Weick and E. Mariani, *Tunable plasmon polaritons in arrays of interacting metallic nanoparticles*, Eur. Phys. J. B **88**, 7 (2015).

[158] S. Lamowski, C.-R. Mann, F. Hellbach, E. Mariani, G. Weick, and F. Pauly, *Plasmon polaritons in cubic lattices of spherical metallic nanoparticles*, Phys. Rev. B **97**, 125409 (2018).

[159] J. H. P. Colpa, *Diagonalization of the quadratic boson hamiltonian*, Physica A **93**, 327 (1978).

[160] R. Shindou, R. Matsumoto, S. Murakami, and J.-i. Ohe, *Topological chiral magnonic edge mode in a magnonic crystal*, Phys. Rev. B **87**, 174427 (2013).

[161] Y.-R. Zhen, K. H. Fung, and C. T. Chan, *Collective plasmonic modes in two-dimensional periodic arrays of metal nanoparticles*, Phys. Rev. B **78**, 035419 (2008).

[162] M. S. Dresselhaus, G. Dresselhaus, and A. Jorio, *Group Theory: Application to the Physics of Condensed Matter* (Springer, 2008).

[163] M. Gell-Mann, *Symmetries of baryons and mesons*, Phys. Rev. **125**, 1067 (1962).

[164] N. Goldman, D. F. Urban, and D. Bercioux, *Topological phases for fermionic cold atoms on the Lieb lattice*, Phys. Rev. A **83**, 063601 (2011).

[165] C. Seoanez, G. Weick, R. A. Jalabert, and D. Weinmann, *Friction of the surface plasmon by high-energy particle-hole pairs*, Eur. Phys. J. D **44**, 351 (2007).

[166] S. R. K. Rodriguez, A. Abass, B. Maes, O. T. A. Janssen, G. Vecchi, and J. Gómez Rivas, *Coupling bright and dark plasmonic lattice resonances*, Phys. Rev. X **1**, 021019 (2011).

[167] N. M. Lawandy, *Localized surface plasmon singularities in amplifying media*, Appl. Phys. Lett. **85**, 5040 (2004).

[168] D. S. Citrin, *Plasmon-polariton transport in metal-nanoparticle chains embedded in a gain medium*, Opt. Lett. **31**, 98 (2006).

[169] M. A. Noginov, G. Zhu, M. Bahoura, J. Adegoke, C. Small, B. A. Ritzo, V. P. Drachev, and V. M. Shalaev, *The effect of gain and absorption on surface plasmons in metal nanoparticles*, Appl. Phys. B **86**, 455 (2007).

[170] M. A. Noginov, G. Zhu, A. M. Belgrave, R. Bakker, V. M. Shalaev, E. E. Narimanov, S. Stout, E. Herz, T. Suteewong, and U. Wiesner, *Demonstration of a spaser-based nanolaser*, Nature **460**, 1110 (2009).

[171] K. J. Savage, M. M. Hawkeye, R. Esteban, A. G. Borisov, J. Aizpurua, and J. J. Baumberg, *Revealing the quantum regime in tunnelling plasmonics*, Nature **491**, 574 (2012).

[172] J. A. Scholl, A. García-Etxarri, A. L. Koh, and J. A. Dionne, *Observation of quantum tunneling between two plasmonic nanoparticles*, Nano Lett. **13**, 564 (2013).

[173] R. Esteban, A. Zugarramurdi, P. Zhang, P. Nordlander, F. J. García-Vidal, A. G. Borisov, and J. Aizpurua, *A classical treatment of optical tunneling in plasmonic gaps: extending the quantum corrected model to practical situations*, Farad. Disc. **178**, 151 (2015).

[174] M. C. Gutzwiller, *Chaos in classical and quantum mechanics* (Springer-Verlag, Berlin, 1990).

[175] M. Brack and K. Bhaduri, *Semiclassical physics, Frontiers in Physics* (Addison-Wesley, Readings, 1997).

[176] C. Tsallis, *Diagonalization methods for the general bilinear hamiltonian of an assembly of bosons*, J. Math. Phys. **19**, 277 (1978).

[177] E. Jones, T. Oliphant, P. Peterson, et al., *SciPy: Open source scientific tools for Python* (2001–), http://www.scipy.org/.

[178] M. Abramowitz and I. A. Stegun, *Handbook of Mathematical Functions* (Dover, New York, 1970), 9th ed.

François FERNIQUE
Collective plasmonic excitations in two-dimensional metamaterials based on near-field coupled metallic nanoparticles

Résumé

L'étude des propriétés plasmoniques est un champ de recherche actuellement très actif. En particulier, la possibilité de manipuler la lumière à des échelles sub-longueur d'ondes rend ce domaine très attractif. Récemment, plusieurs études ont montré que les plasmons collectifs dans des méta-matériaux bi-dimensionnels constitués de nanoparticules métalliques se comportaient de manière similaire aux électrons dans les cristaux et partageaient certaines de leurs propriétés. Dans ce manuscrit, nous présentons une théorie unifiée permettant de décrire les propriétés de tels modes plasmoniques dans des réseaux ordonnés de géométrie arbitraires constitués de nanoparticules métalliques couplées en champ proche. En particulier, nous évaluons les taux de décroissance de ces modes ainsi que leurs décalages en fréquence afin de prédire leur observabilité expérimentale.

Mots-clés : Matière condensée, méta-matériaux, plasmonique, taux de décroissance, effets retard

Summary

The study of plasmonic properties is one of the fields of research currently very active. In particular, the ability to manipulate light at subwavelength scales makes this subject very appealing. Recently, several studies have shown that collective plasmons in two-dimensional meta-materials based on metallic nanoparticles behave similarly to electrons in crystals and share some of their properties. In this manuscript, we present a unified theory for describing the properties of such modes in regular arrays of arbitrary geometries constituted by near-field coupled spherical nanoparticles. In particular, we have evaluated the linewidths of these modes as well as their frequency shifts in order to discussed their experimental observabilities.

Key-words : Condensed Matter, metamaterials, plasmonic excitations, decay rates, retardation effects